TECHNISCHE
UNIVERSITÄT
DRESDEN

Emergence and Breakdown of Quantum Scale Symmetry: From Correlated Condensed Matter to Physics Beyond the Standard Model

Dissertation
zur Erlangung des Hochschulgrades
Doctor rerum naturalium (Dr. rer. nat.)

vorgelegt von

SHOURYYA RAY
geboren am 03.02.1996 in Kolkata

Arbeitsgruppe Quantum Critical Matter
Institut für Theoretische Physik
Fakultät Physik
Bereich Mathematik und Naturwissenschaften
Technische Universität Dresden

2022

1. Gutachter: Prof. Dr. Matthias Vojta
2. Gutachter: Prof. Dr. Holger Gies
3. Gutachter: Dr. Lukas Janssen

Abgabedatum:
Datum der Disputation:

Abstract

Scale symmetry is notoriously fickle: even when (approximately) present at the classical level, quantum fluctuations often break it, sometimes rather dramatically. Indeed, contemporary physics encompasses the study of very different phenomena at very different scales, e.g., from the (nominally) meV scale of spin systems, via the eV of electronic band structures, to the GeV of elementary particles, and possibly even the 10^{19} GeV of quantum gravity. However, there are often – possibly surprising – analogies between systems across these seemingly disparate settings. Studying the possible emergence of quantum scale symmetry and its breakdown is one way to systematically exploit these similarities, and in fact allows one to make testable predictions within a unified technical framework (viz., the renormalization group). The aim of this thesis is to do so for a few explicit scenarios. In the first four of these, quantum scale symmetry emerges in the long-wavelength limit near a quantum phase transition, over length scales of the order of the correlation length. In the fifth example, quantum scale symmetry is restored at very high energies (i.e., at and above the Planck scale), but severely constrains the phenomenology at 'low' energies (e.g., at accelerator scales), despite scale invariance being badly broken there.

We begin with the Gross–Neveu (= chiral) SO(3) transition in $D = 2+1$ spacetime dimensions, which notably has been proposed to describe the transition of certain spin-orbital liquids to antiferromagnets. The chiral fermions that suffer a spontaneous breakdown of their isospin symmetry in this setting are fractionalized excitations (called spinons), and are as such difficult to observe directly in experiment. However, as gapless degrees of freedom, they leave their imprint on critical exponents, which may hence serve as a diagnostic tool for such unconventional excitations. These may be computed using (comparatively) conventional field-theoretic techniques. Here, we employ three complementary methods: a three-loop expansion in $D = 4-\epsilon$ spacetime dimensions, a second-next-leading order expansion in large flavour number N, and a non-perturbative calculation using the functional renormalization group in the improved local potential approximation. The results are in fair agreement with each other, and yield combined best-guess estimates that may serve as benchmarks for numerical simulations, and possibly experiments on candidate spin liquids.

We next turn our attention to spontaneous symmetry breaking at zero temperature in quasi-planar (electronic) semimetals. We begin with Luttinger semimetals, i.e., semimetals where two bands touch quadratically at isolated points of the Brioullin zone; Bernal-stacked bilayer graphene (BBLG) within certain approximations is one example. Luttinger semimetals are unstable at infinitesimal 4-Fermi interaction towards an ordered state (i.e., the field theory is asymptotically free rather than safe). Nevertheless, since the interactions are marginal, there are several pathologies in the critical behaviour. We show how these pathologies may be understood as a collision between the IR-stable Gaußian fixed point and a critical fixed point distinct from the Gaußian one in $d = 2+\epsilon$ spatial dimensions. Observables like the order-parameter expectation value develop essential rather than power-law singularities; their exponent, as shown herein by explicit computation for the minimal model of two-component 'spinors', is distinct from the mean-field one. More tellingly, although finite critical exponents often default to canonical power-counting values, the susceptibility exponent turns out to be one-loop exact, and, in said minimal model takes the value $\gamma = 2\gamma_{\text{mean-field}} = 2$. Such an exact yet non-mean-field prediction can serve as a useful benchmark for numerical methods.

We then proceed to scenarios in $D = 2+1$ spacetime dimensions where Dirac fermions can arise from Luttinger fermions due to low rotational symmetry. In BBLG, the 'Dirac from Luttinger' mechanism can occur both due to explicit and spontaneous breaking of rotational symmetry. The explicit symmetry breaking is due to the underlying honeycomb lattice, which only has C_3 symmetry around the location of the band crossings (so-called K points). As a consequence, the quadratic band crossing points each split into four Dirac cones, which is shown explicitly by computing the two-loop self-energy in the 4-Fermi theory. Within our approximations, we can estimate the critical coupling upto which a semimetallic state survives; it is finite (unlike a quadratic band touching point with high rotational symmetry), but significantly smaller than a vanilla Dirac semimetal. Based on the ordering temperature of BBLG, our rough estimate further shows that the (effective) coupling strength in BBLG may be close to the critical value, in sharp contrast to other quasi-planar Dirac semimetals (such as monolayer graphene). Rotational symmetry in BBLG may also be broken spontaneously, i.e., due to the presence of nematic order, whereby a quadratic band crossing splits into two Dirac cones. Such a scenario is also very appealing for BBLG, since the precise nature of the ordered ground state of BBLG has not been established unambiguously: whilst some experiments show an insulating ground state with a full bulk gap, others show a partial gap opening with four isolated linear band crossings. Here, we show within a simplified phenomenological model using mean-field theory that there exists an extended region of parameter space with coexisting nematic and layer-polarized antiferromagnetic order, with a gapless nematic phase on one side and a gapped antiferromagnetic phase on the other. We then show that the nematic-to-coexistence quantum phase transition has emergent Lorentz invariance to one-loop in $D = 2 + \varepsilon$ as well as $D = 4 - \epsilon$ dimensions, and thus falls into the celebrated Gross–Neveu Heisenberg universality class. Combining previous higher-order field-theoretic results, we derive best-guess estimates for the critical exponents of this transition, with the theoretical uncertainty coming out somewhat smaller than in the monolayer counterpart due to the enlarged number of fermion components. Overall, BBLG may hence be a promising candidate for experimentally accessible Gross–Neveu quantum criticality in $D = 2 + 1$ spacetime dimensions.

Finally, we turn our attention to the 'low-energy' consequences of transplanckian quantum scale symmetry. Extensions to the Standard Model that tend to lower the Higgs mass have many phenomenologically attractive properties (e.g., it would allow one to accommodate a more stable electroweak vacuum). Dark matter is one well-motivated candidate for such an extension. However, even in the most conservative settings, one usually has to contend with a significantly enlarged number of free parameters, and a concomitant reduction of predictivity. Here, we investigate how asymptotic safety (i.e., imposing quantum scale symmetry at the Planck scale and above) may constrain the Higgs mass in Standard Model (plus quantum gravity) when coupled to Yukawa dark matter via a Higgs portal. Working in a toy version of the Standard Model consisting of the top quark and the radial Higgs mode, we show within certain approximations that the Higgs mass may be lowered by the necessary amount if the dark scalar undergoes spontaneous symmetry breaking, as a function of the dark scalar mass, which is the only free parameter left in the theory.

Kurzfassung

Skalensymmetrie ist notorisch für ihre Unbeständigkeit: Selbst wenn sie auf klassischer Ebene (annähernd) gilt, wird sie durch Quantenfluktuationen meist gebrochen, manchmal mit recht dramatischem Ergebnis. In der Tat befasst sich die gegenwärtige Physik mit sehr unterschiedlichen Phänomenen auf sehr unterschiedlichen Skalen, z.B. von der (nominellen) meV-Skala von Spinsystemen, über die eV-Skala elektronischer Bandstrukturen, bis hin zur GeV-Skala von Elementarteilchen – und eventuell sogar der 10^{19} GeV-Skala von Quantengravitation. Es gibt jedoch erstaunlich häufig (möglicherweise überraschende) Analogien zwischen Systemen in diesen scheinbar so verschiedenen Bereichen. Die Untersuchung der möglichen Emergenz von Quantenskalensymmetrie und ihrer Brechung ist eine Art und Weise, diese Ähnlichkeiten systematisch auszunutzen; tatsächlich erlaubt diese Vorgehensweise sogar, prüfbare Vorhersagen innerhalb eines vereinheitlichten technischen Rahmens (nämlich der Renormierungsgruppe) zu machen. Das Ziel dieser Arbeit ist es, ebendies für einige explizite Szenarien zu tun. In den ersten vier dieser Szenarien tritt die Quantenskalensymmetrie im Limes langer Wellenlängen in der Nähe eines Quantenphasenübergangs auf, über Längenskalen in der Größenordnung der Korrelationslänge. Im fünften Beispiel wird die Quantenskalensymmetrie bei sehr hohen Energien (d.h. bei und oberhalb der Planck-Skala) wiederhergestellt, schränkt aber die Phänomenologie bei „niedrigen“ Energien (z.B. bei für Teilchenbeschleuniger relevanten Skalen) stark ein, obwohl die Skaleninvarianz dort stark gebrochen ist.

Wir beginnen mit einem Studium des Gross–Neveu (= chiralen) SO(3) Übergangs in $D = 2+1$ Raumzeitdimensionen. Insbesondere fällt der Übergang einer bestimmten Klasse von Spin-Orbital-Flüssigkeiten zu Antiferromagneten in diese Universalitätsklasse. Die chiralen Fermionen, deren Isospinsymmetrie spontan gebrochen wird, stellen in diesem Zusammenhang fraktionalisierte Anregungen (sog. Spinonen) dar, welche als solche schwer – wenn überhaupt – direkt experimentell beobachtbar sind. Dennoch hinterlassen sie als Anregungen ohne Energielücke ihren Abdruck auf kritischen Exponenten, welche sodann als ein diagnostisches Mittel für solche unkonventionelle Anregungen dienen können. Die kritischen Exponenten wiederum können mit (vergleichsweise) konventionellen feldtheoretischen Techniken berechnet werden. Hier verwenden wir drei sich gegenseitig ergänzende Methoden: Eine Entwicklung zur Dreischleifenordnung in $D = 4 - \epsilon$ Raumzeitdimensionen, eine Entwicklung in großer Flavourzahl N inklusive Korrekturen zweiter Ordnung zum führenden Beitrag, und eine nichtperturbative Rechnung mithilfe der funktionalen Renormierungsgruppe in der verbesserten Lokalpotentialapproximation. Die Ergebnisse der unterschiedlichen Methoden sind in akzeptabler Übereinstimmung miteinander, und liefern kombinierte Schätzungen, die als Vergleichswerte für künftige numerische Simulationen – und möglicherweise sogar für Experimente an Spinflüssigkeit-Kandidaten – dienen können.

Wir widmen uns dann der spontanen Symmetriebrechung bei Null Temperatur in quasiplanaren (elektronischen) Halbmetallen. Wir beginnen mit Luttinger-Halbmetallen, d.h., Halbmetalle, in denen sich zwei Bänder quadratisch an isolierten Punkten der Brillouinzone berühren; AB-geschichteter Zweilagengraphen (BBLG, engl. Bernal-stacked bilayer graphene) in gewisser Näherung ist ein Beispiel dafür. Luttinger-Halbmetalle sind instabil bei infinitesimaler 4-Fermi-Wechselwirkung gegenüber einem geordneten Grundzustand (d.h., die Feldtheorie ist asymptotisch frei anstelle statt sicher). Da diese Wechselwirkungen aber marginal sind, gibt es dennoch einige Pathologien im kritischen Verhalten. Wir zeigen, wie diese Pathologien als Folge einer Kollision zwischen dem IR-stabilen gaußschen Fixpunkt und einem kritischen Fixpunkt, der vom gaußschen Fixpunkt bei $d = 2 + \epsilon$ räumlichen Dimensionen verschieden ist, verstanden werden können. Observablen wie der Erwartungswert des Ordnungsparameters weisen wesentliche Singularitäten auf, anstelle von Singularitäten, die durch Potenzgesetze beschrieben werden können. Der Exponent dieser wesentlichen Singularitäten, wie hier in einer expliziten Berechnung für das minimale Modell mit zweikomponentigen „Spinoren“ gezeigt wird, weicht klar vom Ergebnis der Molekularfeldtheorie ab. Ein bezeichnenderes Ergebnis ist, dass obwohl die meisten endlichen kritischen Exponenten ihre kanonische Werte annehmen, ist der Suszeptibilitätsexponent nicht kanonisch, aber einschleifenexakt, und nimmt im besagten minimalen Modell den Wert $\gamma = 2\gamma_{\text{kan.}} = 2$ an. Solche exakten und dennoch über Molekularfeldtheorie hinausgehende Resultate stellen nützliche Benchmarks für numerische Methoden dar.

Wir wenden uns danach Szenarien in $D = 2 + 1$ Raumzeitdimensionen zu, wo Dirac-Fermionen aus Luttinger-Fermionen aufgrund niedriger Rotationssymmetrie hervorgehen können. In BBLG kann der „Dirac aus Luttinger“-Mechanismus sowohl durch explizite als auch spontane Brechung der Rotationssymmetrie realisiert sein. Der Ursprung der expliziten Symmetriebrechung ist das dem Graphen zugrundeliegende Honigwabengitter, welches nur C_3-Symmetrie um die Berührungspunkte der Bänder aufweisen. Als Folge davon spaltet sich jeder quadratische Bandberührungspunkt in vier Dirac-Punkte auf, was wir durch eine explizite Berechnung der Selbstenergie zur Zweischleifenordnung in der 4-Fermi-Theorie zeigen. Im Rahmen unserer Näherung können wir die kritische Wechselwirkungsstärke bestimmen, bis zu der ein halbmetallischer Grundzustand überlebt; sie ist endlich (im Gegensatz zu einem Luttinger-Halbmetall mit hoher Rotationssymmetrie), aber viel kleiner als wenn die Dispersion in der Nähe der Bandberührungspunkte von Anfang an linear gewesen wäre. Mithilfe dieser Rechnung können wir desweiteren, ausgehend von der Ordnungstemperatur von BBLG, grob die (effektive) Kopplungsstärke in BBLG abschätzen. Sie kommt in der Nähe der kritischen Kopplung heraus, im starken Gegensatz zu anderen quasi-planaren Dirac-Materialen (z.B. Einlagengraphen). Rotationssymmetrie kann in BBLG auch spontan – d.h., in Anwesenheit nematischer Ordnung – gebrochen sein. Dabei spaltet ein quadratischer Bandberührungspunkt in zwei Dirac-Punkte auf. Solch ein Szenario ist ebenfalls in BBLG naheliegend, da die genaue Natur des geordneten Grundzustands von BBLG noch nicht abschließend geklärt ist: Während manche Experimente einen isolierenden Grundzustand mit einer vollen Energielücke finden, weisen andere Experimente auf eine teilweise geöffnete Energielücke mit vier linearen Bandkreuzungen hin. Hier zeigen wir in einem vereinfachten phänomenologischen Modell mittels Molekularfeldtheorie, dass es einen ausgedehnten Bereich im Parameterraum gibt, wo nematische und antiferromagnetische Ordnung koexistieren. Auf der einen Seite diesen Bereichs gibt es eine nematische Phase ohne Energielücke, auf der anderen eine antiferromagnetische Phase mit voller Energielücke. Wir zeigen dann, dass am Übergang von der nematischen in die Koexistenzphase Lorentzsymmetrie emergent ist, zur Einschleifenordnung in $D = 2 + \varepsilon$ und $D = 4 - \epsilon$ Raumzeitdimensionen; der Übergang fällt daher in die berühmte Gross–Neveu–Heisenberg Universalitätsklasse. Insgesamt könnte daher BBLG einen vielversprechenden Kandidaten für experimentell zugängliche Gross–Neveu-Kritikalität in $D = 2 + 1$ Raumzeitdimensionen darstellen.

Schließlich widmen wir uns den „Niederenergie“-Konsequenzen von transplanckscher Quantenskalensymmetrie. Erweiterungen des Standardmodells, welche tendenziell die Higgsmasse erniedrigen, haben viele attraktive Eigenschaften (z.B. würde es ein stabileres elektroschwaches Vakuum zulassen). Dunkle Materie ist ein fundierter Kandidat für eine solche Erweiterung. Allerdings gibt es selbst in den konservativsten Szenarien in der Regel sehr viele zusätzliche freie Parameter, und eine entsprechend erniedrigte Vorhersagekraft. Hier untersuchen wir, wie asymptotische Sicherheit (d.h., die Annahme, dass ab der Planck-Skala Quantenskalensymmetrie herrscht) die Higgsmasse im Standardmodell (mit Quantengravitation), gekoppelt an Yukawa dunkle Materie über ein Higgs-Portal, einschränken kann. Wir rechnen in einer Spielzeugversion des Standardmodells bestehend aus dem Top-Quark und der radialen Mode des Higgsbosons, und zeigen im Rahmen gewisser Approximationen, dass die Higgsmasse um die benötigte Menge gesenkt werden kann, vorausgesetzt im dunklen Sektor findet spontane Symmetriebrechung statt, als Funktion der Masse des dunklen Skalarbosons, welche als einziger freier Parameter in der Theorie übrig bleibt.

The compilation of this thesis is solely due to the author. It does, however, draw heavily upon work done by the author in collaboration with others and published previously over the course of several articles. These publications, whence material is used hereinafter without further reference, are listed below in anti-chronological order, along with the Chapters in the thesis where they primarily appear, for the reader's convenience.

- Eichhorn, A.; Pauly, M.; and Ray, S. (2021): Towards a Higgs mass determination in asymptotically safe gravity with a dark portal. *J. High Energy Phys.* **10** 100 — Chapter 7.
- Ray, S.; and Janssen, L. (2021): Gross-Neveu-Heisenberg criticality from competing nematic and antiferromagnetic orders in bilayer graphene. *Phys. Rev. B* **104** 045101 — Chapter 6.
- Ray, S.; Ihrig, B.; Kruti, D.; Gracey, J. A.; Scherer, M. M.; and Janssen, L. (2021): Fractionalized quantum criticality in spin-orbital liquids from field theory beyond the leading order. *Phys. Rev. B* **103** 155160 — Chapter 3.
- Ray, S.; Vojta, M.; and Janssen, L. (2020): Soluble fermionic quantum critical point in two dimensions. *Phys. Rev. B* **102** 081112(R) — Chapter 4.
- Ray, S.; Vojta, M.; and Janssen, L. (2018): Quantum critical behavior of two-dimensional Fermi systems with quadratic band touching. *Phys. Rev. B* **98** 245128 (Editors' Suggestion) — Chapter 5.

Contents

1 Introduction 1

1.1 Scale invariance – why and where . . . 1

1.1.1 Fundamental quantum field theories . . . 2

1.1.2 Universality . . . 3

1.1.3 Novel phases of matter . . . 6

1.2 Outline of this thesis . . . 9

2 Renormalization Group: A Brief Review 11

2.1 Quantum fluctuations and generating functionals . . . 11

2.2 Renormalization group flow . . . 13

2.3 Basic notions . . . 17

2.4 Scale transformations, scale symmetry and RG fixed points . . . 20

2.5 Characterization and interpretation of RG fixed points . . . 23

2.5.1 Formal aspects . . . 23

2.5.2 Scaling at (quantum) phase transitions . . . 26

2.5.3 Predictivity in fundamental physics . . . 34

2.5.4 Effective asymptotic safety in particle physics and condensed matter 37

3 Gross–Neveu SO(3) Quantum Criticality in $2 + 1$ Dimensions 39

3.1 Effective field theory . . . 42

3.2 Renormalization and critical exponents . . . 43

3.2.1 $4 - \epsilon$ expansion . . . 43

3.2.1.1 Method . . . 43

3.2.1.2 Flow equations . . . 44

3.2.1.3 Critical exponents . . . 45

3.2.2 Large-N expansion . . . 47

3.2.2.1 Method . . . 47

3.2.2.2 Critical exponents . . . 50

3.2.3 Non-perturbative FRG . . . 51

3.2.3.1 Flow equations . . . 53

3.2.3.2 Representation of the effective potential . . . 57

3.2.3.3 Choice of regulator . . . 59

3.2.3.4 Limiting behaviour . . . 60

3.3 Discussion . . . 62

3.3.1 General behaviour and qualitative aspects . . . 62

3.3.2 Quantitative estimates for $D = 3$ . . . 63

3.4 Summary and outlook . . . 65

4 Luttinger Fermions in Two Spatial Dimensions 69
- 4.1 Introduction . . . 69
- 4.2 Action from top-down construction . . . 72
- 4.3 Renormalization . . . 74
  - 4.3.1 4-Fermi formulation . . . 76
  - 4.3.2 Yukawa formulation . . . 77
- 4.4 Fixed-point analysis . . . 80
- 4.5 Non-mean-field behaviour . . . 83
  - 4.5.1 Order-parameter expectation value . . . 83
  - 4.5.2 Susceptibility exponent . . . 86
- 4.6 Bottom-up construction: Spinless fermions on kagome lattice . . . 86
  - 4.6.1 Tight-binding dispersion . . . 87
  - 4.6.2 From Hubbard to Fermi . . . 89
  - 4.6.3 Fate of particle-hole asymmetry . . . 90
- 4.7 Discussion . . . 91

5 Dirac from Luttinger I: Explicit Symmetry Breaking 93
- 5.1 From lattice to continuum . . . 96
  - 5.1.1 Fermions on Bernal-stacked honeycomb bilayer . . . 96
  - 5.1.2 Continuum limit . . . 98
  - 5.1.3 Interactions . . . 101
- 5.2 Mean-field theory . . . 102
- 5.3 Renormalization-group analysis . . . 104
  - 5.3.1 Flow equations . . . 104
  - 5.3.2 Basic flow properties . . . 107
  - 5.3.3 Phase diagrams . . . 109
- 5.4 Discussion . . . 111
- 5.5 Summary and outlook . . . 115

6 Dirac from Luttinger II: Spontaneous Symmetry Breaking 117
- 6.1 Model . . . 119
- 6.2 Phase diagram and transitions . . . 121
- 6.3 Emergent Lorentz symmetry . . . 124
  - 6.3.1 Loop expansion near lower critical dimension . . . 126
    - 6.3.1.1 Minimal 4-Fermi model . . . 126
    - 6.3.1.2 Gross–Neveu–Heisenberg fixed point . . . 127
    - 6.3.1.3 Fate of rotational symmetry breaking . . . 128
  - 6.3.2 Loop expansion near upper critical dimension . . . 129
    - 6.3.2.1 Gross–Neveu–Yukawa–Heisenberg model . . . 129
    - 6.3.2.2 Gross–Neveu–Yukawa–Heisenberg fixed point . . . 130
    - 6.3.2.3 Fate of rotational symmetry breaking . . . 130
- 6.4 Critical exponents . . . 132
- 6.5 Discussion . . . 136

7 Higgs Mass in Asymptotically Safe Gravity with a Dark Portal 139
- 7.1 Review: The asymptotic safety scenario for quantum gravity and matter . 142
- 7.2 Review: Higgs mass, and RG flow in the SM and beyond . . . 143
  - 7.2.1 Higgs mass in the SM . . . 143
  - 7.2.2 Higgs mass bounds in bosonic portal models . . . 145

7.2.3 Higgs mass in asymptotic safety 146
7.2.4 Higgs Portal and Asymptotic Safety 150
7.3 Higgs mass in an asymptotically safe dark portal model 151
7.3.1 The UV regime 154
7.3.2 Flow towards the IR 157
7.3.3 Infrared masses 157
7.3.4 From the UV to the IR – Contrasting effective field theory and asymptotic safety 158
7.4 Discussion 160

8 Conclusions **163**

Appendices **167**
A Position-space propagator for C_3-symmetric QBT 167
B Two-sided Padé approximants for C_3-symmetric QBTs 168
C Corrections to the mean-field nematic order-parameter effective potential due to explicit symmetry breaking 169
D Self-energy in anisotropic Yukawa theory 171
E Master integrals for anisotropic Yukawa theory 173

Bibliography **175**

Chapter 1

Introduction

> *'If you tell yourself something over and over again, right or wrong, it becomes intuitive.'*
>
> Sidney Coleman (1937–2007)

Symmetries and their breakdown by various mechanisms in particular are something of a leitmotif in modern theoretical physics. As far as broken symmetries go, scale symmetry may be considered one of its most ubiquitous exponents. Classically, for a field theory to be scale invariant, it is sufficient to ensure all couplings are dimensionless. However, corrections due to quantum fluctuations(1) break scale invariance – the symmetry is no longer valid at the quantum level, it is said to be anomalous. Contemporary experimental physics encompasses the study of an immense multitude of scales, from the inverse TeV of particle accelerators such as the LHC to the intergalactic scales studied by gravitational wave detectors such as LIGO. Owing to the anomaly of scale symmetry, the physics at different scales in general (and the pertinent degrees of freedom at said scales in particular) may be vastly different. A particle accelarator operating at high enough energies 'sees' (for instance in a proton-proton collision) the constituent quarks interacting by exchanging virtual gluons. At lower energies, such as in an atom, these quarks appear only in triquark bound states, viz., neutrons and the afore-mentioned protons; the virtual quanta they exchange to interact with each other are mesons, themselves quark-antiquark bound states. Strictly speaking, quarks have masses, and hence scale invariance is broken already at the classical level. However, the breaking of scale symmetry due to the non-vanishing quark masses pales in the face of the scale-dependence induced by quantum effects (in this case colour confinement).

1.1 Scale invariance – why and where

Scale symmetry is thus one whose breakdown at the quantum level appears almost inevitable in generic situations. Nevertheless, the study of quantum scale symmetry – along with the concomitant search for the special conditions and systems that allow its realization – turns out to be useful, both for conceptual as well as practical reasons. Let us briefly discuss these reasons in the following.

---

(1) The same is true, *mutatis mutandis*, if the fluctuations are of a thermal nature rather than quantum, as is the case in statistical field theory. The difference is essentially one of Wick rotation, and one we shall not have occasion to pay much attention to during the course of this work.

1.1.1 Fundamental quantum field theories

From the conceptual viewpoint, fundamental quantum field theories[2] are notoriously tricky objects to deal with in a mathematically sound way. Constructing such an object by the usual procedure of quantizing a classical field theory entails evaluating a path integral, which is (informally speaking) an integral with an uncountably infinite domain of integration. Giving a mathematically rigorous meaning to this procedure turns out to be possible in general only for theories that are non-interacting, or can be expanded – at least formally – in a perturbative series near a non-interacting theory. The situation improves if some additional symmetry can be imposed, which would then constrain, e.g., the correlation functions of the full quantized theory. Scale symmetry turns out to be particularly powerful in this regard. In many applications, scale invariance in fact implies *conformal* symmetry (i.e., spacetime transformations that locally preserve angles). This poses constraints so severe that the theory can (at least in principle) be determined uniquely from symmetry considerations alone, without having to confront the path integral – or the ill-definedness thereof, as it were – as an intermediate step. Figuratively, scale invariance thus serves as 'bootstraps' by which the theory pulls itself up (and into mathematically rigorous existence). Indeed, such bootstrap programmes (most prominently the so-called conformal bootstrap) constitute a major part of the current arsenal used to non-perturbatively solve quantum field theories, with many remarkable successes to date.[3] Field theories that exhibit quantum scale symmetry hence act as 'signposts' or 'markers' in the grander endeavour of charting out the landspace of all quantum field theories.

Beyond purely abstract mathematical curiosity, there is one physical context where it is conceptually essential to have a fundamental theory (as opposed to one that is valid only up to a specific scale), viz. the 'Theory of Everything' in elementary particle physics. The Standard Model has survived all experimentally accessible tests thus far; nevertheless, there are theoretical indications that it cannot be the complete story. First, there is the so-called 'triviality' problem which plagues the U(1) gauge sector. This means the fine-structure constant grows beyond bounds and hits a pole (a so-called Landau pole) at some finite scale. This would mean that only the non-interacting (hence 'trivial') version of the theory can be extended to arbitrary scales. The observation that the photon interacts in the infrared with other Standard Model particles (e.g., the existence of a Coulomb interaction between electrically charged particles) negates this scenario. Although the existence of the Landau poles in the Standard Model has been established primarily using perturbation theory, a non-perturbative resolution within the Standard Model has not been found yet. A second reason concerns the fundamental forces of Nature. Although the Standard Model contains the strong and electroweak forces, gravitation is missing completely. Assuming that gravity must be quantized and quantum gravity ultimately will exhibit experimentally measurable consequences at high enough energies (say, at the Planck scale), an extension of the Standard Model must at least contain the graviton. In principle, many extensions to the Standard Model are conceivable, that alleviate (at least some of) these problems. A rather intriguing resolution of both problems is offered by the imposition of (approximate) scale invariance at high energies. In the gravitational context, this programme specifically proposes that at high energies, the (quantized form of the) Einstein–Hilbert action ultimately flows to an interacting scale-invariant theory. In the literature, this is called *asymptotic safety*, following nomenclature introduced by Weinberg (1979). Asymptotic safety may be understood as a generalization of asymptotic freedom to allow for interacting UV-attractive fixed points: recall the similar-sounding notion of asymptotic *freedom*, which is enjoyed by certain non-abelian gauge theories such as quantum chromodynamics (QCD), to quote an example from within the Standard Model. This is tantamount to saying the Gaußian fixed point is UV-attractive. [At asymptotically high energy scales, the theory becomes free (in the sense of non-interacting), hence the name.] The theoretical existence of an asymptotically safe fixed point (the so-called Reuter–Saueressig fixed point) has been confirmed in pure gravity, and it has been shown to be capable of accommodating Standard Model matter; cf., e.g., the textbook of Reuter & Saueressig (2019) for a more detailed account. The proposed scenario is 'minimal' in some sense. For one thing, it does not entail the introduction of new particles beyond the graviton, which may be contrasted with a different symmetry principle such as supersymmetry, which does have the potential to cure (at least to some extent) the proliferation of divergences in perturbation theory (roughly speaking due to the compensating effect of fermions and bosons), but requires a plethora of additional – as of now yet to be observed – particles. It does not necessitate the abandonment of quantum field theory as the ultimate framework of fundamental physics either – unlike, say, string theory. Remarkably, it turns out that this way of solving the gravity problem might also furnish a solution to the triviality problem: Gravity fluctuations modify the running of Standard Model couplings such that those featuring a Landau pole in the absence of quantum gravity become either asymptotically safe or free in its presence.

---

[2] Here and henceforth, we understand a theory to be 'fundamental' if it does not need a short-distance (= ultraviolet, UV) cut-off, or some other equivalent UV regularization, assuming appropriate renormalization of couplings; they are also called UV-complete. Since high energies/momenta correspond to small length scales, UV-completeness means that there is no microscopic structure more fundamental than what is already contained in the theory.

[3] We have nothing to add to the bootstrap literature *per se* in this thesis, but the interested reader is referred to Rychkov (2017) for a more detailed pedagogical introduction as well as further information.

1.1.2 Universality

Reassuringly enough, physical realizations of quantum scale symmetry are not restricted to the trans-Planckian regime. At comparatively terrestrial scales, quantum scale symmetry can be *emergent* in the low-energy limit, as opposed to being restored at high energies. [In terms of the renormalization group (RG), which we shall review in more detail in Chap. 2, this means that we now need to look at fixed points that are – predominantly – attractive towards the infrared (IR).] More specifically, it turns out that quantum scale symmetry emerges at long distances – i.e., in the IR – when (some other) symmetry spontaneously breaks down, provided the order parameter characterizing the ordered (or equivalently, symmetry-broken) phase remains continuous across the transition. These are precisely the so-called continuous phase transitions. The closer one is to such a transition, the longer the length scale (called the *correlation length*) over which correlations of the order parameter fluctuations persist. This corresponds to probing the deep infrared behaviour of the corresponding low-energy effective field theory. At the transition itself, the correlation length diverges; the erstwhile exponential decay of correlation functions is turned into power-law decay, thus signalizing the emergence of scale invariance. Furthermore, observables such as the size of the order parameter (on the symmetry-broken side), the correlation length itself, and other thermodynamic quantities such as specific heat exhibit power-law scaling as a function of distance to criticality.4) The scaling behaviour

---

4) Measurements on a real system will invariably also pick up on background contributions that remain smooth across the transition. Like any background, this has to be subtracted (or modelled separately) before comparing to theory predictions. We shall neglect this background throughout this thesis.

of observables at or near criticality is called critical scaling, and the exponents associated with the power laws are called *critical exponents.* Schematically, this takes the form

$$Y \propto \left(\frac{r - r_{\mathrm{c}}}{r_{\mathrm{c}}}\right)^{\varkappa_Y} \tag{1.1}$$

where Y is a generic observable sensitive to the critical behaviour, $\varkappa_Y$ is the corresponding critical exponent, r is the parameter that tunes the system through the transition and r_{c} its critical value. If r corresponds to temperature, the transition is called a *thermal* phase transition. If r corresponds to a non-thermal parameter (e.g., pressure) and takes place at zero temperature, it is called a *quantum* phase transition (as the transition takes place at zero temperature, the ordered state can only be destroyed by quantum fluctuations).

It turns out the critical exponents are independent of microscopic details of the system in question, and depend only on a few macroscopic characteristics. This is called *universality* – a fact which is not only intellectually remarkable (though a prosaic explanation can be given using the renormalization group), but also useful in practice. Quantum many-body effects allow Nature – aided and abetted by human engineering – to realize a veritable cornucopia of different phases of matter. Critical scaling behaviour of phases in the vicinity of continuous phase transitions equip the 'space' of all continuous transitions between phases of matter with a notion of equivalence and furnish a first classification principle: if two phases of matter show the same critical exponents when one or more of their symmetries are being spontaneously broken (or restored), the assorted transitions are said to be in the same *universality class.*

Whilst critical exponents are insensitive to the finer microscopic details, they are sensitive to those properties of a system that dominate the long-ranged (or equivalently, low-energy) behaviour: the gapless degrees of freedom. In the majority of conventional systems, these are precisely the order-parameter fluctuations, which become gapless precisely at criticality; the universality class is then uniquely determined by the symmetry of the order parameter and the dimensionality of the system. This is usually referred to as the Ginzburg–Landau paradigm. Although the critical exponents follow directly thence in principle, the required calculation is still quite challenging in practice, and affords scope for the application (and refinement) of many sophisticated theoretical techniques. The liquid-to-superfluid transition (often abbreviated to 'lambda transition') in helium-4 may be seen as something of a poster child in this regard, replete even with a figurative 'arms race' between theory and experiment devoted to determining its critical exponents. On the theoretical side, an expansion to six-loop plus Borel resummation has been performed (Guida & Zinn-Justin 1998). In numerical Monte Carlo simulations, linear lattice sizes of up to $L = 512$ (corresponding to $\approx 10^8$ lattice sites in total) have been reached by Hasenbusch (2019). On the experimental side, the singular behaviour of the specific heat has been measured to such a high precision that the experiments had to be performed in a space shuttle in order to reduce the influence of the earth's gravitational field on the critical temperature along the height of the sample (Lipa *et al.* 2003). The significance of superfluid helium-4, however, goes beyond the classification of transitions between phases of matter. One can show that every phase transition governed by – in technical terms – an interacting renormalization group fixed point furnishes an example of asymptotic safety (see Chap. 2 for said technical details); or, as expressed more polemically by Alexander Markovich Polyakov, universality allows one to 'learn about elementary particles by boiling water'.[5] With the advantage of hindsight, the

---

[5] This direct quote goes back to an interview of Polyakov at Princeton in 2003 (see Ashrafi & Schweber

'arms race' between theory and experiment regarding the anomalous magnetic moment of the electron is now seen as a major catalyst in the development of Feynman diagrams and the perturbative theory of renormalization (Schweber 1994). Will we one day, with the advantage of similar hindsight, ascribe to the superfluid transition of helium-4 the same kind of significance with respect to the non-perturbative theory of renormalization and asymptotic safety?

As in any scientific discipline, progress beyond the status quo is made when phenomena that lie outside the conventional paradigm can be found. In the case of Ginzburg–Landau, a natural place to look for these are systems which host gapless excitations beyond order-parameter fluctuations. Quantum phase transitions in systems with non-vanishing Fermi surfaces constitute a prominent example in this regard; the fermionic excitations that 'live' on the Fermi surface are gapless[6] and produce significant corrections to the critical exponents. The simplest[7] realization of this are so-called *semimetals*, where the Fermi surface consists of isolated points (in reciprocal space).

The most well-known representative of this class of materials is graphene; in some sense, it may be seen as the 'superfluid helium-4' of this discipline. The band structure of systems like graphene with honeycomb lattic structure is such that there are linear band crossings at the corners (the so-called K-points) of the Brillouin zone. As a consequence, the low-energy excitations are fermions with massless relativistic dispersion. Following its experimental realization by Novoselov *et al.* (2004), graphene's potential as 'table-top particle accelerators' was soon recognized, and used to create efficient, experimentally accessible testing grounds for non-trivial predictions from relativistic quantum mechanics, such as Klein tunneling (Young & Kim 2009; Stander, Huard & Goldhaber-Gordon 2009) and zitterbewegung (Katsnelson 2009).[8] The interaction-induced quantum phase transition from a semimetallic ground state to a potential ordered one in graphene-like systems are described by so-called *chiral* (often also referred to as *Gross–Neveu*) versions of the corresponding bosonic universality class – i.e., the order-parameter field-theory is Yukawa-coupled to one or more species of chiral fermions (Rosenstein, Yu & Kovner 1993). For instance, the transition to a charge-density wave state, which breaks $\mathbb{Z}_2$ symmetry, is described by a Gross–Neveu–Ising universality class; a transition to an antiferromagnetic state, which breaks SU(2) spin rotation symmetry, falls in the Gross–Neveu–Heisenberg universality class. The precision achieved in determining critical exponents in these chiral universality classes falls some way short of the success achieved previously in

---

2003). A similar sentiment, but with 'elementary particles' replaced by 'deep inelastic scattering', is expressed in Polyakov (2012).

[6] It is crucial that the temperature is zero. To see that it is indeed so, recall that computing a partition function for a system in D spacetime dimensions corresponds to solving a Euclidean quantum field theory in $S^1(1/T) \times \mathbb{R}^{D-1}$, where $S^1(1/T)$ is a circle with the inverse temperature as radius. Along the compact direction, bosons (fermions) have (anti-)symmetric boundary conditions. A field ϕ can be expanded for $(\tau, \boldsymbol{x}) \in S^1(1/T) \times \mathbb{R}^{D-1}$ as $\phi(\tau, \boldsymbol{x}) = \sum_{n\in\mathbb{Z}} \mathrm{e}^{\mathrm{i}\omega_n \tau} \phi_n(\boldsymbol{x})$. (This is essentially a special case of the Kaluza–Klein decomposition.) Here, $\omega_n = 2\pi T(n + \eta/2)$ for $\eta = 0$ (1) are the bosonic (fermionic) Matsubara frequencies. At finite temperature, only the $\omega_n = 0$ can contribute. Thus, apart from effectively reducing the spacetime dimension $D \to D - 1$, it also excludes all fermions, since they have an $O(T)$ gap, from contributing to thermal phase transitions. At zero temperature, however, the gap vanishes: fermions contribute to quantum criticality, as long as they are otherwise gapless. Note also that $S^1(1/T) \times \mathbb{R}^{D-1} \to \mathbb{R}^D$ for $T \to 0$, i.e. there is no coresponding dimensional reduction.

[7] By simple, we mean tractable from an analytical point of view. Generically, the Fermi surface has codimension unity; in two or more spatial dimensions, there would hence be an uncountable infinitude of flavours. Whilst this often leads to a very rich phase diagram, controlled theoretical predictions are made very difficult.

[8] For a more in-depth review, see e.g. Castro Neto *et al.* (2009).

conventional Ginzburg–Landau criticality. In diagrammatic approaches, for example, the need to include an additional particle species leads to a proliferation of diagrams, not just in terms of absolute numbers, but also in terms of permissible diagram topologies and structures of necessary counterterms. The highest order in loop expansion (to name but one such field-theoretic approach) attained thus far is four, by Zerf *et al.* (2017); it is two orders lower than the case for loop expansion in scalar theories. Likewise, the system sizes accessible to numerical methods such as QMC is several orders of magnitude lower. Experimental estimates of graphene's critical exponents are also hard to come by, because graphene appears to be rather weakly interacting in its pristine form in the low-energy limit; in particular, it is too far from the critical interaction strength for spontaneous symmetry breaking to be triggered by the tuning of the usual external control parameters such as pressure.[9] Other materials are rather strongly-correlated and feature stable symmetry-broken ground states, and it is difficult to tune these into symmetric semimetallic phases. Examples in this class are honeycomb iridates or α-RuCl$_3$, in which the spin-orbit coupling is also strong (Shitade *et al.* 2009; Winter *et al.* 2017). Much like the energy frontier of (real) particle accelerators, this 'correlation frontier' is hence one of the current challenges in table-top accelerators, and subject of much on-going endeavour (see also the discussion in Chaps. 5 and 6). Just like the discussion above for helium-4, a similar comment in connection with asymptotic safety is valid: quantum criticality in two-dimensional Dirac semimetals constitute examples of asymptotic safety, with fermionic matter degrees of freedom. Given that all matter particles in the Standard Model (with the exception of the Higgs) are fermionic in nature, they hence provide an intriguing sandbox for ideas concerning asymptotically safe UV completions of the Standard Model. Experimental observation of quantum criticality in low-dimensional semimetals thus contain an additional (figurative) dimension of significance.

1.1.3 Novel phases of matter

The study of low-energy quantum scale symmetry is also closely related to the search for and investigation of novel phases of matter. This follows three main themes:

1.) Critical exponents as fingerprints. Most closely related to the discussion above, this line of inquiry exploits the sensitivity of critical exponents to any and all low-energy degrees of freedom. In particular, such degrees of freedom may be low-energy excitations of exotic ground states. An example is constituted by spin liquids, which are non-classical long-range entangled ground states of magnets with frustrated exchange interactions. They are often characterized by a semimetallic ground state, although the system had no mobile fermions to begin with. Rather, the fermionic degrees of freedom arise due to fractionalization of the local magnetic moments (for a more detailed review, cf., e.g., Vojta 2018). Such degrees of freedom are difficult to observe directly in experiment, as are the corresponding ground states, which are not characterized by a non-vanishing local order parameter, but instead by non-local topological order difficult to establish directly by measurement. However, when an exotic phase such as a spin liquid suffers breakdown of some symmetry, the critical exponent will be modified due to the presence of the novel low-energy excitations. If the state the spin liquid transitions into is a conventional one characterized by

---

[9] Note, however, that transition to ordered states has in fact been observed when an external magnetic field is applied (so-called *magnetic catalysis*). These ideas have in turn been further transported to the quantum gravity context in the form of *gravitational catalysis*. Such settings, however, break several symmetries explicitly, and is not within the scope of the present work.

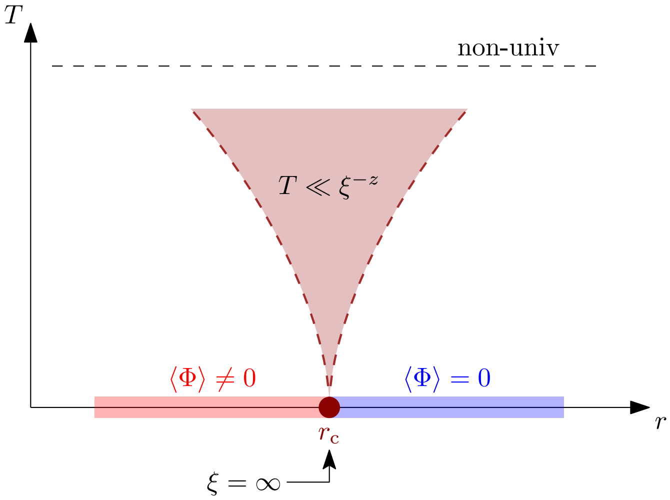

Figure 1.1: (Adapted from Vojta 2003) Quantum critical 'fan' at small but finite temperature associated with a quantum phase transition tuned by control parameter r and characterized by order parameter Φ. At the critical point $r = r_\mathrm{c}$ (maroon circle), the correlation length is infinite. For sufficiently small distance to criticality, $(r - r_\mathrm{c})/r_\mathrm{c} \ll 1$, the correlation length will still be very large, and practically infinite compared to the temperature, $\xi^z \gg 1/T$ (z is the so-called dynamical critical exponent and measures to what degree time scales differently from space at the RG fixed point). In this regime, marked light maroon, observables show scaling behaviour as a function of T. This extended region of the r–T phase diagram hence behaves as a scale invariant phase, although the underlying fixed point has an RG-unstable direction. The dashed line denotes a crossover to regimes where the length scales $T^{-1/z}$ and ξ are comparable in size and scaling behaviour no longer persists. At high enough temperatures, the physics is no longer governed by the zero temperature critical point, marked 'non-univ'. See also Chap. 2 of this thesis for more details, and the review of Vojta (2003) and textbooks such as Herbut (2007) or Sachdev (2010a) for even more details.

non-vanishing local order parameter, the transition will be amenable to detection by usual experimental techniques. Thus, the critical exponents will carry the 'fingerprints' of the erstwhile unconventional state and its emergent low-energy excitations. We shall use this principle ourselves in Chap. 3, where the spin(-orbital) liquid will have emergent fermions (called spinons) with an unusual SO(3) flavour symmetry, and a flavour number that would be uncompatible with Nielsen–Ninomiya theorem if the fermions were complex rather than Majorana. A similar analysis has also been performed for a so-called U(1) Dirac spin liquid, which features, in addition to fractionalized fermionic excitations, gapless excitations of an emergent U(1) gauge field in $D = 3$ spacetime dimensions (not to be confused with the photon of the Standard Model) described by QED$_3$, the three-dimensional analogue of quantum electrodynamics, cf. Janssen *et al.* (2020).

2.) *The quantum critical fan.* A quantum critical point strictly speaking demarcates the boundary between two phases, rather than signifying a phase by itself. Nevertheless, it turns out that in the r-T phase diagram (where T is temperature and r is the tuning parameter for the zero-temperature transition), there is an extended region that shows scale-invariant behaviour of observables as a function of temperature T (Fig. 1.1). Roughly speaking, if the correlation length is much larger than the inverse temperature, the system effectively 'feels' as though the correlation length is practically infinite. Interestingly, this region of the phase diagram often stretches out to rather high temperatures before non-universal effects take over (Vojta 2003), and – somewhat counter-intuitively – 'fans' out away from the critical point $r = r_\mathrm{c}$ at higher temperatures (Sachdev 2010a). If the corresponding RG fixed point is a non-trivial interacting one, then the quantum critical fan as a phase does not feature conventional quasiparticle excitations (i.e., the Green's function has a branch cut singularity rather than an algebraic pole), and the exponents deviate from canonical (e.g., Fermi-liquid-theory) values. As an example of high fundamental as well practical relevance, it has been suggested that the 'strange metal' phase of cuprate high-temperature superconductors may in fact be such a quantum critical fan (cf., e.g., Sachdev 2010b).

3.) Scale-invariant phases of matter. Finally, a stable phase of matter may itself be scale invariant – i.e., governed by a stable RG fixed point. As a matter of principle, this is not extraordinary *per se*: a Gaußian fixed point is often stable and, if all 'masses' vanish, corresponds to the symmetric phase. A perfectly ordinary semimetallic phase, such as the one in graphene, is described by a Gaußian fixed point; the free action $\int_x \bar{\psi}\partial\!\!\!/\psi$ is manifestly scale invariant due to the absence of dimensionful parameters (and there are no quantum corrections due to the absence of interactions). Truly novel phases arise, however, if a *non-Gaußian* fixed point turns out to be IR stable. In this case, one has a bona fide phase of matter with no quasiparticle excitations and non-trivial power laws for observables throughout an extended region of the phase diagram. Though we shall not encounter such scenarios directly in our studies, there are some notable examples in the literature worth mentioning here for completeness. A first example is QED$_3$, whose vacuum has been established to be in a conformal phase for sufficiently large flavour numbers10). QED$_3$ has been proposed to be an effective description for many exotic phases of matter from high-temperature superconductors11) to various avatars of spin liquids12). A beautiful non-abelian gauge-theory example in $D = 4$ spacetime dimensions is given by the Caswell–Banks–Zaks fixed point, which arises in SU(N_c) gauge theory with N_f fermion flavours, for suitable combination of N_f and N_c.13) An interesting non-relativistic realization, also in $D = 4$ spacetime dimensions14), is the Luttinger–Abrikosov–Beneslavskii non-Fermi liquid phase (Abrikosov & Beneslavskii 1971; Abrikosov 1974; Moon *et al.* 2013) which arises in 3D Luttinger semimetals (Luttinger 1956). These are materials where two (or more) bands touch *quadratically* at isolated points of the Brioullin zone, examples of which include grey tin, mercury telluride and some of the pyrochlore iridates (cf., e.g., Witczak-Krempa *et al.* 2014).

---

10) cf., e.g., Appelquist, Nash & Wijewardhana (1988); Hands *et al.* (2004); Braun *et al.* (2014); Raviv, Shamir & Svetitsky (2014); di Pietro *et al.* (2016); Herbut (2016); Janssen (2016). Some authors even suggest that the conformal phase may persist at all flavour numbers (Karthik & Narayanan 2016; Chester & Pufu 2016).

11) cf., e.g., Franz (Tešanović & Vafek); Herbut (2002); Hermele, Senthil & Fisher (2005)

12) cf., e.g., Hermele, Fisher & Balents (2004); Ran *et al.* (2007); He *et al.* (2015); Wang & Senthil (2016)

13) Named after the contributions of Caswell (1974) as well as Banks & Zaks (1982). For a review, see the book of Hollowood (2013).

14) Throughout this work, we shall *always* understand D to be the topological spacetime dimension of the quantum field theory. There is a somewhat different notion of effective dimension when the dynamical critical exponent z is different from unity, which is the scaling dimension of the D-dimensional spacetime volume element $\mathrm{d}^D x$, see Chap. 2 for a more detailed discussion. We shall always refer to this by some other symbol such as D_eff, but *never* D.

1.2 Outline of this thesis

The present thesis is concerned, in a nutshell, with the low-energy physics of quantum scale symmetry. The first four projects are devoted to the study of scenarios where quantum scale symmetry itself emerges at very long length scales, viz. the correlation length near a quantum phase transition, and characterizing the critical properties of said transitions. The last project takes the opposite point of view: assuming quantum scale symmetry to be restored in the deep UV, it asks to what extent the observable phenomenology in the infrared is constrained as a consequence. In some more detail, the roadmap below is the one we shall follow:

In **Chapter 2**, we shall review the formalism of the renormalization group. In modern language, the scale-dependence of physics is expressed in terms of renormalization group flow; finding quantum scale symmetry is then tantamount to finding the fixed point of this flow. The discussion in this Chapter will *inter alia* provide us the opportunity to recapitulate the infrared and ultraviolet perspectives on quantum scale symmetry in a simplified and abstract way, and serve as a conceptual framework for the discussion of the concrete physics in subsequent parts of the thesis.

In **Chapter 3**, we shall encounter our first concrete instance of quantum criticality: the Gross–Neveu SO(3) transition. Unlike its more well-known Ising or Heisenberg counterparts (studied more extensively due to their relevance in the graphene context), the SO(3) universality class has been proposed to describe the quantum phase transition from a certain type of spin-orbital liquid to an antiferromagnet. Spin liquids, as mentioned previously, are notoriously difficult to diagnose experimentally, since they are by definition phases of matter with long-ranged topological order; in particular, the chiral fermions arise microscopically in this realization due to a fractionalization of the underlying localized spin-orbital degrees of freedom, and cannot be 'seen' using usual experimental techniques. Nevertheless, like any gapless degrees of freedom, they leave their 'fingerprints' in the critical exponents. On the other hand, looking past the complicated microscopic connotations, the pertinent quantum field theory is a perfectly conventional Yukawa theory in $D = 3$ spacetime dimensions, and as such amenable to the machinery developed previously for related systems. The aim of this project is to use (several instances of) said machinery to obtain reliable predictions for critical exponents of such transitions, as a first step towards the grander long-term goal of exploiting critical exponents as part of the 'diagnostic toolkit' for quantum spin liquids.

In **Chapter 4**, we shall turn our attention to the quantum criticality of *Luttinger* fermions in $D = 3$. Unlike Dirac fermions, Luttinger fermions have a quadratic low-energy dispersion; it is unlikely they will ever appear as elementary particles (for instance in a hypothetical extension of the Standard Model), but they do emerge as quasiparticles in so-called quadratic band touching materials. From a field-theoretic perspective, this changes the canonical power counting, and makes the 4-Fermi theory of Luttinger fermions perturbatively renormalizable in $D = 3$. In low-energy language, the ground state of Luttinger fermions thus changes depending on the sign of the 4-Fermi interaction: for one sign, the semimetallic state wins, whilst for the opposite sign, a gap in the fermionic spectrum is generated dynamically. The critical value of the interaction strength is hence zero. Nevertheless, we shall see that certain exponents obtain quantum corrections (essentially because the order parameter is a local composite operator); however, the essentially Gaußian nature of the pertinent fixed point kills higher-order corrections and renders these quantities one-loop exact. In view of the general difficulty of calculating critical exponents of fermionic universality classes to high precision (cf.: Chap. 3), such predictions can serve as benchmarks for other methods that are not manifestly exact in this setting but become useful when the loop expansion does not converge, or does so only very slowly.

In **Chapters 5** and **6**, we shall revisit the issue of quantum criticality in Dirac semimetals being difficult to observe experimentally due to their effective interaction strength being too far from the critical point. The main ingredient will be the fact that Luttinger fermions have a weak-coupling instability, but can split into two or four Dirac fermions if the rotational symmetry is broken (the precise number of Dirac fermions per Luttinger fermion depends on the residual rotational symmetry). Chapter 5 concerns the explicit breaking of rotational symmetry down to C_3, whilst Chapter 6 considers the case where the symmetry breaking occurs spontaneously due to the onset of nematic order. Both mechanisms may be realized in Bernal-stacked bilayer graphene, and we shall argue that this material – unlike its decidedly semimetallic monolayer counterpart – may be proximate to both kinds of quantum criticality, which is promising. We shall also compile the critical exponents for the corresponding universality classes; since the flavour number is considerably larger than monolayer graphene, the final estimates come with a somewhat lower uncertainty.

In **Chapter 7**, we shall switch from the IR to the UV. There are reasons to believe that extensions to the Standard Model that tend to lower the Higgs mass are phenomenologically attractive. (For one thing, it would allow one to accommodate a more stable electroweak vacuum.) Such extensions, however, usually come with a significantly enlarged number of free parameters, and a concomitant reduction of predictivity. We therefore investigate to what extent imposing quantum scale symmetry at high energies can restrict the Higgs mass measured at low energies (such as the top scale). We shall perform the concrete calculations in a toy version of the Standard Model (more precisely, a Yukawa system representing the top quark and the radial mode of the Higgs) coupled to Yukawa dark matter via a so-called ‘portal’. It turns out that within reasonable approximations, there is only one free parameter in the asymptotically safe dark sector, as a function of which the predicted (toy model) Higgs mass can be lowered due to mixing effects if the dark sector undergoes spontaneous symmetry breaking.

In **Chapter 8**, we shall close with a summary and an outlook.

Chapter 2

Renormalization Group: A Brief Review

The renormalization group (RG) was originally introduced purely as a computational trick; as a necessary evil to absorb infinities appearing in perturbative quantum field theory, and as a means to resum so-called ‘large logarithms’ arising thence. Over time, beginning with the Migdal–Kadanoff ‘mode decimation’ picture (Migdal 1976; Kadanoff 1966), via the works of Wilson and Polchinski (Wilson 1971; Polchinski 1984) and subsequent refinements (as well as reformulations) due to Wetterich–Morris–Ellwanger (Wetterich 1991; Morris 1994; Ellwanger 1994), a new, more conceptual picture of renormalization emerged. In this picture, renormalization is an expression of ‘locality of scale’; the physics of a given system – provided certain ‘niceness’ properties are satisfied – at a certain scale k should be expressible as an equally ‘nice’ quantum field theory in terms of degrees of freedom that live at energies at or below the scale k; the effect of those that live above this scale are said to have been ‘integrated out’. Thus, renormalization can be understood as a means of organizing physics by the scale at which it takes place. The purpose of the present chapter is to introduce in a (somewhat) pedagogical manner the technique of renormalization, as pertaining to the calculations of the subsequent portions of this thesis. For efficency of exposition, we shall recapitulate the development of the renormalization group in an almost *anti*-chronological manner, beginning with the modern Wetterich–Morris–Ellwanger formulation, and only briefly remark on the perturbative UV divergence picture (mainly by ‘deriving’ it within the Wetterich–Morris–Ellwanger framework). This formulation is also useful for the actual calculations done in the remaining parts of the thesis. Remarks on how quantum scale symmetry is realized at RG fixed points and how their properties relate to the theory of quantum phase transitions on one hand as well as predictivity of (UV completions of) quantum field theories on the other close this chapter.

2.1 Quantum fluctuations and generating functionals

In classical field theory, the dynamics of fields are determined by the principle of extremal action (also called the classical equations of motion),

$$\frac{\delta S}{\delta \phi_\alpha(x)} = 0. \tag{2.1}$$

Here, S is the action that defines the field theory, and ϕ_α contains all fields pertaining to the theory. Once the field theory is quantized and quantum fluctuations are taken into account, Eq. (2.1) will surely cease to be valid exactly – but what should stand in its stead? Quantum field theory is defined by expectation values of the form $\langle\hat{\phi}_{\alpha_1}(x_1)\cdots\hat{\phi}_{\alpha_n}(x_n)\rangle$ (called n-point correlation functions, n-point Green's functions, or simply n-point functions).¹⁾ Note that we take special care in this section to notationally distinguish the quantum mechanical operator $\hat{\phi}$ from its classical counterpart ϕ (in other words, $\hat{\phi}$ is the quantized version of ϕ). The correlation functions are defined by a path integral over all classical field configurations weighted by the exponential of the classical action, to wit:

$$\langle\hat{\phi}_{\alpha_1}(x_1)\cdots\hat{\phi}_{\alpha_n}(x_n)\rangle = \int \mathcal{D}\phi\ \phi_{\alpha_1}(x_1)\cdots\phi_{\alpha_1}(x_n)\,\mathrm{e}^{-S[\phi]} \tag{2.2}$$

Since we work in imaginary time (i.e., in Euclidean quantum field theory), there is a minus sign in the exponent rather than a factor of i, the imaginary unit²⁾. It is often useful to have an object that stores all correlation functions at once rather than having to compute them one-by-one every time. An efficient way to achieve this is using generating functionals, which motivates the construction of the partition function Z as

$$Z[J] := \int \mathcal{D}\phi\ \exp\left[-\left(S[\phi] + \int \mathrm{d}^D x\ J^\alpha(x)\,\phi_\alpha(x)\right)\right], \tag{2.3}$$

where the integral measure is assumed to be normalized such that $Z[J=0]=1$. The J^α are called *sources* conjugate to the fields ϕ_α. Note that the above construction is perfectly analogous to that of the generating function of the moments of a probability distribution in stochastics. Thus, n-point functions are obtained by differentiating Z n-times with respect to the sources and subsequently setting them to zero, to wit:

$$\langle\hat{\phi}_{\alpha_1}(x_1)\cdots\hat{\phi}_{\alpha_n}(x_n)\rangle = \left.\frac{(-1)^n\delta^n Z}{\delta J_{\alpha_1}(x_1)\cdots\delta J_{\alpha_n}(x_n)}\right|_{J\to 0}. \tag{2.4}$$

Taking the analogy with probability theory further, recall that the nth moment typically obtains 'trivial' contributions from lower moments if these have a finite value. For instance, given a random variable X, the second moment $\langle X^2\rangle$ does not quantify the spread of a probability distribution if $\langle X\rangle$ is finite; rather, the latter is given by the variance $\mathrm{Var}(X)$ and is obtained by subtracting the contribution $\langle X\rangle^2$ from $\langle X^2\rangle$, to wit $\mathrm{Var}(X) = \langle X^2\rangle - \langle X\rangle^2$. Correlation functions stripped of finite lower-point contributions,

---

1) Depending on the theory, one might need to consider more general operators $\{\mathcal{O}(\phi_\alpha(x))\}_{\mathcal{O}}$ constructed out of the elementary fields. For instance, when studying spontaneous symmetry breaking in a purely fermionic theory – i.e., when ϕ_α consists solely of fermionic fields and their Grassmann conjugates $\psi, \overline{\psi}$ – the simplest possible local order parameter is a composite operator of the form $(\overline{\psi}\psi)(x)$. The construction in that case, while more tedious, is conceptually analogous.

2) For the purposes of most applications pertinent to the present thesis, this choice is mainly one of convenience. The integral with a minus sign is admittedly slightly better defined in non-interacting theories (in much the same way exponentially suppressed integrands are better than oscillatory ones), but the crucial ill-definedness persists, since the path integral remains in essence an integral with integration domain of (possibly uncountably) infinite dimension. (This is ultimately what makes the twin procedure of regularization and renormalization unavoidable.) Results obtained in a Euclidean framework can be translated to Minkowski spacetime by analytically continuing the time variable to imaginary values, and is called *Wick rotation.* A possible exception is quantum gravity (see Chap. 7), where different metric signatures may lead to inequivalent configuration spaces of metric fluctuations. The question of analytic continuation in this context is non-trivial, and open at the time of writing.

usually simply called *connected* correlation functions,[3] are generated by the so-called Schwinger functional $W[J] := -\ln Z[J]$:

$$\langle \hat{\phi}_{\alpha_1}(x_1) \cdots \hat{\phi}_{\alpha_n}(x_n) \rangle_{\text{conn.}} = \left. \frac{\delta^n W}{\delta J_{\alpha_1}(x_1) \cdots \delta J_{\alpha_n}(x_n)} \right|_{J \to 0}. \tag{2.5}$$

The appearance of the particular term ‘connected’ in the nomenclature above has a diagrammatic origin, in that only connected vacuum diagrams contribute to the Schwinger functional (cf., e.g., Schwartz 2014).

Our original goal was to find a quantum version of Eq. (2.1). To do so, we need to trade the source-dependence for a field-dependence, which may be achieved using a Legendre transform. This yields a further functional Γ defined as

$$\Gamma[\phi] = W[J] - \int \mathrm{d}^D x \; J^\alpha(x)\, \phi_\alpha(x), \qquad \phi_\alpha(x) = \frac{\delta W}{\delta J^\alpha(x)}, \tag{2.6}$$

with the inverse transform given by

$$W[J] = \Gamma[\phi] + \int \mathrm{d}^D x \; J^\alpha(x)\, \phi_\alpha(x), \qquad J^\alpha(x) = \frac{\delta W}{\delta \phi_\alpha(x)}. \tag{2.7}$$

It turns out that Γ is precisely the quantum version of S we are looking for, in the sense that the equation of motion governing the quantum vacuum field configuration reads as

$$\frac{\delta \Gamma}{\delta \phi_\alpha(x)} = 0. \tag{2.8}$$

In analogy with Eq. (2.1), the above is called the *quantum equation of motion*, and Γ the *quantum effective action*. The field configuration $\phi = \phi_{\text{vac}}$ that solves the quantum equation of motion satisfies $\phi_{\text{vac}} = \langle \hat{\phi} \rangle$, and is called the *vacuum expectation value* of $\hat{\phi}$. The quantum effective action has a rather intuitively appealing path integral prescription (cf., e.g., Avramidi 2002):

$$\mathrm{e}^{-\Gamma[\phi]} = \int \mathcal{D}\tilde{\phi} \, \exp\!\left[-\left(S[\phi + \tilde{\phi}] - \int \mathrm{d}^D x \, \frac{\delta \Gamma[\phi]}{\delta \phi_\alpha(x)} \tilde{\phi}_\alpha(x) \right) \right]. \tag{2.9}$$

This means (roughly speaking) that the effective action for a given field configuration is found by integrating over fluctuations on top of it. The effect of the second term in the exponential on the right-hand side is such that when the path integral is evaluated perturbatively, only Feynman diagrams that do not fall into disconnected subgraphs after cutting one internal line survive. Such diagrams are often called one-particle irreducible (1PI) in the field-theory literature, with the quantum effective action often referred to as the *1PI effective action* for this reason.

2.2 Renormalization group flow

We thus know now which functionals to compute in order to go from classical to quantum. Nevertheless, this leaves a potentially ill-defined (in a mathematical sense) path integral to be tackled. The main idea behind ‘mode decimation’ versions of RG is to perform this integration step-by-step. Conceptually speaking, this entails performing the path integral only over fields that fluctuate ‘faster’ than k, with a path integral over modes that fluctuate ‘slower’ than k left to be performed. To this end, one adds to the classical action S a regulator

---

[3] In probability theory, these would be called *cumulants*.

$$\Delta S_k := \int \mathrm{d}^D x \, \mathrm{d}^D x' \; \phi_\alpha(x) \, R_k^{\alpha\alpha'}(x,x') \, \phi_{\alpha'}(x'). \tag{2.10}$$

A useful physical picture for the kernel $R_k(x,y)$ is that of a bilocal generalization of a mass term. Following the same routine of stripping connected components and Legendre transformation as above, this construction leads to a ‘running’ version of the generating functionals, denoted Z_k, W_k, and after Legendre transformation, to the running effective action Γ_k; for $k \to 0$, we have to require $\Delta S_k \to 0$, such that the full quantum generating functional is recovered in this limit (this is often referred to as interpolating between the classical and the quantum action). The major ‘selling point’ of the mode decimation picture is that one can replace the path integral prescription for the full quantum generating functionals by an evolution equation for the running effective action Γ_k of the form

$$k\partial_k \Gamma_k = \frac{1}{2}\,\mathrm{STr}\left[\left(\Gamma_k^{(2)} + R_k\right)^{-1} k\partial_k R_k\right], \tag{2.11}$$

The factor k is there so that $k\partial_k$, the so-called *scale derivative*, is a dimensionless operator (i.e., invariant under scale transformations), which will prove to be the natural language when discussing quantum scale symmetry and its emergence (or breakdown) later. In the above, $\Gamma_k^{(2)}$ is the Hesse matrix of Γ_k, to wit:

$$\Gamma_k^{(2)}[\phi]_{\alpha\alpha'}(x,x') = \overrightarrow{\frac{\delta}{\delta\phi_\alpha(x)}}\,\Gamma_k[\phi]\,\overleftarrow{\frac{\delta}{\delta\phi_{\alpha'}(x')}}. \tag{2.12}$$

The trace Tr is generalized to the so-called ‘supertrace’ STr, which includes a minus sign for fermionic degrees of freedom:

$$\mathrm{STr}\begin{pmatrix} B & * \\ * & F \end{pmatrix} = \mathrm{Tr}\,B - \mathrm{Tr}\,F. \tag{2.13}$$

(Note the capitalization of Tr and STr: it is there to remind us that the trace is to be performed not just over internal indices of ϕ, but also over coordinates.) Eq. (2.11) is called the *Wetterich–Morris–Ellwanger* equation, referring to the pioneering contributions of Wetterich (1991), Morris (1994), and Ellwanger (1994). Since said equation tracks the scale evolution of the full functional, as opposed to only the flow of a restricted set of coupling constants, which is more common in perturbative implementations of RG such as that of Gell-Mann–Low (cf., e.g., Schwartz 2014), the Wetterich–Morris–Ellwanger equation is also referred to as the Functional Renormalization Group (FRG) equation. We shall use the two terms in a synonymous way subsequently.

Let us now sketch the ‘derivation’ of the flow equation for Γ_k. As is common practice in these disciplines, by derivation we shall mean formal manipulation of path integrals to arrive at the flow equation. Since a mathematically rigorous non-perturbative definition of path integrals is outstanding, this is at best a heuristic; the endeavour to turn them into mathematically rigorous proofs is ongoing, see Ziebell (2021b) for the most recent progress in this direction. Having said that, let us begin our ‘derivation’ by noting the path integral for Γ_k, which may be obtained by replacing $S \to S+\Delta S_k$ and $\Gamma \to \Gamma_k+\Delta S_k$ in Eq. (2.9), to wit:

$$\mathrm{e}^{-\Gamma_k-\Delta S_k} = \int \mathcal{D}\tilde{\phi}\, \exp\left(-\Gamma_\Lambda[\phi+\tilde{\phi}] - \Delta S_k[\phi+\tilde{\phi}] + \int \mathrm{d}^D x \frac{\delta(\Gamma_k+\Delta S_k)}{\delta\phi_\alpha(x)}\tilde{\phi}_\alpha(x)\right), \tag{2.14}$$

where the arguments of functionals default to ϕ if unspecified. In the equation above, the classical action S has been automatically implemented as the initial data for the flow, i.e.,

$$\Gamma_\Lambda = S, \tag{2.15}$$

where Λ is the appropriate UV scale for the problem at hand (e.g., the Planck scale in quantum gravity or the inverse band width in semimetals). (In a 'fundamental' theory, one would ultimately like to set $\Lambda \to \infty$ at least in principle, if not in practice.) Eq. (2.14) expresses the evolution from Λ to k. The main 'trick' towards deriving the Wetterich–Morris–Ellwanger equation is to consider instead the evolution from k to $k-\delta k$. *Mutatis mutandis*, Eq. (2.14) then reads as

$$\begin{aligned}\mathrm{e}^{-\Gamma_{k-\delta k}-\Delta S_{k-\delta k}} = \int \mathcal{D}\tilde{\phi}\, \exp\Big(&-\Gamma_k[\phi+\tilde{\phi}] - \Delta S_{k-\delta k}[\phi+\tilde{\phi}] \\ &+ \int \mathrm{d}^D x \frac{\delta(\Gamma_{k-\delta k}+\Delta S_{k-\delta k})}{\delta\phi_\alpha(x)}\tilde{\phi}_\alpha(x)\Big)\end{aligned} \tag{2.16}$$

Let us evaluate the path integral to one-loop order, and expand to this end the exponent on the right-hand side to quadratic order in fluctuations to obtain (upon recalling that R_k is the Hesse matrix of ΔS_k):

$$-\Gamma_k[\phi] - \Delta S_{k-\delta k}[\phi] - \int \mathrm{d}^D x\, \mathrm{d}^D x'\, \tilde{\phi}_\alpha(x) \left(\Gamma_k^{(2)}[\phi]^{\alpha\alpha'}(x,x') + R_{k-\delta k}^{\alpha\alpha'}(x,x')\right) \tilde{\phi}_{\alpha'}(x').$$

We have dropped the term coming from the Jacobi matrix of $\Gamma_k - \Gamma_{k-\delta k}$, since its contribution to the (logarithm of the) path integral would be of order $(\delta k)^2$. Performing the Gaußian integration and taking the logarithm of the determinant using the 'trace-log' formula, we thus arrive at

$$\Gamma_{k-\delta k} = \Gamma_k + \frac{1}{2}\,\mathrm{STr}\ln\left(\Gamma_k^{(2)} + R_{k-\delta k}\right) + \mathcal{N} \tag{2.17}$$

Like in any infinite-dimensional Gaußian integral, there is an arbitrary normalization constant, denoted here as $\mathcal{N}$. In this instance, $\mathcal{N}$ may be fixed, e.g., by imposing continuity of Eq. (2.16) at $\delta k \to 0$, yielding[4)]

$$\mathcal{N} = -\frac{1}{2}\,\mathrm{STr}\ln\left(\Gamma_k^{(2)} + R_k\right). \tag{2.18}$$

Inserting $R_{k-\delta k} \approx R_k - \delta k \partial_k R_k$, we may now expand the logarithm as

$$\begin{aligned}\ln\left(\Gamma_k^{(2)} + R_{k-\delta k}\right) &\approx \ln\left(\Gamma_k^{(2)} + R_k - \delta k\partial_k R_k\right) \\ &\approx \ln\left(\Gamma_k^{(2)} + R_k\right) - \delta k \left(\Gamma_k^{(2)} + R_k\right)^{-1} \partial_k R_k.\end{aligned} \tag{2.19}$$

[4)] This is conceptually similar to fixing $Z[J=0]=1$.

The contribution of the first term cancels against $\mathcal{N}$. Dividing by $(\delta k)/k$ and sending $\delta k \to 0$ yields

$$k\partial_k \Gamma_k = \frac{1}{2}\,\mathrm{STr}\left[\left(\Gamma_k^{(2)} + R_k\right)^{-1} k\partial_k R_k\right], \tag{2.20}$$

thereby verifying Eq. (2.11). Let us conclude with miscellaneous technical remarks:

1.) The flow equation for a generating functional is equivalent to its path integral. Whilst the latter is only a formal object, the flow equation is a mathematically well-defined problem (cf., e.g., Ziebell 2021a). Hence, the flow equation may just as well be seen as a rigorous non-perturbative *definition* of the path integral.

2.) The Wetterich–Morris–Ellwanger equation in particular, and all RG procedures derived from (continuous) 'mode decimation' in general, have a so-called one-loop exact form, in that they entail only a single functional trace. However, information about the full loop expansion is contained in the flow equation, because the Hesse matrix appearing in the functional trace is computed self-consistently from Γ_k (rather than S, as one would in perturbative approaches). In this context, note that the loop expansion performed in going from Eq. (2.16) to Eq. (2.17) is controlled by δk (which is ultimately sent to zero), rather than the presumed smallness of any interaction vertices.

3.) We have thus far not been very precise about how ΔS_k distinguishes 'fast' from 'slow' modes. To give this a well-defined meaning, one needs to declare a quadratic (in fields) positive-definite term in the action as the *kinetic* operator. Let

$$\mathcal{O}_{\mathrm{kin}} = \int \mathrm{d}^D x\, \mathrm{d}^D x'\, \phi_\alpha(x)\, K_{\alpha\alpha'}(x,x')\, \phi_{\alpha'}(x') \subset S \tag{2.21}$$

be this operator, $\{\varepsilon_\lambda\}_\lambda$ a list of the spectral values of the linear operator

$$\phi \mapsto \int \mathrm{d}^D x'\, K_{\alpha\alpha'}(x,x')\, \phi_{\alpha'}(x')$$

induced by $\mathcal{O}_{\mathrm{kin}}$, and $\{u^\lambda\}_\lambda$ the corresponding eigenvectors. Assuming the kinetic operator is 'nice enough' such that $\{u^\lambda\}_\lambda$ fulfils the necessary completeness relations, one may then split ϕ into its slow and fast components as[5]

$$\phi_\alpha(x) = \phi_\alpha^{\mathrm{s}}(x) + \phi_\alpha^{\mathrm{f}}(x) \tag{2.22}$$

$$\phi_\alpha^{\mathrm{s(f)}}(x) := \sum_{\varepsilon_\lambda \lesssim (\gtrsim) k^{d_\varepsilon}} \tilde{\phi}_\lambda u_\alpha^\lambda(x) \tag{2.23}$$

The summation sign is symbolic; in many cases, the spectrum will have continuous parts and the sum will then be replaced by an integral. The spectrum of K is assumed to have units of $(\text{length})^{d_\varepsilon}$ (e.g., $d_\varepsilon = 2$ for the Laplacian, $d_\varepsilon = 4$ for the bi-Laplacian, etc.), such that k always has units of $(\text{length})^{-1}$. In many practically relevant cases, K is translationally invariant. Then, one may write

$$K(x,x') = \tilde{K}(-\mathrm{i}\partial)\, \delta(x-x'); \tag{2.24}$$

---

[5] The '$\lesssim$ ($\gtrsim$)' below is there to remind us that a smooth transition from the slow to fast regime – rather than a sharp cut – is desirable. The precise form is immaterial for the further discussion, since ultimately, the separation of modes is achieved by a suitable choice of ΔS_k.

often, in fact, $\tilde{K}(-\mathrm{i}\partial) = -\partial^2$ is (the negative of) the D-dimensional Laplacian.[6] In this case, $\lambda \equiv p \in \mathbb{R}^D$ is called momentum, and the expansion in plane waves $u_p(x) = \mathrm{e}^{\mathrm{i}p\cdot x}$ is simply the definition of the Fourier decomposition. Since the eigenvalues of the kinetic operator $\varepsilon_p = p^2$ has units of $(\text{length})^{-2}$, it is conventional to use $p^2 \lesssim k^2$ to characterize the 'slow' modes; the RG scale k is thus seen to correspond to a momentum scale. A suitable choice of R_k, the integration kernel of ΔS_k, is then given by[7]

$$R_k(x, x') = -\partial^2\, r(-\partial^2/k^2)\, \delta(x - x') \tag{2.25}$$

with a dimensionless 'shape factor' r satisfying

$$x^2 r(x) \to C > 0 \ (x \to 0) \qquad r(x) \to 0 \ (x \to \infty). \tag{2.26}$$

The former ensures IR modes are suppressed at fixed k, whilst the latter ensures that for $k \to 0$, the full effective action is recovered. A slight modification is useful in non-relativistic theories. There, spacetime is split as $(x_\mu) = (\tau, \boldsymbol{x})$, and the regulator is then defined to leave the τ-axis untouched. Due to a residual $\mathrm{O}(D-1)$ symmetry (spatial rotations), it is sufficient to consider r as a function of $(-\boldsymbol{\partial}^2/k^2)$, the $(D-1)$-dimensional Laplacian.

Momentum-space regulators are by far the most ubiquitous in FRG calculations (cf., e.g., Dupuis *et al.* 2021); this will also be the case in the present thesis. However, the flexibility of the regulator formalism is best illustrated by cases where momentum is *not* a good basis. Apart from the afore-mentioned spacetimes with curvature, examples include ϕ^4 theory on non-commutative spacetime, where one needs to set up the mode decimation in a so-called *matrix basis* (Grosse & Wulkenhaar 2005), although the derivative terms one might naïvely consider to constitute the kinetic operator is diagonal in momentum space.[8] Certain matrix models (e.g., for two-dimensional gravity) have a trivial 'kinetic' term, and the notion of mode decimation has to be defined in a more abstract sense (cf., e.g., Eichhorn & Koslowski 2013). We shall encounter a – by comparison somewhat humble – example of non-momentum-space regularization in Chap. 5 as well as Sec. 4.6.3, where the regularization will be defined via cut-offs in *coordinate* space.

2.3 Basic notions

The Wetterich–Morris–Ellwanger equation contains all the information about the effective action in a non-perturbative, mathematically rigorous way. Nevertheless, it is a non-linear evolution equation for a functional whose domain and co-domain are infinite-dimensional (and often uncountably so), which is hardly convenient. It is therefore more expedient to carry out the discussion of quantum scale symmetry in terms of simpler, derived objects. Assume to this end that the running effective action Γ_k can be written as

$$\Gamma_k[\phi] = \sum_i g_{i,k} \mathcal{O}_i[\phi], \tag{2.27}$$

---

[6] In theories with fermionic degrees of freedom, one may instead have $\tilde{K}(-\mathrm{i}\partial) = -\mathrm{i}\not{\partial}$. In this case, one usually uses the square of the kinetic operator to define fast and slow modes, which reduces again to the Laplacian case. In curved spacetime, the Laplacian construction is still valid, but has to be interpreted more abstractly, since the Laplacian is no longer diagonal in the momentum basis.

[7] Again, in the spinorial case, a corresponding choice is $R_k(x, x') = -\mathrm{i}\not{\partial} r(-\partial^2/k^2)\delta(x - x')$.

[8] Roughly speaking, the matrix basis is to the momentum basis, what coherent states are to plane waves in single-particle quantum mechanics.

where $\{\mathcal{O}_i\}_i$ is a complete set of operators containing the entire field- and spacetime-dependence, but have no dependence on the RG scale k; dependence on the RG scale is instead carried by the $g_{i,k}$, which themselves have no field- or spacetime dependence. (At its heart, this is therefore just another separation ansatz, familiar from the finite-dimensional partial differential equations.) The $g_{i,k}$ are precisely what we shall refer to henceforth as *running couplings*; the space spanned by all couplings g_i is referred to as 'theory space'. Furthermore, we shall refer to the scale derivative of $g_{\mathcal{O},k}$ as *beta functions*,

$$\beta_{g_i} \equiv \beta_i := -k\partial_k g_{i,k}. \tag{2.28}$$

(The minus sign is merely a matter of convention. In statistical mechanics and condensed matter theory, it is common to define the RG 'time' $t := \ln(\Lambda/k)$ such that $t \to \infty$ corresponds to the deep IR, in which case $\partial_t = -k\partial_k$. In anticipation of the discussion of the stability of RG fixed points later, let us note that in this convention, a positive $\beta_i > 0$ thus corresponds to an IR-relevant coupling g_i.) Let us take this opportunity to also review the concept of 'complete' basis of operators. This notion can be somewhat subtle to formalize, since completeness can be meant either in the sense of a Taylor expansion (with a finite radius of convergence), in the sense of an asymptotic expansion (i.e., in the sense of Poincaré) or in the sense of an expansion in an orthonormal basis of function space with respect to a suitably chosen inner product. Instead of an exhaustive mathematical theory on the possible choices of basis, let us discuss the one which is most pertinent to the theories we shall encounter, viz. the basis consisting of the following operators[9]:

$$\mathcal{O}^{(lmn)}_{\alpha_1\ldots\alpha_m,\alpha'_1\ldots\alpha'_n,\mu_1\ldots\mu_n} := \int \mathrm{d}^D x\, \phi_{\alpha_1}\cdots\phi_{\alpha_l}(-\mathrm{i})^m\partial_{\mu_1}\cdots\partial_{\mu_m}\phi_{\alpha'_1}\cdots\phi_{\alpha'_n}. \tag{2.29}$$

If the classical action S – in other words, the initial data for Γ_k – is local (which will turn out to be the case for all theories we shall consider in this thesis), then Γ_k itself can be written as a linear combination of $\mathcal{O}^{(lmn)}$, provided the regulator R_k is smooth enough. Note, however, that the full quantum effective action Γ may be neither analytic in fields, nor local; roughly speaking, this is because the quantum effective action emerges only after infinite 'flow time' $\ln(\Lambda/k) \to \infty$. Keeping track of all elements of a complete basis is only possible in theory (for instance, when proving 'all-order' statements, as we shall do later in this chapter). In practice, only a subset of the $\mathcal{O}^{(lmn)}$ can be taken into account; the choice of this subset defines the so-called *truncation scheme*. For instance, in the *derivative expansion* (which will feature prominently in Chap. 3), one includes to order M_{deriv} all terms with $m \leqslant M_{\text{deriv}}$, and works with generalized 'couplings' that depend on fields, such as the effective potential $U(\phi)$ which corresponds to $m = 0$,

$$U_k(\phi) := \sum_{ln} g_{l0n,k}\mathcal{O}^{(l0n)}. \tag{2.30}$$

Once a flow equation for $U_k(\phi)$ has been derived – which is then a (finite-dimensional) partial differential equation in (k, ϕ) – one can re-expand $U_k(\phi)$ in a different basis, with more favourable convergence properties than a simple Taylor expansion. Another widely used truncation scheme (albeit with no further presence in this thesis) is the *vertex expansion*, wherein one keeps, to order N_{vertex}, all terms with $l + n \leqslant N_{\text{vertex}}$. The name refers to the fact that the sum of all terms $l + n = n_0$ corresponds to the n_0-th functional derivative of Γ_k, often referred to as the n_0-point proper vertex function.

---

[9] It is understood, that the range of lmn are restricted such that every operator appears only once in the list.

Let us close this section by drawing the connection to the perturbative theory of renormalization, since we shall use the loop expansion in several instances later, most notably to higher order in Chap. 3. The loop expansion can be shown to correspond precisely to an iterative solution of the Wetterich–Morris–Ellwanger equation, with the bare action as initial point. Let us briefly sketch how this idea may be formalized [see Codello, Demmel & Zanusso (2014) for details]. To set up the loop expansion, we need to reinstate the reduced Planck quantum by rescaling all actions by $\hbar$, i.e., $\hbar\Gamma_k \mapsto \Gamma_k, \hbar R_k \mapsto R_k$, and make the ansatz

$$\Gamma_k[\phi] = S_\mathrm{B}[\phi] + \sum_{L=1}^{\infty} \hbar^L \Gamma_{L,k}[\phi]. \tag{2.31}$$

The idea is that $\Gamma_{L,k}$ is the L-loop contribution to the effective action, and can be determined by plugging in the above ansatz into the (suitably rescaled) Wetterich–Morris–Ellwanger equation and comparing coefficients of $\hbar^L$. This leads to the recursive prescription

$$k\partial_k S_\mathrm{B}[\phi] = 0 \tag{2.32}$$

$$k\partial_k \Gamma_{1,k}[\phi] = \frac{1}{2}\,\mathrm{STr}\left[\left(S_\mathrm{B}^{(2)}[\phi] + R_k\right)^{-1} k\partial_k R_k\right] \tag{2.33}$$

$$k\partial_k \Gamma_{2,k}[\phi] = \frac{1}{2}\,\mathrm{STr}\left[\Gamma_{1,k}^{(2)}[\phi]\, k\partial_k \left(S_\mathrm{B}^{(2)}[\phi] + R_k\right)^{-1}\right] \tag{2.34}$$

$$\vdots$$

where the superscript '(2)' refers to the Hesse matrix as usual. One can then show order-by-order that the right-hand-side is a total scale-derivative. To do so, however, one needs to commute the supertrace with the scale derivative. Since this may spoil the UV finiteness[10], one needs to additionally regularize the trace,

$$\mathrm{STr}\, k\partial_k = k\partial_k\, \mathrm{STr}_\mathrm{reg.} \tag{2.35}$$

The UV regularization introduces an additional scale k_UV. The arguably most ubiquitous prescription for such a UV regularization is *dimensional regularization* (DREG), where

$$\int_\mathrm{reg} \mathrm{d}^D x := (k_\mathrm{UV})^{D_\mathrm{reg}-D} \int \mathrm{d}^{D_\mathrm{reg}} x, \tag{2.36}$$

i.e., the integral is evaluated in $D_\mathrm{reg} < D$ spacetime dimensions,[11] and the prefactor is such that the integral measure still has units of $(\mathrm{length})^D$. UV divergences show up as poles of the form $1/(D - D_{\mathrm{reg}})^{\ell}$ with $\ell \leqslant L$ at the L-loop level ('t Hooft & Veltman 1972; Breitenlohner & Maison 1997). In perturbative renormalization, these divergences are cancelled by so-called counterterms, whereby the bare action is split into

---

[10] Proving the fact that the insertion of $k\partial_k R_k$ guarantees UV finiteness is somewhat technically involved in general. To get a qualitative idea of the argument, however, one may study the integral $\int_0^\infty \mathrm{d}y\, y^r$ as a 'cartoon' of a generic (possibly divergent) loop integral. If we cut the integral off at an IR scale k – i.e., $\int_0^\infty \mathrm{d}y \to \int_0^\infty \mathrm{d}y\, \Theta(y-k)$ – and perform the scale derivative before integration, then $k\partial_k \Theta(y-k) = -k\delta(y-k)$ automatically UV regularizes the result. On the other hand, if we wish to perform the y-integral before the k-derivative, then we need to additionally UV regularize for $r > -1$.

[11] Defining the integral in non-integer dimensions in a mathematically rigorous as well as consistent way is subtle (Bollini & Gambiagi 1972; 't Hooft & Veltman 1972; Breitenlohner & Maison 1997; Stöckinger 2005); cf. also Siegel (2005) for a more pedagogical account.

$$S_{\mathrm{B}}[\phi] = S_{\mathrm{ren},k,k_{\mathrm{UV}}}[\phi] + S_{\mathrm{CT},k,k_{\mathrm{UV}}}[\phi] \coloneqq S_{\mathrm{ren},k,k_{\mathrm{UV}}}[\phi] + \sum_{L=1}^{\infty} \hbar^{L} \delta S_{L,k,k_{\mathrm{UV}}}[\phi], \tag{2.37}$$

where the dependence on the UV regularization scale k_{UV} has been reintroduced for clarity. How much of the finite part of $\Gamma_{L,k}$ is included in $S_{\mathrm{CT},k,k_{\mathrm{UV}}}$ ultimately defines the *renormalization scheme*; in the most commonly used one, called *modified minimal subtraction* or simply $\overline{\mathrm{MS}}$ (Siegel 2005), the counterterms contain precisely the divergent part,

$$\delta S_{L,k,k_{\mathrm{UV}}}[\phi] \equiv \delta S_{L,k_{\mathrm{UV}}}[\phi] = \Gamma_{L,k=0}[\phi]|_{1/(D-D_{\mathrm{reg}})\text{-poles}} = \Gamma_{L,k=0}[\phi]|_{1/(D-D_{\mathrm{reg}})\text{-poles}}. \tag{2.38}$$

alongwith a rescaling of the renormalization scale $\mu_{\overline{\mathrm{MS}}}^2 \coloneqq k_{\mathrm{UV}}^2 \mathrm{e}^{-\gamma_{\mathrm{E}}}/4\pi$ with Euler-Mascheroni constant γ_{E}.[12] The assertion that the leading divergence is undressed by the FRG scale k is non-trivial to prove in general, but has been checked to two-loop by Codello, Demmel & Zanusso (2014) for single-component scalar ϕ^4 theory at $D = 4$. Demanding that 'physics' (more precisely, the bare action S_{B}) be independent of the renormalization scale $\mu_{\overline{\mathrm{MS}}}$, to wit:

$$\mu_{\overline{\mathrm{MS}}} \frac{\partial}{\partial \mu_{\overline{\mathrm{MS}}}} S_{\mathrm{B}} = 0, \tag{2.39}$$

implicitly defines the $\overline{\mathrm{MS}}$ β functions. The definition of renormalized couplings via UV divergences is useful if one is primarily interested in studying the UV finiteness of the theory, since it is completely oblivious to IR effects. However, when searching for scale invariance, the pertinent quantity is the full effective action; if scale symmetry is broken or restored by the effective action (which contains UV as well as IR physics), it may not be reflected by the UV β functions.[13] For this reason, even when employing a (quasi-)perturbative approach, we shall always assume the running of couplings to be with respect to the IR cut-off scale k, as defined at the beginning of this section. This is not only a conceptual point, but also of technical importance: were we to compute the full effective action Γ by evaluating the (UV regularized if necessary) supertraces directly at $k = 0$ (i.e., by 'switching off' the IR regularization, $\Delta S_k \to 0$), we would not be justified in Taylor expanding the result at all (neither in powers of fields, nor external momenta) which would make the practical implementation of the computation much more involved.

2.4 Scale transformations, scale symmetry and RG fixed points

With the basic definitions at hand, we are now in a position to ask how (quantum) scale symmetry manifests itself in the running of couplings (or lack thereof). Let us begin by recapitulating the concept of a *scale transformation* (also called *dilatation*, see Chap. 3 of Coleman (1985)). By definition, it acts by multiplying coordinates by a global constant, to wit

---

[12] This is purely a matter of convention, as is calling the RG scale μ rather than k_{UV}; the version without rescaling is trivially equivalent and called *minimal subtraction.*

[13] A notable exception is if the interaction vertices are classically dimensionless. In this case, the most significant scale-dependence is of the form $\ln(p^2/\mu^2)$, where p^2 is a placeholder for a suitable combination of momenta involved in the process. Since this diverges both in the UV as well as the IR, there is a one-to-one correspondence between UV and IR running. This is exploited in Sec. 3.2.1.

$$x_\mu \to C x_\mu. \tag{2.40}$$

With $C = 1 - \epsilon$, we may express this infinitesimally as[14],[15]

$$\delta_\epsilon x_\mu = -\epsilon x_\mu. \tag{2.41}$$

The fields themselves, being x-dependent, need to be allowed to transform under scale transformations as

$$\delta_\epsilon \phi_\alpha(x) = \epsilon(-x_\mu \partial_\mu + d_\phi)\phi_\alpha(x), \tag{2.42}$$

where d_ϕ is the *canonical dimension* of ϕ, to be fixed later; likewise, for a general (integrated) operator $\mathcal{O}$ obeying $\delta_\epsilon \mathcal{O} = \epsilon d_{\mathcal{O}} \mathcal{O}$, one refers to $d_{\mathcal{O}}$ as the canonical dimension of $\mathcal{O}$.[16] The canonical dimension of the field is fixed by demanding that the kinetic operator has canonical dimension zero, $d_{\mathcal{O}_{\text{kin}}} = 0$. For instance, in the usual Laplacian case

$$\mathcal{O}_{\text{kin}} = \int \mathrm{d}^D x\, \phi_\alpha(x)\, (-\partial^2)\phi_\alpha(x), \tag{2.43}$$

one finds

$$d_\phi = (D-2)/2. \tag{2.44}$$

Of course, just like the very notion of fast and slow modes, the canonical dimension of a field is tied to what constitutes the kinetic operator; in particular, different components ('species') may have different kinetic operators and thus different canonical dimensions. For instance, if the ('super'-)field $(\phi_\alpha) = (\varphi, \psi, \overline{\psi})$ consists of a scalar φ as well as a Dirac fermion ψ (and its conjugate), then usually they will have different kinetic operators, to wit:

$$\mathcal{O}^{(\varphi)}_{\text{kin}} = \int \mathrm{d}^D x\, \varphi(x)\, (-\partial^2)\varphi(x), \qquad \mathcal{O}^{(\psi,\overline{\psi})}_{\text{kin}} = \int \mathrm{d}^D x\, \overline{\psi}(x)\, (-\mathrm{i}\partial\!\!\!/)\psi(x), \tag{2.45}$$

which would lead to $d_\varphi = (D-2)/2$ whilst $d_\psi = d_{\overline{\psi}} = (D-1)/2$. Again, to avoid clutter, we shall assume all components transform the same way in intermediate steps and reinstate the more general scaling behaviour in the final discussion later.

Intuitively, the canonical dimension is directly related to dimensional analysis. This is essentially because the coefficient in front of the kinetic term is fixed to be a dimensionless number, and the action itself (in natural units) is dimensionless; since the volume element and Laplacian have units

---

[14] In non-relativistic systems, it is useful to consider a slight generalization $\delta_\epsilon x_\mu = -\epsilon z_{\mu\nu} x_\nu$ with $z_{\mu\nu} = \mathrm{diag}(z, 1, \ldots, 1)$. To avoid clutter, we shall restrict ourselves to theories with (Euclidized) Lorentz invariance, and reinstate z only when working out consequences of quantum scale symmetry in Sec. 2.5.

[15] A different view of dilatations is a rescaling of the metric tensor $\delta_\epsilon g_{\mu\nu} = 2\epsilon g_{\mu\nu}$ while leaving coordinates x_μ unchanged, see Morris & Percacci (2019). The power counting is the same if one assumes that two derivatives can be contracted only using an inverse metric tensor.

[16] An often used notation, which we shall use synonymously in subsequent portions of this thesis is $d_{\mathcal{O}} \equiv [\mathcal{O}]$. This is mainly for typographic convenience and legibility.

$$\mathrm{d}^D x \sim (\text{length})^D \qquad -\partial^2 \sim (\text{length})^{-2} \tag{2.46}$$

this implies the field ϕ needs to have units

$$\phi \sim (\text{length})^{-d_\phi} \tag{2.47}$$

to ensure the kinetic piece of the action is indeed dimensionless. Once the canonical dimension of ϕ is fixed, every local operator has a well-defined canonical dimension; for the *lmn*-basis of local operators from the previous section, for instance, $d_{\mathcal{O}(lmn)} = D - m - (l+n)d_\phi$. In general, given an operator $\mathcal{O}$ with canonical dimension $d_{\mathcal{O}}$, the corresponding coupling must then have units

$$g_{\mathcal{O}} \sim (\text{length})^{d_{\mathcal{O}}} \tag{2.48}$$

to be compatible with the requirement that the action be dimensionless. Note, however, that since couplings are 'constants' (i.e., independent of coordinates or fields), they do *not* transform under global scale transformations.

To make the connection between RG running and dilatations, we need the so-called *Ward–Takahashi identity of global scale transformations*, which we state here without proof:[17)]

$$\delta_\epsilon \Gamma = \delta_\epsilon \Gamma_k - \epsilon k \partial_k \Gamma_k . \tag{2.49}$$

The left-hand side, $\delta_\epsilon \Gamma$, is the variation of the quantum effective action under global scale transformations, and measures the breaking of scale invariance of the field theory at the quantum level. As mentioned previously, Γ can have both non-local and non-analytic field-dependencies. However, we can use the above identity to express $\delta_\epsilon \Gamma$ in terms of Γ_k, which can be expanded (at least formally) in powers of derivatives and fields, see Eq. (2.29). Importantly, all such operators have a well-defined behaviour under scale transformation (i.e., they are 'eigenoperators' of δ_ϵ), which we denote for brevity as $\delta_\epsilon \mathcal{O}_i = \epsilon d_{\mathcal{O}_i} \mathcal{O}_i$, and we may write

$$\Gamma_k = \sum_i g_{i,k} \mathcal{O}_i \tag{2.50}$$

as shorthand for the expansion of Γ_k. Acting with δ_ϵ, we then find

$$\delta_\epsilon \Gamma_k = \epsilon \sum_i d_{\mathcal{O}_i} g_{i,k} \mathcal{O}_i . \tag{2.51}$$

On the other hand, acting with $-k\partial_k$, we find upon recalling the definition (2.28) of β functions,

$$-k\partial_k \Gamma_k = \sum_i \beta_i \mathcal{O}_i . \tag{2.52}$$

[17)] The interested reader is referred instead to Morris & Percacci (2019) for a derivation within the path integral framework, as well as a more careful consideration of the $k \to 0$ limit of the identity.

Plugging the two relations into the Ward–Takahashi identity of scale transformations, we find

$$\delta_\epsilon \Gamma = \epsilon \sum_i \left(d_{\mathcal{O}_i} g_i + \beta_i \right) \mathcal{O}_i. \tag{2.53}$$

For quantum scale symmetry, we must therefore have $d_{\mathcal{O}_i} g_i + \beta_i = 0$ for all i. This may be cast into a somewhat more intuitive form by recalling that g_i has units of $(\text{length})^{d_{\mathcal{O}_i}}$, which implies that $\tilde{g}_{i,k} := g_{i,k}/k^{-d_{\mathcal{O}_i}}$ is dimensionless. Acting on $\tilde{g}_{i,k}$ with $-k\partial_k$ using the product rule, we arrive at the condition

$$\forall i \colon \tilde{\beta}_i = 0, \tag{2.54}$$

which may be expressed in words as: *Quantum scale symmetry is realized at a fixed point of the renormalization group flow of the dimensionless couplings.* Since the dimensionless versions of the couplings, $\tilde{g}_{i,k}$, are in some sense more fundamental than the dimensionful $g_{i,k}$ with respect to quantum scale symmetry, we shall henceforth drop the 'tildes' and work exclusively with dimensionless couplings.

Remark (quantum vs classical scale symmetry). The scale symmetry considered here is the invariance of the full quantum effective action including all fluctuation effects, as evinced by the condition $\delta_\epsilon \Gamma = 0$: it is *quantum* scale symmetry. Likewise, one may ask under what conditions scale symmetry holds at the classical level, $\delta_\epsilon S = 0$. Going through the same arguments as above, one finds that all dimensionful couplings have to vanish – the 'dilatation formalism' above thus recovers the (intuitively obvious) classical limit. It is worth noting, however, that classical scale symmetry is *not* a necessary condition for quantum scale symmetry. In many cases – as we shall also see later in several examples in this thesis – it is the balance between the (classical) dimensional scaling and the running due to quantum fluctuations that generates quantum scale symmetry.

2.5 Characterization and interpretation of RG fixed points

2.5.1 Formal aspects

RG fixed points thus furnish a realization of field theories with quantum scale symmetry. Given such a fixed point $g_{i,*}$,[18] it is then natural to ask how small perturbations away from this fixed point flow under RG. For small deviations $\delta g_i := g_i - g_{i,*}$, we may linearize the flow to obtain

$$-k\partial_k \delta g_{i,k} = \mathcal{M}_{ij} \delta g_{j,k}, \tag{2.55}$$

where according to standard Taylor expansion practice, we have introduced the fixed-point Jacobi matrix

$$\mathcal{M}_{ij} := \left. \frac{\partial \beta_i}{\partial g_j} \right|_{g=g_*}. \tag{2.56}$$

---

[18] Note that these are the dimensionless couplings in the sense of the previous section, even though we have dispensed with the explicit 'tilde' notation.

Following the nomenclature of dynamical systems theory, the matrix $\mathcal{M}$ is usually referred to as the *stability matrix* of the fixed point. Let us assume this matrix has an eigenbasis e^I (more precisely, a right-eigenbasis)

$$\mathcal{M}_{ij} {e^I}_j = \theta^{(I)} {e^I}_i. \tag{2.57}$$

The eigenvalues $\theta^{(I)}$ of the stability matrix are called *critical exponents.* (We shall make the connection to the physical critical exponents governing the non-analyticity of thermodynamic observables near phase transitions later.) Clearly, they are independent of the specific choice of basis of operators $\{\mathcal{O}_i\}$ so long as the matrix $({e^I}_i)$ is invertible, which is the case if the basis is truly complete. They are furthermore independent of the specific regulator R_k used to compute the β functions, unlike the fixed-point values of the couplings themselves.[19] In this sense, critical exponents are called *universal.* This technical use of the term universal should not be confused with the 'physical' sense of the word, which is more stringent and used to mean 'independent of UV data'. The completeness of the basis is an important conceptual point here: computing the $\theta^{(I)}$ within a finite subset of the $\mathcal{O}_i$ (in any basis), as done in the course of any practical truncation, will yield results that are generically dependent on the choice of basis as well as regulator. Only if the chosen subset is large enough (or the neglected operators irrelevant enough) will the leading eigenvalues be scheme-independent. Conversely, estimates for the deviation between two generic regulators may be used as measure of the truncation error. This statement itself is dependent upon specifics of the approximation used to derive the β functions: To first order in loop expansion, for instance, the regulator-dependence of dimensionless quantities tend to drop out if the regulator is sufficiently well-behaved (see, for instance, Chap. 3). Scheme-independence then obviously does not mean that the one-loop result is exact – if it is, this has to be demonstrated by other means than mere scheme-independence (see Chap. 4).

Concerning the physical content of the stability matrix eigenvalues $\theta^{(I)}$, there is one further important caveat. The parametrization of the effective action in general contains many redundancies, since there exist field re-definitions – called *frame transformations* – which leave correlation functions invariant. Just like ordinary gauge redundancy, this separates perturbations at an RG fixed point into *essential* and *inessential* (or *redundant*) perturbations. Redundant perturbations contain no physical information, and hence their critical exponents are non-universal *a fortiori.* A frame-covariant formulation of RG accounting for general frame transformations is highly non-trivial, and has been worked out only recently by Baldazzi, Zinati & Falls (2021). Fortunately, at the level of approximations we shall be working with subsequently in this thesis, it is sufficient to consider the comparatively straightforward transformation of rescaling fields by constants, $\phi \to \sqrt{Z_{\phi,k}}\phi$.[20] In the literature, this is commonly referred to as a *wavefunction renormalization.* (As usual, we assume for simplicity that all components of ϕ obtain the same rescaling; the generalization to multiple 'species' with their individual wavefunction renormalization is straightforward.) The value of Z is fixed by demanding that the coefficient of the kinetic term remain RG-invariant. Thus, the contribution of the kinetic operator $\mathcal{O}_{\text{kin}}$ to the action is normalized for a real scalar as

---

[19] The dependence on the choice of regulator is conceptually similar to the dependence on renormalization scheme in perturbative quantum field theory (such as $\overline{\text{MS}}$, on-shell, Coleman–Weinberg, etc.).

[20] In non-relativistic theories, the kinetic term is usually defined to contain only the spatial derivative terms; in any case, the renormalization of time-derivative and spatial-derivative terms are not related by symmetry. For this reason, to maintain the normalization of the time-derivative term, it is necessary to in addition rescale the time coordinate $\tau \to Z_{\omega,k}^{-1}\tau$ along with $\phi \to \sqrt{Z_{\phi,k} Z_{\omega,k}}\phi$, which corrects the dynamical critical exponent, see Chap. 4. In Chap. 6, we shall in fact encounter an even less symmetric setting, where different spatial directions will be equipped with a priori distinct (inverse) dynamical critical exponents.

$$S_{\text{kin}}[\varphi] = \frac{1}{2}\int \mathrm{d}^D x\, \varphi(x)(-\partial^2)\varphi(x), \tag{2.58}$$

where the factor 1/2 is conventional. Likewise, for Dirac fermions, one sets the normalization as

$$S_{\text{kin}}[\psi, \overline{\psi}] = \int \mathrm{d}^D x\, \overline{\psi}(x)\not{\partial}\psi(x) \tag{2.59}$$

Absorbing the renormalization of the kinetic operator into wavefunction renormalizations leads to the *anomalous dimension*

$$\eta_{\phi,k} := -\frac{k\partial_k Z_{\phi,k}}{Z_{\phi,k}}. \tag{2.60}$$

(At a fixed point, it is conventional to drop the index k, i.e., $\eta_\phi \equiv \eta_{\phi,*}$.)

The coupling corresponding to the kinetic operator does not flow in this choice of frame. The wavefunction renormalization furthermore modifies the flow of the remaining couplings, to wit (no summation over i):

$$\beta_i \to \beta_i - \frac{n_{\phi,i}}{2}\eta_\phi g_i, \tag{2.61}$$

where $n_{\phi,i}$ is the number of fields contained in the operator $\mathcal{O}_i$. Henceforth, when referring to β_i, we shall assume the normalization of the kinetic operator has been absorbed into the anomalous dimension of the field(s). It is this system of β functions whose stability matrix has universal eigenvalues (to avoid cluttering of notation, we shall refer to the RG data in this improved frame by the same letters, i.e., $\theta^{(I)}$, e^I, etc.).

The eigenbasis of the stability matrix also allows one to define the operators corresponding to eigenperturbations of the fixed point,

$$\hat{\mathcal{O}}_I := \sum_i e_I{}^i \mathcal{O}_i, \tag{2.62}$$

in the sense that a perturbation $\propto \hat{\mathcal{O}}^I$ flows as

$$\delta\hat{g}^I(k) = \left(\frac{\Lambda}{k}\right)^{\theta^{(I)}} \delta\hat{g}^I(\Lambda), \tag{2.63}$$

One may likewise refer to $\Delta_{\hat{\mathcal{O}}_I} := -\theta^{(I)}$ as the *quantum scaling dimension* of $\hat{\mathcal{O}}_I$ at the given fixed point. The exception is the kinetic operator: being a redundant operator, its quantum scaling dimension is not well-defined. Instead, it fixes the quantum scaling dimension of ϕ as $\Delta_\phi = d_\phi + \eta_\phi/2$ (thus explaining why η_ϕ is called 'anomalous' dimension of ϕ, where the factor 1/2 is conventional). The connection to a quantum version of dimensional analysis can be made by considering correlation functions. For the correlator of ϕ, one finds

$$\big\langle \phi(x)\, \phi(x') \big\rangle \sim \frac{1}{|x - x'|^{2d_\phi + \eta_\phi}}, \tag{2.64}$$

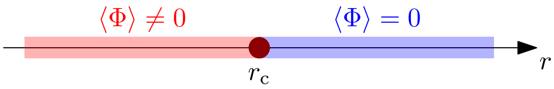

Figure 2.1: Schematic representation of a phase transition tuned by control parameter r. The symmetry-broken phase is characterized by a non-vanishing vacuum expectation value of order parameter Φ. Without loss of generality, it is assumed that the order is destabilized for large enough $r > r_c$. If the phase transition takes place at finite temperature it is called a thermal phase transition. In this case, the control parameter r can be the temperature itself. If the phase transition takes place at zero temperature, it is called a *quantum phase transition.* In this case, r corresponds to some non-thermal control parameter, such as pressure, doping, or magnetic field.

and similarly, since the $\hat{\mathcal{O}}_I$ are a superposition of local operators, we may define the corresponding position-resolved operator $\hat{\mathcal{O}}^\phi_I(x)$ as its 'density' via $\hat{\mathcal{O}}_I \equiv \int_x \hat{\mathcal{O}}^\phi_I(x)$, with correlation function

$$\left\langle \hat{\mathcal{O}}^\phi_I(x)\, \hat{\mathcal{O}}^\phi_{I'}(x') \right\rangle \sim \frac{1}{|x - x'|^{2D-\theta^{(I)}-\theta^{(I')}}}. \tag{2.65}$$

Note that in general, $e^i_I \neq \delta^i_I$, such that operators with a well-defined quantum scaling dimension may be a (possibly infinite) superposition of terms – albeit still local – with different number of fields and derivatives. This is often referred to as *operator mixing.*

2.5.2 Scaling at (quantum) phase transitions

We saw above that perturbations at a fixed point with critical exponent $\theta^{(I)} > 0$ grow over the course of RG flow towards the IR; they – or the respective couplings – are called *relevant.* On the other hand, those with $\theta^{(I)} < 0$ tend to zero in the deep IR, and are called *irrelevant.* At certain fixed points and/or in the presence of special symmetries, there may be $\theta^{(I)} = 0$. The corresponding perturbations are called *marginal.* In this case, if the Hessian of the β function of the marginal coupling is negative (positive) definite, the coupling is called *marginally irrelevant (relevant).* The precise physical interpretation depends on the specific setting. This will be the topic for the remainder of this chapter.

We begin with the arguably more readily accessible realization of quantum scale symmetry in physical systems, viz., in the vicinity of continuous phase transitions. Physically, a phase transition is tuned by some control parameter r, as illustrated in Fig. 2.1. Let us take this opportunity to recall that if this parameter is temperature, the transition is called a *thermal phase transition* (since the ordered state is destabilized by thermal fluctuations). On the other hand, if the tuning parameter is not temperature, the transition may just as well take place at zero temperature. Then, the ordered state can be destroyed only by quantum ('zero-point') fluctuations. Phase transitions at zero temperature are called *quantum phase transitions.* As explained in Sec. 1.1.2, our main focus later shall be primarily on quantum phase transitions, due to their ability to host fermionic degrees of freedom. Nevertheless, it will be useful to warm up by first discussing phenomenological aspects that are common to both thermal and quantum phase transitions, and discuss the additional features of quantum phase transitions afterwards.

Regardless of the precise physical connotation of r, what is important at the moment is that tuning this parameter to its critical value r_c allows the system to display scale-invariant behaviour. Likewise, in RG language, relevant perturbations away from the fixed-point values of couplings need to be tuned to zero, since they would otherwise drive the system away from scale symmetry. Control parameters tuning a transition in a given system hence map to RG-relevant directions in theory space. Typically, different control parameters tune a system into distinct ordered phases. Since direct and continuous order-to-order transitions are usually not allowed,$^{21)}$ continuous phase transitions correspond to RG fixed points with a unique relevant direction; we shall on occasion refer to such fixed points as *critical fixed points*. The symmetry properties of the order parameter (and if applicable additional gapless degrees of freedom) determine the field content of the pertinent field theory. As a very simple example, many thermal ferromagnet-to-paramagnet transitions are captured by a three-component scalar field (φ_a) with O(3) in $D = 3$ 'spacetime' dimensions (the so-called 'Heisenberg model'). (See the discussion in Chap. 1, footnote 6) for the counting of dimensions.) Two different ferromagnets, like the metal iron (Fe) or the carbide halide $\mathrm{Gd_2BrC}$, correspond to different values for couplings to operators such as $\int_x \{\varphi^2, \varphi^4, \varphi^6, (\partial\varphi)^4\}$, etc. at the UV scale (the index structure of φ is neglected for simplicity)$^{22)}$,$^{23)}$. Among these operators, most are irrelevant. Though one could, in principle, determine their values from first principles, it is not necessary (and likely not feasible in any case): rather, over the course of RG flow, they will automatically asymptote to their fixed-point values. The coupling to $\int_x \varphi^2$, conventionally denoted $\frac{1}{2}\bar{m}^2$ ('half the squared scalar mass'), corresponds – modulo operator mixing – to the unique relevant RG direction in theory space. By tuning the temperature to its critical value, the (dimensionless version of) the squared mass is tuned to m_*^2 by hand. As a result, all thermal paramagnet-to-ferromagnet (without isotropies, etc.) transitions in the same number of dimensions show the same *critical exponents*; this is called *universality*, as illustrated for Fe vs $\mathrm{Gd_2BrC}$ in Fig. 2.2 (the comment applies *mutatis mutandis* for other universality classes). Both the notion of 'critical exponents' and 'universality' require further comment.

First, universality in the above 'physical' sense of universal scaling behaviour refers to the fact that certain observables are independent of UV data. This needs to be distinguished from the 'technical' notion of universality in the sense of scheme-independence (or more specifically in the FRG context, regulator-independence). The latter concern any physical measurable quantity, including those which are very much sensitive to UV data. For instance, in scalar ϕ^4 theory, the mass parameter m^2 is a scheme-dependent quantity (both in its dimensionful as well as dimensionless avatars). This is not problematic, since m^2 is only a theory parameter, and not something that can be measured in experiment. What is measurable, on the other hand, is the so-called *pole mass*, i.e., the pole of the real-time connected 2-point function. (It is possible to relate the pole mass to the correlation length, but we shall not use this relation to calculate the correlation length from first principles; the scaling behaviour of the correlation length will turn out to be more readily calculable in terms of stability matrix eigenvalues.) Using m^2 as a proxy for the pole mass is merely an approximation (though one we shall use later, e.g., in Chap. 7), and it is this approximation – more precisely, the neglect of dependence of $\Gamma^{(2)}$ on higher orders of p^2 – that incurs the scheme-dependence; expressed somewhat

---

21) Strictly speaking, this argument holds only within Landau theory (cf., e.g., Landau & Lifshitz 2013), and it is possible to violate this principle if soft modes beyond order-parameter fluctuations are present at the critical point. We shall, however, not encounter such scenarios in this thesis.

22) We write these local monomial (in fields) operators as placeholders for the quantum scaling eigenoperators with the largest matrix elements with said operators.

23) In fact, the natural UV scale itself, being the inverse lattice spacing, also depends on material-specific details of quantum chemistry.

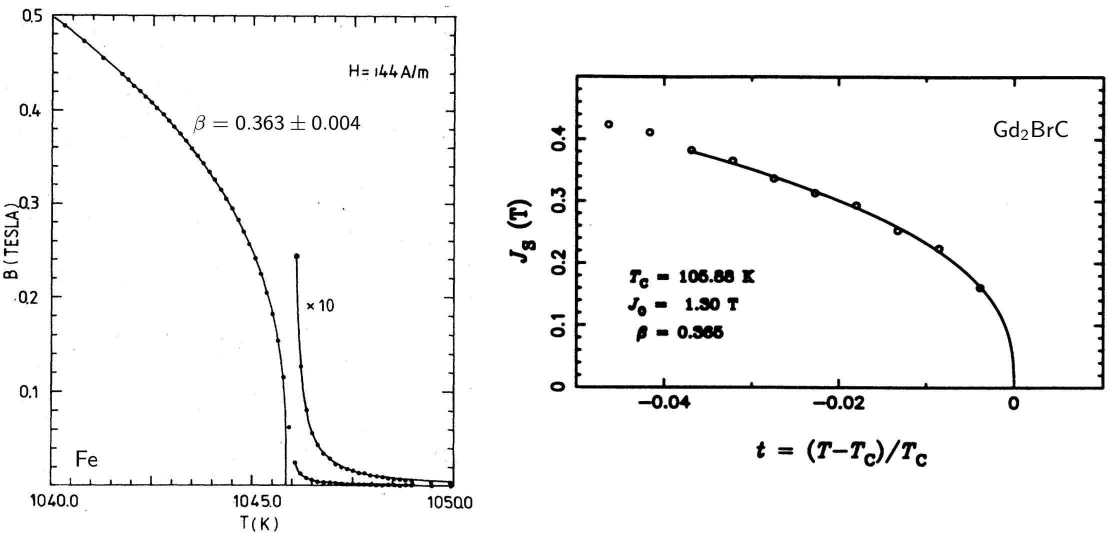

Figure 2.2: Experimentally measured temperature dependence of magnetization (= vacuum expectation value of ferromagnetic order parameter) in Fe (left panel, adapted from Stüsser, Rekveldt & Spruijt 1985) vs $\mathrm{Gd_2BrC}$ (right panel, adapted from Reisser, Kremer & Simon 1995) near their respective critical points. Although non-universal data such as T_c depend on the specific material, the exponent β (see Tab. 2.1 for definitions) does not, and agrees within uncertainties with theoretical estimates of Guida & Zinn-Justin (1998) for the $D = 3$ Heisenberg universality class.

differently, it is a truncation artefact, and the sensitivity of the approximated pole mass to choice of regulator would be a rough measure of the truncation error. Whilst universal in the sense of scheme-independent therefore does not imply universal in the sense of insensitive to UV data, the converse is definitely true: observables that are independent of UV data are also independent of choice of regulator (modulo artefacts introduced by approximation). Henceforth, we shall reserve 'universal' for the more restrictive notion of insensitivity to UV data.

Concerning the universal data characterizing a phase transition, the most expedient way to access them experimentally is through the non-analytic part of observables, which show scaling behaviour as a function of the input parameter, of which there are – broadly speaking – three categories. First, there are thermodynamic variables such as free energy, specific heat, etc., which exhibit scaling behaviour as a function of the tuning parameter,

$$Y \propto |\delta\tilde{r}|^{\varkappa_Y} \qquad (|\delta\tilde{r}| \ll 1) \tag{2.66}$$

with $\delta\tilde{r} := (r - r_{\mathrm{c}})/r_{\mathrm{c}}$ the dimensionless distance to criticality.[24] The scaling exponent of different thermodynamic quantities are usually denoted by different symbols, with definitions summarized in Tab. 2.1. In addition, one may measure (using the usual spectroscopic techniques) the correlation function of the order parameter[25] Φ which

---

[24] We are assuming here that the exponent for $\delta\tilde{r} \to 0^+$ and 0^- (in other words, approaching the critical point from the symmetric and symmetry-broken sides of the transition) are the same. While not true in general – see, e.g., Léonard & Delamotte (2015) and references therein – it is generic, and will certainly be the case in all transitions we shall have occasion to study hereinafter. This remark of course does not apply to the trivial case of observables that vanish on side of the transition, such as the order-parameter expectation value.

[25] We denote the order-parameter field as Φ, to distinguish from the (super-)field ϕ containing all low-energy degrees of freedom.

exponent	definition
ν	$\xi \propto \lvert\delta\tilde{r}\rvert^{-\nu}$
α	$c \propto \lvert\delta\tilde{r}\rvert^{-\alpha}$
β	$\langle\Phi\rangle \propto (-\delta\tilde{r})^{\beta}\Theta(-\delta\tilde{r})$
γ	$\chi \propto \lvert\delta\tilde{r}\rvert^{-\gamma}$
η	$\langle\Phi(x)\Phi(x')\rangle \propto \lvert x-x'\rvert^{-D+2-\eta}$
δ	$\langle\Phi\rangle \propto \lvert J\rvert^{1/\delta}$ $(J \to 0)$

Table 2.1: (Adapted from Herbut 2007) Upper part: Definition of critical exponents asymptotically close to but away from criticality, as appearing in Eq. (2.66), expressed in terms of the asymptotic behaviour of the non-analytic part of observables. Here, c is the specific heat, Φ the order parameter, and χ the static order-parameter susceptibility (usually just abbreviated to 'the' susceptibility). The correlation length ξ is defined by the exponential decay of the order-parameter correlator, $\langle\Phi(x)\Phi(x')\rangle \sim \mathrm{e}^{-|x-x'|/\xi}$. Lower part: Critical exponents defined *at* criticality (i.e., $\delta\tilde{r} = 0$), with J the current conjugate to the order parameter Φ.

shows critical scaling *at criticality* (i.e., $r = r_\mathrm{c}$)

$$\langle\Phi(x)\,\Phi(x')\rangle \sim \frac{1}{|x-x'|^{D-2+\eta}}, \tag{2.67}$$

which introduces the order-parameter anomalous dimension η. If the kinetic operator contains two derivatives, then η corresponds precisely to the field anomalous dimension η_Φ introduced in the previous section [see Eq. (2.60)]. The above equation assumes full rotational symmetry SO(D). [If $D = 2$, then one actually has O(2) instead of SO(2), since inversion at the origin is a rotation by π in two dimensions. We shall tacitly assume this henceforth, and not mention this explicitly again.] In the case of thermal phase transitions, the usual Matsubara—Kaluza–Klein argument shows that the (formal) spacetime dimension D of the quantum field theory is simply the number of spatial dimensions of the physical system. The above equation is simply a static correlation function, and SO(D) means spatial rotational symmetry, which often does emerge in the low-energy limit. For quantum phase transitions, however, the above equation would make a dynamical statement, with D the physical spacetime dimension of the system and SO(D) would be spacetime rotational invariance, the Euclidized avatar of Lorentz symmetry SO$(1, D-1)$. We shall come back to this point later when discussing the phenomenological features of quantum phase transitions which go beyond those of the thermal ones.

A final kind of critical exponent is one which measures the order-parameter expectation value at criticality, but in the presence of a (small) explicit-symmetry-breaking current J (i.e., $S \to S + \int_x J \cdot \Phi$, for instance an external magnetic field for a ferromagnetic transition), and is defined by

$$\langle\Phi\rangle_J \sim |J|^{1/\delta} \qquad (J \to 0, \delta\tilde{r} = 0). \tag{2.68}$$

The exponents $\nu, \alpha, \beta, \gamma, \delta, \eta$ are the ones that are accessible in experiments. The critical exponents $\theta^{(I)}$ and the field anomalous dimensions η_ϕ are the ones that directly come from an RG calculation. As noted above, the anomalous dimension η of both approaches coincide if the kinetic operator is defined suitably. It turns out that the remaining exponents can be expressed in terms of η and the unique positive (RG) critical exponent $\theta_0 := \max_I \theta^{(I)} > 0$. Intuitively speaking, this is because in a scale-invariant setting, the characteristic length scale is set by the size of the relevant perturbation(s) – of which there is only one. Once this length scale is set, the behaviour of observables is fixed by dimensional analysis, with the canonical scaling dimensions replaced by the quantum corrected versions at the pertinent critical RG fixed point. A more formal manipulation invoking scaling functions allows one to derive the explicit relations (cf., e.g., Herbut 2007; Sachdev 2010a):

$$\alpha + 2\beta + \gamma = 2, \tag{2.69}$$

$$\alpha + \beta(\delta + 1) = 2, \tag{2.70}$$

$$\gamma = (2 - \eta)\nu, \tag{2.71}$$

$$\alpha = 2 - \nu D. \tag{2.72}$$

Thus, computing the leading RG critical exponent and the anomalous dimensions of the fields allows one to derive predictions for the scaling behaviour observables measured in experiments. The final equality above assumes that the free energy density scales as $f \propto \xi^{-D}$, called *hyperscaling* (note that it is the only place where the dimensionality enters explicitly). Though it may be violated on occasion, we shall not encounter any such pathologies in our own investigations. Let us also note in passing that beyond critical exponents, there are further universal quantities, called 'amplitude ratios' (Herbut 2007), given schematically by

$$\frac{Y(\delta\tilde{r} \to 0^+)}{Y(\delta\tilde{r} \to 0^-)}. \tag{2.73}$$

These may in principle be sensitive to ratios of fixed-point couplings corresponding to operators of the same canonical dimension, but beyond the scope of the present thesis.

To complete our discussion of universal scaling behaviour, we need to elaborate on the additional features of a quantum phase transition. The discussion here is, upto adjustment of notation, a simplified and somewhat informal version of Vojta (2003), and is meant to recapitulate concepts and relations that will play some role subsequently in this thesis; for a more exhaustive review, see the aforementioned reference. One of the main peculiarities of quantum phase transitions, as compared to thermal ones, is the (topological) spacetime dimension D of the underlying quantum field theory, which now equals the physical spacetime dimension of the system. Thus, for graphene one has $D = 3$ with 2 of them coming from the spatial dimension (since graphene has a quasi-planar structure, cf. Castro Neto *et al.* 2009); a putative quantum phase transition in a 3D Weyl semimetal like (bulk) tantalum arsenide (Witczak-Krempa *et al.* 2014) would be described by a quantum field theory living in $D = 4$. Intuitively, this may be understood by recalling that $S^1(1/T) \times \mathbb{R}^{D-1} \to \mathbb{R}^D$ for $T \to 0$. A first consequence is that the order-parameter correlator $\langle \Phi(x)\Phi(x') \rangle$ thus automatically contains dynamical information. In other words, equilibrium and dynamical phenomenology are connected to each other, which is not the case in thermal phase transitions (cf., e.g., Sachdev 2010a). Let us first consider the case that spacetime rotational invariance $\mathrm{SO}(D)$ [recall that it is the Euclidized version of Lorentz invariance $\mathrm{SO}(1, D-1)$, and that SO is tacitly replaced by O if the argument becomes 2] is actually emergent. This is quite a large symmetry, but will indeed turn out to be emergent in four out of five cases in this thesis. A consequence of spacetime symmetry is that there is only the $\mathrm{SO}(D)$ invariant $(x - x')^2$

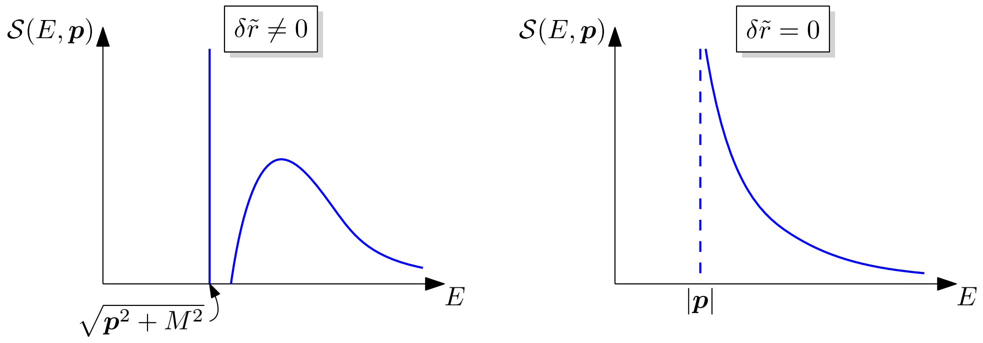

Figure 2.3: Spectral function as a function of frequency. Left: Close to but away from criticality, there is a conventional quasiparticle delta peak separated from a many-particle continuum by a gap, assuming low-energy degrees of freedom can scatter only by exchanging quanta of order-parameter fluctuations Φ. Here, M denotes the actual pole mass of Φ, as opposed to the (renormalized) mass parameter m appearing in the action. Right: At criticality $\delta\tilde{r}\to 0$, the pole mass vanishes and the continuum merges with the delta peak to produce a branch cut.

on which the correlation function can depend. To obtain real-time data, we have to Wick rotate $\mathrm{i}\tau\to t+\mathrm{i}0^+$, where the D-dimensional vector x is split into $1+(D-1)$ components as $(x^\mu)=(\tau,\boldsymbol{x})$, and the $\mathrm{i}0^+$ picks out the retarded Green's function (cf., e.g., Mahan 2000). (The usual caveats concerning Wick rotation discussed in Sec. 2.1 apply.) With this knowledge, we can write the retarded Green's function of the order parameter at criticality as

$$G^{\mathrm{R}}_{\Phi}(t,\boldsymbol{x})\sim\frac{1}{[\boldsymbol{x}^2-(t+\mathrm{i}0^+)^2]^{(D-2+\eta)/2}},\tag{2.74}$$

$$\tilde{G}^{\mathrm{R}}_{\Phi}(E,\boldsymbol{p})\sim\frac{1}{[\boldsymbol{p}^2-(E+\mathrm{i}0^+)^2]^{(2-\eta)/2}},\tag{2.75}$$

where we have eliminated the second spacetime argument $(x'^\mu)=(\tau',\boldsymbol{x}')$ using translational invariance and denoted the Fourier transform of of the retarded Green's function by $\tilde{G}^{\mathrm{R}}_{\Phi}(E,\boldsymbol{p})$. Scattering experiments measure the *spectral function* (called *dynamical structure factor* in case of magnets), which is proportional to the imaginary part of the retarded Green's function, $\mathcal{S}(E,\boldsymbol{p})=(-1/\pi)\,\mathrm{Im}\,G^{\mathrm{R}}_{\Phi}(E,\boldsymbol{p})$. Eq. (2.75) allows us to read off, that if $(2-\eta)/2$ is non-integer (which would be generic at a non-Gaußian fixed point), the usual quasiparticle pole at $E^2=\boldsymbol{p}^2$ is replaced by a branch cut for $E^2>\boldsymbol{p}^2$. This is illustrated in Fig. 2.3. A physical cartoon of the equations above is as follows: If we assume that low-energy degrees of freedom can only scatter by exchanging quanta of order-parameter fluctuations, then close to but away from criticality, there is still a distinct quasiparticle pole. The many-particle continuum is separated from it by the pole mass M of the Φ field. At criticality $\delta\tilde{r}\to 0$, $M\to 0$ (this is not to be confused with the fixed-point value of the mass parameter m_*, which is scheme-dependent and can be zero, positive or even negative). Then, the continuum merges with the delta peak, leaving behind only the branch cut singularity.

Let us now come to the case where $\mathrm{SO}(D)$ does not emerge. This has two consequences: First, even if we assume a residual $\mathbb{Z}_2\times\mathrm{SO}(D-1)$ symmetry (i.e., time-reversal plus spatial rotations), the spacetime separation vector $x-x'$ now contains two independent scales $|\tau-\tau'|$ and $|\boldsymbol{x}-\boldsymbol{x}'|$ (in Euclidean notation). To get rigorous scaling forms for correlators, we need to consider correlators with either time or space fixed, $\langle\Phi(\tau,\boldsymbol{x})\Phi(\tau,0)\rangle$

or $\langle\Phi(\tau,\boldsymbol{x})\Phi(0,\boldsymbol{x})\rangle$. An additional issue that arises is that time coordinates and spatial coordinates are not constrained to transform in the same way under dilatations. The suitable generalization of Eq. (2.41) in this setting reads as

$$\delta_\epsilon \boldsymbol{x} = \epsilon \boldsymbol{x}, \qquad \delta_\epsilon \tau = \epsilon z \tau. \tag{2.76}$$

The weight z is called the *dynamical critical exponent*; its deviation from unity expresses to what extent (Euclidean) time scales differently from space26). The kinetic operator which fixes the wavefunction renormalization is usually defined now to be the leading spatial derivative term. Corrections to the leading time derivative term in the action cannot be compensated completely by wavefunction renormalization due to the lack of Lorentz symmetry; the residual corrections are then absorbed into z, see, e.g., Chap. 4 for a worked example. [It is conventional to denote the canonical value, the 'quantum' value (viz., the non-Gaußian fixed-point value), and the running values of z by the same symbol, and rely on context to clarify the precise meaning (for example, see Herbut 2007). We shall do the same in subsequent parts of this thesis.] One way to express z in terms of measurable correlators is by considering the suitable generalization of Eq. (2.67),

$$\langle\Phi(\tau,\boldsymbol{x})\Phi(\tau,\boldsymbol{x}')\rangle \sim \frac{1}{|\boldsymbol{x}-\boldsymbol{x}'|^{(D-1)+z-2+\eta}}, \tag{2.77}$$

$$\langle\Phi(\tau,\boldsymbol{x})\Phi(\tau',\boldsymbol{x})\rangle \sim \frac{1}{|\tau-\tau'|^{[(D-1)+z-2+\eta]/z}}. \tag{2.78}$$

It is also possible to measure z away from criticality in terms of the correlation time τ_c via $\tau_c \sim \xi^z$, cf., e.g., Sachdev (2010a), but the above will be sufficient for our purposes. The combination $(D-1)+z$ is the scaling dimension of the spacetime volume element, $\delta_\epsilon \mathrm{d}^D x = \delta_\epsilon(\mathrm{d}\tau\,\mathrm{d}^{D-1}\boldsymbol{x}) = \epsilon\,[z+(D-1)]\,\mathrm{d}^D x$. For this reason, $D_{\text{eff}} := (D-1)+z$ is often referred to as the 'effective dimension' of the system near the quantum critical point. Note that this does not in any way imply a change in the topological spacetime dimension of the system, which remains at D. (In our notation, D will *always* refer to the topological dimension of spacetime.) It is, however, precisely the 'dimension' which enters the zero-T version of the hyperscaling assumption, to wit

$$f \propto \xi^{-D_{\text{eff}}}.$$

Consequently, the identities relating thermodynamic critical exponents to their RG counterparts above [Eqs. (2.69)–(2.72)] go through, except that D is replaced by D_{eff} in Eq. (2.72).

Since the tuning parameter r is not the temperature, one can consider in addition the behaviour of the system at non-vanishing temperature (in other words, 'add an axis T to Fig. 2.1'). This leads to the richer phase diagram shown in Fig. 2.4. Obviously, if the temperature is large enough, the system will 'forget' all details about the zero-temperature fixed point; the physics is non-universal, at least from the point of view of said fixed point. We shall assume we find ourselves below this temperature. Even then, scaling behaviour is not expected to arise generically, because the temperature T introduces an extra scale, in addition to the correlation length ξ. More precisely, since the inverse temperature has the same dimensions as Euclidean time τ, the ratio of ξ and $T^{-1/z}$ constitutes an independent dimensionless parameter. For observables to show scaling behaviour governed

---

26)It is worth pointing out that whilst SO(D) invariance implies $z=1$, the converse is not true, see Schwab *et al.* (2021) for an example.

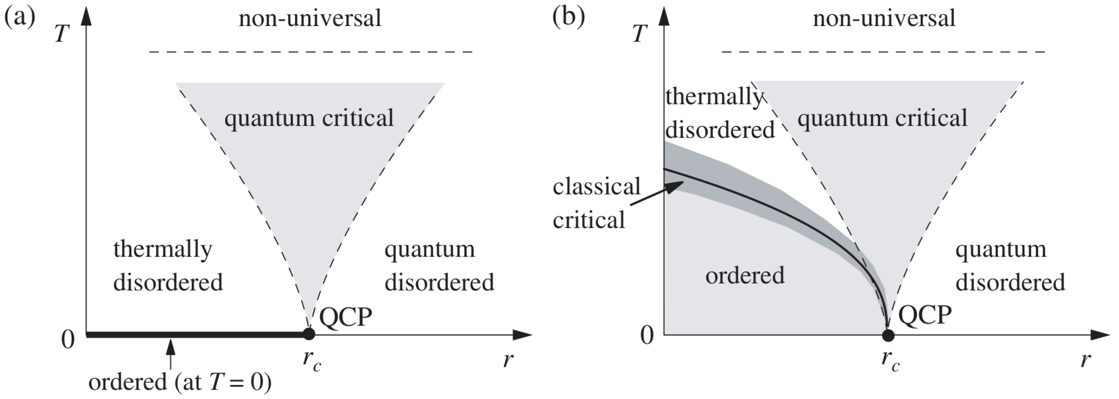

Figure 2.4: (From Vojta 2003) Extension of Fig. 2.1 to include temperature in the quantum phase transition ($r \neq T$) case. The shaded region with dashed boundaries is the quantum critical 'fan', within which the system exhibits scaling behaviour of observables with respect to T, with exponents determined by the critical fixed point. The boundaries of the 'fan' scale as $T_{\text{fan}} \propto |\delta\tilde{r}|^{\nu z}$. At high enough temperatures, marked by a dashed line labeled 'non-universal', the physics is no longer described by the zero-temperature universality class. For $r < r_{\text{c}}$, there are two distinct scenarios depending on specifics of the ordered state. (a) Order exists only at zero temperature (for instance due to obstructions such as the Coleman–Mermin–Wagner theorem). (b) Order exists at finite temperature. In this case, above the solid line, order is destroyed by thermal fluctuations. Close to the solid line, the critical exponents are given by a thermal universality class.

by the quantum critical point, we must have $\xi \gg T^{-1/z}$. Since $\xi \propto |\delta\tilde{r}|^{-\nu}$, in the regime bounded by $T = T_{\text{fan}} \sim |\delta\tilde{r}|^{\nu z}$, ξ is infinite for all practical purposes, and the system only has one independent scale T, as a function of which it then shows universal scaling behaviour. Since ν and z are (in most cases) positive, this region 'fans' out for larger T, which may be deemed counter-intuitive (Sachdev 2010a). The bound on T above which quantum critical is replaced by (non-universal) thermally dominated behaviour is itself non-universal, but can be quite large in practically relevant systems (cf., e.g., Vojta 2003, and references therein). Thus, there is an extended region in the phase diagram where the system exhibits unconventional power laws as a function of temperature, effectively has no conventional quasiparticle excitations, exhibits non-Fermi-liquid behaviour[27], etc.. Even though the behaviour in the quantum critical fan is strictly speaking not governed by an IR-stable fixed point[28], for all practical purposes, it behaves like a novel 'phase of matter'. One example for such T-dependent scaling behaviour we shall have occasion to use later (Chaps. 5 and 6) is the specific heat $c(T)$. It is given by the T-derivative of the internal energy density u, whereby the latter has the same dimensions as the free energy density f. From the quantum scaling hypothesis (but with ξ replaced by $T^{-1/z}$), we may hence derive

$$c(T) \sim \partial_T T^{D_{\text{eff}}/z} \sim T^{D_{\text{eff}}/z-1} = T^{d/z}, \tag{2.79}$$

where $d := D-1$ is an often-used shorthand for the number of spatial dimensions. Another scaling relation involving temperature we shall need later arises if order survives at small but finite T, see Fig. 2.4(b). Close to the critical point, we can estimate the excitation gap of order-parameter fluctuations on the ordered side as $\Delta \sim (-\delta\tilde{r})^{\nu z}$, where we have used the fact that energy, like temperature T, has length dimension $(-z)$, and the only pertinent length scale in the system is $\xi \sim |\delta\tilde{r}|^{-\nu}$. For temperature to destroy order, T has to be of the order of the excitation gap. Hence, one has the relation

---

[27] A nice review of Fermi liquid theory has been given by Polchinski (1992).

[28] An example of a non-Gaußian IR-stable fixed point would be the Banks–Zaks fixed point in SU(N_c) gauge theory (cf., e.g., Hollowood 2013). By contrast, a quantum critical point has a unique IR-relevant direction.

$$T_\mathrm{c} \sim (-\delta\tilde{r})^{\nu z} \tag{2.80}$$

for $\delta\tilde{r}$ small enough, which we shall use later, for instance, to estimate the effective interaction strength in bilayer graphene from its ordering temperature (Chap. 6).

2.5.3 Predictivity in fundamental physics

From an effective field theory (EFT) perspective, which we have assumed tacitly thus far, one starts at some UV scale Λ and wishes to make predictions at $k < \Lambda$. To achieve this, one only needs to keep track of perturbations from the fixed point at $k = \Lambda$ which are not too irrelevant; due to Eq. (2.63), these deviations will be small at the scale k if the operator is irrelevant enough. (In the study of universal scaling at phase transitions above, one can in fact make k as small as one wishes, such that all irrelevant perturbations can be neglected entirely.) From the point of view of fundamental physics, however, one would like to predict physics at *all* scales. The matching scale $\Lambda \equiv k_\mathrm{ref}$ is then not so much the upper boundary of validity of the theory (since a fundamental theory or 'theory of everything' should have no such thing), but a reference scale at which free parameters of the theory are to be fixed by comparison ('matching') with experiment. From this point of view, an operator having negative $\theta^{(I)}$ provides scant relief: for $k > k_\mathrm{ref}$ deviations from the fixed point will become increasingly large. All operators, no matter relevant or irrelevant, are potentially important; whether they are relevant or not determines whether they become important at $k < k_\mathrm{ref}$ or $k > k_\mathrm{ref}$. There are hence *a priori* infinitely many free parameters, and the theory is not predictive above the reference scale k_ref. Some further set of constraints, for instance in the form of an additional symmetry principle, is needed to narrow down the space of admissible parameters to a finite-dimensional one. Quantum scale symmetry, or more precisely, the assumption that quantum scale symmetry is restored in the deep ultraviolet ($k \to \infty$), is one such way. The basic mechanism for this is based on the consideration that if one measures a violation of quantum scale symmetry $\delta\hat{g}^I(k_\mathrm{ref}) \neq 0$ at some reference scale k_ref, then at higher scales[29] $k > k_\mathrm{ref}$, $\delta\hat{g}^I(k) = \delta\hat{g}^I(k_\mathrm{ref})(k/k_\mathrm{ref})^{-\theta^{(I)}}$. If quantum scale symmetry is to be restored in the UV, $\delta\hat{g}^I(k) \to 0$ $(k \to \infty)$ for all I, one therefore needs

$$\forall k\colon\ \delta\hat{g}^I(k) = 0 \text{ if } \theta^{(I)} < 0.$$

In other words, quantum scale symmetry in the UV is tantamount to fixing all irrelevant couplings to their fixed-point value *at all scales*; the relevant couplings are the only free parameters of the theory and need to be fixed by measurement at some reference scale k_ref, as illustrated in Fig. 2.5. The assertion that this leads to predictivity is equivalent to saying that the number of relevant couplings at the pertinent RG fixed point is finite.

---

[29] This procedure of continuing RG flow 'backwards' towards the UV is a purely formal exercise. Physically, it is only the flow towards the IR, i.e., integrating out high-energy modes, that is well-defined; 'integrating in' high-energy modes is per se unphysical. A more rigorous discussion would require one to consider instead the momentum- and mass-dependence of the set of all proper n-point functions $\Gamma^{(n)}$. In this sense, the RG scale k may be seen as a crude representative for the typical momenta and masses in a scattering process, which will be sufficient for our purposes.

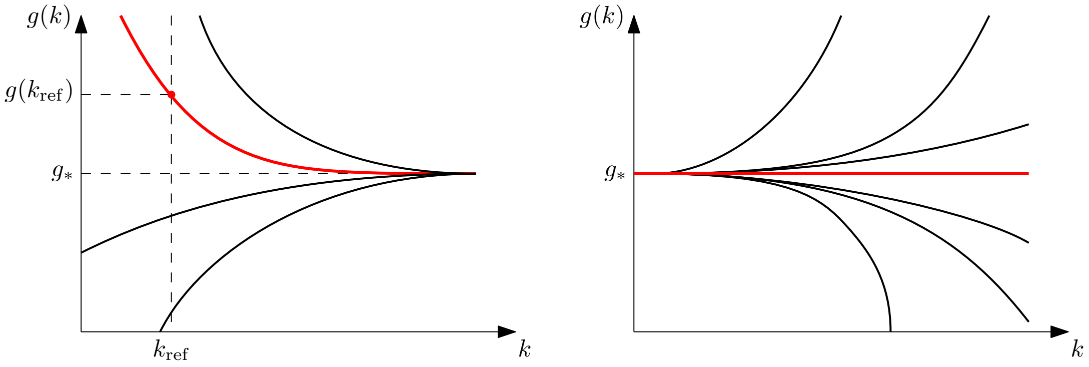

Figure 2.5: Relevant vs irrelevant couplings with respect to quantum scale symmetry in the UV [$g_* = 0$ ($\neq 0$): coupling is asymptotically free (safe)]. Left: If the coupling g is relevant, there are several trajectories compatible with quantum scale symmetry in the UV. The correct one (red, fat) needs to be fixed by measuring the value of g at some experimentally accessible scale k_{ref}. Right: If g is irrelevant, then only one trajectory is compatible with quantum scale symmetry: the coupling is predicted at all scales. For simplicity, the trajectory emanating from the fixed point is drawn flat. In general, threshold effects may lead to certain degrees of freedom decoupling dynamically at some scale, in which case even the critical trajectory will be curved, at least below that scale. Notably, this occurs in asymptotically safe quantum gravity, whereby metric fluctuations decouple dynamically from matter around the Planck scale, see Eichhorn & Held (2018a).

The simplest fixed points are of course the Gaußian ones, where an operator's scaling dimension is equal to its canonical dimension. In particular, it is then straightforward to show using dimensional analysis that the scaling dimension of an operator $\mathcal{O}$ containing n_ϕ powers of fields and n_∂ derivatives is

$$d_{\mathcal{O}} = n_\phi (D - n_{\partial,\text{kin}})/2 + n_\partial - D \tag{2.81}$$

where $n_{\partial,\text{kin}}$ is the number of derivatives in the kinetic operator [in other words, $(D - n_{\partial,\text{kin}})/2 \equiv d_\phi$ is the canonical dimension of the field ϕ]. Since there are no quantum corrections, this is equal to minus the stability matrix eigenvalue, $\theta^{(\mathcal{O})} = -d_{\mathcal{O}}$. Since generically[30] $d_\phi > 0$, there are only finitely many relevant couplings. The fact that the Gaußian fixed point must be approached upon (formally) continuing the flow back to $k \to \infty$ implies that all irrelevant interactions have to vanish in the classical action. Such theories are called *perturbatively renormalizable*, because UV divergences arising in the perturbative evaluation of the effective action can be absorbed into a finite number of counterterms. On the other hand, canonically irrelevant interactions require the introduction of new counterterms at every order of perturbation theory, and are hence called perturbatively non-renormalizable. In the perturbative approach to quantum field theory, predictivity is hence synonymous with perturbative renormalizability. The only admissible interactions compatible with a UV Gaußian fixed point hence correspond to relevant or, possibly, marginal couplings. Of the former, no fundamental examples are known in Nature. Examples of the latter in $D = 4$ include scalar self-couplings, Yukawa couplings, and gauge couplings. Among marginal interactions, marginally irrelevant ones cannot be continued backwards to arbitrarily large k, and hence the only theory compatible with quantum scale symmetry is the non-interacting theory. This is often

---

[30] i.e., excluding degenerate cases such as scalar field theory in $D = 2$, where $d_\phi = 0$, and there are infinitely many operators with canonical dimension zero.

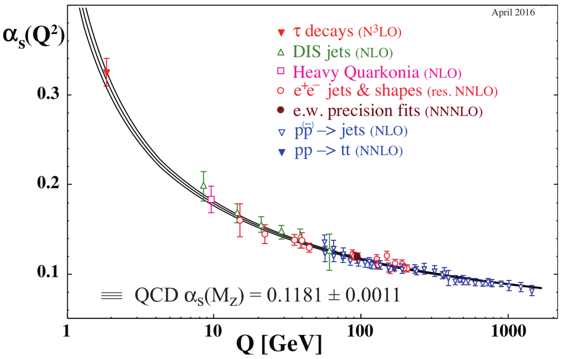

Figure 2.6: (From Particle Data Group 2016) Measurements of the running QCD gauge coupling ($\alpha_s := g^2_{\mathrm{SU}(3)}/4\pi$) using various processes. The parantheses denote the level of perturbative QCD used to extract the coupling from experimental cross-sections (NLO = next-to-leading order, NNLO = next-to-next-to-leading order, etc.). The coupling decreases for increasing values of the RG scale, and is expected to vanish in the deep UV.

referred to as *triviality*. On the other hand, non-zero values of marginally relevant interactions are compatible with a Gaußian fixed point in the deep UV. This is more commonly referred to as *asymptotic freedom*. Much like canonically irrelevant interactions can be excluded within perturbation theory using the proliferation of UV divergences, marginally irrelevant interactions can be argued to be incompatible with a fundamental theory valid at all scales without referencing quantum scale symmetry. Rather, the flow of marginally relevant couplings is such that they diverge at a finite UV scale. This is called a *Landau pole*, and the location of the pole is an upper bound for the validity of the theory.

An example of asymptotic freedom within the Standard Model is the theory of the strong interaction, quantum chromodynamics (QCD), see Fig. 2.6. On the other hand, the abelian gauge coupling, the Yukawa couplings and the quartic Higgs self-coupling have Landau poles. The fact that their low-energy values have been measured to be nonzero is, at least in principle, incompatible with a theory of everything valid at all scales. However, these poles occur at extremely high energies [for the U(1) hypercharge in the electroweak Standard Model, the Landau pole is at $10^{53}\,\mathrm{GeV}$ (Andrianov *et al.* 2013)]. Already below such utopic scales, there is a more pressing issue, namely the gravitational constant G_{N} (also called Newton constant). In the low-energy limit, it describes the mutual gravitational attraction of two masses $m_{1,2}$ as $F^{12}_{\mathrm{grav}} = -G_{\mathrm{N}}\, m_1 m_2 / r^2_{12}$, where r_{12} is the separation of the respective centres of mass. As a canonically irrelevant coupling, its nonzero infrared value of $G_{\mathrm{N}} \approx 6.7 \times 10^{-39}\,(\mathrm{GeV})^{-2}$ translates into a breakdown of predictivity (in a perturbative or EFT sense) at the Planck scale, $M_{\mathrm{Pl}} = 1/\sqrt{G_{\mathrm{N}}} \approx 1.2 \times 10^{19}\,\mathrm{GeV}$ (values taken from Tiesinga *et al.* 2021).

Whilst the proliferation of UV divergences does not have a straightforward non-perturbative generalization, quantum scale symmetry does: *asymptotic safety* (AS), as introduced by Weinberg (1979), is simply the generalization of asymptotic freedom to interacting fixed points. Whilst irrelevant couplings are still predicted by the fixed-point values, these can now be nonzero. The fact that an asymptotically safe theory remains predictive is equivalent to the assumption that (negative) quantum corrections to scaling dimensions are bounded (and do not, for instance, scale with the number of fields or derivatives). It turns out that this is usually the case in non-pathological theories. In practical examples, in fact, one gets more: The correction to scaling dimensions of

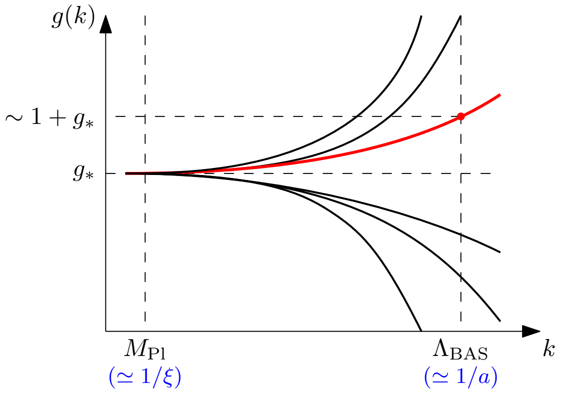

Figure 2.7: Illustration of effective asymptotic safety. Assume that the universe (red) lives on an RG trajectory where an irrelevant coupling deviates from its fixed-point value significantly ('~ 1') at a very large scale $\Lambda_{\rm BAS}$. At this point, the asymptotically safe description will break down and physics 'beyond asymptotic safety' will be observable. However, around the Planck scale (and at even lower scales such as those pertaining to particle colliders), these deviations will not be measurable. In condensed-matter realizations near a continuous phase transition, the role of $\Lambda_{\rm BAS}$ is played by the inverse lattice spacing $1/a$, whilst the IR scale is given by the inverse correlation length $1/\xi$.

operators is often positive (or equivalently, the corrections to RG critical exponents is negative). Though this has no significant effect on dimension 2 operators (i.e., they remain relevant), marginal operators often become (weakly) irrelevant, rendering the asymptotically safe fixed point *more* predictive than the Gaußian one. (This will feature prominently in Chap. 7.)

2.5.4 Effective asymptotic safety in particle physics and condensed matter

From a top-down approach, invoking UV quantum scale symmetry is a way to fix infinitely many undetermined parameters to non-trivial values. On the other hand, from a bottom-up perspective, realizing quantum scale symmetry in the UV requires one to tune infinitely many parameters to arbitrary precision. This is, however, not necessarily a serious obstruction to observing phenomenology derived from AS in experimentally relevant scales (such as those probed in contemporary colliders or astrophysical obervations). Let us assume to the contrary that there is a finite deviation δ_0 along an irrelevant direction I_0 from the fixed-point values at some 'beyond-AS' scale $\Lambda_{\rm BAS}$. The corresponding deviation translated to the Planck scale $M_{\rm Pl}$ will be

$$\delta\hat{g}^{I_0}(M_{\rm Pl}) = \delta_0 \left(M_{\rm Pl}/\Lambda_{\rm BAS}\right)^{-\theta^{(I_0)}} . \tag{2.82}$$

If there is a large enough separation of scales, $\Lambda_{\rm BAS} \gg M_{\rm Pl}$, then the asymptotic safety prediction of the corresponding fixed-point value will be indistinguishable from a putative theory that will ultimately supersede the AS theory of quantum gravity at even larger scales (Fig. 2.7). In the literature, scenarios of this kind are collectively referred to as *effective asymptotic safety* (cf., eg., Held 2020, and references therein).

This mechanism parallels the situation in continuous phase transition in a very appealing way. There, the equivalent of the 'beyond-AS' scale has a different physical origin; in solids, for instance, a rough estimate is the inverse lattice spacing (though a more refined estimate would need to account for hopping amplitudes, and will ultimately boil down to something of the order of the bandwidth). At this scale, irrelevant perturbations are of order one. However, upon flowing down to the IR scale $k_{\mathrm{IR}} \approx 1/\xi$, i.e., to scales of the order of the inverse correlation length, these deviations decay according to their quantum scaling dimensions. Since by tuning the system close to the transition one can make $1/\xi$ arbitrarily small, the ratio $\Lambda_{\mathrm{BAS}}/k_{\mathrm{IR}}$ can be made arbitrarily large. The situation that emerges in the deep IR is hence no different from one where all irrelevant couplings have been set to their fixed-point values at $k = \infty$ from the outset. Thus, although a given condensed-matter system is decidedly not asymptotically safe, and there is a clear upper bound to the scales at which the effective field theory describing the order parameter fluctuations and their coupling to other gapless modes must inevitably break down31), its (ultra) long-range behaviour is the same as a (hypothetical) asymptotically safe universe – albeit with possibly non-Standard Model matter and fundamental interactions.

---

31) For instance, for energy scales larger than the bandwidth, inter-band scattering will become important. At scales beyond the inverse lattice spacing, the solid will simply melt, and thereby go into a very different universality class altogether.

Chapter 3

Gross–Neveu SO(3) Quantum Criticality in $2+1$ Dimensions

In this chapter, we shall study the SO(3) incarnation of the Gross–Neveu (= chiral) universality class in three spacetime dimensions. Already from a purely theoretical standpoint, this is of interest. Gross–Neveu universality classes in three spacetime dimensions host at least one interacting fixed point with one (or at most very few) IR-relevant directions. As discussed in the previous chapter, such fixed points also correspond to highly predictive asymptotically safe quantum field theories, similar to the kind one – at least as far as adherents of the asymptotic safety paradigm are concerned – would wish to see realized in the Standard Model (plus quantum gravity). The analogy goes deeper due to the field content of theories pertaining to these chiral universality classes. In Yukawa systems, one may roughly understand the effect of metric fluctuations as lowering the effective spacetime dimension. More precisely, the total beta function (to a decent level of approximation) splits into the usual Standard Model part and a metric fluctuations contribution,

$$\beta_g = \beta_g^{\mathrm{SM}} + \beta_g^{\mathrm{QG}} \tag{3.1}$$

for the least irrelevant couplings $g \in \{y, \lambda\}$ near $D = 4$, viz., the Yukawa coupling y and the quartic scalar self-coupling λ. The gravitational contribution to leading order has the form

$$\beta_y^{\mathrm{QG}} = -f_y(G_*, \Lambda_*)y \qquad \beta_\lambda^{\mathrm{QG}} = -f_\lambda(G_*, \Lambda_*)\lambda, \tag{3.2}$$

where $f_{y,\lambda}$ are numbers that depend on the fixed-point values of the Newton coupling G_* and the cosmological constant Λ_*, but not directly on y and λ (see Chap. 7 for details). Thus, the radiative corrections from gravitons act as though the couplings live in a lower dimension.$^{1)}$ It is precisely this dimensional reduction what converts a potentially trivial theory into one supporting an interacting fixed point. The major difference in this regard

---

1) Defining the spacetime dimension rigorously is itself a subtle issue, especially if the metric itself is a fluctuating object to be averaged over in the path integral. The topological dimension of spacetime, for instance, remains fixed at 4. A more 'covariant' notion is that of *spectral dimension* D_{spec}, which essentially relates the average return probability of a test particle walking randomly for time duration T without backreaction in a given spacetime manifold as $P(T) \sim T^{-D_{\mathrm{spec}}/2}$. This has a nontrivial value in quantum theories of gravity, see Lauscher & Reuter (2005) for details on the asymptotic-safety perspective, as well as a brief review of other quantum gravity approaches. For our purposes, it will be sufficient to consider the analogy at the level of the effective power-counting dimension of couplings.

between the asymptotically safe completion of the Higgs-Yukawa sector of the Standard Model and Gross–Neveu quantum criticality in $D = 3$ spacetime dimensions is that in the latter, the reduction is performed 'by hand' (or more precisely by engineering), whereas in the former it occurs dynamically. The fact that one needs to handle bona fide interacting fixed points in a theory containing more than just scalar[2] fields makes obtaining high-accuracy predictions difficult. Whilst this aspect is common to both asymptotically safe Standard Model plus quantum gravity as well as the $D = 3$ Gross–Neveu universality classes, there is a significant difference in the additional structure that needs to be tackled in the two cases. In the case of quantum gravity, the precise dimension the couplings 'sense' depends on the particle species whose interaction it describes [$D = 4 - f_y(G_*, \Lambda_*)$ for the Yukawa coupling, $D = 4 - f_\lambda(G_*, \Lambda_*)$ for the scalar self-coupling] and the precise value of the f's depend on the fixed-point values of gravitational couplings, which requires one to also obtain a good handle on, at the very least, an interaction theory of spin-2 massless bosons (at the most naïve level, it entails adding one more spacetime index to the gauge field compared to Yang-Mills; more tellingly, the gauge group now entails the group of diffeomorphisms of four-dimensional spacetime, and is infinite-dimensional). By contrast, the Gross–Neveu universality classes only feature massless fermions beyond the usual scalar fields. It is hence a logical 'training ground' in which to refine the methods needed to solve (strongly) interacting quantum field theories before tackling the full quantum gravity plus Standard Model problem.

The above feature is generic to all $D = 3$ Gross–Neveu universality classes, and falls roughly within the aformentioned Polyakov vision of 'learning about elementary particles by boiling water'. The SO(3) incarnation, however, has features unique to itself, which make it interesting also from a condensed-matter perspective. Although the SO(3) group is a simple Lie group (meaning it has no generator which commutes with all others), spontaneous symmetry breaking (SSB) thereof does not gap out the fermions completely. This is in contrast to the Gross–Neveu $\mathbb{Z}_2$ (= Ising)[3] or SU(2) (= Heisenberg)[4] universality classes, which have been studied more extensively already in the graphene context, where they describe the quantum phase transition from the semimetallic ground state to charge density wave or antiferromagnetic order respectively; in such cases, SSB leaves no gapless fermionic modes behind[5]. Thus, the Gross–Neveu SO(3) universality class may be understood as describing a *semimetal-to-semimetal* quantum phase transition, which is interesting in its own right.

However, the major condensed-matter motivation to study Gross–Neveu SO(3) quantum criticality arguably comes from a concrete microscopic realization proposed by Seifert *et al.* (2020). There – unlike, say, in graphene – the semimetallic state is not formed by physical electrons. The microscopic system in question is in fact a priori an

---

[2] Under the term 'scalar', we shall understand bosonic fields that transform as scalars under spacetime transformations. There may be additional (internal) symmetries under which these fields are allowed to transform non-trivially.

[3] cf., e.g., Hands, Kocić & Kogut (1993); Vasil'ev, Derkachev & Stepanenko (1993); Gracey (1994b); Vojta, Zhang & Sachdev (2000a,b); Braun, Gies & Scherer (2011); Gracey, Luthe & Schröder (2016); Mihaila *et al.* (2017); Zerf *et al.* (2017); Iliesiu *et al.* (2018); Ihrig *et al.* (2018)

[4] cf., e.g., Janssen & Herbut (2014); Parisen Toldin *et al.* (2015); Otsuka, Yunoki & Sorella (2016); Zerf *et al.* (2017); Knorr (2018); Gracey (2018)

[5] Let us note in passing that at the level of order parameter (i.e., upon artificially switching off the Yukawa coupling to the fermions 'by hand'), both the SU(2) and SO(3) transitions are described by O(3) ϕ^4 theories; it is hence a nice illustration of how the presence of chiral fermions (and the internal symmetry properties thereof) change the critical properties *qualitatively*, in addition to the (sizeable) quantitative corrections to, e.g., critical exponents.

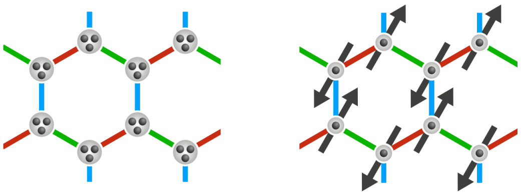

Figure 3.1: (Adapted from Seifert *et al.* 2020) Left: Illustration of the 'semimetallic' ground state of a Kitaev spin-orbital liquid, where the fractionalization of the local moment sitting at each lattice site gives rise, among others, to itinerant Majorana fermions [the three-fold degeneracy is specific to the present SO(3) setup]. Right: Antiferromagnet which wins over the spin-orbital liquid in the presence of strong enough antiferromagnetic Heisenberg exchange.

insulator consisting only of local spin-orbital moments on a honeycomb lattice, and has no (quasi-)free fermions to form a Fermi surface. The fermions instead arise if the exchange interactions of the local moments have a certain bond-dependent structure, viz., XX, YY or ZZ depending on bond direction, which was considered originally by Kitaev (2006) for SU(2) spins and generalized since to include orbital degrees of freedom by various authors6). This kind of exchange leads to *frustration*, in that the moment vector cannot point in a specific direction (including spatial modulation) to minimize the exchange energy. The resulting ground state is instead a highly non-trivial long-range entangled state called a *quantum spin liquid*, where each spin(-orbital) moment *fractionalizes* into a family of Majorana fermions called *spinons*. It is these fermions (more precisely, the itinerant ones among them) that form the semimetallic ground state, as illustrated in the left panel of Fig. 3.1. Probing such states experimentally is very difficult in practice, since their main defining characteristic is their lack of conventional magnetic order. In particular, it is impossible to excite a single spinon in an experiment, since they are not gauge invariant and thus cannot couple individually to physical perturbations7). On the other hand, switching on a sufficiently strong conventional exchange interaction, such as an antiferromagnetic Heisenberg interaction, leads to a conventional symmetry-broken state: in the SO(3) version we are interested in here, it results in an antiferromagnet (right panel of Fig. 3.1). Such an order is characterized by a local order parameter and can be detected experimentally using the usual techniques. Critical exponents of quantum phase transitions to such symmetry-broken states can hence serve as a diagnostic tool in the study of quantum spin liquids. From the universal point of view, however, if we look past the complicated microscopic connotations, the theory we need to deal with is a perfectly conventional Yukawa theory, and hence amenable to field theory techniques established before for calculations in particle physics. In some sense, we can thus 'learn about' frustrated magnets by (theoretically) colliding elementary particles – the Polyakov paradigm in reverse.

The remainder of this chapter is organized as follows: Sec. 3.1 describes the pertinent low-energy effective field theory. We shall then determine its critical exponents using a $4-\epsilon$ expansion at $\mathcal{O}(\epsilon^3)$, a large-N expansion to $\mathcal{O}(1/N^2)$ and the FRG in improved local potential approximation (LPA′) in Sec. 3.2. The main focus of the present exposition will be on the technical aspects of the LPA′ applied to the Gross–Neveu SO(3) universality class; the application of the $4-\epsilon$ and large-N expansions to this problem have been

---

6) cf. Yao, Zhang & Kivelson (2009); Wu, Arovas & Hung (2009); Nakai, Ryu & Furusaki (2012); de Carvalho *et al.* (2018); Natori & Knolle (2020); Chulliparambil *et al.* (2020)

7) The excitations of the gauge field in question, however, are gapped near the quantum critical point, and hence do not have any effect on the critical exponent (Seifert *et al.* 2020).

described in detail elsewhere[8]. We discuss our numerical results in Sec. 3.3, including in particular the practical extraction of best-guess estimates in physically relevant cases from combining the complementary field-theoretical approaches. The chapter closes with a summary and outlook in Sec. 3.4.

3.1 Effective field theory

The continuum field theory describing the Gross–Neveu SO(3) universality class is given by the action $S = \int \mathrm{d}^D x \mathcal{L}$ with (Seifert *et al.* 2020)

$$\mathcal{L} = \overline{\psi}\gamma^\mu \partial_\mu \psi + \frac{1}{2}\phi_a \left(-\partial^2 + m^2\right)\phi_a + \lambda \left(\phi_a \phi_a\right)^2 - y\phi_a \overline{\psi}\left(\mathbb{1}_{2N/3} \otimes L_a\right)\psi \tag{3.3}$$

in D Euclidean spacetime dimensions. Here and henceforth, implicit summation over repeated indices $\mu = 0, \ldots, D-1$ and $a = 1, 2, 3$ is assumed. The above expression uses conventions wherein the Dirac matrices γ^μ form a $2N$-dimensional representation of the Clifford algebra, $\{\gamma^\mu, \gamma^\nu\} = 2\delta^{\mu\nu}\mathbb{1}_{2N}$; in other words, N corresponds to the number of two-component fermion flavours. The spinor ψ and its Dirac conjugate $\overline{\psi} \equiv \psi^\dagger \gamma^0$ thus have $2N$ components each. The interaction Lagrangian comprises the SO(3)-counterpart of the Heisenberg–Yukawa interaction (Herbut, Juričić & Roy 2009; Janssen & Herbut 2014), parameterized by its Yukawa coupling y, and a quartic boson self-interaction with coupling λ.[9]

As in standard Yukawa models (Hands, Kocić & Kogut 1993), the Dirac matrices commute with the Yukawa vertex operator, $[\gamma^\mu, \mathbb{1}_{2N/3} \otimes L_a] = 0$. The 3×3 matrices L_a are generators of SO(3) in the fundamental representation, corresponding to isospin 1. The order-parameter field ϕ_a is a scalar under space-time rotations, but transforms as a vector under SO(3). In $D = 2$ and $D = 3$ space-time dimensions, this requires that N be a multiple of three, whereas in $D = 4$, N would need to be a multiple of six in any physical realization. However, in what follows, it will be useful to compute the critical behaviour for general $2 < D < 4$ and arbitrary $0 \leqslant N \leqslant \infty$, allowing one to analytically continue also to non-integer values of both D and N. Since Aslamazov–Larkin diagrams vanish for ungauged Yukawa theories (Boyack, Rayyan & Maciejko 2019), the critical exponents ν, η_ϕ, and η_ψ do not depend on whether the theory is defined in terms of reducible or suitable copies of irreducible fermion flavours.[10] The physical case realized in the spin-orbital models (Seifert *et al.* 2020) corresponds to $N = 3$ and $D = 3$.

The zero-temperature phase diagram of the Gross–Neveu SO(3) model as a function of the tuning parameter m^2 can be understood on the level of mean-field theory, see Fig. 3.2. In this case, the fluctuations of the order parameter ϕ_a are neglected. Formally, this corresponds to the strict limit $N \to \infty$. For $m^2 > 0$, the ground state is symmetric and the spectrum consists of N gapless Dirac cones. For $m^2 < 0$, the order parameter field acquires a finite vacuum expectation value $\langle \phi_a \rangle \neq 0$ and the SO(3) flavor symmetry is spontaneously broken. However, since L_a has a zero eigenvalue, only $2N/3$ of the Dirac cones acquire a mass gap, while the remaining $N/3$ Dirac cones remain gapless throughout the long-range-ordered phase. That the mean-field picture remains qualitatively correct for finite values of N has been established previously to leading order in quantum corrections by Seifert *et al.* (2020). The main aim of this work is to produce quantitative estimates by incorporating higher-order corrections.

---

[8] See in particular Ihrig (2021) and Gracey (2021).

[9] It is common to sometimes define the quartic self-coupling by $\lambda/4!$, as we ourselves shall do, e.g., in Chap. 7.

[10] Note, however, that sub-leading exponents, such as the so-called ω, corresponding to the corrections to scaling, may depend on whether the theory is defined in terms of N flavours of two-component fermions or $N/2$ flavours of four-component fermions, see Gehring, Gies & Janssen (2015).

3.2 Renormalization and critical exponents

3.2.1 $4-\epsilon$ expansion

The field theory defined in Eq. (3.3) has an upper critical space-time dimension $D_{\text{up}} = 4$, where both, the Yukawa coupling g and the quartic bosonic self-interaction λ, become simultaneously marginal. In $D = 4-\epsilon$ dimensions, interactions are of order ϵ at the critical fixed point. This allows for a controlled loop expansion of critical exponents. In particular, since the interaction vertices are dimensionless at $D_{\text{up}} = 4$ (or equivalently, have dimension ϵ in $D = 4-\epsilon$), there is a one-to-one correspondence between the formal $1/\epsilon$ poles from UV divergences and the IR running of the effective action in the sense of Sec. 2.3, which allows one to use the computationally very convenient dimensional regularization (DREG) and modified minimal subtraction scheme ($\overline{\text{MS}}$). This section briefly presents the calculation of the renormalization group functions at three-loop order, and the extraction of the correlation-length exponent ν, the boson anomalous dimension η_ϕ, and the fermion anomalous dimension η_ψ at order $\mathcal{O}(\epsilon^3)$; a more detailed account of the technical machinery has been given by Ihrig (2021).

3.2.1.1 Method

The bare Lagrangian is defined by replacing fields and couplings in Eq. (3.3) by their bare counterparts, $\psi \mapsto \psi_0$, $\phi_a \mapsto \phi_{a,0}$, $g \mapsto g_0$ and $\lambda \mapsto \lambda_0$. The renormalized Lagrangian reads as

$$\begin{aligned}\mathcal{L} = {} & Z_\psi \bar{\psi}\gamma^\mu \partial_\mu \psi - Z_{\phi\bar{\psi}\psi}\, y \mu^{\epsilon/2} \phi_a \bar{\psi}\left(\mathbb{1}_{2N/3} \otimes L_a\right)\psi \\ & + \frac{Z_\phi}{2}(\partial_\mu \phi_a)^2 + \frac{Z_{\phi^2}}{2} m^2 \phi_a \phi_a + Z_{\phi^4}\lambda \mu^\epsilon (\phi_a\phi_a)^2\,, \end{aligned} \tag{3.4}$$

with the renormalization constants Z_ψ, Z_ϕ, $Z_{\phi\bar{\psi}\psi}$, Z_{ϕ^2}, and Z_{ϕ^4}. The kinetic terms in the renormalized and bare Lagrangian can be related to each other upon identifying $\psi_0 = \sqrt{Z_\psi}\psi$ and $\phi_0 = \sqrt{Z_\phi}\phi$. The energy scale μ parametrizes the renormalization group flow. It is introduced upon shifting the couplings $g^2 \mapsto \mu^\epsilon g^2$ and $\lambda \mapsto \mu^\epsilon \lambda$ after

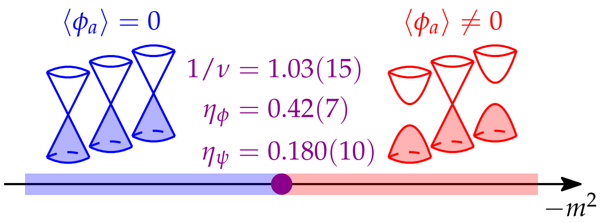

Figure 3.2: Quantum phase diagram of the $(2+1)$-dimensional Gross–Neveu SO(3) model as function of tuning parameter m^2. The theory exhibits a quantum critical point between a Dirac semimetal and a long-range-ordered phase in which two Dirac cones acquire a mass gap, while one remains gapless, as depicted in the insets. The goal of this chapter is to provide improved estimates for the universal critical exponents $1/\nu$, η_ϕ, and η_ψ, characterizing this universality class.

the integration over $(4-\epsilon)$-dimensional spacetime. The renormalized mass and the renormalized couplings are then related to the corresponding bare quantities as

$$m^2 = m_0^2 Z_\phi Z_{\phi^2}^{-1}\,, \tag{3.5}$$

$$y^2 = y_0^2 \mu^{-\epsilon} Z_\psi^2 Z_\phi Z_{\phi\bar{\psi}\psi}^{-2}\,, \tag{3.6}$$

$$\lambda = \lambda_0 \mu^{-\epsilon} Z_\phi^2 Z_{\phi^4}^{-1}\,. \tag{3.7}$$

The renormalization constants were computed to three-loop order using DREG and $\overline{\text{MS}}$. This requires the evaluation 1,815 Feynman diagrams. This was done by employing a sophisticated chain of computer algebra tools originally developed for loop calculations in high-energy physics: First, the Feynman diagrams are generated by the programme `QGRAF` (Nogueira 1991, 2006). These are further processed by the programs `q2e` and `exp` (Haarlander, Seidensticker & Steinhauser 1998; Seidensticker 1999), which allow one to reduce the diagrammatic expressions to single-scale Feynman integrals. Algebraic structures from the Clifford algebra and the SO(3) generators are contracted in `FORM` (Vermaseren 2000; Kuipers *et al.* 2013; Ruijl, Ueda & Vermaseren 2017). Finally, the Feynman integrals are rewritten in terms of known master integrals via integration-by-parts identities (Czakon 2005). Herein, the vertex functions are computed by setting one or two external momenta to zero and subsequently mapping to massless two-point functions, which are implemented in `MINCER` (Gorishnii *et al.* 1989; Larin, Tkachov & Vermaseren 1991).

3.2.1.2 Flow equations

The beta functions for the squared Yukawa coupling y^2 and the quartic scalar coupling λ are defined as

$$\beta_{y^2} = \frac{\mathrm{d}y^2}{\mathrm{d}\ln\mu}\,, \qquad \beta_\lambda = \frac{\mathrm{d}\lambda}{\mathrm{d}\ln\mu}\,. \tag{3.8}$$

It is convenient to further rescale the couplings as $y^2/(8\pi^2) \mapsto y^2$ and $\lambda/(8\pi^2) \mapsto \lambda$, such that the β functions at three-loop order read as[11]

$$\begin{aligned}\beta_{y^2} = {} & -\epsilon y^2 + \frac{2}{3}(N+6)y^4 \\ & - \frac{1}{2}y^2\left[(7+6N)y^4 + 80y^2\lambda - 80\lambda^2\right] \\ & + 10y^6\lambda(5N+24) + 10y^4\lambda^2(48-5N) - 440y^2\lambda^3 \\ & + 6\zeta_3 y^8(N+3) + \frac{1}{8}y^8(6N^2+37N-118)\,,\end{aligned} \tag{3.9}$$

$$\begin{aligned}\beta_\lambda = {} & -\epsilon\lambda + 44\lambda^2 - \frac{1}{3}y^2N(y^2-4\lambda) \\ & + \frac{1}{3}y^2N(5y^4+4y^2\lambda-88\lambda^2) - 1104\lambda^3 \\ & + \frac{1}{72}\Big\{-3y^8N(66N+19) + 2y^6\lambda N(562N-4761) \\ & - 48y^4\lambda^2N(22N-521) + 49632y^2\lambda^3N + 3469248\lambda^4 \\ & - 36\zeta_3\big[y^4N(7y^4+120y^2\lambda-792\lambda^2) - 56832\lambda^4\big]\Big\}\,.\end{aligned} \tag{3.10}$$

---

[11] These multiloop expansion results have been obtained by B. Ihrig and M. M. Scherer, and have been published in our joint paper (Ray *et al.* 2021).

Here, $\zeta_s := \zeta(s)$ is the Riemann zeta function. The terms in Eqs. (3.9) and (3.10) have been sorted such that the first lines show the tree level and one-loop contributions, the second lines show the two-loop contributions, and the remaining lines show the three-loop contributions. The wave function renormalization functions γ_ϕ and γ_ψ are defined as $\gamma_{\phi/\psi} = \mathrm{d}\ln Z_{\phi/\psi}/(\mathrm{d}\ln\mu)$. At three-loop order they read

$$\begin{aligned}\gamma_\phi &= \frac{2}{3}Ny^2 + 40\lambda^2 - \frac{4}{3}Ny^4 + \frac{41y^6N^2}{36}\\ &+ \frac{y^2}{24}N(21y^4 + 400y^2\lambda - 1200\lambda^2) - 440\lambda^3\,, \qquad (3.11)\\ \gamma_\psi &= y^2 - \frac{2N+1}{4}y^4\\ &- \frac{y^2}{48}\left[y^4(4N^2 - 84N - 9) - 960y^2\lambda + 2640\lambda^2\right]. \qquad (3.12)\end{aligned}$$

Finally, let us consider the mass renormalization function as $\gamma_{\phi^2} = \mathrm{d}\ln Z_{\phi^2}/(\mathrm{d}\ln\mu)$, which at three-loop order reads

$$\begin{aligned}\gamma_{\phi^2} &= -20\lambda - \frac{2}{3}Ny^4 + \frac{40}{3}Ny^2\lambda + 240\lambda^2 + \frac{61}{3}Ny^6\\ &- \frac{130}{3}Ny^4\lambda - 160Ny^2\lambda^2 - \frac{4}{9}N^2y^4(7y^2 - 15\lambda)\\ &- 2\zeta_3 Ny^4(y^2 + 50\lambda) - 12920\lambda^3\,. \qquad (3.13)\end{aligned}$$

The corresponding β function for the bosonic mass is then computed from the dimensionless mass $\tilde{m}^2 = \mu^{-2}m^2$ as

$$\beta_{\tilde{m}^2} = (2 - \gamma_\phi + \gamma_{\phi^2})\tilde{m}^2\,. \qquad (3.14)$$

Note that in the limit $y^2 \to 0$, one recovers the three-loop results for the O(3)-symmetric real scalar ϕ^4 theory (Kompaniets & Panzer 2017).

3.2.1.3 Critical exponents

The above β functions feature several renormalization group fixed points, i.e., coupling values g_*^2 and λ_* at which the flow vanishes, $\beta_{y^2}(y_*^2, \lambda_*) = \beta_\lambda(y_*^2, \lambda_*) = 0$. At the fixed points, the system becomes scale invariant, giving rise to quantum critical behaviour. The Gaußian fixed point at $(y_*^2, \lambda_*) = (0, 0)$ and the purely bosonic Wilson–Fisher fixed point $(y_*^2, \lambda_*) = (0, \lambda_*)$ are characterized by two and one relevant directions within the critical plane $\tilde{m}^2 = 0$, respectively. They are thus unstable and cannot be accessed in a system with a single control parameter without fine tuning. A further pair of interacting fixed points at finite $y_*^2 \neq 0$ is found, one of which is fully infrared stable. To the leading order, the corresponding critical couplings are

$$(y_*^2, \lambda_*) = \left(\tfrac{3}{2(N+6)}, \tfrac{\sqrt{N^2+120N+36}-N+6}{88(N+6)}\right)\epsilon + \mathcal{O}(\epsilon^2)\,, \qquad (3.15)$$

in agreement with previous calculation of Seifert *et al.* (2020). The corresponding higher-order contributions up to $\mathcal{O}(\epsilon^3)$ are lengthy but straightforward expressions that can be obtained from Eqs. (3.9) and (3.10) analytically, and will be used in the following.

The critical behaviour is determined by the renormalization group flow at and near the stable fixed point. The anomalous dimensions are given by the wave function renormalization functions γ_ψ and γ_ϕ at the fixed point,

$$\eta_\psi = \gamma_\psi(y_*^2, \lambda_*)\,, \quad \eta_\phi = \gamma_\phi(y_*^2, \lambda_*)\,. \qquad (3.16)$$

The inverse of the correlation-length exponent is extracted from the flow of the bosonic mass, which acts as tuning parameter,

$$\frac{1}{\nu} = \left.\frac{\mathrm{d}\beta_{\tilde{m}^2}}{\mathrm{d}\tilde{m}^2}\right|_{(y_*^2,\lambda_*)} = 2 - \eta_\phi + \gamma_{\phi^2}(y_*^2, \lambda_*)\,. \tag{3.17}$$

Electronic versions of the exponents for general N are available for download.[12)]

For $N = 3$, which corresponds to the situation relevant for the spin-orbital models (Seifert *et al.* 2020), the exponents read

$$\begin{aligned}\frac{1}{\nu} &= 2 - \tfrac{5\sqrt{5}+9}{22}\epsilon + \tfrac{937\sqrt{5}-3182}{31944}\epsilon^2 \\ &\quad + \tfrac{264\left(576665-306864\sqrt{5}\right)\zeta_3+5132520\sqrt{5}-113996279}{834888384\sqrt{5}}\epsilon^3 + \mathcal{O}(\epsilon^4) \\ &\approx 2 - 0.917\epsilon - 0.0340\epsilon^2 - 0.0735\epsilon^3 + \mathcal{O}(\epsilon^4)\,,\end{aligned} \tag{3.18}$$

$$\begin{aligned}\eta_\phi &= \tfrac{1}{3}\epsilon + \tfrac{80\sqrt{5}+89}{2904}\epsilon^2 - \tfrac{351384\zeta_3+66393\sqrt{5}-357226}{6324912}\epsilon^3 + \mathcal{O}(\epsilon^4) \\ &\approx 0.333\epsilon + 0.0922\epsilon^2 - 0.0338\epsilon^3 + \mathcal{O}(\epsilon^4)\,,\end{aligned} \tag{3.19}$$

$$\begin{aligned}\eta_\psi &= \tfrac{1}{6}\epsilon + \tfrac{105\sqrt{5}+79}{8712}\epsilon^2 - \tfrac{234256\zeta_3+72458\sqrt{5}-187711}{8433216}\epsilon^3 + \mathcal{O}(\epsilon^4) \\ &\approx 0.167\epsilon + 0.0360\epsilon^2 - 0.0303\epsilon^3 + \mathcal{O}(\epsilon^4)\,.\end{aligned} \tag{3.20}$$

Note that the above expansions are asymptotic series with vanishing radius of convergence. It is reassuring, however, that the coefficients of the two- and three-loop corrections are still small compared to the one-loop values. For comparison with the large-N expansion, we also state the expressions that we have obtained upon further expanding the general $(4-\epsilon)$-expansion results in $1/N$. We obtain

$$\begin{aligned}\frac{1}{\nu} &= 2 - \epsilon - \left[9\epsilon - \tfrac{39}{4}\epsilon^2 + \tfrac{9}{16}\epsilon^3\right]\frac{1}{N} \\ &\quad + \left[459\epsilon - \tfrac{5895}{8}\epsilon^2 + \tfrac{27}{32}(153 - 184\zeta_3)\epsilon^3\right]\frac{1}{N^2} \\ &\quad + \mathcal{O}(\epsilon^4, 1/N^3)\,,\end{aligned} \tag{3.21}$$

$$\begin{aligned}\eta_\phi &= \epsilon + \left[-6\epsilon + \tfrac{15}{4}\epsilon^2 + \tfrac{21}{16}\epsilon^3\right]\frac{1}{N} \\ &\quad + \left[36\epsilon - \tfrac{261}{8}\epsilon^2 - \tfrac{9}{32}(72\zeta_3 + 95)\epsilon^3\right]\frac{1}{N^2} \\ &\quad + \mathcal{O}(\epsilon^4, 1/N^3)\,,\end{aligned} \tag{3.22}$$

$$\begin{aligned}\eta_\psi &= \left[\tfrac{3}{2}\epsilon - \tfrac{9}{8}\epsilon^2 - \tfrac{9}{32}\epsilon^3\right]\frac{1}{N} + \left[-9\epsilon + \tfrac{369}{16}\epsilon^2 - \tfrac{513}{64}\epsilon^3\right]\frac{1}{N^2} \\ &\quad + \left[54\epsilon - \tfrac{4023}{16}\epsilon^2 + \tfrac{243}{32}(33 - 4\zeta_3)\epsilon^3\right]\frac{1}{N^3} \\ &\quad + \mathcal{O}(\epsilon^4, 1/N^4)\,.\end{aligned} \tag{3.23}$$

For any fixed N, we extract estimates for the physical dimension $\epsilon = 1$ by employing standard Padé approximants

$$[m/n] = \frac{a_0 + a_1\epsilon + \cdots + a_m\epsilon^m}{1 + b_1\epsilon + \cdots + b_n\epsilon^n}\,, \tag{3.24}$$

[12)] `https://journals.aps.org/prb/supplemental/10.1103/PhysRevB.103.155160` with $m, n \in \{0, 1, 2, 3\}$ and $m + n = 3$. The coefficients $a_0, \dots, a_m$ and $b_1, \dots, b_n$ are obtained from matching the Taylor series of $[m/n]$ order by order with the ϵ expansions. The discussion of the resulting estimates for $1/\nu$, η_ϕ, and η_ψ for different values of N is deferred to Sec. 3.3.

3.2.2 Large-N expansion

In the limit of a large number of fermion flavours $N \to \infty$, the fluctuations of the order-parameter field ϕ_a freeze out, which allows one to compute the critical exponents in arbitrary $2 < D < 4$ in a systematic expansion in powers of $1/N$; this is the topic of the present section.

3.2.2.1 Method

This was achieved by employing the large-N critical point method developed originally for the scalar O(N) model (Vasil'ev, Pis'mak & Honkonen 1981a; Vasil'ev, Pis'mark & Honkonen 1981b; Vasil'ev, Pis'mak & Honkonen 1982), and later extended to the Gross–Neveu Ising universality class by Gracey (1991), Derkachov *et al.* (1993), Vasil'ev, Derkachev & Stepanenko (1993), Vasil'ev & Stepanenko (1993), Gracey (1994a) and Gracey (1994b). As the latter formalism has already been applied to variations of the Gross–Neveu Ising universality class, we shall only briefly review the key differences here. Indeed, given the strong overlap with the chiral SU(2) (= chiral Heisenberg) model that the present SO(3) study is similar to, the reader is referred to the account of Gracey (2018) for the finer details of the technique. In addition, a more detailed treatise for arbitrary non-abelian flavour groups has been given by Gracey (2021).

One of the first steps is to recognize that the Lagrangian which serves as the basis for the method of Vasil'ev, Pis'mak & Honkonen is that of the universal theory that resides at the stable fixed point in all dimensions $2 < D < 4$. It is a simpler version of Eq. (3.3) in that only the fermion kinetic term and the three-point vertex are the essential ones needed to define the canonical dimensions of the fields at the fixed point, together with a quadratic term in the boson field. Specifically,

$$\mathcal{L}_{\text{univ}} = \overline{\psi}\partial\!\!\!/\psi - \phi_a\overline{\psi}\left(\mathbb{1}_{2N/3} \otimes L_a\right)\psi + \frac{1}{2}\phi_a\phi_a\,, \tag{3.25}$$

where $\partial\!\!\!/ \equiv \gamma^\mu\partial_\mu$ with γ^μ again being $(2N) \times (2N)$ Dirac matrices, such that the spinors ψ and $\overline{\psi}$ have $2N$ components, as in the original Lagrangian [Eq. (3.3)]. The scalar ϕ_a has been rescaled since at criticality the perturbative coupling constant is fixed and does not run. The quartic interaction present in Eq. (3.3) is required in four dimensions to ensure renormalizability. Its contribution in $\mathcal{L}_{\text{univ}}$ is automatically accounted for through closed fermion loop diagrams with four external boson fields (Hasenfratz & Hasenfratz 1992). The other main aspect of the setup concerns the algebra of the SO(3) generators L_a, which satisfy the relation

$$(L_a)_{ij}(L_a)_{kl} = \delta_{il}\delta_{jk} - \delta_{ik}\delta_{jl}\,. \tag{3.26}$$

This has been employed to determine the group-theory factors associated with the Feynman diagrams that contribute to the large-N formalism.

In general, the method of Vasil'ev, Pis'mak & Honkonen entails analyzing the behaviour of various Schwinger–Dyson equations in the approach to criticality. At the stable fixed point, the propagators of the fields have a simple scaling behaviour where

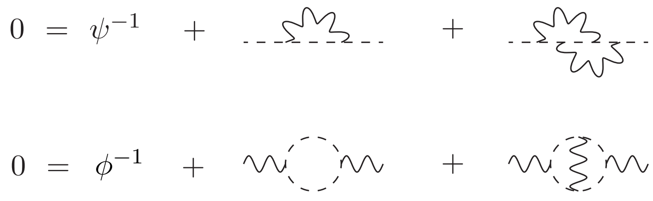

Figure 3.3: Skeleton Schwinger-Dyson two-point functions used to determine $\eta_{\not{\psi}}$ at $\mathcal{O}(1/N^2)$. Dashed inner lines correspond to critical fermion propagators [Eq. (3.27)] and wiggly inner lines correspond to critical boson propagators [Eq. (3.28)].

the exponent of the propagator corresponds to the full scaling dimension. Specifically, in coordinate space the propagators take the asymptotic forms

$$\not{\psi}(x) \sim \frac{A\not{x}}{(x^2)^{\alpha}}\left[1 + A'(x^2)^{\lambda}\right], \tag{3.27}$$

$$\phi(x) \sim \frac{B}{(x^2)^{\beta}}\left[1 + B'(x^2)^{\lambda}\right], \tag{3.28}$$

where the name of the field has been used as a shorthand for the propagator at criticality, with the scaling exponents

$$\alpha = \tfrac{1}{2}(D + \eta_{\not{\psi}}), \qquad\qquad \beta = 1 - \eta_{\not{\psi}} - \chi. \tag{3.29}$$

Here, $\eta_{\not{\psi}}$ is the fermion anomalous dimension, which has been computed to three loops at criticality in Sec. 3.2.1. The anomalous dimension of the boson-fermion vertex is denoted by χ so that

$$\eta_{\phi} = 4 - D - 2\eta_{\not{\psi}} - 2\chi. \tag{3.30}$$

In addition to these leading exponents, each propagator includes a correction term involving the exponent λ.[13] At criticality, this exponent corresponds to the correlation-length exponent as $1/\nu = 2\lambda$. The canonical dimension of λ is $(D-2)/2$. The quantities A, B, as well as A' and B' are x-independent amplitudes. The first two always appear in the combination A^2B, but this plays an intermediate role in deriving exponents. The first terms of the respective equations in Fig. 3.3 represent the asymptotic scaling forms of the two-point functions and have been given by Gracey (1991). They are derived from Eqs. (3.27) and (3.28) and have a similar scaling form to these, although A and B occur in the denominator.

Skeleton Schwinger-Dyson equations. To determine the anomalous dimensions of the two fields, one focuses on the two-point Schwinger–Dyson equations shown in Fig. 3.3, as well the three-point vertex function, for which the first correction is depicted in Fig. 3.4. For both the two- and three-point functions the contributing diagrams are computed with the asymptotic propagators, Eqs. (3.27) and (3.28). Since the power of the leading term of each propagator includes the nonzero anomalous dimensions of Eq. (3.29), there are no self-energy corrections on the contributing diagrams in order to

---

[13] We are abusing notation somewhat by denoting this exponent appearing in the asymptotic form of the propagator by the symbol which is conventional in the large-N formalism. There should be no scope for confusion, since the scalar self-coupling (usually also denoted by the same symbol) is accounted for automatically and does not appear explicitly in the large-N setup.

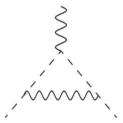

Figure 3.4: Leading-order skeleton Schwinger-Dyson three-point function used to determine χ at $\mathcal{O}(1/N)$.

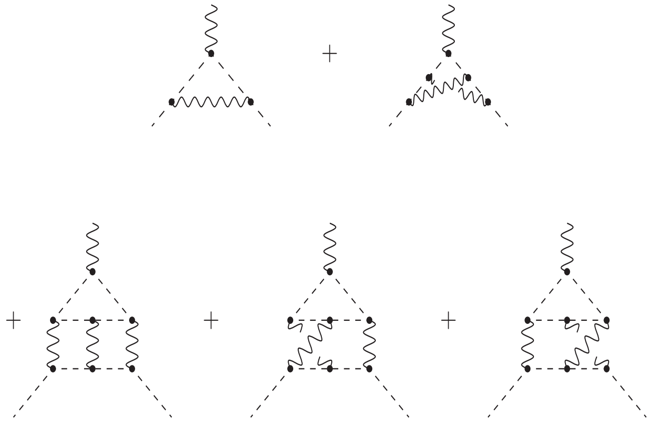

Figure 3.5: Diagrams contributing to large-N conformal bootstrap formalism to deduce η_ψ at $\mathcal{O}(1/N^3)$. Black dots refer to Polyakov conformal triangles, see Gracey (2018) for details.

avoid double counting. By evaluating the diagrams and solving the equations of Fig. 3.3 self-consistently (eliminating the product A^2B in the process), one obtains an expression for η_ψ at $\mathcal{O}(1/N^2)$. The value of χ at $\mathcal{O}(1/N)$ is required for this to ensure that no $\ln(x^2)$ terms remain after renormalization. This value for χ is deduced from the scaling behavior of the diagram of Fig. 3.4. Moreover, this produces η_ϕ at $\mathcal{O}(1/N)$ as a corollary from Eq. (3.30). For the next order of χ, one extends the critical-point evaluation of the higher-order diagrams to the three-point function, which are given by the decorations of the leading-order diagram of Fig. 3.4 with vertex corrections, as well as the non-planar and three-loop diagrams shown in Fig. 3.5. This produces χ and hence η_ϕ at $\mathcal{O}(1/N^2)$.

Once the anomalous dimensions of the fields have been established at $\mathcal{O}(1/N^2)$, the correction to scaling terms in Eqs. (3.27) and (3.28) can be included in order to determine $1/\nu$ via the determination of λ. Since the correction terms involve $(x^2)^\lambda$, the two-point Schwinger-Dyson consistency equation contains terms of different dimensions. These split into terms which are independent of the correction to scaling amplitudes, A' and B', and those that are not. It is the latter ones that determine λ to $\mathcal{O}(1/N^2)$ (Vasil'ev, Pis'mark & Honkonen 1981b), since a consistency equation can be formed from the 2×2 matrix defined by the coefficients of A' and B' in each equation of Fig. 3.3. Finding the solution to the equation formed by setting the determinant of this matrix to zero defines the consistency equation. For the Gross–Neveu universality classes there is a known complication in that while all the propagators of the diagrams of Fig. 3.3 include the correction terms, extra diagrams are needed due to the same reordering that arises in the original Gross–Neveu Ising model (Gracey 1991; Derkachov *et al.* 1993; Vasil'ev & Stepanenko 1993; Gracey 1994a). This necessitates the inclusion of the higher-order Feynman diagram as given in Fig. 4 of Gracey (2018), but with the appropriate group factor for the present model.

Large-N conformal bootstrap technique. The final step is to apply what is termed the large-N conformal bootstrap technique to compute the $\mathcal{O}(1/N^3)$ contribution to η_ψ. This method was originally developed for the O(N) scalar model by Vasil'ev, Pis'mak & Honkonen (1982) using the early work of Polyakov (1970), Parisi (1972), and d'Eramo, Peliti & Parisi (1972). It was subsequently extended to the Gross–Neveu Ising universality class (Derkachov *et al.* 1993; Vasil'ev, Derkachev & Stepanenko 1993; Gracey 1994b), and more recently to the Gross–Neveu Heisenberg model by Gracey (2018) and the Gross–Neveu U(1) (= XY) model by Gracey (2021). The reader is referred to that later article for more details of the large-N conformal bootstrap technique for the present context. However, it is worth noting some of the key aspects of the approach. Rather than focusing on the skeleton Schwinger–Dyson two-point functions, the underlying self-consistency equations that ultimately produce η_ψ at $\mathcal{O}(1/N^3)$ are derived from the vertex functions. By contrast to the two-point function approach, one is in effect performing perturbation theory in the vertex anomalous dimension χ. The relevant diagrams are given in Fig. 3.5. Again, while there is no dressing on the propagators, there are no vertex corrections unlike the diagrams in Fig. 3.3. Instead, the contributions that underlie the vertex structure are subsumed into the black dots, which denote Polyakov conformal triangles. These are designed in such a way that the sum of the critical exponents of the propagators connected to the vertex is $(D+1)$. This value means that all the scalar-fermion vertices are unique in the sense of conformal integration (Gracey 1991; Derkachov *et al.* 1993; Vasil'ev & Stepanenko 1993; Gracey 1994a). It is hence possible to evaluate all the diagrams to the necessary order to determine η_ψ at $\mathcal{O}(1/N^3)$.

3.2.2.2 Critical exponents

Having summarized the large-N critical point formalism, we are now in a position to discuss the results. Expressions in general space-time dimensions $2 < D < 4$ for all the exponents we have determined are available electronically [see footnote $^{12)}$]. However, the ϵ expansion of the large-N expressions must agree with the explicit three-loop exponents derived from the renormalization group functions at the stable fixed point. Expanding each of η_ψ, η_ϕ, and $1/\nu$ around $D = 4-\epsilon$, one finds

$$\begin{aligned}\frac{1}{\nu} &= 2-\epsilon+\left[-9\epsilon+\tfrac{39}{4}\epsilon^2-\tfrac{9}{16}\epsilon^3-\tfrac{9}{64}(1+16\zeta_3)\epsilon^4+\tfrac{3}{256}(208\zeta_3-144\zeta_4-3)\epsilon^5\right]\frac{1}{N}\\ &\quad+\Big[459\epsilon-\tfrac{5895}{8}\epsilon^2+\tfrac{27}{32}(153-184\zeta_3)\epsilon^3+\tfrac{27}{64}(320\zeta_5-276\zeta_4+1376\zeta_3+203)\epsilon^4\\ &\qquad+\tfrac{9}{1792}(4795-90496\zeta_5+6720\zeta_3^2-123984\zeta_3+33600\zeta_6+86688\zeta_4)\epsilon^5\Big]\frac{1}{N^2}\\ &\quad+\mathcal{O}(\epsilon^6,1/N^3)\,,\end{aligned}\tag{3.31}$$

$$\begin{aligned}\eta_\phi &= \epsilon+\left[-6\epsilon+\tfrac{15}{4}\epsilon^2+\tfrac{21}{16}\epsilon^3+\tfrac{3}{64}(11-32\zeta_3)\epsilon^4+\tfrac{3}{256}(80\zeta_3-96\zeta_4+19)\epsilon^5\right]\frac{1}{N}\\ &\quad+\Big[36\epsilon-\tfrac{261}{8}\epsilon^2-\tfrac{9}{32}(72\zeta_3+95)\epsilon^3+\tfrac{9}{64}(472\zeta_3-108\zeta_4+45)\epsilon^4\\ &\qquad+\tfrac{9}{256}(97-288\zeta_5+1416\zeta_4-1248\zeta_3)\epsilon^5\Big]\frac{1}{N^2}\\ &\quad+\mathcal{O}(\epsilon^6,1/N^3)\,,\end{aligned}\tag{3.32}$$

$$\begin{aligned}\eta_\psi &= \left[\tfrac{3}{2}\epsilon-\tfrac{9}{8}\epsilon^2-\tfrac{9}{32}\epsilon^3+\tfrac{3}{128}(16\zeta_3-3)\epsilon^4+\tfrac{9}{512}(16\zeta_4-16\zeta_3-1)\epsilon^5\right]\frac{1}{N}\\ &\quad+\left[-9\epsilon+\tfrac{369}{16}\epsilon^2-\tfrac{513}{64}\epsilon^3-\tfrac{9}{128}(128\zeta_3+69)\epsilon^4+\tfrac{9}{512}(1008\zeta_3-384\zeta_4-89)\epsilon^5\right]\frac{1}{N^2}\\ &\quad+\Big[54\epsilon-\tfrac{4023}{16}\epsilon^2+\tfrac{243}{32}(33-4\zeta_3)\epsilon^3+\tfrac{27}{256}(2184\zeta_3-216\zeta_4+493)\epsilon^4\end{aligned}$$

$$+\tfrac{27}{1024}(6552\zeta_4 - 576\zeta_5 - 20024\zeta_3 - 2375)\epsilon^5\Big]\frac{1}{N^3}$$
$$+\mathcal{O}(\epsilon^6, 1/N^4)\,. \tag{3.33}$$

All terms to $\mathcal{O}(\epsilon^3)$ agree exactly with Eqs. (3.21)–(3.23), which is a highly non-trivial check on the D-dimensional expressions computed above. In the above equations, included additional terms to $\mathcal{O}(\epsilon^5)$ have been included to provide checks for future higher-loop computations.

With this check of the D-dimensional exponents satisfied, one can now deduce their values in the $1/N$ expansion in fixed $D = 2 + 1$ space-time dimensions. One arrives at[14)]

$$\begin{aligned}
\frac{1}{\nu} &= 1 - \frac{16}{\pi^2 N} + \frac{324\pi^2 + 2624}{3\pi^4 N^2} + \mathcal{O}(1/N^3) \\
&\approx 1 - \frac{1.62114}{N} + \frac{19.92200}{N^2} + \mathcal{O}(1/N^3)\,, && (3.34)\\
\eta_\phi &= 1 - \frac{20}{\pi^2 N} + \frac{2(81\pi^2 - 1028)}{3\pi^4 N^2} + \mathcal{O}(1/N^3) \\
&\approx 1 - \frac{2.02642}{N} + \frac{1.56428}{N^2} + \mathcal{O}(1/N^3)\,, && (3.35)\\
\eta_\psi &= \frac{4}{\pi^2 N} + \frac{304}{3\pi^4 N^2} \\
&\quad + \frac{972\pi^2 \ln(2) + 255\pi^2 - 10206\zeta_3 - 3796}{9\pi^6 N^3} + \mathcal{O}(1/N^4) \\
&\approx \frac{0.40528}{N} + \frac{1.04029}{N^2} - \frac{0.79721}{N^3} + \mathcal{O}(1/N^4)\,. && (3.36)
\end{aligned}$$

In effect, three terms in the expansion of each exponent are available, but involve different powers of $1/N$. Let us note that the leading two terms of $1/\nu$ and the leading terms of η_ϕ and η_ψ are the same as those of the Gross–Neveu SU(2) model (Gracey 2018). However, the $\mathcal{O}(1/N^2)$ term of $1/\nu$ is nearly twice that of its SU(2) counterpart and the coefficients of the subsequent terms of η_ϕ and η_ψ are also significantly larger here, with the exception of the $\mathcal{O}(1/N^2)$ term in η_ϕ.

For extrapolating the large-N series to finite N, one again needs to use Padé approximants

$$[m/n] = \frac{a_0 + a_1 N^{-1} + \cdots + a_m N^{-m}}{1 + b_1 N^{-1} + \cdots + b_n N^{-n}}\,, \tag{3.37}$$

where now $m, n \in \{0, 1, 2\}$ ($m, n \in \{0, 1, 2, 3\}$) and $m + n = 2$ ($m + n = 3$) for $1/\nu$ and η_ϕ (η_ψ). The numerical estimates for different values of N are discussed in Sec. 3.3.

3.2.3 Non-perturbative FRG

The starting point of the FRG calculation is the Wetterich–Morris–Ellwanger equation (cf., e.g., Dupuis *et al.* 2021), which we already encountered in Sec. 2.2. To recapitulate, it reads as

$$k\partial_k \Gamma_k = \frac{1}{2}\,\mathrm{STr}\,\frac{k\partial_k R_k}{\Gamma_k^{(2)} + R_k}. \tag{3.38}$$

[14)] These $1/N$ expansion results have been obtained by J. A. Gracey and have been published in our joint paper (Ray *et al.* 2021).

Here, Γ_k is the scale-dependent quantum effective action. It is defined as the usual 1PI effective action, but where quantum contributions from 'slow' modes (i.e., virtual particles at momenta $q < k$) have been suppressed. This suppression is achieved by adding a momentum-dependent mass (the so-called 'regulator') R_k to the propagator. The function $R_k(q)$ needs to satisfy $R_k(q \ll k) = C_k$, $C_k > 0$; this ensures that slow modes are indeed suppressed as advertised. In order to ensure that the full 1PI effective action is recovered for $k \to 0$, one needs to impose $R_{k\to 0}(q) = 0$ for all virtual momenta q. The final ingredient appearing in the Wetterich–Morris–Ellwanger equation is the Hessian

$$\Gamma_k^{(2)} = \frac{\overrightarrow{\delta}}{\delta \Phi^\top} \Gamma_k \frac{\overleftarrow{\delta}}{\delta \Phi}, \tag{3.39}$$

where the field $\Phi = (\phi_a, \psi, \overline{\psi})$ contains all pertinent fields of the theory. The supertrace STr represents the usual extension of the trace to include anticommuting (i.e., Grassmann) fields, schematically:

$$\operatorname{STr}\begin{pmatrix} B & * & * \\ * & F_1 & * \\ * & * & F_2 \end{pmatrix} = \operatorname{Tr} B - \operatorname{Tr}\begin{pmatrix} F_1 & * \\ * & F_2 \end{pmatrix}. \tag{3.40}$$

The Wetterich–Morris–Ellwanger equation itself is exact, but generically not exactly soluble.

The crucial ingredient in the FRG recipe is the ansatz for the running effective action Γ_k we choose to feed in to the Wetterich–Morris–Ellwanger equation; the choice of terms to keep or neglect defines the approximation scheme. Here, we pursue an ansatz in the spirit of a derivative expansion,

$$\Gamma_k = \int \mathrm{d}^D x \left[Z_{\psi,k} \overline{\psi} \gamma^\mu \partial_\mu \psi + \frac{1}{2} Z_{\phi,k} (\partial_\mu \phi_a)^2 - y_k \phi_a \overline{\psi} (\mathbb{1}_{2N/3} \otimes L_a) \psi + U_k(\varrho) \right], \tag{3.41}$$

with ϱ the SO(3)-scalar given by $\varrho = \frac{1}{2}\phi_a \phi_a$. General field-dependence of renormalization group functions is allowed only in U_k, the so-called average boson effective potential[15]. Pure fermionic interactions, such as four-fermion terms, that may be generated in the nonperturbative regime, are neglected. The next-to-leading order contributions come from the kinetic terms, whose scale-dependences are approximated by field-independent renormalization constants $Z_{\Phi,k}$; all higher-order terms in the gradient expansion are neglected. This truncation of the effective average action is commonly referred to as 'improved local potential approximation' (LPA′). As such, this truncation represents the leading terms of the so-called derivative expansion. Its convergence does not rely on proximity to special values of the flavour number N or the spacetime dimension D. Whether the derivative expansion converges at all (and at what speed) is a subtle question, see Dupuis *et al.* (2021) and references therein. More pragmatically, we may take encouragement from the fact that the derivative expansion, already at the order to which we are working (i.e., LPA′), has proven to yield reliable results in a number of similar Yukawa models[16].

---

[15] Recall that by definition, the effective potential is the effective action evaluated for constant field configurations.

[16] cf., e.g., Rosa, Vitale & Wetterich (2001); Höfling, Nowak & Wetterich (2002); Gies *et al.* (2010); Braun, Gies & Scherer (2011); Scherer, Braun & Gies (2013); Janssen & Herbut (2014); Classen *et al.* (2016); Classen, Herbut & Scherer (2017); Janssen & Herbut (2017); Torres *et al.* (2018, 2020).

3.2.3.1 Flow equations

Before computing the flow of the individual scale-dependent quantities appearing in our LPA$'$ ansatz, we need to first evaluate the Hessian. Its independent non-vanishing components are

$$\Gamma^{(2)}_{\phi_a\phi_b,k}(x_1,x_2) = \big(Z_{\phi,k}\partial^2 + U_k'(\varrho(x_1))\,\delta_{ab} + U_k''(\varrho(x_1))\phi_a(x_1)\phi_b(x_1)\big)\,\delta(x_1-x_2), \tag{3.42}$$

$$\Gamma^{(2)}_{\psi\overline{\psi},k}(x_1,x_2) = \big(Z_{\psi,k}\gamma^\mu\partial_\mu - y_k\phi_a(x_1)\mathbb{1}_{2N/3}\otimes L_a\big)\,\delta(x_1-x_2), \tag{3.43}$$

$$\Gamma^{(2)}_{\phi_a\overline{\psi},k}(x_1,x_2) = -y_k\psi(x_1)\delta(x_1-x_2)\,\mathbb{1}_{2N/3}\otimes L_a. \tag{3.44}$$

The remaining non-vanishing components (corresponding to the field index constellations $\overline{\psi}\psi$, $\phi\psi$, $\psi\phi$, $\overline{\psi}\phi$) can be recovered from the ones quoted above by Hermitian and/or Dirac conjugation. In the course of our calculation, we shall also need the third derivatives of Γ_k:

$$\Gamma^{(3)}_{\phi_a\overline{\psi}\psi,k}(x_1,x_2,x_3) = -y_k\delta(x_1-x_2)\delta(x_2-x_3)\,\mathbb{1}_{2N/3}\otimes L_a \tag{3.45}$$

$$\begin{aligned}\Gamma^{(3)}_{\phi_a\phi_b\phi_c}(x_1,x_2,x_3) = \big[&U_k''(\varrho(x_1))\,(\delta_{ab}\phi_c(x_1)+\delta_{bc}\phi_a(x_1)+\delta_{ac}\phi_b(x_1))\\ &+U_k'''(\varrho(x_1))\phi_a(x_1)\phi_b(x_1)\phi_c(x_1)\big]\,\delta(x_1-x_2)\delta(x_2-x_3)\end{aligned} \tag{3.46}$$

Let us now proceed to the flow of $U_k(\varrho)$. By definition, it is simply the effective action evaluated at vanishing fermion fields and constant boson fields. For this configuration of fields, the Hessian becomes diagonal in momentum space; we shall refer to it as the 'propagator'.17) At this stage, we need to also specify a suitable form for the regulator. Following Janssen & Herbut (2014), we make the ansatz

$$R_k(x_1,x_2) = \int \mathrm{d}^D p\, \mathrm{e}^{-\mathrm{i}p\cdot(x_1-x_2)} R_k(p) \tag{3.47}$$

$$R_{\phi_a\phi_b,k}(p) = Z_{\phi,k}p^2\delta_{ab}\, r_\phi(p^2/k^2) \tag{3.48}$$

$$R_{\psi\overline{\psi},k}(p) = \mathrm{i}Z_{\psi,k}\gamma^\mu p_\mu\, r_\psi(p^2/k^2) \tag{3.49}$$

with $r_{\phi/\psi}$ the so-called dimensionless shape functions parameterizing the choice of regulator. It is useful to demand

$$1 + r_\phi(x) = [1 + r_\psi(x)]^2 =: P(x)/x \tag{3.50}$$

for reasons of power counting (recall that in the classical action, the bosonic kinetic term contains two derivatives whilst the fermionic kinetic term contains only one).

Note that upto the shape function factors, the regulator has the same form as the unregularized propagator. This has both conceptual and practical significance: Conceptually, it allows one to maintain as many symmetries of the classical Lagrangian $\mathcal{L}$ as possible, also at the level of the regularized theory. (This is the only choice that does so, at least in a manifest manner.) On the practical side, this choice of regulator means we do not need any techniques beyond what we would have to use any way to compute the propagator. In the present setting, the theory is translationally invariant, which makes the

---

17) Note that this is somewhat different from usual perturbation theory, where the propagator only contains 'bare' quantities. However, since the derivative expansion in general and the LPA$'$ treatment in particular is a self-consistent, the fact that all quantities appearing on the right-hand side are 'dressed' is left implicit.

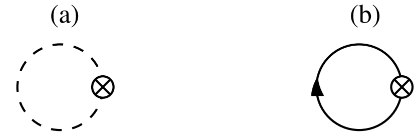

Figure 3.6: Diagrammatic representation of contributions to the flow of the boson average effective potential $U_k(\varrho)$. A dashed line stands for G_ϕ [Eq. (3.51)] and a solid line stands for G_ψ [Eq. (3.52)]. A circled cross represents the insertion of $k\partial_k R_k$.

regularized propagator diagonal in momentum space. Choosing without loss of generality $\phi(x) = (0, 0, \sqrt{2\varrho})$ and working explicitly in the basis where $L_3 = \mathrm{diag}(1, 0, -1)$, we find

$$\begin{aligned} G_\phi^{11}(p) = G_\phi^{11}(p) &= \frac{1}{Z_{\phi,k}\,(1 + r_\phi(p^2/k^2))\,p^2 + U_k'(\varrho)}, \\ G_\phi^{33}(p) &= \frac{1}{Z_{\phi,k}\,(1 + r_\phi(p^2/k^2))\,p^2 + U_k'(\varrho) + 2\varrho U_k''(\varrho)}, \end{aligned} \tag{3.51}$$

$$\begin{aligned} G_\psi(p) = \mathbb{1}_{N/(3d_\gamma)} \otimes \Bigg[&\frac{-\mathrm{i}Z_{\psi,k}\left(1 + r(p^2/k^2)\right)\tilde{\gamma}^\mu p_\mu - y_k\sqrt{2\varrho}}{Z_{\psi,k}^2\left(1 + r(p^2/k^2)\right)^2 p^2 + 2\varrho y_k^2} \\ &\oplus \frac{-\mathrm{i}\tilde{\gamma}^\mu p_\mu}{Z_{\psi,k}\,(1 + r(p^2/k^2))\,p^2} \oplus \frac{-\mathrm{i}Z_{\psi,k}\left(1 + r(p^2/k^2)\right)\tilde{\gamma}^\mu p_\mu + y_k\sqrt{2\varrho}}{Z_{\psi,k}^2\left(1 + r(p^2/k^2)\right)^2 p^2 + 2\varrho y_k^2}\Bigg], \end{aligned} \tag{3.52}$$

whereby all omitted components of G_ϕ vanish and we have assumed blockdiagonal γ-matrices $\gamma_\mu = \mathbb{1}_{N/(3d_\gamma)} \otimes \tilde{\gamma}_\mu$ with d_γ-dimensional 'building blocks' $\tilde{\gamma}_\mu$. If we now evaluate the right-hand side of the Wetterich–Morris–Ellwanger equation for the afore-mentioned field configuration

$$\psi(x) = \overline{\psi}(x) = 0 \qquad \phi_a(x) = (0, 0, \sqrt{2\varrho}), \tag{3.53}$$

the resulting expression can be expressed diagrammatically as[18)]

$$k\partial_k U_k(\varrho) = \text{Fig. 3.6(a)} + \text{Fig. 3.6(b)}. \tag{3.54}$$

Satisfyingly, it is given by one-loop 1PI vacuum graphs, but with the propagators computed self-consistently from Γ_k (rather than from the classical action as one usually does in perturbation theory). For this reason, RG schemes such as that of Wetterich–Morris–Ellwanger are called 'one-loop exact' schemes. The diagrammatic consideration goes through for higher-point functions as well: The right-hand side of the Wetterich–Morris–Ellwanger equation is then given by 1-loop 1PI graphs with a single insertion of $k\partial_k R_k$ and a suitable constellation of external legs.

Upon evaluating the matrix algebra, one arrives at

$$\begin{aligned} k\partial_k u(\varrho) = &-Du_k(\varrho) + (D - 2 + \eta_\phi)\varrho u'(\varrho) \\ &+ 2v_D \ell_0^{(\mathrm{B}),D}\big(u'(\varrho) + 2\varrho u''(\varrho); \eta_\phi\big) \\ &+ 4v_D \ell_0^{(\mathrm{B}),D}\big(u'(\varrho); \eta_\phi\big) \\ &- 4v_D\left[\frac{2N}{3}\ell_0^{(\mathrm{F}),D}(2\varrho y^2; \eta_\psi) + \frac{N}{3}\ell_0^{(\mathrm{F}),D}(0; \eta_\psi)\right]. \end{aligned} \tag{3.55}$$

[18)] Here and throughout the remainder of the thesis, symmetry factors and signs are considered part of the diagram and not written explicitly. In the present case, for instance, diagram (a) has symmetry factor 1/2, whilst (b) has a negative sign due to the closed fermion loop (cf. the definition of 'supertrace').

In the above and in what follows, the couplings have been rescaled as

$$Z_{\phi,k}^{-1} Z_{\psi,k}^{-2} k^{D-4} y_k^2 \mapsto y_k^2 \qquad Z_{\phi,k}^{-1} k^{D-2} \varrho \mapsto \varrho \qquad k^{-D} U_k\Big(Z_{\phi,k}^{-1} k^{D-2} \varrho\Big) \mapsto u_k(\varrho), \tag{3.56}$$

and the index k has been dropped (and will be dropped henceforth) for legibility. The powers of k are given by the mass dimensions and simply amount to making the couplings canonically dimensionless, whilst the Z factors in the definition of the dimensionless couplings account for the fact that the kinetic terms are redundant operators (recalling our discussion in Sec. 2.5). The wavefunction renormalization in turn also gives rise to the anomalous dimensions

$$\eta_{\phi/\psi,k} = -\frac{k\partial_k Z_{\phi/\psi,k}}{Z_{\phi/\psi,k}}, \tag{3.57}$$

with the index k again suppressed in equations for brevity.

In Eq. (3.55), the factor $v_D \equiv [2^{D+1}\pi^{D/2}\Gamma(D/2)]^{-1}$ arises from integration over the surface of the sphere in D-dimensional Fourier space. The threshold functions $\ell_0^{(\mathrm{B}),D}$ and $\ell_0^{(\mathrm{F}),D}$ contain the remaining radial integration and encode the dependence on the shape function, see Berges, Tetradis & Wetterich (2002) for formal definitions. The first line of Eq. (3.55) represents the tree-level flow and arises due to the rescaling in Eq. (3.56). The second and third line represent scalar contributions, two of which have squared mass $u'(\varrho)$ and the other one has mass $u'(\varrho) + 2\varrho u''(\varrho)$. If the vacuum is located at $\varrho = 0$ (i.e., in the symmetric phase), all scalar modes have the same mass. That the squared mass is indeed $u'(0)$ can be seen from a Taylor expansion of the effective potential,

$$u(\varrho) = u'(0)\varrho + \mathcal{O}(\varrho^2) \equiv \frac{1}{2} m^2 \phi_a \phi_a + \mathcal{O}(\phi^4). \tag{3.58}$$

In the spontaneously symmetry-broken (SSB) phase, on the other hand, the minimum of $u(\varrho)$ lies at some $\varrho_0 \neq 0$. It is governed by (Gies *et al.* 2010)

$$\frac{\partial u_k(\varrho)}{\partial \phi_a} = \phi_a u_k'(\varrho) = 0 \implies u_k'(\varrho_{0,k}) = 0. \tag{3.59}$$

Note that the location of the minimum $\varrho_{0,k}$ – the so-called vacuum expectation value (vev) – is scale-dependent, just like the effective potential u_k it minimizes *per constructionem.* In the SSB phase, the two modes with mass $u'(\varrho)$ are in fact massless and hence correspond to Goldstone modes. On the other hand, $2\varrho_0 u''(\varrho_0)$ is precisely the curvature of the effective potential at ϱ_0; it is the mass of the Higgs mode. (We shall henceforth drop the index k on the vev ϱ_0 in equations, like we have decided to do for all other running quantities.) The scalar contribution to the flow of the effective potential is hence in full agreement with the chiral SU(2) case (Janssen & Herbut 2014). This is not surprising, since both theories become O(3) ϕ^4 theories if the coupling to fermions is 'switched off'. Finally, let us note that in the fermion bubble contribution (last line), the first term corresponds to the $2N/3$ gapped modes with mass $2\varrho y^2$, and the second term to the $N/3$ modes that remain gapless in the presence of a constant background ϱ.

To close the flow equation, we need to find the flow of y and the anomalous dimensions $\eta_{\phi/\psi}$. Unlike the effective potential $u(\varrho)$ which is defined for all field values, the remaining quantities encode fluctuations on top of the vacuum. Therefore, in Feynman diagrams, henceforth (inverse) propagators and vertices are evaluated at the vacuum field configuration $\psi(x) = \overline{\psi}(x) = 0$, $\phi_a(x) = (0, 0, \sqrt{2\varrho_0})$ with $\varrho_0 = 0$ (symmetric phase)

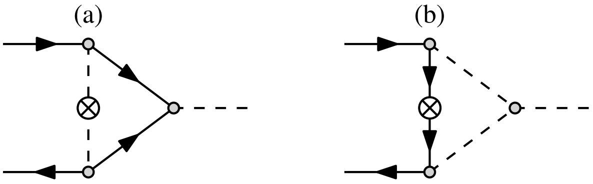

Figure 3.7: Diagrams contributing to Yukawa vertex correction. The propagators are given by Eq. (3.51) and (3.52), while the three-point vertices are Eq. (3.45)–(3.46), all evaluated at the vacuum field configuration $\psi(x) = \overline{\psi}(x) = 0$, $\phi_a(x) = (0, 0, \sqrt{2\varrho_0})$. The regulator insertion may sit on any of the other internal lines; these permutations give the same value, and are not displayed explicitly.

or $\varrho_0 \neq 0 \wedge u'(\varrho_0) = 0$ (SSB phase). Let us begin with the flow of g_k. The resulting flow of the Yukawa coupling is shown in Fig. 3.7; since $\Gamma_k^{(3)}$ is point-like per ansatz, we only need to compute it for vanishing external momenta.

In the symmetric phase, the above prescription goes through without any difficulty, since all scalar modes are equivalent. In the SSB phase, on the other hand, an unambiguity arises, since the Yukawa coupling of fermions to Goldstone and Higgs modes may be different. When studying quantum criticality, an often-used approximation is to define the Yukawa vertex as the coupling to the Goldstone modes; it is assumed to be the one primarily important for critical behaviour (Janssen & Gies 2012; Janssen & Herbut 2014), since the Goldstone bosons are the massless ones in the SSB phase. The flow of the Yukawa coupling thus works out to

$$\begin{aligned} k\partial_k y^2 &= (D - 4 + \eta_\phi + 2\eta_\psi) y^2 + 8v_D \ell_{11}^{(\mathrm{FB}),D}(2\varrho_0 y^2, u_0'; \eta_\psi, \eta_\phi) y^4 \\ &\quad - 16 v_D \varrho_0 u_0'' \ell_{111}^{(\mathrm{FBB}),D}(2\varrho_0 y^2, u_0', u_0' + 2\varrho_0 u_0''; \eta_\psi, \eta_\phi) y^4. \end{aligned} \tag{3.60}$$

Here, the shorthand $u_0^{(n)} = u^{(n)}(\varrho_0)$ has been introduced, along with further threshold functions $\ell_{11}^{(\mathrm{FB}),D}$ and $\ell_{111}^{(\mathrm{FBB}),D}$.

For the wave function renormalization, the contributing diagrams are Fig. 3.8(a) for Z_ψ and (b) + (c) for Z_ϕ.[19] In both cases, it is sufficient to expand in powers of external momenta.[20] The zeroth order in external momentum contains no new information: for the fermion self-energy, it vanishes in the symmetric phase due to chiral symmetry. In the SSB phase, it renormalizes the squared fermion mass $2\varrho_0 y^2$. However, the flow thereof is already uniquely determined by the flow of $u(\varrho)$ and y^2 computed above. The bosonic self-energy diagrams are likewise simply the second derivative of the flow of the effective potential with respect to ϕ. To first non-trivial order, the fermion self-energy is proportional to $\gamma^\mu p_\mu$, and is precisely what needs to be absorbed into Z_ψ (reassuringly enough, no other matrix structure is generated at this order). One thus arrives at

$$\eta_\psi = \frac{16 v_D}{3D} \Big[m_{12}^{(\mathrm{FB}),D}(0, u_0'; \eta_\psi, \eta_\phi) + m_{12}^{(\mathrm{FB}),D}(2\varrho_0 y^2, u_0'; \eta_\psi, \eta_\phi)$$

---

[19] Note that diagram 3.8(c) is the same as in scalar O(3) ϕ^4 theory; it is thus known from literature (cf., e.g., Litim & Vergara 2004) and hence requires no original computation on our part.

[20] This is a somewhat non-trivial fact, given that the theory contains massless degrees of freedom. The fact that this nevertheless creates no non-analytic dependence of diagrams on external momenta has its origin in the way the RG scale k is implemented. In general, any scheme where the RG scale is used to suppress IR modes (sufficiently quickly) will only feature analytic dependence on external momenta. This in particular means any scheme that implements a 'mode decimation' version of RG, such as the present one, permits an expansion of diagrams in external momenta; we shall, however, also encounter field-theoretic versions of this argument in Chaps. 4 and 6.

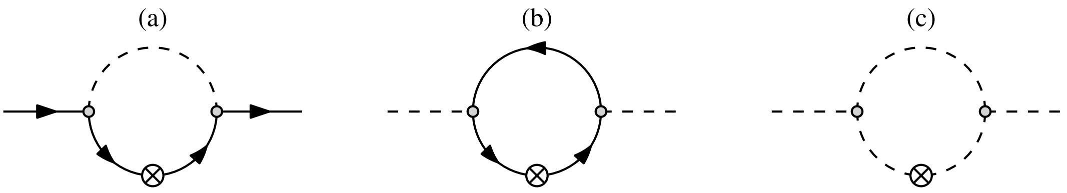

Figure 3.8: Diagrams contributing to anomalous dimensions. Conventions for lines and vertices same as in Fig. 3.7. As usual, graphs with the regulator insertion sitting on the other internal line exist, but are not displayed.

$$+ m_{12}^{(\mathrm{FB}),D}(2\varrho_0 y^2, u_0' + 2\varrho_0 u_0''; \eta_\psi, \eta_\phi)\Big] y^2. \tag{3.61}$$

Similarly, the momentum-dependent part of the boson self-energy begins at $\mathcal{O}(p^2)$ and leads to

$$\eta_\phi = \frac{32 N v_D}{3D} m_4^{(\mathrm{F}),D}(2\varrho_0 y^2; \eta_\psi) y^2 + \frac{16 v_D}{D} m_{22}^{(\mathrm{B}),D}(u_0', u_0' + 2\varrho_0 u_0''; \eta_\phi)\varrho_0 u_0''^2. \tag{3.62}$$

Like the ℓ-functions we encountered previously, the m-functions are further threshold integrals (cf., e.g., Janssen & Gies 2012).

A fixed point is defined as a solution of $k\partial_k y^2 = 0$ and $k\partial_k u(\varrho) = 0$. Whilst the former is – for appropriate choice of regulator – an algebraic equation, the second amounts, even for conveniently chosen regulators, to a nonlinear ordinary differential equation. This necessitates the choice of a suitable representation of $u(\varrho)$.

3.2.3.2 Representation of the effective potential

In the present project, $u(\varrho)$ was expanded in two different ways: (i) a Taylor expansion and (ii) a pseudospectral decomposition using Chebyshev polynomials. We have verified that our numerical results from the two approaches converge to the same values within error bars.

Taylor expansion. The first (and arguably simpler) ansatz is a truncated Taylor expansion

$$u(\varrho) = \sum_{i=1}^{n/2} \frac{1}{i!}\lambda_i\, \varrho^i, \tag{3.63}$$

where the fixed point is assumed to be located in the symmetric regime, such that the minimum of the potential is at $\varrho = 0$. In the SSB regime, an alternative expansion

$$u(\varrho) = \sum_{i=2}^{n/2} \frac{1}{i!}\hat{\lambda}_i\, (\varrho - \varrho_0)^i \tag{3.64}$$

is more expedient, where ϱ_0 minimizes $u(\varrho)$. (Recall that it is related to the vev of the order parameter by $2\varrho_0 = \langle\phi_a\rangle^2$.) Note that the linear term in the Taylor expansion is absent due to Eq. (3.59).

For practical computations, the ansatz (3.63) is truncated at some finite order $n \in 2\mathbb{N}$. This defines the so-called LPAn'. The validity of this polynomial truncation can be checked *a posteriori* by verifying convergence of the results upon increasing n. The expansion of the effective potential introduces a plethora of coupling constants, of which $\lambda_1 = m^2 > 0$ is the squared boson mass and $\lambda_2 = 4!\lambda$ is the quartic boson self-coupling. Inclusion of the higher-order couplings $\lambda_{i>2}$ is a minimal way to incorporate nonperturbative corrections in space-time dimensions $D < 4$, in addition to the effects from the nonperturbative propagator.

The flow of the bosonic self-couplings are determined from the flow of $u(\varrho)$ by differentiating successively with respect to ϱ. In the symmetric regime, this is straightforward to implement:

$$k\partial_k\lambda_i = \Big[(\partial_\varrho)^i\, k\partial_k u(\varrho)\Big]_{\varrho\to 0} \qquad (i \in \mathbb{N}_{\geqslant 1}). \tag{3.65}$$

The corresponding system of equations in the SSB regime is given by

$$k\partial_k\hat{\lambda}_i = \Big[(\partial_\varrho)^i\, k\partial_k U(\varrho)\Big]_{\varrho\to\varrho_0} + \hat{\lambda}_{i+1} k\partial_k\varrho_0 \quad (i \in \mathbb{N}_{\geqslant 2}), \tag{3.66}$$

and has to be supplemented by a flow equation for the vev:

$$k\partial_k\varrho_0 = -\frac{1}{\hat{\lambda}_2}\left[\partial_\varrho k\partial_k u(\varrho)\right]_{\varrho\to\varrho_0}. \tag{3.67}$$

The latter follows from $u'(\varrho_0) = 0$ in the SSB regime (Gies *et al.* 2010).

Pseudospectral decomposition. In the context of the present work, we aim at systematically comparing the results from different quantum-field-theoretical methods between two and four dimensions. Near two dimensions, a breakdown of the convergence of a local expansion in the effective potential is possible. This is because the canonical dimension $[\cdot]$ of the bosonic field ϕ is given by $[\phi] = (D-2)/2$; the dimension of the operator ϱ^i is thus $(D-2)i$. The canonical dimension of the corresponding coupling $[\lambda_i] = D - (D-2)i$. Potentially, for $D \to 2$, more and more couplings with higher i become canonically relevant until they all have the same canonical dimension of two in $D = 2$.

In lieu of a local Taylor expansion for the effective potential, non-local expansion schemes can be advantageous in terms of tractability, accuracy, and fast convergence. An approximation scheme that has been explored in the context of FRG fixed-point and flow equations is based on pseudospectral methods [see, for instance, the book by Boyd (2001) for an introduction]. Importantly, these methods facilitate, e.g., an efficient and high-precision resolution of global aspects of the effective potential including the correct description of a model's asymptotic behaviour[21)].

In the present case, the fixed-point equation for the effective potential requires us to find an approximate solution to an ordinary differential equation in one variable defined on the domain $\operatorname{dom} u = \mathbb{R}^+ := [0, \infty)$. To that end, one expands the effective potential $u(\varrho)$ into a series of Chebyshev polynomials, where $\operatorname{dom} u$ is decomposed into two subdomains according to $\mathbb{R}_+ = [0, \varrho_\mathrm{m}] \cup [\varrho_\mathrm{m}, \infty)$. The expansion then reads as

$$u(\varrho) \approx \begin{cases} \displaystyle\sum_{i=0}^{n_T} t_i T_i\left(\frac{2\varrho}{\varrho_\mathrm{m}} - 1\right), & \varrho \leqslant \varrho_\mathrm{m}\,, \\ \displaystyle u_\infty(\varrho)\sum_{i=0}^{n_R} r_i R_i(\varrho - \varrho_\mathrm{m})\,, & \varrho \geqslant \varrho_\mathrm{m}\,. \end{cases} \tag{3.68}$$

[21)] cf., e.g, Litim & Vergara (2004); Fischer & Gies (2004); Borchardt & Knorr (2015); Borchardt, Gies & Sondenheimer (2016); Borchardt & Knorr (2016); Borchardt & Eichhorn (2016); Knorr (2016, 2018)

Here, the $T_i(x)$ are the Chebyshev polynomials of the first kind, and the $R_i(x) = T_i\left(\frac{x-L}{x+L}\right)$ are rational Chebyshev polynomials with a free parameter L which parameterizes the compactification in the argument x.

Further, $u_\infty(\varrho)$ is the leading asymptotic behaviour of the effective potential for large field arguments $\varrho \to \infty$, which is fixed by the dimensional scaling terms in the flow equation. The matching point ϱ_m separates the subdomains and is another free parameter that has to be chosen large enough such that the minimum of the effective potential appears for $\varrho = \varrho_0 < \varrho_\mathrm{m}$. The parameters L and ϱ_m can be used to further optimize numerical convergence. The values of the effective potential and its derivatives for all field arguments ϱ are straightforwardly obtained by employing efficient recursive algorithms (Boyd 2001). In fact, in the present setting, only a relatively small number of expansion coefficients t_i and r_i turn out to be necessary due to a fast convergence of the series.

For the determination of the coefficients t_i and r_i in the Chebyshev expansion, we use the collocation method, i.e., the ansatz in Eq. (3.68) into the flow Eq. (3.38) and evaluate it on a given set of collocation points. The collocation points are chosen to be the nodes of the highest Chebyshev polynomials in the respective domain, and we add the origin $\varrho = 0$. Finally, to accomplish smoothness, we implement matching conditions for the values of the effective potential and its derivatives at ϱ_m. The resulting set of algebraic equations is then solved with the Newton-Raphson method. In practice, we actually expand the derivative $u'(\varrho)$ along these lines, and optimize L and ϱ_m as well as the number of collocation points until convergence in numerical results is reached. For the present model, we observe numerical convergence of the first four significant digits already starting at $n_T = n_R = 9$; as a sanity check, we have also increased the number of collocation points up to 18 in each subdomain for selected cases, without significant difference in the final results.

The anomalous dimensions of the quantum critical point are then obtained directly from the fixed-point solution of $u'(\varrho)$ using the FRG flow equations specified in the next section. To obtain the inverse correlation-length exponent, we use the pseudospectral expansion from the first subdomain, i.e., $\varrho < \varrho_\mathrm{m}$, rewriting it as a local expansion around its minimum. With the latter expansion, we then calculate the stability matrix and extract the eigenvalues at the fixed-point potential. The largest positive eigenvalue is the inverse correlation-length exponent.

3.2.3.3 Choice of regulator

For concrete calculations, specific choices for the regulator need to be made. In this chapter, we shall use two schemes: the linear regulator and the sharp regulator. The shape functions for these are given by

$$\begin{aligned} r_\phi^{\mathrm{lin}}(x) &= (x-1)\,\Theta(1-x) \\ r_\psi^{\mathrm{lin}}(x) &= \left(\sqrt{x}-1\right)\Theta(1-x) \end{aligned} \tag{3.69}$$

$$\begin{aligned} r_\phi^{\mathrm{sh}}(x) &= (x-1)\,\Theta(1-x) \qquad a \to \infty \\ r_\psi^{\mathrm{sh}}(x) &= \left[\sqrt{a\,(x-1)+1}-1\right]\Theta(1-x) \qquad a \to \infty \end{aligned} \tag{3.70}$$

with the $a \to \infty$-limit understood to be taken after the loop integration has been performed (Reuter & Saueressig 2002). The linear regulator has been shown by Litim (2001) to fulfil certain optimality criteria; in the literature, the linear regulator is hence also referred to as 'the optimal regulator'. Universal quantities such as critical exponents are supposed to be scheme-independent. As such, the residual regulator-dependence, as measured by the difference between the results computed with the linear and sharp regulators, is used to provide a (very rough) estimate of the truncation error in FRG.

Both regulators have the very convenient feature that threshold functions can be expressed in closed form, and have been tabulated, e.g., by Janssen & Gies (2012).

3.2.3.4 Limiting behaviour

Before discussing the numerical results for general but fixed spacetime dimension and flavour number, let us discuss some limiting cases, where some approximate analytical progress may be made.

Near upper critical dimension. Near $D = 4$, we may take inspiration from the loop expansion, and the fact that the interactions $y_*, \lambda_* = \mathcal{O}(\epsilon)$ where $\epsilon = 4 - D$. In this case, we may expect quantum corrections to be small, and thus $\eta_\psi, \eta_\phi = \mathcal{O}(\epsilon)$. This means that operators that are strongly irrelevant canonically will remain so even after quantum corrections have been incorporated. Standard power counting then shows that all operators $\mathcal{O} \notin \mathrm{LPA4}'$ have $[\mathcal{O}] \lesssim \epsilon - 1$ and may be safely neglected. Let us further assume that the fixed point is in the symmetric regime, and identify the coefficients of the Taylor expanded boson effective potential with parameters appearing in the classical action as $\lambda_1 = m^2$, $\lambda_2 = 4!\lambda$. Making the ansatz $y_*^2, \lambda_*, m_*^2 = \mathcal{O}(\epsilon)$ for the fixed-point values and expanding the flow equations to leading order in ϵ, one arrives at the fixed-point equations

$$0 = -Ny_{*,\mathrm{reg}}^2 - 6y_{*,\mathrm{reg}}^2 + 12\pi^2 \tag{3.71}$$

$$0 = 16Ny_{*,\mathrm{reg}}^4 - 8Ny_{*,\mathrm{reg}}^2\lambda_{*,\mathrm{reg}} - 33\lambda_{*,\mathrm{reg}}^2 + 48\pi^2\lambda_{*,\mathrm{reg}} \tag{3.72}$$

$$0 = -8Ny_{*,\mathrm{reg}}^2 + 15\lambda_{*,\mathrm{reg}} + 96C_{\mathrm{reg}}\pi^2 m_{*,\mathrm{reg}}^2 \tag{3.73}$$

for reg $\in \{\mathrm{lin}, \mathrm{sh}\}$ with $C_{\mathrm{lin}} = 2C_{\mathrm{sh}} = 2$. The fixed point pertinent to the present universality class needs to fulfil $y_*^2 > 0$, $\lambda_* > 0$ and $m_*^2 > 0$.[22] This leads to

$$y_{*,\mathrm{sh}}^2 = y_{*,\mathrm{lin}}^2 = \frac{12\pi^2}{N+6}\epsilon + \mathcal{O}(\epsilon^2), \tag{3.74}$$

$$\lambda_{*,\mathrm{sh}} = \lambda_{*,\mathrm{lin}} = \frac{8\pi^2\left(-N + \sqrt{N(N+120)+36} + 6\right)}{11(N+6)}\epsilon + \mathcal{O}(\epsilon^2), \tag{3.75}$$

$$m_{*,\mathrm{reg}}^2 = \frac{49N - 5\left(\sqrt{N(N+120)+36} + 6\right)}{44(N+6)C_{\mathrm{reg}}}\epsilon + \mathcal{O}(\epsilon^2). \tag{3.76}$$

Rather satisfyingly, to $\mathcal{O}(\epsilon)$, the regulator-dependence drops out in quantities which are canonically dimensionless in $D = 4$. The only residual dependence is in the fixed-point value of the dimensionless squared mass, whose underlying coupling has canonical dimension 2 (for all D). This is a manifestation of the stronger principle that dimensionless fixed-point quantities are one-loop universal for almost all RG schemes. It is then straightforward to check that the critical exponents calculated using the above fixed-point values are in agreement with the $4-\epsilon$ expansion presented in Sec. 3.2.1, regardless of choice of regulator.

---

[22] The first two are needed for unitarity, whilst the last constraint ensures a vanishing fixed-point vev. We may disregard the fixed points featuring $y_*^2 = 0$, because they are unstable with respect to perturbations of the Yukawa coupling, in addition to the usual instability to perturbations with a large component in operator space along the direction of the mass term (Janssen & Herbut 2014).

Near lower critical dimension. As D deviates further from $D_{\mathrm{up}} = 4$, the loop expansion in the Yukawa theory becomes increasingly badly controlled. However, for $D \to D_{\mathrm{low}} = 2$, a new control parameter arises: the ratio $G_{\mathrm{F}} := y^2/m^2$, the so-called *Fermi coupling.* That this is likely to be so may be anticipated simply by dimensional analysis: whilst the canonical dimension of the squared mass $[m^2] = 2$ is fixed, the canonical dimension of the squared Yukawa coupling grows for decreasing D as $[y^2] = 4 - D$. At $D = D_{\mathrm{low}}$, the two coincide; D_{low} is called the lower critical dimension[23]. Physically, G_{F} is the amplitude for the leading-order meson exchange process. The fact that G_{F} becomes dimensionless suggests that one should trade the Yukawa vertex for an effective four-fermion vertex

$$\sum_M -\frac{1}{2} G_{\mathrm{F},M} \left(\overline{\psi} M \psi\right)^2 \tag{3.77}$$

to get a perturbatively renormalizable description, for suitably chosen matrices M.[24] Even without knowing these matrices M, and without performing explicit calculations, it is possible to derive the relations (Gehring, Gies & Janssen 2015)

$$1/\nu = \epsilon + \mathcal{O}((D-2)^2), \tag{3.78}$$

$$\eta_\psi = \mathcal{O}((D-2)^2). \tag{3.79}$$

The fact that the one-loop corrections in the above are valid independently of the precise flavour content of the theory is referred to as *super-universality.* Let us check in the following to what extent our LPA′ approximation respects these relations. In the sharp regularization scheme, one finds the critical fixed point is characterized by the couplings

$$y^2_{*,\mathrm{sh}} = \frac{3\pi}{N} + \mathcal{O}(D-2), \tag{3.80}$$

$$m^2_{*,\mathrm{sh}} = \frac{1}{D-2}\left[\frac{2}{1-\gamma_{\mathrm{E}}+\ln(4\pi)} + \mathcal{O}(D-2)\right], \tag{3.81}$$

where γ_{E} is the Euler-Mascheroni constant. Using these relations, it is straightforward to check that the super-universality relations are fulfilled. An important conceptual point is the large fixed-point value of the mass: it is necessary to ensure that at the lower critical dimension, the four-fermion process is indeed point-like. Indeed, if one considers the tree-level 'meson-exchange' amplitude $y^2/(p^2+m^2)$ and rewrites it as an expansion in an effective field theory sense, one finds

$$y^2\left[\overline{\psi}\left(\mathbb{1}_{2N/3}\otimes L_a\right)\psi\right]\left[\overline{\psi}\left(\mathbb{1}_{2N/3}\otimes L_a\right)\frac{1}{\partial^2+m^2}\psi\right]$$

---

[23] Not to be confused with the lower critical dimension in the Colemna–Mermin–Wagner sense.

[24] To recover the Yukawa description, one needs to perform a so-called Hubbard–Stratonovich transformation (cf., e.g., the textbook of Altland and Simons 2010). Each bilinear $\overline{\psi}M\psi$ maps to a scalar field ϕ_M which couples to the fermion bilinear with assorted Yukawa coupling y_M; for $M = \mathbb{1}_{2N/3}\otimes L_a$ (which we assume hereinafter if unspecified), one recovers the ϕ-field we have been working with thus far in our calculations.

$$= \frac{y^2}{m^2}\left[\overline{\psi}\left(\mathbb{1}_{2N/3}\otimes L_a\right)\psi\right]^2 + \frac{y^2}{m^4}\left[\overline{\psi}\left(\mathbb{1}_{2N/3}\otimes L_a\right)\partial_\mu\psi\right]^2 + \cdots . \tag{3.82}$$

Only the first term on the right-hand side is momentum-independent, for which the one-loop fermion self-energy is a tadpole and leads to a vanishing η_ψ at one-loop. Higher-order diagrams are suppressed by powers of the mass, which scale with $D-2$. On the other hand, in the linear scheme,

$$y^2_{*,\mathrm{lin}} = \frac{6\pi}{N}(D-2) + \mathcal{O}((D-2)^2). \tag{3.83}$$

The fixed-point equation for $m^2_{*,\mathrm{lin}}$ turns out to be intractable analytically, but one may argue that since $G_\mathrm{F} = y^2/m^2$ is dimensionless, $m^2_{*,\mathrm{lin}} = \mathcal{O}(1)$. Hence, in the linear regularization scheme, the one-loop self-energy is not a tadpole graph, and yields a finite contribution to η_ψ, thereby violating super-universality, as demonstrated previously by Janssen & Herbut (2014) using numerical means. A similar violation exists also for $1/\nu$, but requires more involved algebraic techniques, and is hence left for future work.

3.3 Discussion

The quantum critical point is characterized by a set of universal exponents. Our focus in the following will be on the leading exponents ν and η_ϕ, as well as the fermion anomalous dimension η_ψ.[25] When applying the computations to fractionalized criticality in spin-orbital models, one needs to keep in mind that the fermionic correlator is not gauge invariant in the spin-orbital models; η_ψ does not strictly speaking correspond to an observable quantity in that setting. However, as the Gross–Neveu SO(3) universality may in principle also be realized in a model of interacting fermions, in which case η_ψ *is* measurable, it is worth discussing this quantity regardless[26]. Subleading quantities that control the corrections to scaling upon approaching the quantum critical point, such as ω, can in principle also be computed within the present approaches, but are left for future work.

3.3.1 General behaviour and qualitative aspects

Figure 3.9 shows the results for $1/\nu$, η_ϕ, and η_ψ as a function of space-time dimension $2 < D < 4$ and $0 < N < \infty$ flavours of two-component Dirac fermions. The case pertaining to the afore-mentioned fractionalized fermions in spin-orbital models studied by Seifert *et al.* (2020) corresponds to $D = 3$ and $N = 3$. For the results from the $4-\epsilon$ and large-N expansions, we have employed different Padé approximants, marked as '$[m/n]$' with integer m and n in the plots. The difference between the different approximants provides a simple estimate for the systematic error of the extrapolation to finite ϵ and $1/N$, respectively. For the same purpose, in the FRG calculation, we have applied two different regularization schemes, marked as 'lin' for the linear cut-off and 'sh' for the sharp cut-off.

In the FRG calculation using the sharp cut-off scheme, there is no stable fixed point for $2.104 < D < 2.366$ as a consequence of fixed-point collisions at the lower and upper bound of this interval. In this scheme, the fixed point in $D = 2 + \varepsilon$ dimensions for small ϵ is therefore *not* adiabatically connected to the fixed point in $D = 4 - \epsilon$ dimensions. This annihilation goes away for large enough flavour numbers $N \gtrsim 7$. In the linear cut-off, the fixed points at $D = 4 - \epsilon$ and $2 + \varepsilon$ are connected adiabatically. However, as demonstrated analytically above – and also checked numerically, cf., e.g., Janssen & Herbut (2014) – the fixed point that does emerge in the linear cut-off at $D = 2 + \varepsilon$ violates the super-universality relations of Gehring, Gies & Janssen (2015). This violation becomes milder for increasing N though, and vanishes in the strict mean-field limit. As for the (quasi-)perturbative approaches employed in this work, the fixed-point collision in question cannot be excluded conclusively. The $4 - \epsilon$ expansion is by design not suited to access the behaviour for $D \to 2$. The large-N approach expands asymptotically around the mean-field limit, such that the partner fixed point (which is likely non-perturbative in $1/N$ in addition to $4 - D$) may easily evade detection. Hence, the precise nature of the present universality class at small dimension $D \ll 3$ and small $N \lesssim 7$ remains an open question. Nevertheless, all three methods agree (to the order of approximation employed herein) that the fixed point in $D \geqslant 3$ and $N \geqslant 3$ is adiabatically connected to the $(D, N) = (4 - \epsilon, 3)$ and the $(D, N) = (3, \infty)$ theories. Indeed, in Fig. 3.9, all curves approach each other for $D \to 4$ (left panels) and $N \to \infty$ (right panels), which is reassuring. As an aside, let us also note that in the FRG calculation in both cut-off schemes, the fixed point for $N = 3$ is located in the symmetric regime for $D = 2 + \varepsilon$ and $D = 4 - \epsilon$ for small ϵ, ε, but in the symmetry-broken regime for $D = 3$. Hence, the FRG critical exponents become non-analytic as a function of D. Likewise, as a function of N at fixed D, the FRG fixed point at large N is located in the symmetric regime, but shifts to the SSB regime at small N. Non-analyticity of critical exponents *per se* is not an exceptionally exotic phenomenon. For instance, the coefficients of critical exponents in the $4 - \epsilon$ expansion are generically non-analytic as a function of N (essentially because one has to find the roots of polynomials to arrive at the fixed-point values of couplings). The interesting feature in the present scenario is that the non-analyticity 'percolates' into jump discontinuities of $1/\nu$ at the corresponding critical values of D and N.

---

[25] Recall that the exponent ν determines the divergence of the correlation length ξ upon approaching the quantum critical point, while the boson and fermion anomalous dimensions η_ϕ and η_ψ govern the scaling forms of the respective correlators.

[26] See Liu *et al.* (2021) for one such realization where η_ψ is in fact a measurable quantity.

3.3.2 Quantitative estimates for $D = 3$

The numerical estimates for the physical dimension $D = 2+1$ from the different techniques are displayed in Tab. 3.1 for $N = 3$ and in Tabs. 3.2–3.3 for larger values of N. Overall, the three different approaches exhibit a fair agreement in their estimates. In order to obtain final estimates for the three exponents from the combination of the three different approaches, first the values of the different Padé approximant and regularization schemes are averaged over, respectively, within a given approach, followed by an average over the mean values of the three approaches. The spread of the three mean values yield a rough estimate for the accuracy of our final result. This way, one arrives at the critical exponents for the physically relevant case of $N = 3$ flavours of two-component Dirac fermions in $D = 2 + 1$ space-time dimensions as

$$N = 3: \qquad 1/\nu = 1.03(15), \qquad \eta_\phi = 0.42(7), \qquad \eta_\psi = 0.180(10). \tag{3.84}$$

Equation (3.84) represents the main quantitative result of this chapter. As there appears to be no dangerously irrelevant coupling in the theory, we expect hyperscaling to be satisfied. The critical exponents α, β, γ, and δ can then be obtained from ν and η_ϕ with the help of the usual hyperscaling relations (Herbut 2007). For completeness, let us also

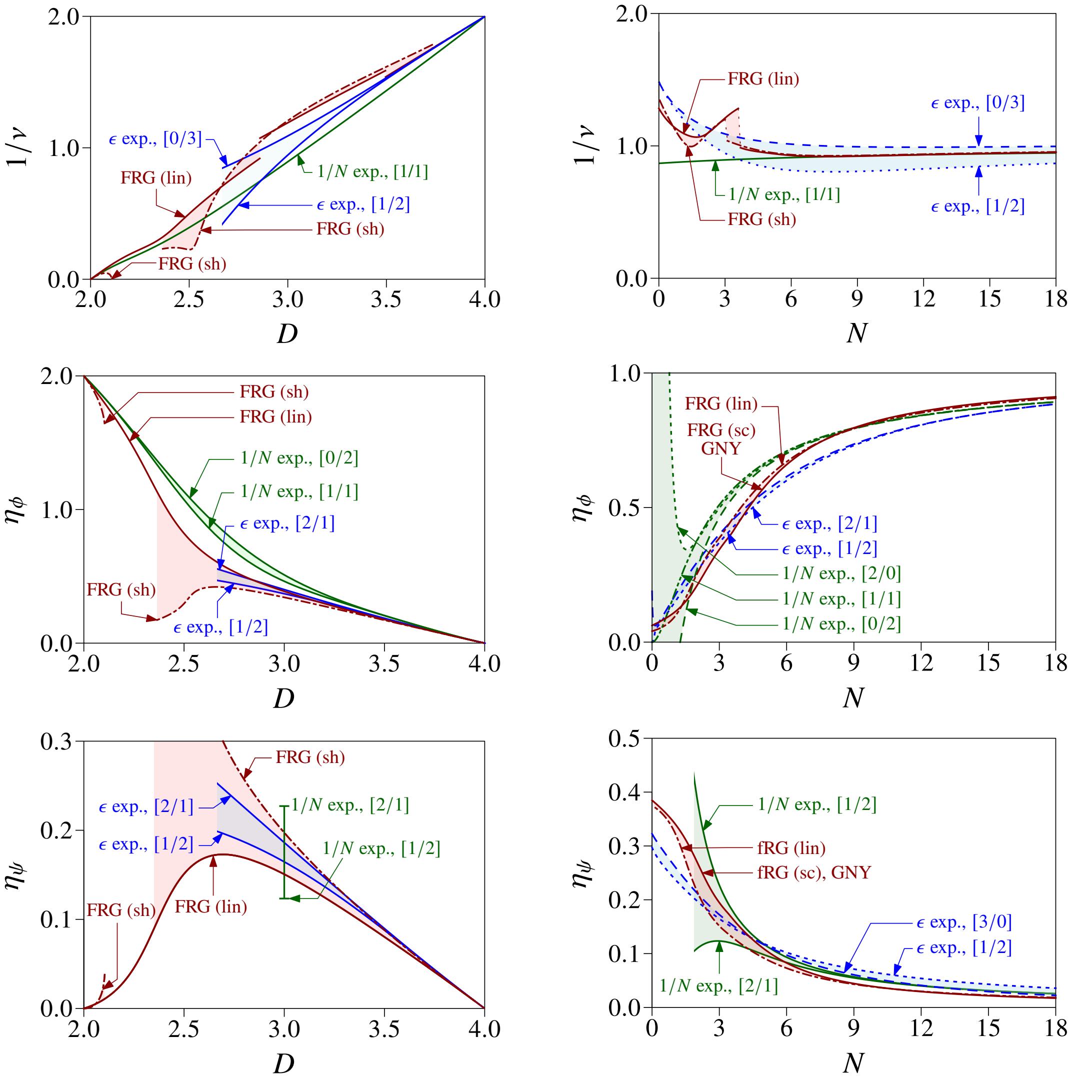

Figure 3.9: Critical exponents of the Gross–Neveu SO(3) universality class as a function of space-time dimension and flavour number from three-loop $4-\epsilon$ expansion, second-order $1/N$ expansion (third-order for η_ψ), and FRG in LPA16′ using linear (lin) and sharp (sh) regulators. $[m/n]$ correspond to different Padé approximants. Left: Fixed flavour number $N=3$ of two-component fermions, variable spacetime dimension $2 \leqslant D \leqslant 4$. Right: Fixed spacetime dimension $D=3$, varying flavour number.

Table 3.1: Critical exponents for the Gross-Neveu-SO(3) universality class for $N = 3$ flavors of two-component fermions in $D = 2 + 1$ space-time dimensions as relevant for the spin-orbital model on the honeycomb lattice Seifert *et al.* (2020) from three-loop $4 - \epsilon$ expansion, second-order $1/N$ expansion (third-order for η_ψ), and functional renormalization group. $[m/n]$ correspond to different Padé approximants. For the $(4 - \epsilon)$-expansion results ($1/N$-expansion results), we have refrained from showing approximants that exhibit a singularity in $D \in (2, 4)$ [in $N \in (0, \infty)$], marked with "sing."; those that do not exist are marked "n.-e.". A dash (—) signifies that the approximant either entails the computation of terms which go beyond the scope of this work, or conversely does not exhaust all the terms computed in the preceding sections. To obtain the FRG results in LPA′, we have treated the bosonic effective potential using a Taylor expansion [i.e., LPAn', with $n \leqslant 16$ (28) for the linear (sharp) regulator; the error bars correspond to the uncertainty in extrapolating to $n \to \infty$] as well as a pseudospectral decomposition in terms of Chebyshev polynomials.

$N = 3$			$1/\nu$	η_ϕ	η_ψ
$4 - \epsilon$ expansion		naïve	0.97516	0.39181	0.17234
		[1/2]	0.94472	0.40086	0.16458
		[2/1]	sing.	0.36989	0.18622
		[0/3]	1.09000	n.-e.	n.-e.
$1/N$ expansion		naïve	2.67318	0.49833	—
		[1/1]	0.89397	0.46276	—
		[0/2]	sing.	0.51074	n.-e.
		naïve	—	—	0.22116
		[1/2]	—	—	0.12337
		[2/1]	—	—	0.22716
		[0/3]	—	—	n.-e.
FRG	Taylor	linear	1.1901(10)	0.38781(6)	0.15068(8)
		sharp	1.209(4)	0.3434(5)	0.1966(6)
	pseudospectral	linear	1.18974	0.38781	0.15072
		sharp	1.20465	0.34340	0.19649

work out the estimates for larger values of N, which may be relevant for models with microscopic fermionic degrees of freedom,

$$N = 6: \qquad 1/\nu = 1.00(13), \qquad \eta_\phi = 0.66(5), \qquad \eta_\psi = 0.091(15), \tag{3.85}$$

and

$$N = 12: \qquad 1/\nu = 0.93(4), \qquad \eta_\phi = 0.83(4), \qquad \eta_\psi = 0.039(9). \tag{3.86}$$

3.4 Summary and outlook

This chapter was devoted to investigating the critical behaviour of the $(2+1)$-dimensional Gross–Neveu SO(3) universality class in terms of the universal critical exponents ν, η_ϕ, and η_ψ by means of different sophisticated field-theoretical techniques.

The chiral SO(3) theory is different from the previously studied Gross–Neveu-type models, as it features a symmetry-breaking transition between two semimetallic phases,

Table 3.2: Same as Table 3.1, but for $N = 6$.

$N = 6$			$1/\nu$	η_ϕ	η_ψ
$4 - \epsilon$ expansion		naïve	0.86069	0.61414	0.09720
		[1/2]	0.81514	0.60023	0.10216
		[2/1]	0.96700	0.61484	0.12551
		[0/3]	1.01291	n.-e.	n.-e.
$1/N$ expansion		naïve	1.28320	0.70572	—
		[1/1]	0.91136	0.70076	—
		[0/2]	1.26614	0.71005	n.-e.
		naïve	—	—	0.09275
		[1/2]	—	—	0.08341
		[2/1]	—	—	0.09317
		[0/3]	—	—	n.-e.
FRG	Taylor	linear	0.9294(6)	0.66947(6)	0.073170(17)
		sharp	0.926(3)	0.6598(4)	0.08257(16)
	pseudospectral	linear	0.92961	0.66948	0.073165
		sharp	0.93245	0.65980	0.082570

Table 3.3: Same as Table 3.1, but for $N = 12$. For the FRG results, we have omitted the error bars corresponding to the uncertainty in the extrapolation of the Taylor expansion of the effective potential, as they are smaller than 2×10^{-5}.

$N = 12$			$1/\nu$	η_ϕ	η_ψ
$4 - \epsilon$ expansion		naïve	0.84820	0.80614	0.04095
		[1/2]	0.82616	0.80659	0.05391
		[2/1]	0.91427	0.80775	sing.
		[0/3]	0.99001	n.-e.	n.-e.
$1/N$ expansion		naïve	1.00325	0.84199	—
		[1/1]	0.93326	0.84134	—
		[0/2]	0.98522	0.84280	n.-e.
		naïve	—	—	0.04054
		[1/2]	—	—	0.03995
		[2/1]	—	—	0.04056
		[0/3]	—	—	n.-e.
FRG	Taylor	linear	0.93660	0.85180	0.02992
		sharp	0.93282	0.85700	0.02941
	pseudospectral	linear	0.93660	0.85180	0.02992
		sharp	0.93282	0.85700	0.02941

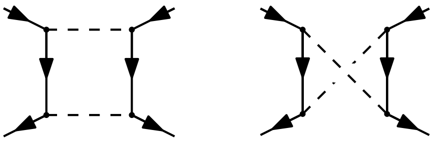

Figure 3.10: Box diagrams that can generate other 4-Fermi channels not transformable in the Hubbard–Stratonovich sense into the Yukawa interaction considered in the present work. Such contributions become important for $D \searrow 2$.

with only a partial gap opening in the ordered phase. This leads to values for the critical exponents that strongly differ from those of the semimetal-to-insulator Gross–Neveu Ising and Heisenberg transitions (Zerf *et al.* 2017). In particular, the order-parameter anomalous dimension η_ϕ in the Gross–Neveu SO(3) model is significantly smaller than η_ϕ in any of the other Yukawa models for the same number of fermion flavours. These differences may be readily observable in numerical simulations of suitable lattice models.

An important aspect of the three-pronged approach employed in the present study is that the spread between different methods surpasses by far the internal notion of uncertainty, i.e., the regulator-dependence in FRG or the spread of different Padé approximants in the series expansions. A major reason behind this is the fact that the number of well-behaved Padé approximants can turn out to be small to the level of approximation employed herein; the knowledge of higher-order terms may furnish access to a ‘statistically significant’ number of well-behaved approximants and thereby allow one to derive more confident ‘internal’ error estimates. Furthermore, experience from other problems teaches that the regulator dependence of FRG results actually first increases as a function of the truncation order of derivative expansion, before settling down at sufficiently large orders. In this case, derivative expansion beyond LPA′ may be indispensable to obtain reliable FRG estimates – both in terms of the precision of final results as well as more realistic internal estimates for the uncertainty. Overall, the findings presented here may thus also serve as a cautionary tale against relying solely on ‘internal’ error estimates in regimes where the approximation cannot be proven to converge rigorously, or is not guaranteed to be controlled in an asymptotic sense.

A very intriguing aspect of the present universality class is the fate of the critical fixed point at low dimensions. At the present level of approximation, viz. LPA′, the FRG fixed point was found to be unstable for $D \in (D_{\text{c},1}, D_{\text{c},2})$ with $D_{\text{c},1}(N=3) \approx 2.104$ and $D_{\text{c},1}(N=3) \approx 2.366$. This naturally raises several questions: First, one may ask whether this phenomenology persists (possibly with a different $D_\text{c}(N)$) to high orders of derivative expansion. As an intermediate step, one may also look to reproduce this phenomenon in a different but superuniversality-compliant cut-off scheme (in other words, one may ask whether avoiding this fixed-point annihilation is equivalent to violating super-universality in $D = 2 + \varepsilon$).

A further interesting aspect that has been neglected entirely in the present analysis is the influence of competing channels. The lower the spacetime dimension, the less canonically irrelevant 4-Fermi operators of the form $(\overline{\psi}M\psi)^2$ become. At the level of Yukawa vertices, an interaction of the form $\phi_M\overline{\psi}M\psi$ can only renormalize itself; a different Yukawa vertex $\phi_{M'}\overline{\psi}M'\psi$ ($M \neq M'$) does not get generated by quantum corrections if absent at the classical level. At the 4-Fermi level, however, box diagrams like the one shown in Fig. 3.10 can generate not only $(\overline{\psi}M\psi)^2$ (if the spinor-space structure of the Yukawa vertex is M) but also – to first order in perturbation theory – terms like $(\overline{\psi}M\gamma^\mu\psi)^2$. These in turn can generate further 4-Fermi interactions not present in the original action. The competition of multiple 4-Fermi channels has been shown to yield very rich phenomenology in other settings (cf., e.g., Szabo & Roy 2021). An extension of the present FRG calculation to include a Fierz-complete 4-Fermi basis for the chiral SO(3) system would hence be an excellent direction for future research. The fact that the 4-Fermi interaction $[\overline{\psi}(\mathbb{1}_{2N/3} \otimes L_a)\psi]^2$ is not closed unter renormalization would also necessitate the inclusion of higher-spin (in the sense of the D-dimensional rotation group) fields in the large-N formalism when going beyond the present order in $1/N$, which appears to be an interesting technical challenge. In terms of the loop expansion, a complementary $2 + \varepsilon$ expansion27) may be instructive. In fact, preliminary investigations by the present author have shown that close to certain critical flavour numbers, the putative non-perturbative collision partner may fall within the weak-coupling regime. This may allow one to disconnect the $D = 4 - \epsilon$ fixed point from the $D = 2 + \varepsilon$ one in a perturbatively controlled manner.

---

27) Recall that this is simply a loop expansion in the 4-Fermi theory, since that is the perturbatively renormalizable version of the theory at $D = 2$

Chapter 4

Luttinger Fermions in Two Spatial Dimensions

4.1 Introduction

The critical exponents of $(2+1)$-dimensional Dirac fermions are challenging to predict with high precision, at least for practically relevant flavour numbers. We saw explicitly in Chap. 3,(1) that obtaining full consensus between the three complementary theoretical approaches we employed – the functional renormalization group in the improved local potential approximation, the $4-\epsilon$ expansion to three-loop order, and the $1/N$ expansion in next-to-next leading order (NNLO) – remains a challenge. It is difficult to obtain reliable 'internal' error bounds for the individual methods (at least at the level of sophistication that is currently the state of the art), and as such, it is not possible to judge which method is closer to the ultimate correct value.(2) An equally weighted – in the spirit of maximum ignorance – average over the three methods allows one to salvage some best-guess estimates with comparatively high-confidence error bars, but this ultimately leads to uncertainties that are quite large. On the numerical side, the presence of gapless fermionic degrees of freedom means the lattice sizes currently attainable in, e.g., quantum Monte Carlo simulations, are much smaller than in purely bosonic systems. This again increases the uncertainty in extrapolations to the thermodynamic limit.

In this chapter, we shall (re-)visit quantum criticality in two-dimensional(3) *Luttinger* fermions, and point out that it can serve as a welcome counterexample to the above difficulties. Luttinger fermions are gapless fermions with a *quadratic* low-energy dispersion,

$$\varepsilon_{\pm}(\boldsymbol{p}) = \pm\boldsymbol{p}^2.$$

The notion of quadratically dispersing particles *per se* is not entirely unknown; in 'Nature', they abound in the limit of Galilean mechanics, where the kinetic energy of an object with momentum $\boldsymbol{p}$ is given by $\varepsilon(\boldsymbol{p}) = \boldsymbol{p}^2/2m$. The crucial distinction of Luttinger fermions is the gaplessness of the spectrum. When deriving the non-relativistic limit of a massive relativistic particle, the actual dispersion – including both the particle and anti-particle 'branches' – reads as

---

(1) Although we specifically studied only the SO(3) flavour symmetry, this is true for all flavour symmetry groups.

(2) This is not to say that there are no internal error estimates for the individual methods at all. However, they are not rigorous upper bounds; taking any of them at face value would (probably erroneously) invalidate the other two methods.

(3) Here and throughout the remainder of this chapter, 'dimension' by itself shall refer to *spatial* dimension by default. This is because the system we study from hereon in has no relativistic symmetry.

$$\varepsilon_{\pm}^{\text{non-rel}}(\boldsymbol{p}) = \pm mc^2 \left(1 + \frac{\boldsymbol{p}^2 c^2}{2m^2 c^4} + \mathcal{O}(\boldsymbol{p}^4/c^4) \right),$$

where the speed of light c has been reinstored temporarily for illustration. Importantly, there is an energy gap the size of the rest energy $\varepsilon_0 = mc^2$. The fact that there is no such mass gap in Luttinger fermions means they cannot arise directly in 'Nature' from elementary particles, but only emerge as quasiparticles of some many-body ground state. The usual avenue is by a quadratic crossing of two bands, such as in Bernal-stacked bilayer graphene to good approximation [cf., e.g., Cvetkovic, Throckmorton & Vafek (2012) and references therein], as well as in 3D semimetals such as grey tin and mercury telluride [cf., e.g., Witczak-Krempa *et al.* (2014) for a review]; we shall revisit the issue of explicit microscopic (lattice) realizations of the pertinent field theory later in this chapter.

The fact that the two bands cross quadratically means the density of states at the Fermi energy is significantly enhanced; using a simple dimensional argument, one can estimate $\varrho(\varepsilon) = \text{const.} + \mathcal{O}(|\varepsilon - \varepsilon_{\text{F}}|)$ for the density of states ϱ at energies ε close to the Fermi level ε_{F}. A constant density of states near the Fermi surface is a feature of two-dimensional *metals*. As such, it is natural to expect such a Luttinger semimetal to be unstable with respect to spontaneous symmetry breaking at infinitesimal interactions. This naïve picture survives a more rigorous RG calculation (Sun *et al.* 2009).

Dimensional analysis (i.e., Gaußian power counting) can also be used to obtain an intuitive quantum field theoretic picture. The d-dimensional spatial volume element has inverse length dimension $-d$ *per definitionem*, i.e., $[\mathrm{d}^d x] = -d$. The dimension of the Euclidean time line element is $[\mathrm{d}\tau] = -z$, the (negative) dynamical critical exponent. Assuming a canonical form for the temporal part of the kinetic term,

$$S_0 \supset \int \mathrm{d}\tau \, \mathrm{d}^d x \, \psi^\dagger \partial_\tau \psi, \tag{4.1}$$

one can deduce[4] $[\psi] = d/2$. Consider now a 4-Fermi (in other words, generalized 'density-density') interaction of the form

$$S_{\text{int}} \supset -\frac{g}{2} \int \mathrm{d}\tau \, \mathrm{d}^d x \, (\psi^\dagger M \psi)^2 \tag{4.2}$$

with an unspecified matrix M acting in combined spinor-flavour space, and corresponding coupling g. Requiring the action be dimensionless then yields $[g] + 4[\psi] = d + z$, whence using $[\psi] = d/2$ one obtains

$$[g] = z - d. \tag{4.3}$$

We thus see that if $d = z$, the 4-Fermi interaction becomes dimensionless (i.e., canonically marginal). Specializing to Luttinger fermions ($z = 2$), this occurs at $d = 2$ spatial dimensions. It is usually referred to as the lower critical dimension $d_{\text{low}} = d_{\text{low}}(z)$, which depends only on the dynamical critical exponent.[5] Hence, the leading term of its

---

[4] To derive this explicitly, use the fact that the action must be dimensionless, $[S] = 0$, and that derivatives scale opposite to line elements, $[\partial_\tau] = -[\mathrm{d}\tau] = z$

[5] The dynamical critical exponent at the lower critical dimension is not renormalized to one-loop order due to kinematic reasons.

β-function is[6)]

$$\beta_g = Ag^2 + \cdots , \tag{4.4}$$

where A a numerical constant. Unless it vanishes by accident or by dint of symmetry, we may then change variables to $\tilde{g} = Ag$, with β-function $\beta_{\tilde{g}} = \tilde{g}^2 + \cdots$. Integrating out the flow to scales $k < \Lambda$, one hence finds

$$\tilde{g}(k) = \frac{1}{1/\tilde{g}(\Lambda) - \ln(\Lambda/k)}. \tag{4.5}$$

If the flow is initialized at a negative $\tilde{g}(\Lambda) < 0$, one obtains $\tilde{g}(k) \to 0$ for $k \to 0$. The ground state is thus given by the non-interacting semimetal. On the other hand, for a positive initial condition $\tilde{g}(\Lambda) > 0$, $\tilde{g}(k)$ hits a pole at a critical scale $k_{\text{SSB}} = \Lambda \mathrm{e}^{-1/\tilde{g}(\Lambda)}$, signalizing the onset of spontaneous symmetry breaking (SSB). Both scenarios incidentally have counterparts in the Standard Model (in $D = 4$ spacetime dimensions) with the coupling g roughly corresponding to the *square* of the gauge coupling, $g = e^2 > 0$. As such, the sign of the initial condition is always fixed: $\operatorname{sgn} \tilde{g}(\Lambda) = \operatorname{sgn} A$. The case $A > 0$ occurs, for instance, in the SU(3) gauge sector – i.e., quantum chromodynamics (QCD). At low energies, the elementary fermions, called quarks, do not occur freely, but only in bound states; the simplest example of them are quark-antiquark states called mesons. The case $A < 0$ is realized in the U(1) gauge sector, quantum electrodynamics. The infrared behaviour of QED is known to be unspectacular: (quasi-) free electrons abound in Nature at low energies; the gauge coupling is screened by vacuum polarization, and thus the electron-electron repulsion (or equivalently electron-positron attraction) becomes weaker at lower energies.

In the case of 4-Fermi interactions in Luttinger semimetals, both signs of g are allowed; one of the allowed signs will always exhibit a low-energy instability. The sign of g for which this occurs will essentially decide whether the fermions in the ordered state will be bound into (generalized) excitons or Cooper pairs.[7)] The fact that the instability is triggered at infinitesimal interaction means the transition is governed by a Gaußian fixed point, $g_* = 0$. This fixed point, however, is not critical – strictly speaking, it is *trans-critical* (i.e., marginally relevant for $g \to 0^s$ and marginally irrelevant for $g \to 0^{-s}$, with $s \in \{+, -\}$ fixed by internal details of the theory). As a theoretical consequence, some critical exponents are rendered ill-defined (of the form 0, ∞, or '$0 \cdot \infty$'). One of the aims of this chapter is to 'make sense' of these pathologies. In case of vanishing or infinite critical exponents, this means working out the leading (essential) singularity of the observable; in case of '$0 \cdot \infty$', it entails deriving the power law exponent. Rather interestingly, it turns out that both the essential singularity as well as the formally indeterminate power law significantly deviate from the corresponding canonical or mean-field prediction, in spite of the Gaußian nature of the fixed point. For the former, we show this by explicit computation of the (Callan–Symanzik-improved) order-parameter effective potential directly in $d = 2$ dimensions. For the latter (which concerns the so-called susceptibility exponent γ), we shall see via an excursion to $d = 2 + \epsilon$ spatial dimensions that this value is *one-loop exact*. The key conceptual ingredient behind this is the fact that the order parameter, being bilinear in the fermion fields, is a composite operator. As a

---

[6)] We restrict to the case where there is only one coupling g, since this will mostly be sufficient for our purposes in this chapter. A more general case appears in Chap. 6.

[7)] It turns out that in the case we will be interested in, the instability is excitonic. However, most of our calculation would go through for a superconducting instability.

by-product of our RG analysis, we revisit the concept of reformulating the theory in a way such that the order parameter is promoted to an elementary field by means of a (scale-dependent) Hubbard–Stratonovich transformation (i.e., trading the one-particle irreducible 4-Fermi vertex for a reducible 'meson' exchange process). As pointed out for relativistic 4-Fermi theories (specifically, in the setting of Gross–Neveu–Ising and –Heisenberg quantum criticality) by Janssen & Herbut (2014), the physically correct point-like 4-Fermi limit of meson exchange arises dynamically at the lower critical dimension only if the regularization scheme is chosen judiciously enough. We investigate to what extent this holds in the present non-relativistic setting of Luttinger fermions.

Throughout, we shall focus on the 'maximally minimal' theory comprising two-component spinors. The smallness of the spinor space dimension, allied with the Grassmann nature of fermionic fields, means there is precisely one Fierz-independent 4-Fermi interaction channel, and ensures the calculations remain tractable at all stages. We remark here that the corresponding relativistic version of the problem in $d = d_{\text{low}}(z = 1) = 1$ is degenerate in some sense: the so-called Gross–Neveu theory in $D = 2$ spacetime dimensions with 2-component spinors is equivalent to the Thirring model, which is integrable with infinitely many conserved quantities (among other things, this makes the β-function of the 4-Fermi coupling vanish to all loop orders).

The material in this chapter is organized as follows: In Sec. 4.2, we review the construction of the Luttinger fermion from symmetry considerations. Subsequently, we derive the β-functions in both 4-Fermi and Yukawa formulations in Sec. 4.3. The fixed points of the theory at $d > 2$ and their collision for $d \to 2$ are elucidated in Sec. 4.4. We shall then demonstrate in Sec. 4.5 that some non-mean field behaviour survives this collision, and that the fixed-point collision actually renders the non-mean field exponent one-loop exact. Sec. 4.6 is devoted to an explicit microscopic realization of two-dimensional Luttinger semimetals, namely on a kagome lattice. The chapter closes with a summary and outlook in Sec. 4.7.

4.2 Action from top-down construction

In this section, we review the 'top-down' construction of Luttinger fermions, following Janssen & Herbut (2015). Assume a canonical non-interacting action $S_0 = \int \mathrm{d}\tau \mathrm{d}^d x \mathcal{L}_0$ with Lagrangian

$$\mathcal{L}_0 = \psi^\dagger \left[\partial_\tau + \mathcal{H}_0(-\mathrm{i}\boldsymbol{\partial})\right] \psi. \tag{4.6}$$

The function $\mathcal{H}_0(\boldsymbol{p})$ is precisely what is usually called the *single-particle Hamiltonian.* Choose as ansatz for $\mathcal{H}_0$ the form

$$\mathcal{H}_0(\boldsymbol{p}) = T_{ij} p_i p_j \tag{4.7}$$

with implicit summation over $i, j = 1, \ldots, d$. A rotationally invariant and particle-hole symmetric spectrum[8] $\varepsilon_\pm(\boldsymbol{p}) = \pm \boldsymbol{p}^2$ can be achieved by requiring $\mathcal{H}_0^2 = \boldsymbol{p}^2 \mathbb{1}_{d_\text{s}}$ with d_s the dimension of the 'spinor' space. This in turn can be shown to lead to the following conditions for the algebra of the entries of (T_{ab}):

$$\{T_{ij}, T_{kl}\} = 0 \qquad (i,j) \neq (k,l) \wedge i \neq j \tag{4.8}$$

---

[8] An overall factor is needed to ensure the Hamiltonian has units of energy. This factor is usually denoted $1/2m^*$, and m^* is referred to as the 'effective band mass'. In the RG approach, this factor can be absorbed into field (re-)normalization.

$$4T_{\underline{ij}}T_{\underline{ij}} + \{T_{\underline{kk}}, T_{\underline{ll}}\} = 2 \qquad a \neq b \tag{4.9}$$

$$T_{ii} = 0 \tag{4.10}$$

(no implicit summation over underlined indices). To satisfy these conditions simultaneously, one requires at least $\frac{1}{2}(d+2)(d-1)$ mutually anticommuting matrices.

Specializing to $d = 2$, the minimal spinor dimension is thus $d_\text{s} = 2$, and the T_{ij} can be represented using Pauli matrices:

$$(T_{ij}) = \begin{pmatrix} \sigma_z & \sigma_x \\ \sigma_x & -\sigma_z \end{pmatrix}. \tag{4.11}$$

Inserting into Eq. (4.7), we find explicitly

$$\mathcal{H}_0(\boldsymbol{p}) = d_a(\boldsymbol{p})\,\sigma_a. \tag{4.12}$$

The index $a = 1, 2$ labels[9] spatial directions similar to $i = 1, \ldots, d$ above. However, we specifically use letters from the beginning of the Latin alphabet to remind ourselves that objects carrying an index a transforms as rank-2 tensors under spatial rotations. The $d_a(\boldsymbol{p})$ are the $\ell = 2$ spherical harmonics, $(d_a(\boldsymbol{p})) = \left(p_x^2 - p_y^2, 2p_xp_y\right)$. Under a spatial rotation $p_i \mapsto (R_\theta)_{ij}p_j$ with $R_\theta \in \mathrm{O}(2)$, it follows from explicit computation[10] that $d_a(\boldsymbol{p}) \mapsto (R_{2\theta})_{ab}p_b$. The fact that the form factor 'rotates twice as fast' as the Dirac Hamiltonian $p_i\sigma_i$ can be shown to imply that the Berry flux of a quadratic band touching (QBT) point is twice that of a Dirac point. Since Berry flux is only conserved modulo 2π, the usual fermion-doubling restriction does not apply, and a two-dimensional spinor space is sufficient.

The fact that we have a very small spinor space greatly simplifies the structure of 4-Fermi interactions: the only non-vanishing quartic in Grassmann fields is given by

$$\psi_1^*\psi_2^*\psi_1\psi_2$$

with $\psi = (\psi_1, \psi_2)^\top$ and 'star' denoting the Grassmann conjugate. Thus, any 4-Fermi term $(\psi^\dagger M\psi)^2$ with $M \in \mathbb{C}^{2\times 2}$ can be expressed in the above form – a particularly simple but also severe example of a Fierz identity. Amongst the many equivalent ways of writing the 4-Fermi interaction, one form is particularly well-suited, especially in view of, e.g., a subsequent rewriting as a Yukawa interaction using the Hubbard–Stratonovich transformation: the $(\psi^\dagger\sigma_y\psi)^2$ channel. This is because it is the only channel where a vacuum expectation value (vev) of the corresponding bilinear, $\langle\psi^\dagger\sigma_y\psi\rangle \neq 0$, leads to a full gap in the spectrum,[11] and hence constitutes the leading instability (Sun *et al.* 2009). Thus, we write the interacting part of the action as $S_\text{int} = \int \mathrm{d}\tau\mathrm{d}^dx\mathcal{L}_\text{int}$ with

$$\mathcal{L}_\text{int} = -\frac{g}{2}(\psi^\dagger\sigma_y\psi)^2. \tag{4.13}$$

---

[9] Note that this means we have a cyclically permuted sequence of Pauli matrices, $\sigma_\alpha = (\sigma_z, \sigma_x, \sigma_y)$. This representation has the advantage that time reversal is represented simply by complex conjugation. At the level of quantum field theory, this will be neither particularly important nor useful. However, it will play a prominent role when relating the quantum field theory to the microscopic lattice model later in Sec. 4.6.

[10] This is easiest to see in polar coordinates $\boldsymbol{p} = p(\cos\varphi, \sin\varphi)$. In these variables, $R_\theta \in \mathrm{O}(2)$ acts as $\varphi \mapsto \varphi + \theta$ while p is invariant. The assertion follows from the observation that $(d_a(\boldsymbol{p})) = p^2(\cos 2\varphi, \sin 2\varphi)$.

[11] By contrast, a vev $\langle\psi^\dagger\sigma_a\psi\rangle$ $(a = z, x)$ splits the QBT into two Dirac points. The axis joining the two Dirac points picks out an axis in momentum space – the spontaneously broken symmetry is thus spatial rotational invariance. We shall revisit this form of spontaneous symmetry breaking in Chap. 6.

The full Lagrangian of the Luttinger 4-Fermi theory is then given by $\mathcal{L}_{\mathrm{L4F}} = \mathcal{L}_0 + \mathcal{L}_{\mathrm{int}}$.

By means of a Hubbard–Stratonovich transformation, one can always trade – at least in principle – a 4-Fermi theory for a Yukawa theory. The resulting Lagrangian, which we call the Luttinger–Yukawa Lagrangian $\mathcal{L}_{\mathrm{LY}}$, reads as

$$\mathcal{L}_{\mathrm{LY}} = \mathcal{L}_0' + \mathcal{L}_{\mathrm{int}}' \tag{4.14}$$

$$\mathcal{L}_0' = \mathcal{L}_0 + \frac{1}{2}\phi\left(-\partial_\tau^2/c^2 - \boldsymbol{\partial}^2 + r\right)\phi \tag{4.15}$$

$$\mathcal{L}_{\mathrm{int}}' = -h\phi\psi^\dagger\sigma_y\psi. \tag{4.16}$$

The equivalence between $\mathcal{L}_{\mathrm{L4F}}$ and $\mathcal{L}_{\mathrm{LY}}$ requires the identification

$$g = \frac{h^2}{r}. \tag{4.17}$$

The field ϕ can be related to the fermion bilinear to which it couples via the Yukawa vertex $\mathcal{L}_{\mathrm{int}}'$ using the equations of motion $\delta S/\delta\phi = 0$:

$$\psi^\dagger\sigma_y\psi = \frac{r}{h}\phi \tag{4.18}$$

Although the kinetic terms of ϕ do not appear directly upon Hubbard–Stratonovich transformation, they would be generated under the RG flow; we may hence just as well include them in the action from the outset. The 'propagation velocity' c of the ϕ-field is necessary to account for the broken Lorentz invariance in the free fermionic part $\mathcal{L}_0$.

Let us now work out the canonical scaling dimensions of the new variables. Since $[\boldsymbol{\partial}^2] = 2$, the canonical dimensions of r and c as well as the ϕ-field are fixed due to the presence of the Laplacian term in $\mathcal{L}_0'$, to wit:

$$[r] = 2, \tag{4.19}$$

$$[c] = z - 1, \tag{4.20}$$

$$[\phi] = (d + z - 2)/2. \tag{4.21}$$

This then implies for the Yukawa interaction

$$[h^2] = 6 - d - z. \tag{4.22}$$

4.3 Renormalization

The diagrams needed to evaluate the pertinent β-functions and anomalous dimensions are shown in Fig. 4.1. From a Yukawa perspective, the only restriction is that diagrams should be one-particle irreducible (1PI) with respect to both fermion and boson lines. For the renormalization of the 4-Fermi version of the theory, the 'diagrammar' has to be modified as follows: (i) diagrams need to be 1PI only with respect to fermion lines – ϕ-reducible graphs are perfectly admissible; (ii) there should be no external ϕ-legs; and (iii) internal ϕ-lines are replaced by $1/r$.(12) Thus, diagrams 4.1(a)–(e) renormalize $\mathcal{L}_{\mathrm{LY}}$,(13) whilst (d)–(c″) are responsible for the renormalization of $\mathcal{L}_{\mathrm{L4F}}$.(14)

---

(12) Note that the ϕ-field still carries 3-momentum (as far as, e.g., momentum conservation at vertices is concerned), even though the prescription is tantamount to evaluating the propagator at vanishing 3-momentum. In other words, the dynamics of the ϕ-field is 'switched off' by hand.

(13) Note that the diagrams Fig. 4.1(d,e) have four fermion legs, i.e., it does not correspond to a term already present in $\mathcal{L}_{\mathrm{LY}}$. As we shall see, it will be absorbed by a non-multiplicative renormalization of ϕ.

(14) The explicit one-loop β-function of the 4-Fermi coupling g was computed previously in fixed dimension $d = 2$ by Sun *et al.* (2009) as $\beta_g = g^2/(4\pi)$. The reference is unclear on the regularization scheme

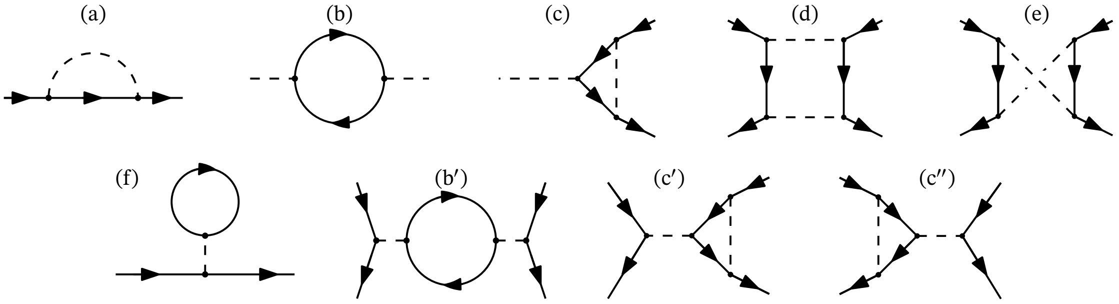

Figure 4.1: Feynman diagrams that renormalize the theory of Luttinger fermions at one-loop order. The bottom row contains ϕ-reducible diagrams that are only admissible in the 4-Fermi formulation, whilst the top row contains two diagrams with external ϕ-legs, which are only allowed in the Yukawa version of the theory. The dashed line stands for the free boson propagator $(\omega^2/c^2 + \boldsymbol{p}^2 + r)^{-1}$ in the Yukawa formulation, and reduces simply to $1/r$ in the 4-Fermi formulation.

Let us first write down the general expression for the diagrams, whilst remaining agnostic as to the regularization and renormalization scheme to be used. We find (with G_0 and D_0 the free fermion and boson propagators respectively):

$$\text{Fig. 4.1(a)} = -h^2 \int \frac{\mathrm{d}\omega' \mathrm{d}^d\boldsymbol{p'}}{(2\pi)^{d+1}}\, \sigma_y\, G_0(\omega', \boldsymbol{p'})\, \sigma_y\, D_0(\omega - \omega', \boldsymbol{p} - \boldsymbol{p'}) \tag{4.23}$$

$$\text{Fig. 4.1(b)} = h^2 \int \frac{\mathrm{d}\omega' \mathrm{d}^d\boldsymbol{p'}}{(2\pi)^{d+1}}\, \mathrm{tr}[\sigma_y\, G_0(\omega', \boldsymbol{p'})\, \sigma_y\, G_0(\omega - \omega', \boldsymbol{p} - \boldsymbol{p'})] \tag{4.24}$$

$$\text{Fig. 4.1(c)} = -h^3 \int \frac{\mathrm{d}\omega' \mathrm{d}^d\boldsymbol{p'}}{(2\pi)^{d+1}}\, \sigma_y\, G_0(\omega', \boldsymbol{p'})\, \sigma_y\, G_0(\omega', \boldsymbol{p'})\, \sigma_y\, D_0(\omega', \boldsymbol{p'}) \tag{4.25}$$

$$\begin{aligned}\text{Fig. 4.1(d,e)} = -h^4 \int \frac{\mathrm{d}\omega' \mathrm{d}^d\boldsymbol{p'}}{(2\pi)^{d+1}}\, &\sigma_y\, G_0(\omega', \boldsymbol{p'})\, \sigma_y\, D_0(\omega', \boldsymbol{p'}) \\ &\otimes \sigma_y \left[G_0(\omega', \boldsymbol{p'}) + G_0(-\omega', -\boldsymbol{p'})\right] \sigma_y\, D_0(\omega', \boldsymbol{p'})\end{aligned} \tag{4.26}$$

$$\text{Fig. 4.1(f)} = -g \int \frac{\mathrm{d}\omega' \mathrm{d}^d\boldsymbol{p'}}{(2\pi)^{d+1}}\, \mathrm{tr}[\sigma_y\, G_0(\omega', \boldsymbol{p'})]\, \sigma_y \tag{4.27}$$

$$\text{Fig. 4.1(b}') = g^2 \sigma_y \otimes \sigma_y \times [\text{Fig. 4.1(b)}]/h^2 \tag{4.28}$$

$$\text{Fig. 4.1(c}') = g^2 \sigma_y \otimes [\text{Fig. 4.1(c)}]_{D_0 \to 1/r}/h^3 = \text{Fig. 4.1(c}'') \tag{4.29}$$

In the expressions for Fig. 4.1(d,e) above, the replacement $D_0 \to 1/r$ when computing the renormalization constants in the 4-Fermi theory is implicit; the replacement is noted explicitly from the outset for the ϕ-reducible diagrams. In said diagrams, we have also recombined $h^2/r \to g$; the fact that this is always possible may also be seen as a first sanity check. The vertex renormalization condition is usually formulated at vanishing external 3-momentum. That we have done so from the outset requires further comment. In general, the momentum dependence of proper vertex functions will be non-analytic; as such, Taylor expansion in external 3-momenta is not mathematically well-defined. However, since we are working in $d = 2 + \epsilon > 2$, the loop integrals will be IR-finite and

---

used to compute the quoted β-function. However, since g is a dimensionless coupling, the coefficient $1/(4\pi)$ is expected to be universal at one-loop order. Primarily for reasons of academic curiosity, we shall arrive at the same β-function using a family of different regularization schemes to confirm this expected universality does hold.

as such continuous in the limit of vanishing external 3-momenta. Thus, it is sufficient for our purposes.

4.3.1 4-Fermi formulation

We begin with the 4-Fermi version of the theory, for the following reason: since the interaction vertex g is dimensionless (in other words, canonically marginal) at $d = 2$, the coefficient(s) of the β function is expected to be scheme-independent. Let us choose a 'field-theoretic' scheme, i.e., we integrate over all loop 3-momenta (modulo suppression of certain parts of momentum space due to regularization). Promoting all quantities in $\mathcal{L}_{\text{LY}}$ to bare ones – i.e., $g \to Z_g g, (\psi, \psi^\dagger) \to \sqrt{Z_\psi Z_\omega}(\psi, \psi^\dagger), \mathrm{d}\tau \to Z_\omega^{-1}\mathrm{d}\tau$, and $\partial_\tau \to Z_\omega \partial_\tau$ – and putting $Z = 1 + \delta Z$, we arrive at the counter-term Lagrangian

$$\begin{aligned}\mathcal{L}_{\text{L4F, C.T.}} = \psi^\dagger \left[(\delta Z_\omega + \delta Z_\psi)\, \partial_\tau + \delta Z_\psi d_a(-\mathrm{i}\boldsymbol{\partial})\, \sigma_a \right] \psi \\ - \frac{1}{2}\left(\delta g + 2g\delta Z_\psi + 3g\delta Z_\omega\right)\left(\psi^\dagger \sigma_y \psi\right)^2,\end{aligned} \tag{4.30}$$

with $\delta g := \delta Z_g g$ as per convention. Since the fermionic self-energy diagrams, Figs. 4.1(a) and (f), are tadpole graphs if ϕ is not a dynamical field, we have

$$\delta Z_\psi = \delta Z_\omega = 0. \tag{4.31}$$

To find δg, we need to evaluate Figs. 4.1(d,e,b′,c′,c″). For simplicity, we define the analytical continuation of the loop integrals to $d \neq 2$ by performing the spinor algebra and angular integration at fixed $d = 2$ and perform only the radial integration in d dimensions.

When regularizing the loop integrals, we leave the frequency integration untouched. The result is then essentially fixed by dimensional analysis; any pertinent one-loop 4-Fermi diagram $\mathcal{G}$ comes down to a momentum integral of the form

$$\mathcal{G} = \frac{a_{\mathcal{G}}\, g^2}{2(2\pi)^{1+\epsilon}} \int \frac{\mathrm{d}|\boldsymbol{p}|}{|\boldsymbol{p}|^{1-\epsilon}}. \tag{4.32}$$

Here, $a_{\mathcal{G}}$ is a diagram-dependent but regularization-independent numerical pre-factor (consisting of factors from symmetry, spinor algebra, and possible negative signs due to closed fermion loops). The $\boldsymbol{p}$-dependence of the integrand is constrained by rotational invariance to a $|\boldsymbol{p}|$-dependence; it is the only dimensionful constant that can come out of the frequency integration. The power of the denominator is fixed by comparing units: since g has units of (length)$^\epsilon$, $\mathcal{G}$ which renormalizes it should too.

The integral is UV-divergent, with superficial degree of divergence ϵ. We regularize it by multiplying the integral measure by a function f, to wit:

$$\int_{\text{reg.}} \mathrm{d}|\boldsymbol{p}| \cdots = \int_0^\infty \mathrm{d}|\boldsymbol{p}|\, f(|\boldsymbol{p}|/\Lambda) \cdots . \tag{4.33}$$

A change in the choice of f corresponds to a different choice of regularization. Substituting $u = |\boldsymbol{p}|/\Lambda$, we now arrive at

$$\mathcal{G} = \frac{a_{\mathcal{G}}\, g^2 \Lambda^\epsilon}{2(2\pi)^{1+\epsilon}} \int_0^\infty \frac{\mathrm{d}u\, f(u)}{u^{1-\epsilon}} =: \frac{a_{\mathcal{G}}\, g^2 \Lambda^\epsilon}{2(2\pi)^{1+\epsilon}} \frac{C_{\epsilon,f}}{\epsilon} \tag{4.34}$$

The regularization dependence now resides in the constant $C_{\epsilon,f}$. Let us quantify this more precisely. For the function f, we impose that (i) $f(u) = o(u^{-\epsilon})$ for $u \to \infty$, and (ii)

$f(u) \to 1$ for $u \to 0$. Property (i) is a necessary consequence of the fact that f should improve the UV-convergence of integrals. Property (ii) expresses that the IR-behaviour of a given loop integral is unchanged by the UV regularization. Both properties are obviously physically motivated. We can now estimate $C_{\epsilon,f}$ using integration by parts:

$$C_{\epsilon,f} = \int_0^\infty \mathrm{d}u\, f(u)\, \epsilon u^{\epsilon-1} = [f(u)u^\epsilon]_0^\infty - \int_0^\infty \mathrm{d}u\, f'(u)\, u^\epsilon \tag{4.35}$$

The first term vanishes for every ϵ at the upper limit due to property (i) and at the lower limit due to property (ii). The second term hence is the only one that survives, and yields[15] in the limit $\epsilon \to 0$: $C_{0,f} = f(0) = 1$. Thus, the regularization dependence drops out entirely in the limit $\epsilon \to 0$, and the β-function becomes one-loop universal as expected of a canonically marginal coupling. Note that when inserting the renormalization constant into the β-function, the $1/\epsilon$-pole cancels against the factor of ϵ coming from the scale derivative, to wit: $\mathrm{d}\Lambda^\epsilon/\mathrm{d}\ln\Lambda = \epsilon\Lambda^\epsilon$. A pedagogically interesting point is that working at finite (but small) ϵ ensured the loop integral only had one kind of divergence. In the present setting, the parameter $\epsilon > 0$ increases the spatial dimension, and as such leads to more divergent UV behaviour. However, IR divergences are cured. The regularization thus needs to introduce only one scale.[16] The absence of other dimensionful parameters in the theory then ensures that the loop integrands have a very obvious structure fixed entirely by dimensional analysis. A similar simplification will be exploited in Chap. 6, but there, ϵ will serve to *reduce* the spacetime dimension. The role of UV and IR will then be reversed, and the renormalization scale will enter through the need to regularize the IR behaviour, with the UV-finiteness guaranteed a priori.

Summing up the graph-dependent factors $a_{\mathcal{G}}$ and introducing the dimensionless 4-Fermi coupling $C_{\epsilon,f}\Lambda^\epsilon g/(2\pi)^\epsilon \mapsto g$, the β-function in $d = 2 + \epsilon$ dimensions reads as

$$\beta_g = -\epsilon g + \frac{g^2}{4\pi}. \tag{4.36}$$

4.3.2 Yukawa formulation

The renormalization in the Yukawa case is more involved. For one thing, it contains more dimensionful parameters, which means the final result is no longer completely determined by dimensional analysis. Furthermore, diagrams can have widely varying degrees of divergence, and they can occur both in the UV and the IR. To treat them on a level footing within a conceptually clean framework, we employ a 'mode-decimation' or 'Wilsonian' version of RG. At one-loop, it is sufficient to do so again at the level of the loop integration measure, similar to how we regularized the 4-Fermi loop integrals in a 'field-theoretic' manner. We thus set

$$\int_{\text{reg.}} \frac{\mathrm{d}\omega\,\mathrm{d}^d\boldsymbol{p}}{(2\pi)^{d+1}} \cdots = \int_{-\infty}^{\infty} \frac{\mathrm{d}\omega}{2\pi} \int \frac{\mathrm{d}^d\boldsymbol{p}}{(2\pi)^d}\, F(|\boldsymbol{p}|/k; l_{\mathrm{F}}, l_{\mathrm{B}})\, \Theta(\Lambda - |\boldsymbol{p}|) \cdots \tag{4.37}$$

The second factor, the Heaviside step function, simply imposes a UV cut-off. The factor F is to be chosen such that it suppresses IR modes below the RG scale k. We allow it to depend on the number of internal fermionic and bosonic lines l_{F}, l_{B} (essentially, so that it can mimick the effect of a momentum-dependent mass on an operative level). Note that the the integration over Matsubara frequencies is left unrestricted, as is common in non-relativistic field theories. To complete the specification of the RG scheme, we need to define the renormalization constants. We define the renormalized fields and couplings as

---

[15] The derivative may need to be interpreted in a weak sense, e.g., if $f(u) = \Theta(1-u)$ (commonly referred to as 'sharp cut-off').

[16] By contrast, at critical dimensions – both upper and lower – both UV and IR divergences are present, and one needs at least *two* dimensionful parameters.

$$\Gamma_k[\Phi; X; \tau] \simeq S\Big[Z_{\Phi,k}^{1/2} Z_\omega^{1/2} \Phi; X_k; Z_\omega^{-1} \tau\Big], \tag{4.38}$$

i.e., the 1PI effective action computed with unrenormalized fields $\Phi = (\phi, \psi, \psi^\dagger)$ and couplings $X = (h, r, c)$ as input and with all fluctuation modes suppressed below the IR scale k should be equivalent to the classical action we started with, but evaluated at suitably renormalized fields and couplings. Note that the time coordinate also needs renormalization, due to the non-relativistic dispersion relation contained in the classical action; in the absence of Lorentz invariance, the classical value of the dynamical critical exponent is not protected against quantum corrections. The scheme outlined above essentially amounts to a 'quenched' approximation to one-loop exact RG schemes such as that of Ellwanger–Morris–Wetterich – instead of self-consistently inserting an ansatz for the 'average effective action', we instead feed in the classical action S and iterate once (see Sec. 2.2 for details); to first order in interactions, this is equivalent to the 'usual' loop expansion. Note also that throughout, the dependence on the UV cut-off Λ is notationally suppressed. This is justified, because for typical regulators, the evolution equation is local in k and the Λ-dependence drops out.

In Eq. (4.38) above, the symbol '$\simeq$' is there to remind us that the average effective action Γ_k should be expanded in fields and their derivatives, and only those terms should be kept which are already present in the classical action S. A subtlety arises in the form of the two diagrams Figs. 4.1(d) and (e). These are 1PI in both ϕ and ψ fields, and are furthermore canonically marginal; as such, they cannot be discarded outright. Their contribution can, however, be absorbed as an additional contribution to the Yukawa vertex by performing a Hubbard–Stratonovich transformation on the average effective action Γ_k (Janssen & Herbut 2017). In the context of mode decimation-inspired schemes, this is often called 'dynamical bosonization', since it corresponds to performing the transformation *after* the mode decimation step (Gies & Wetterich 2002; Floerchinger & Wetterich 2009). In field-theoretic language, it corresponds to a non-multiplicative renormalization of the ϕ field, as pointed out by Luperini & Rossi (1991) in the context of the $(1+1)$-dimensional Gross–Neveu model. If we denote by $\delta g_{\mathrm{box},k}$ the result of the 'box diagrams' 4.1(d) and (e), then the correction to the Yukawa vertex can be shown to amount to[17)]

$$h_k \to h_k + \frac{r}{2h} \delta g_{\mathrm{box},k}. \tag{4.39}$$

Evaluating the diagrams allows us to read off the pertinent renormalization constants, and thence the β-functions as $\beta_X = -k\partial_k X_k$ for the couplings $X = (h, r, c)$ as well as the anomalous dimensions $\eta_\Phi = -k\partial_k \ln Z_\Phi$ for the fields $\Phi = (\phi, \psi, \psi^\dagger)$. Finally, the running dynamical critical exponent is given by $z = 2 - \eta_\psi + k\partial_k \ln Z_\omega$. In general, it is expedient to evaluate the scale derivative *before* the loop integration. On an operative level, this simply amounts to evaluating the diagrams, but with the substitution

$$F(|\boldsymbol{p}|/k; l_\mathrm{F}, l_\mathrm{B}) \to \frac{|\boldsymbol{p}|}{k} F'(|\boldsymbol{p}|/k; l_\mathrm{F}, l_\mathrm{B}) \tag{4.40}$$

[17)] We are working within one-loop approximation; since $\delta g_{\mathrm{box},k}$ is formally already of one-loop order, the prefactor $r/2h$ contains no quantum corrections.

in the integral measure, with 'prime' denoting differentiating with respect to the first argument.

For our main calculations, we use the 'sharp' regularization

$$F_{\mathrm{sh}}(|\boldsymbol{p}|/k; l_{\mathrm{F}}, l_{\mathrm{B}}) = \Theta(|\boldsymbol{p}|/k - 1); \tag{4.41}$$

we shall later also study the use of a regulator that suppresses the IR modes more gradually, viz.,

$$F_{\mathrm{lin}}(|\boldsymbol{p}|/k; l_{\mathrm{F}}, l_{\mathrm{B}}) = \Theta(|\boldsymbol{p}|/k - 1) + \Theta(1 - |\boldsymbol{p}|/k)\left(|\boldsymbol{p}|^2/k^2\right)^{l_{\mathrm{F}}/2 + l_{\mathrm{B}}}. \tag{4.42}$$

This is meant to mimic linear regulators in FRG, which fulfil certain optimality criteria for RG flow in bosonic theories (Litim 2001). However, there are indications that it may be incompatible with a nearly point-like 4-Fermi vertex, which is the case close to the lower critical dimension (cf., e.g., Janssen & Herbut 2014, or Chap. 3 of this thesis). For the sharp regulator, the derivative is given by

$$F'_{\mathrm{sh}}(|\boldsymbol{p}|/k; l_{\mathrm{F}}, l_{\mathrm{B}}) = \delta(|\boldsymbol{p}|/k - 1). \tag{4.43}$$

In this case, all contributions to RG flow essentially come from a thin shell around the RG scale k. For this reason, it is common to refer to a scheme that uses a sharp cut-off as an IR regulator 'momentum-shell RG' (Herbut 2007; Sachdev 2010a). We now explicitly evaluate the Feynman diagrams 4.1(a)–(e) in sharp cut-off regularization:

$$-k\partial_k\,[\text{Fig. 4.1(a)}] = \frac{h^2}{k^{4-d}(2\pi)^d}\left[\frac{2\pi \mathrm{i}\omega\, k^2/c^2}{(1 + r/k^2 - k^2/c^2)^2} + \frac{\pi d_a(\boldsymbol{p})\,\sigma_a}{(1 + r/k^2 - k^2/c^2)^3}\right] \tag{4.44}$$

$$-k\partial_k\,[\text{Fig. 4.1(b)}] = \frac{h^2}{k^{4-d}(2\pi)^d}\left(\frac{\pi}{2k^2}\omega^2 + \pi\boldsymbol{p}^2 - 2\pi k^2\right) \tag{4.45}$$

$$-k\partial_k\,[\text{Fig. 4.1(c)}] = \frac{h^3\pi}{k^{4-d}(2\pi)^d}\,\frac{\sigma_y}{1 + r/k^2 + \sqrt{(1 + r/k^2)\,k^2/c^2}} \tag{4.46}$$

$$\begin{aligned} -k\partial_k\,[\text{Fig. 4.1(d,e)}] = {}& -\frac{h^4\pi}{k^{6-d}(2\pi)^d}\,\frac{\sigma_y \otimes \sigma_y}{(1 + r/k^2)^{3/2}\,(1 + r/k^2 - k^2/c^2)^3} \\ & \times \Big[\left(1 + r/k^2\right)^{5/2} - 5k^2/c^2\left(1 + r/k^2\right)^{3/2} \\ & \quad + 5k^3/c^3\left(1 + r/k^2\right) - k^5/c^5\Big] \end{aligned} \tag{4.47}$$

This now allows one to read off the β- and η-functions as well as the running dynamical critical exponent. Upon introducing dimensionless couplings as $r/k^2 \mapsto r$, $k^2/c^2 \mapsto 1/c^2$ and $(2\pi)^{-\epsilon}k^{-(2+\epsilon)}h^2 \mapsto h^2$ with $\epsilon = d - 2$ as usual, these take the form:

$$z = 2 - \frac{h^2}{4\pi}\left[\frac{1}{(1 + r - c^{-2})^3} - \frac{2c^{-2}}{(1 + r - c^{-2})^2}\right] \tag{4.48}$$

$$\eta_\phi = \frac{h^2}{4\pi} \tag{4.49}$$

$$\eta_\psi = \frac{h^2}{4\pi}\,\frac{1}{(1 + r - c^{-2})^3} \tag{4.50}$$

$$\beta_r = (2 - \eta_\phi)\,r - \frac{h^2}{2\pi} \tag{4.51}$$

$$\beta_{1/c^2} = (-2-\eta_\phi)\,\frac{1}{c^2} + \frac{h^2}{8\pi} \tag{4.52}$$

$$\begin{aligned}\beta_{h^2} = (2-\epsilon-\eta_\phi-2\eta_\psi)\,h^2 - \frac{h^4}{4\pi}\Bigg[&\frac{2}{1+r+c^{-1}(1+r)^{1/2}} \\ &- \frac{(1+r)^{5/2}-5c^{-2}(1+r)^{3/2}+5c^{-3}(1+r)-c^{-5}}{(1+r)^{3/2}(1+r-c^{-2})^3}\Bigg]\end{aligned} \tag{4.53}$$

4.4 Fixed-point analysis

We begin again with the 4-Fermi version of the theory. The only fixed-point condition then is that the right-hand side of Eq. (4.36) vanish. Apart from the Gaußian solution $g_{*,\mathrm{LSM}} = 0$, there is an interacting one at $g_{*,\mathrm{QCP}} = 4\pi\epsilon$. The labelling of the fixed points anticipate their physical content. Since $\beta_g'(g_{*,\mathrm{LSM}}) = -\epsilon < 0$, the associated fixed point is IR-attractive, and hence represents a stable phase of matter. Since all symmetries remain intact, it a semimetal – the Luttinger semimetal (LSM). On the other hand, we have $\beta_g'(g_{*,\mathrm{QCP}}) = \epsilon > 0$. The interacting fixed point is hence repulsive – since the theory space has no other directions, it is a quantum critical point (QCP). Furthermore, we can read off $\nu = 1/\epsilon$ for the quantum phase transition from the LSM to the SSB-induced insulator. We also note that, for kinematic reasons, there is no correction at one-loop to the dynamical critical exponent and the fermion anomalous dimension, $\eta_\psi, z-2 = \mathcal{O}(\epsilon^2)$.

The Luttinger–Yukawa theory requires to solve three equations, viz. for β_r, β_{1/c^2} and β_{h^2} [Eqs. (4.51), (4.52) and (4.53) respectively]. Obviously, there is again a Gaußian fixed point, $h_* = c_* = r_* = 0$. It is, however, *not* the LSM fixed point identified in the 4-Fermi theory, since it has too many IR-relevant directions. When searching for non-interacting fixed points, the equations (especially $\beta_{h^2} = 0$) contain complicated non-linear combinations of the unknown quantities. Let us make the simplifying assumption that $r_* \gg 1$. It can be motivated as follows: From a formal point of view, the boson anomalous dimension $\eta_\phi \to 2$ for $\epsilon \to 0$.[18] Since $\eta_\phi \sim h^2$ from Eq. (4.49), this implies $h_*^2 = \mathcal{O}(1)$ $(\epsilon \to 0)$ for both LSM and QCP. Now h_*^2 and r_* are both dimensionful, and as such their values depend on details of the regularization. However, their ratio $(h^2/r)_*$ is dimensionless, and should hence be scheme-independent at one-loop. Furthermore, from the Hubbard–Stratonovich transformation, we know it is equal to g_* and must therefore vanish for $\epsilon \to 0$, as demonstrated in the 4-Fermi analysis above. Hence, $r_* \to \infty$ for $\epsilon \to 0$, and we automatically enter the large-mass limit provided ϵ is small enough.

Let us now convert the heuristic picture above into a serious calculation. Expanding β_{h^2} in powers of $1/r$, we obtain[19]

$$\beta_{h^2} = (2-\epsilon)h^2 - \frac{h^4}{4\pi} - \frac{h^4}{4\pi r} + \mathcal{O}(1/r^2). \tag{4.54}$$

For convenience, we also rewrite using chain rule the β-function of r in terms of $1/r$ as follows:

$$\beta_{1/r} = -\left(2-\frac{h^2}{4\pi}\right)\frac{1}{r} + \frac{h^2}{2\pi}\frac{1}{r^2}. \tag{4.55}$$

---

[18] This itself follows from dimensional analysis. Due to 4-Fermi Gaußian power counting, one has $[\psi] = 1$ and thus on one hand $\langle\phi(0,\boldsymbol{x})\phi(0,\boldsymbol{y})\rangle \sim |\boldsymbol{x}-\boldsymbol{y}|^4$ (since ϕ is bilinear in ψ). On the other hand, this exponent is equal to $d+z-2+\eta_\phi$ per definitionem. Hence, $\eta_\phi = 2$, q.e.d.

[19] Note that β_r and β_{1/c^2} are independent of r and do not require further expansion.

As a first sanity check, we note using the product rule that

$$\beta_{h^2/r} = \frac{\beta_{h^2}}{r} - h^2\beta_{1/r} = -\epsilon\frac{h^2}{r} + \frac{1}{4\pi}\left(\frac{h^2}{r}\right)^2 , \tag{4.56}$$

in agreement with the calculation in the 4-Fermi theory. For $\epsilon > 0$, we can now read off two non-trivial fixed points

$$\text{LSM} : \left(r_{*,\text{LSM}}, 1/c^2_{*,\text{LSM}}, h^2_{*,\text{LSM}}\right) = \left(\infty, \frac{1}{4} - \frac{1}{16}\epsilon, 4\pi(2-\epsilon)\right) \tag{4.57}$$

$$\text{QCP} : \left(r_{*,\text{QCP}}, 1/c^2_{*,\text{QCP}}, h^2_{*,\text{QCP}}\right) = \left(\frac{1}{\epsilon}, \frac{1}{4} - \frac{1}{8}\epsilon, 8\pi(1-\epsilon)\right) \tag{4.58}$$

We have again chosen the labelling of the fixed points in anticipation of their correspondence to those found in the 4-Fermi theory above. The relation is easiest to check by studying the number of relevant directions. To do so, we form the stability matrix $(\partial_X \beta_{X'})|_{X,X'=\left(r_*,1/c^2_*,h^2_*\right)}$; the number of positive eigenvalues is then precisely the number of relevant directions. For the LSM, we find only negative eigenvalues, thus verifying its IR-stability. For the QCP, on the other hand, there is precisely only positive eigenvalue, $\lambda_+ = \epsilon + \mathcal{O}(\epsilon^2)$. Hence, the correlation length exponent is $\nu = 1/\lambda_+ = 1/\epsilon + \mathcal{O}(\epsilon^0)$. Note that one-loop universality for dimensionless quantitites is maintained, as we can now check explicitly: First, the fixed-point 4-Fermi coupling extracted from the Luttinger–Yukawa theory, $g^{(\mathcal{L}_{\text{LY}})}_{*,\text{QCP}} = (h^2/r)_{*,\text{QCP}} = 4\pi\epsilon$ agrees with the result found from field-theoretically renormalizing the 4-Fermi Lagrangian $\mathcal{L}_{\text{L4F}}$. Furthermore, the separatrix formed by the ray from LSM to the trivial fixed point at the origin, satisfies $(h^2/r)_{\text{c}} = 4\pi\epsilon$ for all (in particular also non-fixed-point) values of r. We remark in passing that the loop expansion in the Yukawa formulation is still controlled, even though the Yukawa vertex is of order one. This is because every higher-order 1PI graph must have an increasing number of boson lines, which allows the large boson mass to provide the necessary suppression.

4-Fermi superuniversality and regularization. Near their lower critical dimension and to one-loop order, some of the critical exponents of 4-Fermi theories are not only universal, but *superuniversal.* More precisely, the exponents $1/\nu$ as well as η_ψ and z are in fact independent of the concrete field content of the theory$^{20)}$. The exponents η_ψ and corrections to z is an obvious consequence of momentum conservation, since they require a non-vanishing momentum-dependence of the self-energy and at one-loop the only self-energy diagram is a tadpole graph. The superuniversality of $1/\nu$ is a consequence of the fact that the only non-vanishing β-functions, that of the 4-Fermi coupling(s), is given by a family of bilinear forms of the same coupling(s) (for a more detailed proof, see Gehring, Gies & Janssen 2015). It has, however, been observed that in Yukawa (also known as 'partially bosonized') formulation of the same theory, these relations are violated for the so-called linear regulator (cf., e.g., Janssen & Herbut 2014). We attempt to elucidate further the mechanism underlying this violation within the present set-up. To do so, it is sufficient to re-evaluate the scale derivative of the vacuum polarization diagram, $-k\partial_k$[Fig. 4.1(b)], but with the regulator F_{lin} instead of F_{sh}.$^{21)}$ More specifically, the

---

20) This statement is of course non-trivial for z only in the absence of Lorentz symmetry.

21) We also note that the (1 + 1)D Gross–Neveu theory can be treated within the current set-up if we modify the inverse fermionic propagator

$$\mathrm{i}\omega + d_a(\boldsymbol{p})\,\sigma_a \to p_i\sigma_i \tag{4.59}$$

anomalous dimension η_ϕ is fixed by the $\sim \boldsymbol{p}^2$ part of the diagram. We furthermore work to leading order in ϵ, where the dominant contribution arises when the scale derivative hits the power part of F_{lin}. We thus arrive at

$$\eta_\phi^{\text{lin}} \sim \left(\int_0^k \frac{\mathrm{d}|\boldsymbol{p}'|}{|\boldsymbol{p}'|^{1-\epsilon}} + \mathcal{O}(1) \right) \frac{h^4}{k^2} \sim \frac{h^4}{k^{2+\epsilon}} \left(\frac{1}{\epsilon} + \mathcal{O}(1) \right). \tag{4.61}$$

Let us now use the fact that we are only interested in fixed points that recover 4-Fermi canonical power-counting in the $\epsilon \to 0$ limit. This is equivalent to requiring that $\eta_\phi = 2 + \mathcal{O}(\epsilon)$ (see the discussion in Footnote $^{18)}$). This, however, when combined with the leading-order behaviour of η_ϕ^{lin} above, implies

$$h^2_{*,\text{QCP}}\big|_{\text{lin}} = \mathcal{O}(\epsilon). \tag{4.62}$$

On the other hand, the ratio h^2/r, being canonically dimensionless, has to show the same one-loop universal $\mathcal{O}(\epsilon)$ behaviour as in the case of the sharp cut-off. Hence, $r_{*,\text{QCP}} = \mathcal{O}(1)$. Thus, the physics will not be that of a point-like 4-Fermi vertex, but instead that of a weakly coupled Yukawa theory. This fact is at the heart of superuniversality violation. As an example, for finite r, the dynamics of the ϕ-field is no longer effectively frozen – the fermion self-energy diagram Fig. 4.1(a) is then no longer effectively a tadpole; the lack of this kinematic obstruction means η_ψ and quantum corrections to z are generically $\mathcal{O}(\epsilon)$. On the other hand, if r_* is large enough – at least $\mathcal{O}(1/\epsilon)$, as is the case with the sharp cut-off – then $z - 2 = \mathcal{O}(1/r^3)$ and $\eta_\psi = \mathcal{O}(1/r^2)$ from Eqs. (4.48) and (4.50) respectively and hence vanish to first order in ϵ, in agreement with the expectation from the tadpole nature of the fermion self-energy graph in the 4-Fermi theory.

To summarize, at the lower critical dimension, the suppression of IR modes by the linear cut-off is too slow to adequately regularize the IR divergences arising from the gapless nature of the fermionic excitations. Intuitively, these are the same divergences that are physically responsible for ‘asymptotic freedom’ in 4-Fermi theories at the lower critical dimension: the IR divergences are so violent that already at arbitrarily small 4-Fermi interactions, Nature prefers a ground state that spontaneously breaks some symmetry and in doing so cures said divergences (e.g., by gapping out the fermion spectrum). Precisely what constitutes an ‘optimal’ regulator may be worth revisiting in the context of fermionic theories near their lower (in the 4-Fermi sense) critical dimension. As far as this work is concerned, we shall restrict ourselves to making predictions using the sharp regularization scheme, being both analytically tractable and compatible with superuniversality.

Boson anomalous dimension. We close this section by computing the leading correction to η_ϕ, working again in the ‘sharp’ regularization scheme F_{sh} (however, we suppress the analogous superscript ‘sh’ for brevity). We find upon inserting

$$\eta_\phi|_{\text{LSM}} = 2 - \epsilon, \tag{4.63}$$

$$\eta_\phi|_{\text{QCP}} = 2 - 2\epsilon. \tag{4.64}$$

---

where $(p_i) = \boldsymbol{p}$ and $(\sigma_i) = (\sigma_z, \sigma_x)$; to complete the implementation of the dimensional reduction, we also need a suitably modified prescription for $\int_{\text{reg.}}$ in Eq. (4.37), to wit:

$$F_{\text{lin}}(\boldsymbol{p}/k) \to \delta(\omega) F_{\text{lin}}(\boldsymbol{p}/k). \tag{4.60}$$

At the LSM fixed point, all higher orders vanish, since the boson mass is infinite. To all loop orders, the LSM $\eta_\phi|_{\mathrm{LSM}}$ hence satisfies $d + z - 2 + \eta_\phi = 4[\psi]$ where $[\psi] = d/2$ is the canonical dimension of the fermion field; η_ϕ is hence merely that what is required to change the scaling dimension of the ϕ-field from its canonical value to the one compatible with fermionic canonical power counting, $[\phi] \to 2[\psi]$. On the other hand, $\eta_\phi|_{\mathrm{QCP}}$ at $\mathcal{O}(\epsilon)$ deviates from canonical scaling and is a true quantum correction.

4.5 Non-mean-field behaviour

Unlike usual ϵ expansions, the physical case of interest corresponds to sending $\epsilon \to 0$. As illustrated in Fig. 4.2, in this limit, the QCP and LSM fixed points collide.[22] This raises the question regarding to what extent the scaling one would observe at such a transition deviates from simple dimensional analysis. Indeed, as far as observables such as order-parameter correlation functions and the expectation value in an external field is concerned, there is in fact no difference. Certain observables like the correlation length and order parameter expectation value show essential singularities. However, such a behaviour also arises generically in mean-field theory. We shall show by explicit computation that the exponent of the leading singularity of the order parameter expectation value is different from the mean-field theory prediction by a factor of 2 (Subsec. 4.5.1). Finally, the susceptibility turns out to be an observable that shows power law behaviour but cannot be derived simply from dimensional analysis, because the exponent becomes indeterminate; we shall show that by computing it first in $2 + \epsilon$ dimensions first and then letting $\epsilon \to 0$ gives a well-defined answer which is not mean-field but still exact (Subsec. 4.5.2).

4.5.1 Order-parameter expectation value

The effective potential is the effective action evaluated at constant values, to wit: $V_{\mathrm{eff}}(\phi)\mathcal{V} = \Gamma[\phi]|_{\phi=\mathrm{const.}}$ where $\mathcal{V}$ is the spacetime volume. The quantum equation of motion, $\delta\Gamma/\delta\phi = 0$, for constant fields translates to the condition

$$V'_{\mathrm{eff}}(\langle\phi\rangle) = 0 \tag{4.65}$$

for the vev $\langle\phi\rangle$. Since we already have anomalous dimensions and β-functions at hand, it is most expedient to compute it using the Callan–Symanzik equation[23]

$$\left(\Lambda\frac{\partial}{\partial\Lambda} - \gamma_{h^2} h^2 \frac{\partial}{\partial h^2} - \gamma_r r \frac{\partial}{\partial r} - \frac{1}{2}\eta_\phi \phi \frac{\partial}{\partial\phi}\right) V_{\mathrm{eff}}(\phi) = 0. \tag{4.66}$$

Here, Λ is the UV cut-off and $\gamma_X = \beta_X/X - [X]$ describes the 'anomalous' scaling of the coupling, while η_ϕ is the anomalous dimension of the field ϕ as before. Let us

---

[22] Let us note in passing that a collision of fixed points appears generically in gauge theories, where they usually disappear into the complex plane after the collision (Halperin *et al.* 1974; Gies & Jaeckel 2006; Kaplan *et al.* 2009; Braun *et al.* 2014; Herbut & Janssen 2014; Nahum *et al.* 2015; Janssen 2016; Herbut 2016; Janssen & Herbut 2017; Ihrig *et al.* 2019; Faedo *et al.* 2020). A collision of fixed points can also occur in systems without gauge invariance, with and without fixed-point complexification (Gehring, Gies & Janssen 2015; Janssen & Herbut 2016a; Gorbenko, Rychkov & Zan 2018a,b; Roscher & Herbut 2018; Gracey, Herbut & Roscher 2018).

[23] See, for instance, Schwartz (2014).

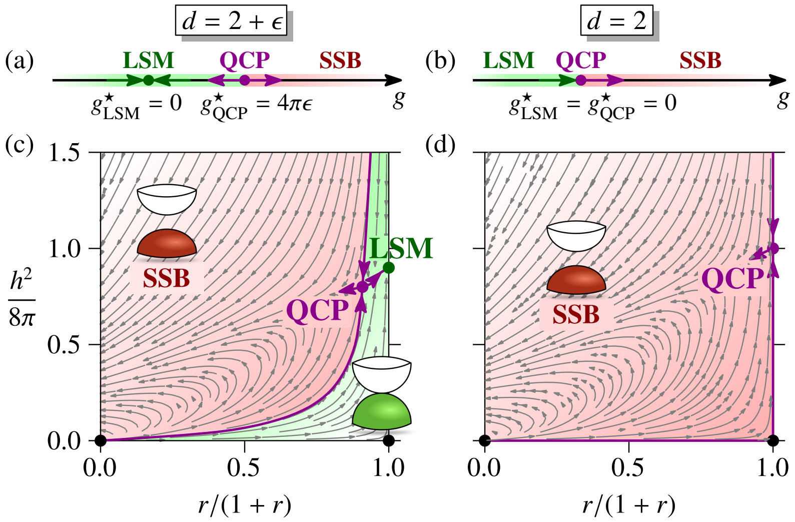

Figure 4.2: RG flow in the 4-Fermi theory (a,b) and the Luttinger–Yukawa theory for $c = c_*(d = 2)$ (c,d) in $d = 2 + \epsilon$ (a,c) and $d = 2$ (b,d) dimensions. The two fixed points at $g_{*,\text{LSM}} = 0$ and $g_{*,\text{QCP}} = 4\pi\epsilon$ in the 4-Fermi theory correspond to the non-Gaußian fixed points denoted as LSM and QCP, respectively, in the Luttinger-Yukawa model. For $\epsilon \to 0$, the two fixed points approach each other in both theories.

quickly recapitulate the ingredients appearing in the Callan–Symanzik recipe in the limit $h^2/r \ll 1$:

$$\eta_\phi = \frac{h^2}{4\pi\Lambda^2} \equiv \eta_\phi^{\text{MF}}, \tag{4.67}$$

$$\gamma_r = -\frac{h^2}{4\pi\Lambda^2} - \frac{h^2}{2\pi r} \equiv \gamma_r^{\text{MF}}, \tag{4.68}$$

$$\gamma_{h^2} = -\frac{h^2}{4\pi\Lambda^2} - \frac{h^2}{4\pi r} \equiv \gamma_{h^2}^{\text{MF}} - \frac{h^2}{4\pi r}. \tag{4.69}$$

For future reference, we have split the contributions further into two parts: those coming from (i) diagrams without internal ϕ-lines (hence mean-field, 'MF') – i.e., the vacuum polarization diagram Fig. 4.1(a) – and (ii) diagrams with virtual ϕ-bosons, which would not survive in the mean-field limit. The latter concerns the last term in γ_{h^2}, and is given by the sum of the triangle diagram [Fig. 4.1(c)] and the bosonization of the box diagrams [Figs. 4.1(d) and (e)].

To complete the set-up, let us recall the structure of the full effective potential to all loop orders, which is given by

$$V_{\text{eff}}(\phi) = \frac{h^2\phi^2}{2h^2/r} \sum_{n=0}^{\infty} \sum_{m \leqslant n} C_{n,m} \left(\frac{1}{16\pi}\frac{h^2}{r}\right)^n \left(\ln\frac{h^2\phi^2}{4\Lambda^4}\right)^m. \tag{4.70}$$

(This is essentially a consequence of Collins' theorem.) Formally, the contributions at fixed n arise from n-loop vacuum diagrams. However, even to leading order in h^2/r, observables such as the vacuum expectation value $\langle\phi\rangle$ are sensitive to so-called 'leading logarithms' (i.e., those terms with $m = n$ in the series above). Thankfully, these contributions (including higher-loop ones, i.e., $n \geqslant 2$) are fixed *entirely* by the one-loop RG functions.(24)

---

(24) We refer again to standard textbooks such as that of Schwartz (2014) for the demonstration.

Hence, in addition to the one-loop coefficients $C_{1,0}$ and $C_{1,1}$, we can compute all coefficients $C_{n,n}$ for arbitrary n by inserting the initial 'seed' $C_{0,0} = 1$ obtained by matching to the classical potential $V_{\text{cl}}(\phi) = r\phi^2/2 = h^2\phi^2/(2h^2/r)$ into the Callan–Symanzik equation [Eq. (4.66)] and iterating using the one-loop RG functions above. For the one-loop contribution to the effective potential, we thus obtain $C_{1,1} = 2$ and $C_{1,0} = -2$. Writing out explicitly, it reads as

$$V_{\text{eff}}^{(n\leqslant 1)}(\phi) = \frac{r}{2}\phi^2 + \frac{h^2\phi^2}{16\pi}\left(\ln\frac{h^2\phi^2}{4\Lambda^4} - 1\right) = V_{\text{eff}}^{\text{MF}}(\phi). \tag{4.71}$$

The last equality expresses the fact that the one-loop effective potential is the same regardless of whether one computes it with the mean-field version of the RG functions or the full version. We may use Eq. (4.71) above to derive the mean-field expectation value of ϕ,

$$h\langle\phi\rangle_{\text{MF}} = \Lambda^2\,\mathrm{e}^{-4\pi/g}. \tag{4.72}$$

This agrees with the computation of Sun *et al.* (2009), and we shall require this result to compare with the quantum value which also incorporates order-parameter fluctuations. The latter corrections may be expected to be particularly important in the present setting, since the spinor space is as small as algebraically permissible (recall that mean-field theory becomes exact in the limit of infinitely many flavours). Interating for the higher $C_{n,n}$ coefficients, we find $C_{2,2} = C_{1,1}/2 = 1$, which goes beyond the mean-field level. Remarkably, all further leading logarithms vanish in this theory: $C_{n,n} = 0\;\forall n \geqslant 3$. Thus, the effective potential given by

$$V_{\text{eff}}(\phi) = \frac{h^2\phi^2}{2h^2/r}\left[1 + \frac{h^2/r}{8\pi}\left(\ln\frac{h^2\phi^2}{4\Lambda^4} - 1\right) + \left(\frac{h^2/r}{16\pi}\ln\frac{h^2\phi^2}{4\Lambda^4}\right)^2\right] \tag{4.73}$$

includes leading logarithms to all loops and subleading logarithms to one loop. Minimizing (4.73) with respect to ϕ yields

$$h\langle\phi\rangle = \Lambda^2\,\mathrm{e}^{-8\pi/g}. \tag{4.74}$$

As advertised, the exponent is twice as large as in mean-field theory.

Dimensional transmutation. To conclude this subsection, we interpret the above result in terms of *dimensional transmutation.* This concept was originally introduced in the context of massless scalar electrodynamics by Coleman & Weinberg (1973), and refers to 'trad(ing) a dimensionless parameter … on which physical quantities can depend in a complicated way, for a dimensional one … on which physical quantities must depend in a trivial way, governed by dimensional analysis.' In the present 4-Fermi setting, the dimensionless parameter is the 4-Fermi coupling g. A natural candidate for the dimensionful parameter is k_{SSB}, the scale at which the running 4-Fermi hits a pole; by explicitly integrating the RG flow, it works out to $k_{\text{SSB}} = \Lambda\,\mathrm{e}^{-4\pi/g}$. Comparing with Eq. (4.74), we indeed find that

$$\langle\psi^\dagger\sigma_y\psi\rangle \sim (k_{\text{SSB}})^{2[\psi]}\,, \tag{4.75}$$

in agreement with dimensional transmutation. [Note on the other hand that the mean-field result (4.72) violates dimensional transmutation due to the missing order-parameter fluctuations.] A similar observable is the scaling of the free energy near criticality; in our set-up, it simply corresponds to the effective potential evaluated at the vev, $V_{\text{eff}}(\langle\phi\rangle)$. It is readily obtained by inserting Eq. (4.74) into Eq. (4.73) and yields

$$V_{\text{eff}}(\langle\phi\rangle) \propto \Lambda^4 \, \mathrm{e}^{-16\pi/g} \sim (k_{\text{SSB}})^{d+z} \,, \tag{4.76}$$

which furnishes a further test for dimensional transmutation.

4.5.2 Susceptibility exponent

Unlike the observables considered in the previous section, the power-law behaviour of the susceptibility $\chi \propto (\delta g)^{-\gamma}$ survives the fixed-point collision. Assuming hyperscaling,[25] we may use Fisher's scaling law $\gamma = (2 - \eta_\phi)\,\nu$. Working directly in $d = 2$ and using $\eta_\phi = 2$ (as dictated by dimensional analysis) and $\nu = \infty$ (representing the essential singularity) yields a formally indeterminate '$0 \times \infty$'. However, working in $d = 2 + \epsilon$ and using $\eta_{\phi,\text{QCP}} = 2 - 2\epsilon$ and $\nu = 1/\epsilon$ yields $\gamma = 2 + \mathcal{O}(\epsilon)$.

To appreciate that this is truly a quantum result, consider the result of using instead a mean-field η_ϕ in place of the true quantum value. Since it coincides with canonical power counting in the 4-Fermi sense, we do not need a separate calculation, but can simply use dimensional analysis in the form $d + z - 2 + \eta_{\phi,\text{MF}} = 4[\psi]$. With $d = 2 + \epsilon$, $z = 2 + \mathcal{O}(\epsilon^2)$ and $[\psi] = 1 + \epsilon/2 + \mathcal{O}(\epsilon^2)$ [since $\eta_\psi = \mathcal{O}(\epsilon^2)$], it follows that $\eta_{\phi,\text{MF}} = 2 - \epsilon$, whence $\gamma_{\text{MF}} = 1 + \mathcal{O}(\epsilon)$. We thus see that the susceptibility exponent contains physics beyond mean-field theory. Just as importantly, although fluctuation effects at one-loop survive the fixed-point collision for $\epsilon \to 0$, higher-order corrections vanish. The final result at the physical number of dimensions $d = 2$ reads as

$$\gamma = 2, \tag{4.77}$$

and is *one-loop exact.*

We close this subsection by noting the somewhat curious fact that $\gamma = 2\gamma_{\text{MF}}$. There is hence the same mismatch by a factor of 2 in the exponent between mean-field theory and the correct result, as we found previously for the vacuum expectation value. Whether this is a coincidence or contains a deeper connection is left for future investigation.

4.6 Bottom-up construction: Spinless fermions on kagome lattice

Thus far, we have studied the universal physics emerging in the IR within a low-energy effective field theory. In this section, we shall now turn our attention to an explicit microscopic realization. To this end, we shall study an extended t–V model for spinless fermions on the kagome lattice. In Subsec. 4.6.1, we shall show that the tight-binding dispersion features a QBT that is rotationally invariant and can be made particle-hole symmetric for suitably chosen hopping ratios. The exercise of projecting the tight-binding

---

[25] If we accept dimensional transmutation (whose validity we checked explicitly for two observables in Subsec. 4.5.1), hyperscaling follows as a trivial consequence of $[\xi] = -1$ and $[V_{\text{eff}}] = d + z$. Our argument ultimately does not rest on hyperscaling directly at $d = 2$, but rather at small but finite $\epsilon = d - 2$. In the latter case, the fact that the fixed point QCP governing the transition has precisely one relevant direction is sufficient to guarantee hyperscaling (cf., e.g, Herbut 2007). The critical exponent we derive for the susceptibility χ will turn out to have a regular $\epsilon \to 0$-limit, implying the survival of the power law (modulo subleading logarithmic corrections).

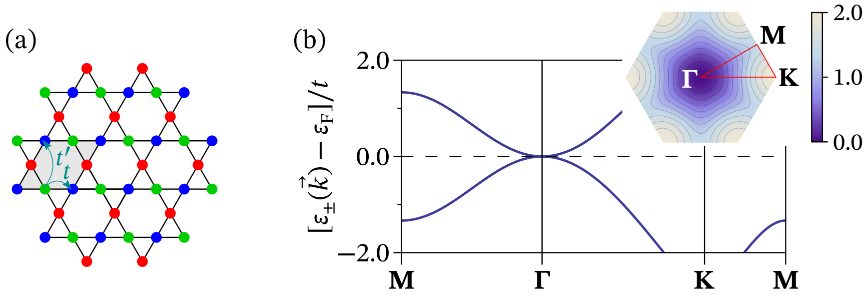

Figure 4.3: (a) Kagome lattice. The unit cell (shaded rhombus) consists of three sites (red, green, and blue dots). (b) Spectrum of the tight-binding Hamiltonian H_0 (for $t' = -t/3$) along high-symmetry lines, displaying the quadratic band touching point at the center of the Brillouin zone. The dashed line denotes the Fermi level for 2/3-filling (1/3-filling) for $t > 0$ ($t < 0$). Inset: Conduction-band dispersion in the first Brillouin zone (color plot) and path used in the main panel (red line).

model down to the universal single-particle Hamiltonian will also provide us with a mapping between the fermionic operators on the lattice and the low-energy spinor degrees of freedom appearing thus far in the low-energy effective field theories. This knowledge can be used to match microscopic short-ranged interactions to the UV initial condition for the 4-Fermi interaction, which we shall do explicitly for nearest and next-to-nearest neighbour extended Hubbard interactions in Subsec. 4.6.2. To finish our study, we shall finally elucidate the fate of small deviations from the particle-hole symmetric point by a two-loop self-energy calculation (Subsec. 4.6.3).

4.6.1 Tight-binding dispersion

The tight-binding Hamiltonian including up to next-nearest hopping is given by

$$H_0 = -t \sum_{\langle ij \rangle} c_i^\dagger c_j - t' \sum_{\langle\langle ij \rangle\rangle} c_i^\dagger c_j + \text{H.c.} \tag{4.78}$$

where t (t') is the hopping amplitude for nearest (next-nearest) neighbours $\langle ij \rangle$ ($\langle\langle ij \rangle\rangle$) on the kagome lattice, and c_i ($c_i^\dagger$) annihilates (creates) a fermion at site i [see Fig. 4.3(a)]. In momentum space, it can be written as

$$H_0 = \int_{\boldsymbol{p} \in \mathrm{BZ}} \frac{\mathrm{d}^2 \boldsymbol{p}}{(2\pi)^2} \Psi^\dagger(\boldsymbol{p}) \, \mathscr{H}_0(\boldsymbol{p}) \, \Psi(\boldsymbol{p}), \tag{4.79}$$

where the momentum integration is to be performed over the first Brillouin zone (BZ). The fermion operators on the sublattices A, B, and C are collected into a three-component vector $\Psi^\dagger(\boldsymbol{p}) = \left(c_\mathrm{A}^\dagger(\boldsymbol{p}), c_\mathrm{B}^\dagger(\boldsymbol{p}), c_\mathrm{C}^\dagger(\boldsymbol{p})\right)$; $\mathscr{H}_0(\boldsymbol{p})$ is a 3×3 matrix acting in this space for every $\boldsymbol{p} \in \mathrm{BZ}$, whose non-vanishing entries are given by

$$\mathscr{H}_0^{12}(\boldsymbol{p}) = \mathscr{H}_0^{21}(\boldsymbol{p}) = 2t\cos(\boldsymbol{\delta}_\mathrm{AB} \cdot \boldsymbol{p}) + 2t' \cos(\boldsymbol{\delta}'_\mathrm{AB} \cdot \boldsymbol{p}) \tag{4.80}$$

$$\mathscr{H}_0^{13}(\boldsymbol{p}) = \mathscr{H}_0^{31}(\boldsymbol{p}) = 2t\cos(\boldsymbol{\delta}_\mathrm{AC} \cdot \boldsymbol{p}) + 2t' \cos(\boldsymbol{\delta}'_\mathrm{AC} \cdot \boldsymbol{p}) \tag{4.81}$$

$$\mathscr{H}_0^{23}(\boldsymbol{p}) = \mathscr{H}_0^{32}(\boldsymbol{p}) = 2t\cos(\boldsymbol{\delta}_\mathrm{BC} \cdot \boldsymbol{p}) + 2t' \cos(\boldsymbol{\delta}'_\mathrm{BC} \cdot \boldsymbol{p}). \tag{4.82}$$

In the above, $\boldsymbol{\delta}_\mathrm{AB}$ ($\boldsymbol{\delta}'_\mathrm{AB}$) denotes the (next-)nearest neighbour displacement vectors between A and B atoms, and likewise for AC and BC. Explicitly, these may be written as

$$\boldsymbol{\delta}_\mathrm{AB} = \frac{1}{2}\left(1, -\sqrt{3}\right)^\top \qquad \boldsymbol{\delta}_\mathrm{BC} = \frac{1}{2}\left(1, \sqrt{3}\right)^\top \qquad \boldsymbol{\delta}_\mathrm{AC} = (1, 0)^\top \tag{4.83}$$

$$\boldsymbol{\delta}'_{\mathrm{AB}} = \frac{1}{2}\left(3, \sqrt{3}\right)^\top \qquad \boldsymbol{\delta}'_{\mathrm{BC}} = \frac{1}{2}\left(3, -\sqrt{3}\right)^\top \qquad \boldsymbol{\delta}'_{\mathrm{AC}} = (0,3)^\top \tag{4.84}$$

with the lattice constant set to unity for notational convenience. Anticipating the QBT point to be located at $\boldsymbol{p} = 0$, we may expand $\mathscr{H}_0(\boldsymbol{p})$ for small momenta. To zeroth order, this leads to the eigenvalues

$$\varepsilon_{1,2}(\boldsymbol{p}) = 2t\left(1 + t'/t\right) + \mathcal{O}(\boldsymbol{p}^2), \tag{4.85}$$

$$\varepsilon_3(\boldsymbol{p}) = -4t\left(1 + t'/t\right) + \mathcal{O}(\boldsymbol{p}^2). \tag{4.86}$$

The degenerate pair is simply the manifestation of the band crossing at zero momentum. Its eigenspace – henceforth referred to as the low-energy subspace – can be spanned for instance by

$$u_1 = \left(\sqrt{1/6}, -\sqrt{2/3}, \sqrt{1/6}\right)^\top, \tag{4.87}$$

$$u_2 = \left(-\sqrt{1/2}, 0, \sqrt{1/2}\right)^\top. \tag{4.88}$$

Given the eigenbasis, we may now construct the projector $\mathcal{P}$ onto the low-energy subspace in usual fashion as a sum of dyads, to wit:

$$\mathcal{P} = u_1 u_1^\top + u_2 u_2^\top. \tag{4.89}$$

The third eigenvector at $\boldsymbol{p} = 0$ is given by

$$u_3 = \left(\sqrt{1/3}, \sqrt{1/3}, \sqrt{1/3}\right)^\top. \tag{4.90}$$

The orthogonal transformation which diagonalizes $\mathscr{H}_0(\boldsymbol{p} = 0)$ can now be constructed from the three eigenvectors as

$$\mathcal{U} = (u_1, u_2, u_3)\,. \tag{4.91}$$

Since the low-energy subspace and its complement are clearly separated, we can perform a Schrieffer–Wolff transformation to obtain the low-energy content of H_0 up to order $\mathcal{O}(\boldsymbol{p}^2)$ by first expanding $\mathscr{H}_0(\boldsymbol{p})$ to $\mathcal{O}(\boldsymbol{p}^2)$, then projecting onto the low-energy subspace using $\mathcal{P}$, and finally blockdiagonalizing using $\mathcal{U}$, to wit:[26]

$$H_0 = \int_{\boldsymbol{p}} \psi^\dagger(\boldsymbol{p})\, \mathcal{H}_0(\boldsymbol{p})\, \psi(\boldsymbol{p}) + \cdots \tag{4.92}$$

$$\begin{pmatrix} \mathcal{H}_0(\boldsymbol{p}) & 0 \\ 0 & 0 \end{pmatrix} = \frac{1}{2}\mathcal{U}^\dagger \mathcal{P}\left[(\partial_\kappa)^2\, \mathscr{H}_0(\kappa\boldsymbol{p})\right]_{\kappa\to 0} \mathcal{P}\mathcal{U}. \tag{4.93}$$

$$\psi_i = u_i^j\, \Psi_j \qquad (i = 1,2) \tag{4.94}$$

The ellipsis has been used to suppress terms that are (i) bilinears from the high-energy subspace and (ii) constant energy shifts within the low-energy subspace. (Note that terms at $\mathcal{O}(|\boldsymbol{p}|)$ vanish due to the C_6 symmetry of the kagome lattice.) Evaluating the above expression for $\mathcal{H}_0(\boldsymbol{p})$ yields

$$\mathcal{H}_0(\boldsymbol{p}) = \begin{pmatrix} tp_x^2 + 3t'p_y^2 & (t - 3t')p_x p_y \\ (t - 3t')p_x p_y & 3t'p_x^2 + tp_y^2 \end{pmatrix} = \frac{1}{2}(t - 3t')\, d_a(\boldsymbol{p})\, \sigma_a + \frac{1}{2}(t + 3t')\boldsymbol{p}^2 \mathbb{1}_2. \tag{4.95}$$

---

[26] The reader is referred to Bravyi, DiVincenzo & Loss (2011) for details of the proof as well as an analysis of the limits in which this is a good approximation.

The offending piece is the last term $\propto \mathbb{1}_2$, since it generates particle-hole asymmetry.[27)] In order to arrange for it to vanish, we need to impose $t'/t = -1/3$. At the particle-hole symmetric point, the single-particle Hamiltonian matches precisely that of the low-energy effective field theory, up to a global factor of t. This is to some extent a happy accident: in the generic case, the single-particle Hamiltonian defined by Eq. (4.93) may incur an additional rotation of the σ_a basis, which would then have to be compensated by a suitable redefinition of ψ. In the present case, however, Eq. (4.94) is sufficient. For future reference, let us quote the inverse mapping explicitly in the following form:

$$\begin{pmatrix} c_{\mathrm{A}} \\ c_{\mathrm{B}} \\ c_{\mathrm{C}} \end{pmatrix} = \begin{pmatrix} \frac{1}{\sqrt{6}} & -\frac{1}{\sqrt{2}} \\ -\sqrt{\frac{2}{3}} & 0 \\ \frac{1}{\sqrt{6}} & \frac{1}{\sqrt{2}} \end{pmatrix} \begin{pmatrix} \psi_1 \\ \psi_2 \end{pmatrix} \tag{4.96}$$

4.6.2 From Hubbard to Fermi

To complete the study of the microscopic realization on the Kagome lattice, we need to match the Hubbard-like interactions to their low-energy 4-Fermi counterpart. We shall consider explicitly the nearest and next-nearest neighbour interactions

$$H_{\mathrm{int}} = V \sum_{\langle ij \rangle} c_i^\dagger c_i c_j^\dagger c_j + V' \sum_{\langle\langle ij \rangle\rangle} c_i^\dagger c_i c_j^\dagger c_j . \tag{4.97}$$

(Note that since we are working with spinless fermions, there is no on-site Hubbard interaction.) To leading order in gradient expansion, these are contact terms, since (second-)nearest neighboring sites belong to different sublattices. We thus find for the low-energy content of H_{int} in the continuum limit

$$\begin{aligned} H_{\mathrm{int}} = 2(V+V') \int_{\boldsymbol{x}} \Big[& c_{\mathrm{A}}^\dagger(\boldsymbol{x})\, c_{\mathrm{A}}(\boldsymbol{x})\, c_{\mathrm{B}}^\dagger(\boldsymbol{x})\, c_{\mathrm{B}}(\boldsymbol{x}) + c_{\mathrm{A}}^\dagger(\boldsymbol{x})\, c_{\mathrm{A}}(\boldsymbol{x})\, c_{\mathrm{C}}^\dagger(\boldsymbol{x})\, c_{\mathrm{A}}(\boldsymbol{x}) \\ & + c_{\mathrm{B}}^\dagger(\boldsymbol{x})\, c_{\mathrm{B}}(\boldsymbol{x})\, c_{\mathrm{C}}^\dagger(\boldsymbol{x})\, c_{\mathrm{C}}(\boldsymbol{x}) \Big] + \mathcal{O}(\partial c(\boldsymbol{x})) \end{aligned} \tag{4.98}$$

where $c_{\mathrm{A}}^\dagger(\boldsymbol{x})$ creates a particle in the sublattice A at position $\boldsymbol{x}$, and analogously for the sublattices B and C. Using Eq. (4.96), we can rewrite these in terms of the spinor $\psi = (\psi_1, \psi_2)^\top$ appearing in the low-energy theory. This yields

$$\begin{aligned} H_{\mathrm{int}} &= 2(V+V') \int_{\boldsymbol{x}} \psi_1^\dagger(\boldsymbol{x})\psi_1(\boldsymbol{x})\psi_2^\dagger(\boldsymbol{x})\psi_2(\boldsymbol{x}) && (4.99) \\ &= -2(V+V') \int_{\boldsymbol{x}} \frac{1}{2} \left(\psi^\dagger(\boldsymbol{x})\sigma_y\psi(\boldsymbol{x})\right)^2 . && (4.100) \end{aligned}$$

To complete the matching, we need to recall that the single-particle Hamiltonian $\mathcal{H}_0(\boldsymbol{p})$ derived microscopically had a global factor of t. The universal theory was defined with the factor of the kinetic term normalized to unity. The most efficient way to absorb this factor is by rescaling the Euclidean time as $\tau \to \tau t$. Physically, it corresponds to measuring temperatures (and energies) in units of t. For the 4-Fermi interaction, this implies $g(\Lambda) = 2(V+V')/t$. Satisfyingly, this is a dimensionless quantity, which maps nicely to the power-counting we did in the top-down construction.

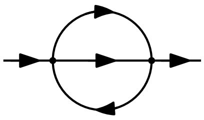

Figure 4.4: Two-loop self-energy contributing to the flow of particle-hole asymmetry α.

4.6.3 Fate of particle-hole asymmetry

The universal theory we worked with in this chapter had particle-hole symmetry. However, as we saw in Subsec. 4.6.1, this is subject to tuning the ratio of hopping amplitudes t'/t at the microscopic level. Since any experimental set-up has uncertainties, this naturally raises the question whether the fixed point is stable under particle-hole symmetry-breaking perturbations. To prepare our theory set-up, let us extend the quadratic part of the universal theory [Eq. (4.12)] by a term

$$\mathcal{L}_\alpha = -\alpha \psi^\dagger \boldsymbol{\partial}^2 \psi \tag{4.101}$$

with dimensionless parameter α. It is in fact the only perturbation that is compatible with the remaining symmetries (viz. spatial rotation and time-reversal) whilst not being canonically irrelevant. In microscopic terms, α is related at the UV scale $\Lambda \sim 1/a$ (with lattice constant a) to the hopping amplitudes by the relation $\alpha(\Lambda) \sim (t + 3t')/t$. The flow of α is determined by the self-energy. Since the one-loop diagram in 4-Fermi theories is a tadpole, we need to got to two-loop order in order to get a definitive answer. The diagram we therefore need to compute is shown in Fig. 4.4. This diagram has a sunset topology, which allows the loop integration to be performed efficiently by going to position space and back (Groote, Körner & Pivovarov 1999), during the course of which the two coupled integrals over 3-momenta essentially decompose into two independent Fourier transforms. The contribution of the sunset diagram is given by

$$\text{Fig. 4.4} = g^2 \int \mathrm{d}\tau\, \mathrm{d}^2\boldsymbol{x}\, \mathrm{e}^{-\mathrm{i}(\omega\tau + \boldsymbol{p}\cdot\boldsymbol{x})}\, \sigma_y\, \tilde{G}_0(\tau, \boldsymbol{x})\, \sigma_y\, (\mathrm{tr} - 1) \Big[\tilde{G}_0(-\tau, -\boldsymbol{x})\, \sigma_y\, \tilde{G}_0(\tau, \boldsymbol{x})\, \sigma_y\Big] \tag{4.102}$$

where

$$\tilde{G}_0(\tau, \boldsymbol{x}) = \int \frac{\mathrm{d}\omega\, \mathrm{d}^2\boldsymbol{x}}{(2\pi)^3} \frac{\mathrm{e}^{\mathrm{i}(\omega\tau + \boldsymbol{p}\cdot\boldsymbol{x})}}{\mathrm{i}\omega + d_a(\boldsymbol{p})\, \sigma_a + \alpha \boldsymbol{p}^2} \tag{4.103}$$

is the position-space propagator. For small particle-hole asymmetry $|\alpha| \ll 1$, all expressions may be expanded in powers of α. For the propagator in momentum space, this leads to

$$G_0(\omega, \boldsymbol{p}) = \frac{-\mathrm{i}\omega + d_a(\boldsymbol{p})\, \sigma_a}{\omega^2 + \boldsymbol{p}^4} + \alpha\, \frac{\boldsymbol{p}^2 \left(\omega^2 - \boldsymbol{p}^4\right) + 2\mathrm{i}\omega \boldsymbol{p}^2 d_a(\boldsymbol{p})\, \sigma_a}{\left(\omega^2 + \boldsymbol{p}^4\right)^2} + \mathcal{O}(\alpha^2). \tag{4.104}$$

Let us now compute the Fourier transform of the above to derive the position-space propagator. The integral over ω is elementary. For the spatial part of the Fourier transform, it is expedient to introduce polar coordinates $\boldsymbol{p} = p(\cos\varphi, \sin\varphi)$, $\boldsymbol{x} = \varrho(\cos\vartheta, \sin\vartheta)$. Then, $\boldsymbol{p}\cdot\boldsymbol{x} = p\varrho \cos(\varphi - \vartheta)$, and subsequently we may use the Jacobi–Anger identity to write the exponential factor as

$$\mathrm{e}^{\mathrm{i}\boldsymbol{p}\cdot\boldsymbol{x}} = J_0(p\varrho) + 2 \sum_{m=0}^{\infty} \mathrm{i}^m J_m(p\varrho) \left[\cos(m\varphi)\cos(m\vartheta) + \sin(m\varphi)\sin(m\vartheta)\right], \tag{4.105}$$

---

[27] This may be seen in a more pedestrian way by observing that the spectrum is given by $\varepsilon_\pm(\boldsymbol{p}) = \frac{1}{2}\left[(t + 3t') \pm (t - 3t')\right] \boldsymbol{p}^2$.

where $J_m(\cdot)$ is the Bessel function of the first kind and order m. The integral over φ can now be performed by exploiting the orthogonality of sines and cosines, for instance over $L^2([0, 2\pi])$, and the series conveniently terminates at $m = 2$ since rotational invariance is still intact. The final integral over ϱ turns out to be expressible in terms of elementary functions as well, yielding neat expressions for the tree-level position-space propagator to the desired order in α:

$$\begin{aligned}\tilde{G}_0(\tau, \boldsymbol{x}) = {} & \frac{\mathrm{e}^{-\boldsymbol{x}^2/(4|\tau|)}}{8\pi\tau} + \frac{\mathrm{e}^{-\boldsymbol{x}^2/(4|\tau|)}\left(\boldsymbol{x}^2 + 4|\tau|\right) - 4|\tau|}{8\pi\boldsymbol{x}^2|\tau|} \frac{d_a(\boldsymbol{x})}{\boldsymbol{x}^2}\sigma_a \\ & + \frac{\mathrm{e}^{-\boldsymbol{x}^2/(4|\tau|)}}{32\pi\tau^2}\left[\boldsymbol{x}^2 - 4|\tau| + \operatorname{sgn}(\tau)\, d_a(\boldsymbol{x})\,\sigma_a\right]\alpha \\ & + \mathcal{O}(\alpha^2). \end{aligned} \tag{4.106}$$

To obtain the selfenergy in momentum space, we have to perform the inverse Fourier transform, followed by an expansion in powers of external momentum p to extract renormalization constants. The integral is both infrared and ultraviolet divergent, which we may efficiently regularize using a sharp cut-offs. The procedure is technically similar to how we regularized the Luttinger–Yukawa theory (Subsec. 4.3.2), except that we are now regularizing in position rather than momentum space. *Mutatis mutandis*, we thus have

$$\int_{\text{reg.}} \mathrm{d}\tau\, \mathrm{d}^2\boldsymbol{x} = \int_{-\infty}^{\infty} \mathrm{d}\tau \int \mathrm{d}^2\boldsymbol{x}\, \Theta(|\boldsymbol{x}| - 1/k)\,\Theta(1/\Lambda - |\boldsymbol{x}|), \tag{4.107}$$

where we have used that $k, \Lambda \sim (\text{length})^{-1}$ when defining the position-space UV and IR cut-offs. The scale derivative then converts the Θ-function into a δ-function. Hence, for small external momenta, $|\boldsymbol{p}| \ll k$, we may expand the diagram in powers of external momentum prior to integration, which simplifies the angular integration greatly (the radial integration is trivial due to the aforementioned δ-function). We thus find

$$\begin{aligned} -k\partial_k[\text{Fig. 4.4}] &= \frac{g^2}{4\pi^2}\left[\frac{1}{24} d_a(\boldsymbol{p})\,\sigma_a + \left(\frac{1}{9} - \frac{1}{4}\ln\frac{4}{3}\right)\alpha\boldsymbol{p}^2\right] + \mathcal{O}(\omega, \boldsymbol{p}^4) & (4.108) \\ &\equiv \eta_\psi\, d_a(\boldsymbol{p})\,\sigma_a + (\eta_\psi\alpha + \beta_\alpha)\,\boldsymbol{p}^2 + \mathcal{O}(\omega, \boldsymbol{p}^4). & (4.109) \end{aligned}$$

Hence, we may read off the β-function

$$\beta_\alpha = -\frac{g^2}{4\pi^2}\left(\frac{1}{4}\ln\frac{4}{3} - \frac{5}{72}\right)\alpha. \tag{4.110}$$

Importantly, the derivative of the right-hand side with respect to α is negative, and shows that small particle-hole asymmetry is an irrelevant perturbation. In other words, although there is some tuning of the hopping ratio t'/t needed to get the system somewhat close to particle-hole symmetry, there is no need for *fine-tuning*; deviations from the particle-hole symmetric point, provided they are small enough, are guaranteed to die out over the course of RG flow.

4.7 Discussion

We have studied an example of a QCP between a stable semimetallic phase with quadratic dispersion and an interaction-induced insulator. The QCP is characterized by a collision (or more aptly, a ‘coalescence’) of two fixed points. Although some exponents revert to their canonical values as a consequence of this collision, there are observables that still exhibit deviations from mean-field theory. Many observables of this kind (such as the correlation length and the order-parameter expectation value) have essential singularities, which may be interesting in their own right, for instance due to similarities with the Berezhinskii–Kosterlitz–Thouless transition (cf., e.g., Herbut 2007), though the precise extraction of their exponents from experiment (both on the computer or in the laboratory) may be challenging. The most promising observable is the susceptibility, which shows a power-law decay; its exponent is distinct from dimensional analysis, but is computable exactly at one-loop (essentially because the Gaußian participant in the fixed-point collision kills all loops higher than one). The fact that the one-loop correction survives at all is connected in turn to the fact that the correlation length has an essential singularity (i.e., that the correlation-length exponent is formally divergent). Such exact non-canonical exponents are especially useful as a benchmark for numerical methods. In particular, there has been much effort in simulating systems that suffer from the so-called sign problem, using techniques such as Lefschetz thimbles (cf., e.g., Cristoforetti, di Renzo & Scorzato 2012; Alexandru, Başar & Bedaque 2016), but also beyond (Alexandru *et al.* 2016). The explicit lattice construction presented above may serve as an interesting test case in this regard, being unamenable to techniques that rely on the absence of a sign problem, whilst also coming with exact benchmarks. How to construct a two-dimensional Luttinger semimetal using ultracold atoms has been demonstrated before, for instance, by Sun *et al.* (2012). This also raises the possiblity that (slightly modified versions of) the QCP proposed here may also be experimentally accessible in the laboratory.

Chapter 5

Dirac from Luttinger I: Explicit Symmetry Breaking

The quantum criticality of Dirac fermions in $d = 2$ spatial dimensions (or equivalently, in $D = 3$ spacetime dimensions) is a challenging problem. We had a first-row view of this in Chap. 3, where we studied the breaking of SO(3) flavour symmetry. The results from a three-loop ϵ expansion, an NNLO leading-order large-N expansion and FRG in LPA$'$ approximation had significant deviations from each other. A similar story unfolds in theories describing graphene-like systems (see also the discussion in Subsec. 1.1.2). Alas, an experimental realization of quantum critical $D = 3$ Dirac fermions proves difficult. In graphene, the interactions are usually too weak to trigger spontaneous symmetry breaking. Finding a material with a Kitaev spin-orbital liquid groundstate, as appearing in proposals such as that of Seifert *et al.* (2020), and then unambiguously identifying it as one, is also likely very challenging – both technically and conceptually.

Compared to graphene, Luttinger fermions (as realized in quadratic band touching semimetals) in $d = 2$ has something of an embarassment of riches – they order already at infinitesimal interaction strength (see also Chap. 4). Topologically, however, one might argue quadratic band touching (QBT) points are not elementary. This may be quantified by the fact that they have Berry charge ± 2, whilst Dirac cones by comparison only have charge ± 1 (cf., e.g., McCann & Koshino 2013). In principle, therefore, a Luttinger fermion may split into Dirac fermions under suitable conditions (i.e., symmetry breaking, which we shall discuss in more detail subsequently). In such a system, the physics at long length scales, as near a quantum phase transition, will be governed by Dirac fermions: it will realize Gross–Neveu quantum criticality. On the other hand, the proximity to the Luttinger parent state may lead to a lower value of the critical interaction strength. Hence, low-symmetry Luttinger fermions may provide experimental access to Gross–Neveu universality classes.

Fig. 5.1 illustrates the two minimal – as measured, for instance, by the number of 'reaction products' – scenarios for the splitting of one Luttinger fermion into Dirac fermions. In both cases, the line(s) joining the Dirac points with their 'centre of mass' selects an axis or several axes in momentum space, and thus breaks rotational symmetry O(2) down to a discrete subset. The solution with the lowest number of Dirac fermions requires two of them, and corresponds to the splitting of Berry charge according to $2 \to 1 + 1$.[1] The line joining the two Dirac points selects precisely one axis, which

---

[1] For definiteness, we consider a Luttinger fermion with positive Berry charge, but the discussion is obviously just as valid if the sign of every Berry charge is flipped.

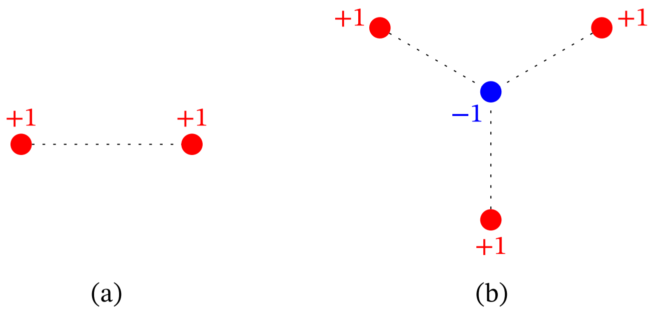

Figure 5.1: Scenarios for the splitting of a Luttinger fermion into (a) two and (b) four Dirac cones. The label denotes the Berry charge of each fermion.

corresponds to breaking the rotational symmetry down to C_2, cf. Fig. 5.1(a). A second scenario is '$2 \to (-1) + 3 \times 1$'. In this case, there are three axes related by rotational symmetry, and the final state has three-fold rotational symmetry C_3.

A paradigmatic realization is provided by electrons on the Bernal-stacked bilayer honeycomb lattice. At the level of the nearest-neighbour tight-binding model – an often-used approximation used to describe Bernal-stacked bilayer graphene (BBLG), see McCann & Fal'ko (2006) – the spectrum features band crossings at the corners of the Brillouin zone (the so-called K points). Unlike its monolayer cousin where these are Dirac points, the band crossings in the bilayer system are quadratic, giving rise to Luttinger fermions with their aforementioned instability at infinitesimal coupling. Indeed, experiments on Bernal-stacked bilayer graphene find an ordered ground state at low temperatures, though the precise nature of the order has not been established conclusively.2) As we shall see, in addition to the potential for realizing a plethora of exotic ordered phases, Bernal-stacked bilayer graphene may be a good candidate to realize at least one of – if not both – 'Dirac from Luttinger' scenarios discussed above. The low symmetry needed to render QBTs on the Bernal-stacked honeycomb bilayer fragile has two origins. In case of the '$2 \to (-1) + 3 \times 1$' mechanism, the rotational symmetry is broken explicitly by the lattice, since the rotational symmetry about the K points of the Brillouin zone of the honeycomb lattice (bilayer or otherwise) is only C_3. This is roughly speaking the subject of the present chapter. On the other hand, the symmetry breaking needed for the '$2 \to 1 + 1$' mechanism is spontaneous; that, along with its accompanying phenomenology, is the topic of Chap. 6.

The appearance of Dirac cones on the Bernal-stacked honeycomb bilayer can already be 'seen' at the tight-binding level, if one allows for hopping beyond nearest-neighbour bonds – more specifically, this is what happens when interlayer hopping beyond the shortest range (so-called *trigonal warping*) is taken into account (McCann & Koshino 2013). One of the main goals of this chapter is to demonstrate explicitly that, even when the trigonal warping terms are absent in the microscopic Hamiltonian, the presence of higher-order terms, despite being irrelevant in the RG sense, generate effective trigonal warping at low energy. This leads to a stable semimetallic phase at weak short-range interactions and a nontrivial quantum critical point at finite coupling. We establish the relevant $(2+1)$-dimensional Gross–Neveu universality class for the transition and map out the pertinent phase diagram in the plane of temperature T and interaction strength g.

---

2) cf., e.g., Feldman, Martin & Yacoby (2009); Martin *et al.* (2010); Weitz *et al.* (2010); Velasco Jr. *et al.* (2012); Freitag *et al.* (2012); Bao *et al.* (2012); Veligura *et al.* (2012).

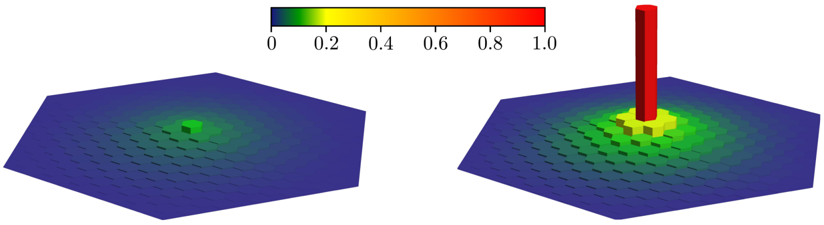

$U = 2$ $U = 3$

Figure 5.2: (Adapted from Pujari *et al.* 2017) Quantum Monte Carlo results for the antiferromagnetic structure factor of Hubbard model on honeycomb bilayer as a function of Hubbard interaction strength U. Note that infinitesimal U is insufficient: onset of order occurs only once a critical strength is exceeded. This, along with the fact that the dynamical critical exponent is $z = 0.9(2)$ near the transition (cf. *ibid.*) suggests a Dirac semimetal ground state at weak coupling.

Our calculations will thereby confirm the schematic RG picture previously purported by Pujari *et al.* (2017) in the context of quantum Monte Carlo simulations of the Hubbard model on the bilayer honeycomb lattice (see also Fig. 5.2). In the absence of trigonal warping, the numerics pointed to an extended gapless phase at weak coupling and a quantum critical point to a gapped ordered phase at a finite Hubbard interaction. The measured values for the dynamic critical exponent $z = 0.9(2)$ and the correlation-length exponent $\nu = 1.0(2)$ were broadly consistent with the $(2+1)$-dimensional Gross–Neveu universality class, the particular type of which, however, had not been possible to establish unambiguously. The crucial ingredients for this mechanism are the interaction-induced corrections to the fermion self-energy. However, at the one-loop order, which has been thoroughly investigated in previous works,[3)] the self-energy correction happens to vanish as a consequence of the interaction being local.[4)] A consistent field-theoretic understanding of the quantum criticality observed in the numerical simulations therefore necessitates one to go beyond one-loop. This is a daunting task, since not only is Euclidean spacetime rotation symmetry SO(3) absent, even the spatial rotation symmetry O(2) is broken down to the discrete subgroup C_3. As a result, a proper RG analysis of this physics has, to the best of our knowledge, thus far been lacking in the literature. It is one of the main technical advances of this chapter to demonstrate that the two-loop self-energy corrections can be computed in an analytical way by employing a suitably adapted regularization scheme in position space. We shall construct a minimal continuum low-energy field theory that captures the salient physics of interacting C_3-symmetric QBTs. We shall then evaluate all loop corrections to the leading nonvanishing order. This, most importantly, shall include the crucial two-loop self-energy diagrams and it will allow us to derive improved RG flow equations. This will then enable us to construct the corresponding quantum phase diagram, and to reveal the pertinent universality class and its critical exponents. We shall also compare with mean-field solutions, which are controlled in a certain large-N limit, and discuss the behaviour at finite trigonal warping on the microscopic level.

[3)] For instance, see Sun *et al.* (2009); Zhang *et al.* (2010); Vafek & Yang (2010); Vafek (2010); Uebelacker & Honerkamp (2011); Scherer, Uebelacker & Honerkamp (2012); Lang *et al.* (2012); Song, Liang & Haas (2012); Cvetkovic, Throckmorton & Vafek (2012).

[4)] The one-loop correction is finite, however, if long-range interactions are present (Sinner & Ziegler 2010).

The body of this chapter is organized as follows: Sec. 5.1 introduces the minimal effective field theory starting from the tight-binding model on a Bernal-stacked bilayer honeycomb lattice. Mean-field solutions are studied in Sec. 5.2. In Sec. 5.3, we shall then proceed to evaluating the leading loop corrections and investigate the phase diagram arising from the RG flow equations. Section 5.4 is devoted to discussing critical exponents and the finite-temperature phase diagram. A brief summary and an outlook (Sec. 5.5) closes the chapter.

5.1 From lattice to continuum

This section serves to motivate a minimal continuum field theory that shall subsequently constitute the main object of study in this chapter. For concreteness, we shall begin with a specific microscopic model on a lattice with C_3 symmetry and derive thence a Euclidean action serving as an effective low-energy description. The pure QBT theory with $z = 2$ on the one hand and the relativistic Gross–Neveu theory with $z = 1$ on the other hand are recovered from this continuum field theory in two opposite limiting cases. It is worth emphasizing, however, that the physics investigated herein is independent of the particular lattice model and quite generally applies to any interacting two-dimensional Fermi system with QBT and C_3 rotational symmetry.

5.1.1 Fermions on Bernal-stacked honeycomb bilayer

Consider a model of spinless fermions on the Bernal-stacked bilayer honeycomb lattice at half filling, defined by the tight-binding Hamiltonian (Castro Neto *et al.* 2009)

$$H_0 = -t \sum_{\langle ij \rangle} \sum_{m=1}^{2} a_{im}^\dagger b_{jm} - t_\perp \sum_i a_{i1}^\dagger b_{i2} - t_\mathrm{w} \sum_{\langle ij \rangle} a_{i1}^\dagger b_{j2} + \text{H.c.} \tag{5.1}$$

The operators a_{im} (b_{im}) annihilate a fermion in layer m and sublattice A (B) at position $\boldsymbol{R}_i$ of the Bravais lattice. The parameter t corresponds to hopping processes between nearest neighbours $\langle ij \rangle$ within the same honeycomb layer, while $t_\perp$ corresponds to hopping between sites that are located on top of each other and belong to different layers and different sublattices. The third term in H_0, parametrized by t_w, denotes the trigonal warping term allowed by C_3 symmmetry; it corresponds to next-nearest-neighbour interlayer hopping processes. The primitive Bravais lattice vectors are denoted as $\boldsymbol{a}_1 = \big(1/2, \sqrt{3}/2\big)$ and $\boldsymbol{a}_2 = \big(1/2, -\sqrt{3}/2\big)$, with the lattice constant set to unity, $a = 1$, for notational simplicity. Proper units of a will be restored below whenever needed. In reciprocal space and upon collecting the Fourier-transformed fermion operators into a vector $c^\dagger(\boldsymbol{k}) = \Big(a_1^\dagger(\boldsymbol{k}), b_2^\dagger(\boldsymbol{k}), a_2^\dagger(\boldsymbol{k}), b_1^\dagger(\boldsymbol{k})\Big)$, the tight-binding Hamiltonian can be written in matrix notation as

$$H_0 = \int_{\boldsymbol{k} \in \mathrm{BZ}} \frac{\mathrm{d}^2 \boldsymbol{k}}{(2\pi)^2}\, c^\dagger(\boldsymbol{k})\, \mathcal{H}_0(\boldsymbol{k})\, c(\boldsymbol{k}), \tag{5.2}$$

where the $\boldsymbol{k}$-integration is over the Brillouin zone (BZ). The Hermitian 4×4 matrix $\mathcal{H}_0$ reads in block notation

$$\mathcal{H}_0(\boldsymbol{k}) = \begin{pmatrix} \mathcal{H}_{11}(\boldsymbol{k}) & \mathcal{H}_{12}(\boldsymbol{k}) \\ \mathcal{H}_{12}^\dagger(\boldsymbol{k}) & \mathcal{H}_{22}(\boldsymbol{k}) \end{pmatrix}, \tag{5.3}$$

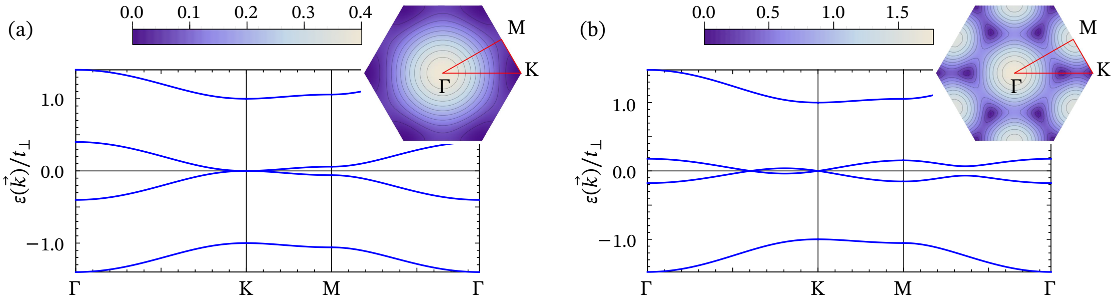

Figure 5.3: Tight-binding dispersion along the high-symmetry line Γ–K–M–Γ from Eq. (5.7) for $t/t_\perp = 0.25$. The insets show the dispersion of the low-energy conduction band in the first Brillouin zone (color plot) and the path used in the main panels (red line). In (a), there is no trigonal warping, $t_\mathrm{w}/t_\perp = 0$, and only the two QBTs at $\boldsymbol{k} = \pm\boldsymbol{K}$ touch the Fermi level at $\varepsilon = 0$. For nonzero $t_\mathrm{w}/t_\perp = 0.1$ (b), the two QBTs split into two central Dirac cones at $\boldsymbol{k} = \pm\boldsymbol{K}$ and six 'satellite' Dirac cones at incommensurate wavevectors between Γ and K.

with the 2×2 blocks having nonvanishing entries only on the off-diagonal,

$$\mathcal{H}_{11}(\boldsymbol{k}) = -t_\mathrm{w} \begin{pmatrix} 0 & f^*(\boldsymbol{k}) \\ f(\boldsymbol{k}) & 0 \end{pmatrix}, \tag{5.4}$$

$$\mathcal{H}_{12}(\boldsymbol{k}) = -t \begin{pmatrix} 0 & f(\boldsymbol{k}) \\ f^*(\boldsymbol{k}) & 0 \end{pmatrix}, \tag{5.5}$$

$$\mathcal{H}_{22}(\boldsymbol{k}) = -t_\perp \begin{pmatrix} 0 & 1 \\ 1 & 0 \end{pmatrix}. \tag{5.6}$$

Here, $f(\boldsymbol{k}) = \sum_{\boldsymbol{\delta}} \mathrm{e}^{\mathrm{i}\boldsymbol{k}\cdot\boldsymbol{\delta}}$ is the nearest-neighbor form factor of the honeycomb lattice, with $\boldsymbol{\delta} \in \{(1,0), \boldsymbol{a}_1, \boldsymbol{a}_2\}$ the three nearest-neighbor displacement vectors. The spectrum of $\mathcal{H}_0(\boldsymbol{k})$ consists of four bands with dispersion $\pm\varepsilon_\pm(\boldsymbol{k})$, given by

$$\begin{aligned} \varepsilon_\pm^2(\boldsymbol{k}) = \frac{1}{2}\Big[& t_\perp^2 + (2t^2 + t_\mathrm{w}^2)|f|^2 \pm \big\{ t_\perp^4 + t_\mathrm{w}^2 \left(4t^2 + t_\mathrm{w}^2\right)|f|^4 \\ & + 2t_\perp |f|^2 \left(2t^2 t_\perp - t_\perp t_\mathrm{w}^2 + 4t^2 t_\mathrm{w} \operatorname{Re} f\right)\big\}^{1/2}\Big]. \end{aligned} \tag{5.7}$$

Here, the momentum dependence of the form factor $f \equiv f(\boldsymbol{k})$ has been suppressed for notational brevity. The above spectrum exhibits particle-hole symmetry, which shall be assumed throughout from hereon in. Note, however, that it will be broken upon inclusion of longer-ranged terms in the tight-binding Hamiltonian (5.1), such as next-nearest neighbor intralayer hopping (McCann & Koshino 2013). The additional physics due to broken particle-hole symmetry is interesting in its own right, and will be left for future work.

At half filling and low temperatures, only the two bands at $\pm\varepsilon_-(\boldsymbol{k})$ contribute to physical observables. The general properties of the spectrum now depend crucially on whether the trigonal warping t_w is finite or vanishes; let us therefore discuss these two cases separately in the following.

First, when the trigonal warping is tuned to zero, $t_\mathrm{w} \to 0$, the two low-energy bands touch at $\boldsymbol{k} = \pm\boldsymbol{K}$, where $\boldsymbol{K} = (4\pi/3, 0)$ denotes the high-symmetry K point at one of the corners of the hexagonal Brillouin zone. To see that these two band crossings are indeed quadratic, let us expand the form factor around $\pm\boldsymbol{K}$ as

$$f(\pm\boldsymbol{K} + \boldsymbol{p}) = \mp\frac{\sqrt{3}}{2}|\boldsymbol{p}|\,\mathrm{e}^{\mp\mathrm{i}\varphi} + \frac{1}{8}|\boldsymbol{p}|^2\,\mathrm{e}^{\pm 2\mathrm{i}\varphi} + \mathcal{O}(|\boldsymbol{p}|^3), \tag{5.8}$$

where $\varphi = \arg(p_x + \mathrm{i}p_y)$ denotes the polar angle of the local momentum $\boldsymbol{p} = \boldsymbol{k} \mp \boldsymbol{K}$. Upon subsequent expansion of the low-energy spectrum to next-to-leading order in $|\boldsymbol{p}|$, we find

$$\varepsilon_-^2(\pm\boldsymbol{K} + \boldsymbol{p}) = \frac{9t^4}{16t_\perp^2}|\boldsymbol{p}|^4 \left(1 \mp \frac{|\boldsymbol{p}|}{\sqrt{3}} \cos 3\varphi\right) + \mathcal{O}(|\boldsymbol{p}|^6), \tag{5.9}$$

valid for $|\boldsymbol{p}| \ll t_\perp/t$. This demonstrates the existence of two two-fold degenerate QBT points located at the two inequivalent K points in the Brillouin zone and at energy $\varepsilon_-(\pm\boldsymbol{K}) = 0$. By inspection of the full band structure given by Eq. (5.7), one can readily convince oneself that there are no further bands crossing the zero-energy level, cf. Fig. 5.3(a). In the half-filled case, the Fermi level is therefore fixed precisely at the two QBT points.

Note that the leading-order term $\propto |\boldsymbol{p}|^4$ in Eq. (5.9) exhibits a continuous O(2) rotational symmetry in momentum space. The next-to-leading order term $\propto |\boldsymbol{p}|^5 \cos 3\varphi$, by contrast, breaks this symmetry explicitly down to C_3, reflecting the lattice symmetry of the honeycomb model.

At the level of the free theory, the O(2) rotational symmetry therefore emerges dynamically if one restricts the window of observation to sufficiently low energies. We shall see, however, that this is no longer true once interactions are taken into account.

Let us now switch on a small finite $t_\mathrm{w} > 0$, and expand the spectrum again to next-to-leading order in local momentum, but now keeping the leading t_w correction in each power of $|\boldsymbol{p}|$. The low-energy spectrum then takes the form

$$\varepsilon_-^2(\pm\boldsymbol{K} + \boldsymbol{p}) = \frac{3t_\mathrm{w}^2}{4}|\boldsymbol{p}|^2 \left(1 \pm \frac{\sqrt{3}t^2}{t_\perp t_\mathrm{w}}|\boldsymbol{p}| \cos 3\varphi\right) + \mathcal{O}(|\boldsymbol{p}|^4). \tag{5.10}$$

Note the lower exponent of the leading-order term as compared to Eq. (5.9). Consequently, the local dispersion near $\pm\boldsymbol{K}$ is no longer quadratic, but linear, and the spectrum exhibits Dirac cones at $\boldsymbol{k} = \pm\boldsymbol{K}$. In addition, for each Dirac cone at one of the high-symmetry K points, there are three 'satellite' Dirac cones located at incommensurable wavevectors $\boldsymbol{k} = \pm\boldsymbol{K} + \boldsymbol{p}$ with

$$|\boldsymbol{p}| = \frac{4t_\perp t_\mathrm{w}}{\sqrt{3}t^2} \quad \text{and} \quad \varphi = (4n + 1 \pm 1)\frac{\pi}{6}, \tag{5.11}$$

where $n = 0, 1, 2$ and we have assumed $t_\perp > 0$ and $t_\mathrm{w} > 0$ for concreteness. The full dispersion in the presence of trigonal warping is illustrated in Fig. 5.3(b). This concludes the discussion at the non-interacting level. In particular, the fermiologies in the QBT and Dirac cases are distinct, and going from the former to the latter requires 'switching on' a parameter like t_w by hand, as done above. In the presence of fermion-fermion interactions, however, this occurs dynamically. To elucidate this further, we need a pertinent low-energy continuum field theory.

5.1.2 Continuum limit

For the non-interacting part, let us begin by writing down the Hamiltonian for QBT in the case of $t_\mathrm{w} = 0$. In a 4×4 representation, it can be written as[5)]

$$\mathcal{H}_0^{(2)}(\boldsymbol{p}) = d_a(\boldsymbol{p})\,(\sigma^a \otimes \mathbb{1}_2), \qquad a = 1, 2, \tag{5.12}$$

[5)] cf., e.g., Sun *et al.* (2009); Vafek (2010); Janssen & Herbut (2015). We have encountered the discussion concerning the single-particle QBT Hamiltonian, upto a slight change of notation and representation, already in Chap. 4; the discussion is repeated here partly for recapitulation, but mainly to fix notation. The discussion of the symmetry-breaking terms, on the other hand, is specific to the current set-up.

with implied summation over repeated indices. In the above equation, the diagonal factor $\mathbb{1}_2$ can be understood to act on the valley index. The 2×2 matrices σ^a anticommute with each other and square to one, and may be represented by the usual Pauli matrices, $\sigma^1 \equiv \sigma_x$ and $\sigma^2 \equiv \sigma_y$. The time-reversal operator can then be defined as $\mathcal{T} = (\sigma_x \otimes \sigma_x)\mathcal{K}$, where $\mathcal{K}$ denotes complex conjugation. The functions $d_a(\boldsymbol{p})$ are $\boldsymbol{p}^2$ times the real spherical harmonics of angular momentum $\ell = 2$, which in two dimensions simply become $d_1(\boldsymbol{p}) = p_x^2 - p_y^2 = \boldsymbol{p}^2 \cos 2\varphi$ and $d_2(\boldsymbol{p}) = 2p_x p_y = \boldsymbol{p}^2 \sin 2\varphi$.

Under O(2) spatial rotations with angle θ,

$$p^a \mapsto (R_\theta)^a{}_b\, p^b, \quad R_\theta = \begin{pmatrix} \cos\theta & -\sin\theta \\ \sin\theta & \cos\theta \end{pmatrix} \in \mathrm{O}(2), \tag{5.13}$$

the d_a and σ^a transform respectively as

$$d_a(\boldsymbol{p}) \mapsto (R_{2\theta})_a{}^b\, d_b(\boldsymbol{p}), \qquad\qquad \sigma^a \mapsto (R_{2\theta})^a{}_b\, \sigma^b. \tag{5.14}$$

While the former equation follows from direct computation, the latter is to be understood in the sense that the σ^a transform as components of the second-rank tensor (Janssen & Herbut 2015)

$$\begin{pmatrix} \sigma^1 & \sigma^2 \\ \sigma^2 & -\sigma^1 \end{pmatrix} \mapsto R_\theta^\top \begin{pmatrix} \sigma^1 & \sigma^2 \\ \sigma^2 & -\sigma^1 \end{pmatrix} R_\theta. \tag{5.15}$$

With the above definitions, it is straightforward to verify that the product $\sigma^1\sigma^2$ is also invariant under rotations. Consequently, the two remaining matrices $\sigma^0 \equiv \mathbb{1}_2$ and $\sigma^3 = -\mathrm{i}\sigma^1\sigma^2$ that together with σ^1 and σ^2 span the space of 2×2 matrices, are rotationally invariant. At the quadratic order $\mathcal{O}(|\boldsymbol{p}|^2)$, therefore, the only possible term in the Hamiltonian that is compatible with the C_3 symmetry and diagonal in valley space is the O(2) invariant one present in the above $\mathcal{H}_0^{(2)}$. The upshot is that any free 2D Fermi system with QBT and C_n symmetry with $n \geqslant 3$ has emergent O(2) symmetry at low energies.

At the linear order $\mathcal{O}(|\boldsymbol{p}|)$, however, a C_3 invariant term that breaks O(2) is perfectly possible. For instance, the term

$$\mathcal{H}_0^{(1)}(\boldsymbol{p}) = \overline{p}_a(\sigma^a \otimes \sigma^3) \tag{5.16}$$

with $(\overline{p}_a) = (p_x, -p_y)$ transforms under rotations as $\mathcal{H}_0^{(1)}(\boldsymbol{p}) \mapsto \overline{p}_a (R_{3\theta})^a{}_b \sigma^b$ and is therefore only symmetric under the C_3 symmetry, but not continuous O(2) rotations.

At the cubic order $\mathcal{O}(|\boldsymbol{p}|^3)$, an analogous term is C_3 symmetry allowed,

$$\mathcal{H}_0^{(3)}(\boldsymbol{p}) = \boldsymbol{p}^2\, \overline{p}_a(\sigma^a \otimes \sigma^3), \tag{5.17}$$

which manifestly has the same symmetry properties as $\mathcal{H}_0^{(1)}$.

A general non-interacting low-energy Hamiltonian consistent with C_3 rotational symmetry can therefore be written in terms of three parameters f_1, f_2, and f_3 as

$$\mathcal{H}_0(\boldsymbol{p}) = \sigma^a \otimes \left[f_1 \overline{p}_a \sigma^3 + f_2 d_a(\boldsymbol{p}) \mathbb{1}_2 - f_3 \boldsymbol{p}^2 \overline{p}_a \sigma^3 \right] + \mathcal{O}(|\boldsymbol{p}|^4), \tag{5.18}$$

where the signs of f_1, f_2 and f_3 have been chosen for later convenience. The spectrum of $\mathcal{H}_0(\boldsymbol{p})$ is given by

$$\varepsilon^2(\boldsymbol{p}) = f_1^2|\boldsymbol{p}|^2 + 2f_1f_2|\boldsymbol{p}|^3 \cos 3\varphi + (f_2^2 - 2f_1f_3)|\boldsymbol{p}|^4 - 2f_2f_3|\boldsymbol{p}|^5 \cos 3\varphi$$

$$+\,\mathcal{O}(|\boldsymbol{p}|^6), \tag{5.19}$$

which reproduces the tight-binding dispersion near the K point at $\boldsymbol{k} = +\boldsymbol{K}$ [Eqs. (5.9) and (5.10)] for

$$f_1 = \frac{\sqrt{3}t_{\mathrm{w}}a}{2}, \qquad f_2 = \frac{3t^2a^2}{4t_\perp}, \qquad f_3 = \frac{a^3}{2\sqrt{3}}\frac{3t^2}{4t_\perp}, \tag{5.20}$$

and the same equations hold, up to a suitable change of the local momentum basis $\boldsymbol{p} \mapsto \overline{\boldsymbol{p}}$, near the second K point at $\boldsymbol{k} = -\boldsymbol{K}$ as well. Here, the lattice constant a has been reinstated in order to make the physical units more readily apparent. In the following, we shall in particular be interested in the situation in which f_1 is tuned to zero at the microscopic level (which corresponds to $t_{\mathrm{w}} = 0$ in the tight-binding Hamiltonian) describing a system whose bare spectrum has a QBT (referred to henceforth as 'the QBT limit'), and study the dynamical generation of f_1 due to interactions.

The Lagrangian is constructed from Eq. (5.18) in canonical fashion, namely

$$\mathcal{L}_0 = \psi_i^\dagger \left[\partial_\tau + \mathcal{H}_0(-\mathrm{i}\boldsymbol{\partial})\right] \psi^i, \tag{5.21}$$

where τ denotes imaginary time and ψ^i, $\psi_i^\dagger$ are four-component complex spinors with 'flavour' index $i = 1, \dots, N_{\mathrm{f}}$. On the honeycomb bilayer and in the limit of vanishing trigonal warping $t_{\mathrm{w}} \ll t^2/t_\perp$, for which the spectrum has a QBT, the flavour number N_{f} can be understood as the real-spin degeneracy of each band, with $N_{\mathrm{f}} = 1$ for spinless fermions. For the sake of generality, however, we shall keep the flavour number N_{f} arbitrary in the calculations to come. This will also allow us to make contact with the limiting cases $N_{\mathrm{f}} \to \infty$, which represents the mean-field limit, and $N_{\mathrm{f}} = 1/2$, which can be understood as a Fermi system with a single point of QBT in the Brillouin zone, as realizable for spinless fermions on the Kagome and checkerboard lattices Sun *et al.* (2009). Note, however, that for the latter systems, the linear and cubic terms in Eqs. (5.16) and (5.17) are forbidden by time-reversal symmetry, and the QBT is therefore protected for $N_{\mathrm{f}} = 1/2$.

It is worth emphasizing that the above Hamiltonian $\mathcal{H}_0$, with the correct interpretation, is sufficient to capture the behaviour at substantial trigonal warping as well. In this limit, Eq. (5.18) describes massless Dirac fermions subject to a quadratic perturbation $\propto f_2$, with the spectrum given by Eq. (5.10). Some care is needed when it comes to the flavour content of the low-energy Dirac theory. Since a separate fermion flavour has to be introduced for each Fermi point, one requires four Dirac points for every valley in the QBT theory. Flavour symmetry between the 'satellite' and the central Dirac point can be restored by a suitable rescaling of the local momentum, viable in the low-energy limit.

In conclusion, therefore, the Lagrangian (5.21) constitutes two different continuum field theories describing two opposite limits of the low-energy physics of fermions on the bilayer honeycomb lattice: On the one hand, the QBT limit for vanishing or infinitesimally small trigonal warping $t_{\mathrm{w}} \ll t^2/t_\perp$ is described by Eq. (5.21) with flavour number $N_{\mathrm{f}} = N/2$, where N is the number of valleys in the QBT limit. On the other hand, the Dirac limit for $t_{\mathrm{w}} \gg t^2/t_\perp$ is described by the same Eq. (5.21) in the low-energy limit, but now with $N_{\mathrm{f}} = 2N$ (Dirac) fermion flavours. Hence, the number of four-component fermion flavours in the low-energy description is

$$N_{\mathrm{f}} = \begin{cases} N/2 & \text{for } f_1/f_2 \ll 1/a, \\ 2N & \text{for } f_1/f_2 \gg 1/a. \end{cases} \tag{5.22}$$

As noted above, the concrete lattice realization of spinless fermions on a honeycomb bilayer corresponds to $N = 2$.

5.1.3 Interactions

A generic four-fermion interaction can be written in the form

$$\frac{1}{2} g_{rs} (\psi_i^\dagger A_r^{ij} \psi_j)(\psi_k^\dagger A_s^{kl} \psi_l) \tag{5.23}$$

with coupling parameters g_{rs}, where $r, s = 1, \dots, 16$ (Herbut, Juričić & Roy 2009; Gies & Janssen 2010). The smallest subspace closed under the RG flow for $N \geqslant 2$ consists of three independent (i.e., Fierz irreducible) couplings Vafek (2010). The nature of the concrete state that emerges upon spontaneous symmetry breaking is sensitive to the form of interactions present microscopically in the system. Our primary interest, however, is in the question whether spontaneous symmetry breaking takes place at all for arbitrarily small couplings (as one would expect for a symmetry-protected QBT), rather than the competition (or cooperation) between the different possible orders. For this purpose, it is sufficient to restrict the calculations to a single interaction channel. For definiteness, let us choose $A_r^{ij} = A_s^{ij} = (\sigma^3 \otimes \sigma^3)\delta^{ij}$, corresponding to

$$\mathcal{L}_{\text{int}} = -\frac{1}{2} g \Big[\psi_i^\dagger (\sigma^3 \otimes \sigma^3) \psi^i \Big]^2 , \tag{5.24}$$

where the sign convention has been chosen such that the ordered state is stabilized for positive values of g. This particular choice of $\mathcal{L}_{\text{int}}$ is natural and appropriate for the following reasons: Firstly, note that $\sigma^3 \otimes \sigma^3$ anticommutes with $\mathcal{H}_0$. A finite bilinear condensate in the above interaction channel, i.e., $\langle \psi_i^\dagger (\sigma^3 \otimes \sigma^3) \psi^i \rangle \neq 0$, would therefore correspond to a state with a full mass gap in the spectrum, which is typically energetically favored within mean-field treatments (Sun *et al.* 2009; Herbut & Janssen 2014; Janssen & Herbut 2015). The state is characterized by an imbalance of the number of particles on layer 1 compared to layer 2 and thus breaks inversion symmetry between the layers. Time reversal, by contrast, remains intact and the new ground state thus represents a topologically trivial interaction-induced insulator. In fact, precisely this interaction channel has been found as the dominant ordering tendency in the t-V model of spinless fermions on the Bernal-stacked honeycomb bilayer subject to a repulsive nearest-neighbor interaction V within a multi-channel RG analysis (Vafek 2010).

Secondly, this channel is readily identified with the simplest possible Lorentz scalar, $[\psi_i^\dagger (\sigma^3 \otimes \sigma^3) \psi^i]^2 \equiv (\overline{\psi}_i \psi^i)^2$, where $\overline{\psi}_i = \psi_i^\dagger (\sigma^3 \otimes \sigma^3)$ is the Dirac conjugate. This is the familiar Gross–Neveu–Ising interaction, which in the Dirac limit $t_\text{w} \gg t^2/t_\perp$ has a well-understood quantum critical point at finite g.6) Furthermore, to leading order in $1/N$, it turns out that the above interaction channel is closed under RG in the sense that no further interactions are generated upon integrating out high-energy modes if absent on the microscopic level. We also note that for $N = 1$, in which case there are in total only two spinor components in the QBT limit, any finite four-fermion interaction must be proportional to $\psi^\dagger \sigma^3 \psi$. The single-channel approximation is therefore exact not only for $N \to \infty$, but also at $N = 1$. Although bilayer graphene with $N = 2$ falls in neither class, we expect our major conclusions, concerning in particular the existence of a quantum critical point at finite coupling in the QBT limit, to hold also in this case. The effect of other interactions will be briefly commented upon when discussing the universality class of the transition, see Sec. 5.4.

---

6) cf., e.g., Hands, Kocić & Kogut (1993); Vasil'ev, Derkachev & Stepanenko (1993); Gracey (1994b); Vojta, Zhang & Sachdev (2000a,b); Braun, Gies & Scherer (2011); Gracey, Luthe & Schröder (2016); Mihaila *et al.* (2017); Zerf *et al.* (2017); Iliesiu *et al.* (2018); Ihrig *et al.* (2018)

The full action describing both the situations with and without a finite trigonal warping term is hence given by

$$S = \int \mathrm{d}\tau\, \mathrm{d}^2\boldsymbol{x}\, (\mathcal{L}_0 + \mathcal{L}_{\text{int}})\,. \tag{5.25}$$

Let us conclude this section by reading off the mass dimensions of the quantities appearing in the theory. In the QBT limit, we would like to renormalize the fields such that the coefficient f_2 in front of the QBT term remains fixed during the RG. Then, in the noninteracting limit, the dynamical critical exponent is $z = 2$. Consequently, the linear coefficient has mass dimension $[f_1] = 1$ and is RG-relevant, while the cubic coefficient is RG-irrelevant with $[f_3] = -1$. The four-fermion coupling becomes dimensionless, $[g] = 0$, i.e., the interaction is marginal at tree level. In the opposite Dirac limit, the renormalization scheme should fix the coefficient f_1 of the linear term. Hence, in this case $z = 1$, $[f_2] = -1$, $[f_3] = -2$, and the four-fermion coupling becomes irrelevant, $[g] = -1$.

5.2 Mean-field theory

Let us begin by discussing the large-N limit, which can be solved exactly in the framework of mean-field theory. To distinguish the ordered from the disordered phase, it is useful to think in terms of the composite field $\phi \propto \psi_i^\dagger(\sigma^3 \otimes \sigma^3)\psi^i$. Then, the symmetric phase corresponds to $\langle\phi\rangle = 0$, whilst long-range order is characterized by ϕ developing a finite vacuum expectation value via spontaneous symmetry breaking. A finite $\langle\phi\rangle \neq 0$ acts as an effective mass term and opens up a full gap in the fermion spectrum. For the present interaction channel, the new ground state spontaneously breaks inversion symmetry between the layers. Let us rewrite the action solely in terms of ϕ by performing a Hubbard–Stratonovich transformation and then carrying out the path integral over the fermion fields. This results in an effective action,

$$S_{\text{eff}}[\phi] = \int \mathrm{d}\tau\, \mathrm{d}^2\boldsymbol{x}\, \frac{1}{2}\phi^2 - \operatorname{Tr}\ln\left[\partial_\tau + \mathcal{H}_0(-\mathrm{i}\boldsymbol{\partial}) - \sqrt{g}\,\phi\left(\sigma^3 \otimes \sigma^3\right)\right], \tag{5.26}$$

where the trace $\operatorname{Tr}(\,\cdot\,)$ is taken over spinor and flavour indices as well as coordinate space. A meaningful large-N limit is obtained by fixing $gN_{\mathrm{f}} = \text{const.}$ and $\phi^2/N_{\mathrm{f}} = \text{const.}$ Let us reiterate that the fermion flavour number N_{f} is equivalent to the number of QBT points $N/2$ in the limit of vanishing trigonal warping, while $N_{\mathrm{f}} = 2N$ when each QBT point splits into four Dirac cones. From the trace over the flavour indices, the action (5.26) for ϕ attains an overall factor of N_{f}. In the large-N limit, the path integral over ϕ is then dominated by the extremum of $S_{\text{eff}}[\phi]$. If we assume constant field configurations $\phi(x) \equiv \phi = \text{const.}$, this leads to the effective potential $V_{\text{eff}}(\phi) = \mathcal{V}^{-1}\, S_{\text{eff}}[\phi]\big|_{\phi(x)=\phi}$, where $\mathcal{V}$ is the spacetime volume. The mean-field analysis then boils down to minimizing $V_{\text{eff}}(\phi)$. It proves to be technically more convenient to evaluate $V_{\text{eff}}'(\phi)$ by differentiating (5.26) once with respect to ϕ and performing the trace over the spinor and flavour indices, yielding in momentum space

$$V_{\text{eff}}'(\phi) = \phi - 4N_{\mathrm{f}} \int \frac{\mathrm{d}\omega\, \mathrm{d}^2\boldsymbol{p}}{(2\pi)^3} \frac{g\phi}{\omega^2 + \mathcal{H}_0(\boldsymbol{p})^2 + g\phi^2}. \tag{5.27}$$

The divergence occurring for large frequency ω and large momentum $\boldsymbol{p}$ is handled by introducing a finite ultraviolet cut-off Λ. In the QBT case, it is expedient to implement this as the restriction $|\omega| \leqslant f_2\Lambda^2$ and $|\boldsymbol{p}| \leqslant \Lambda$, in agreement with the dynamic scaling exponent $z = 2$ for $f_1 = 0$. By contrast, in the Dirac limit for finite f_1, the integral is more efficiently regularized as $\sqrt{\omega^2 + f_1^2 \boldsymbol{p}^2} \leqslant |f_1|\,\Lambda$, respecting the different dynamic exponent $z = 1$ for $f_2 = f_3 = 0$.

Let us first recapitulate the case of pure QBT with $N_\mathrm{f} = N/2$ and $f_1 = f_3 = 0$ (Sun *et al.* 2009). Then, $\mathcal{H}_0(\boldsymbol{p})^2 = f_2^2 \boldsymbol{p}^4$ and the integral is soluble in terms of standard functions. Expanding around $\Lambda \to \infty$ and rescaling $\phi/(\sqrt{f_2}\Lambda^2) \mapsto \phi$ and $g/f_2 \mapsto g$, one finds

$$V_\mathrm{eff}'(\phi) \propto \phi \left[1 + \frac{gN}{8\pi} \ln\!\left(\tfrac{1}{4} g \phi^2\right)\right]. \tag{5.28}$$

Thus, the minimum for *all* $g > 0$ is located not at $\phi = 0$, but at the new minimum

$$\phi_0 = 2 g^{-1/2} \mathrm{e}^{-4\pi/(gN)}. \tag{5.29}$$

Hence, infinitesimal g leads to spontaneous symmetry breaking for a rotationally invariant QBT, in agreement with the various previous works on the subject.[7] Let us next investigate the stability of the symmetry-broken phase under perturbation by an infinitesimal Dirac term, realized by switching on small non-vanishing f_1. To this end, consider the curvature of the effective potential around ϕ_0 and expand it in powers of $|f_1/(f_2\Lambda)| \ll \phi_0$ to obtain

$$V_\mathrm{eff}''(\phi_0) \propto \frac{gN}{4\pi} \left[1 - \mathrm{e}^{8\pi/(gN)} (f_1/4f_2)^4\right], \tag{5.30}$$

where we have rescaled $f_1/(f_2\Lambda) \mapsto f_1/f_2$. The ordered phase is stable (or at least metastable) as long as $V_\mathrm{eff}''(\phi_0) > 0$. For a given fixed and small f_1, this condition holds if and only if $g > g_\mathrm{c}$, with the critical coupling

$$g_\mathrm{c}(f_1/f_2) \simeq \frac{2\pi}{N} \left(-\ln\left|\frac{f_1/f_2}{4}\right|\right)^{-1} \tag{5.31}$$

valid for $|f_1/f_2| \ll 1$. The inclusion of f_3 is possible as well by numerical means. However, within mean-field theory, this does not lead to qualitatively new physics since the crucial self-energy corrections, which are prerequisite to obtaining a finite g_c in the QBT limit $f_1/f_2 = 0$, are suppressed for large N (as we shall show explicitly later). At the mean-field level, therefore, spontaneous symmetry breaking occurs for $g > g_\mathrm{c} \geqslant 0$ with $g_\mathrm{c} \to 0$ for $f_1/f_2 \to 0$.

Let us now turn to the opposite limit of $N_\mathrm{f} = 2N$ Dirac flavours perturbed by a small f_2 term. We investigate an instability towards the symmetry-broken state by studying the curvature $V_\mathrm{eff}''(0)$ at the origin $\phi = 0$. Since g now has mass dimension $[g] = z - 2 = -1$, we rescale $g\Lambda/f_1 \mapsto g$, $\phi/(\sqrt{f_1}\Lambda^{3/2}) \mapsto \phi$, and $f_1/(f_2\Lambda) \mapsto f_1/f_2$. To the leading non-vanishing order in $(f_1/f_2)^{-1}$, the curvature is

$$V_\mathrm{eff}''(0) \propto 1 - \frac{4gN}{\pi^2} \left[1 + \frac{8}{63} \left(\frac{f_1}{f_2}\right)^{-2}\right]. \tag{5.32}$$

The phase boundary occurs when the curvature of the effective potential at the origin vanishes, yielding

$$g_\mathrm{c}(f_1/f_2) \simeq \frac{\pi^2}{4N} \left[1 - \frac{8}{63} \left(\frac{f_1}{f_2}\right)^{-2}\right], \tag{5.33}$$

---

[7] cf., e.g., Sun *et al.* (2009); Zhang *et al.* (2010); Vafek & Yang (2010); Vafek (2010); Uebelacker & Honerkamp (2011); Lang *et al.* (2012); Scherer, Uebelacker & Honerkamp (2012); Cvetkovic, Throckmorton & Vafek (2012); Song, Liang & Haas (2012)

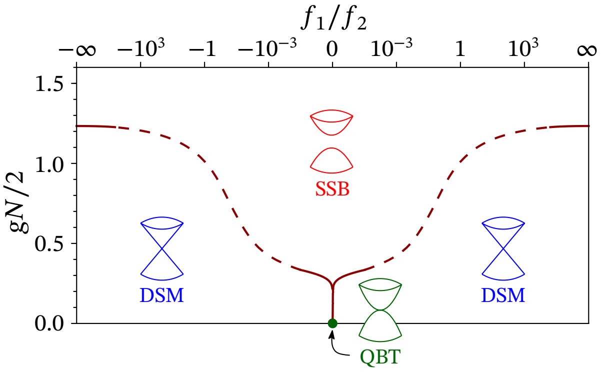

Figure 5.4: Mean-field phase diagram for $f_3 = 0$ using Eqs. (5.31) and (5.33), showing the Dirac semimetal (DSM) phase for small $g < g_c$ and finite f_1/f_2 and the spontaneous-symmetry-broken (SSB) phase for $g > g_c$. At the origin, $(f_1/f_2, g) = (0, 0)$, the fermion spectrum exhibits a quadratic band touching (QBT). The dashed curve at intermediate $|f_1/f_2| \simeq 1$ is given as a guide to the eye.

valid for $|f_1/f_2| \gg 1$. Note that, within our continuum field theory, the two limiting cases $f_1/f_2 \to \infty$ and $f_1/f_2 \to -\infty$ are in fact equivalent, as they are related by momentum inversion $\boldsymbol{p} \mapsto -\boldsymbol{p}$. Eq. (5.33) in this limit precisely agrees with the known large-N critical coupling in the relativistic Gross–Neveu theory with $2N$ four-component Dirac flavours in $2+1$ dimensions (Hands, Kocić & Kogut 1993; Braun, Gies & Scherer 2011). The perturbation $\propto (f_1/f_2)^{-2}$ is new and represents the influence of the quadratic term in the dispersion $\varepsilon(\boldsymbol{p})$. It decreases the critical coupling, which is consistent with the general expectation that an increase in the density of states tends to destabilize the disordered semimetallic state. The combined mean-field phase diagram, showing the phase boundaries both for $|f_1/f_2| \ll 1$ in the QBT regime as well as for $|f_1/f_2| \gg 1$ in the Dirac regime, is depicted in Fig. 5.4.

5.3 Renormalization-group analysis

5.3.1 Flow equations

To go beyond the mean-field level, we now turn to an RG analysis. Since we are dealing with a gapless model, the loop integrals will not only have UV, but also IR divergences. The most efficient way to regularize the theory is to use both a UV cut-off Λ as well as an IR cut-off k. The precise implementation of these cut-offs is, as usual, dictated by the detailed structure of the quantum corrections. In the present setting, the leading loop diagrams are shown in Fig. 5.5. (Possible diagrams of the same order that are not shown vanish in the the present single-channel approximation.) Note that the one-loop self-energy diagram is absent due to kinematics: It is independent of the external momentum (i.e., a so-called tadpole graph) and hence can at most generate a mass term, which is forbidden by symmetry. For completeness, let us also specify the definition of the renormalized fields and couplings. These are defined as

$$\Gamma_k\big[\psi, \psi^\dagger; X; \tau\big] \simeq S\Big[Z_{\psi,k}^{1/2} Z_\omega^{1/2}(\psi, \psi^\dagger); X_k; Z_\omega^{-1}\tau\Big], \tag{5.34}$$

i.e., the 1PI effective action computed with unrenormalized fields $(\psi, \psi^\dagger)$ and couplings $X = (g, f_1, f_2, f_3)$ as input and with IR cut-off k should be equivalent to the classical action we started with, but evaluated at suitably renormalized fields and couplings. We have suppressed the dependence on Λ, since it will usually drop out if the scheme is chosen judiciously enough in any case. Evaluating the loop diagrams in Fig. 5.5 allows us to read off the pertinent renormalization constants, and thence the β-functions as $\beta_X = -k\partial_k X_k$ for the couplings $X = (g, f_1, f_2, f_3)$ as well as the anomalous dimensions $\eta_\phi = -k\partial_k \ln Z_\psi$ for the fields. Finally, the running dynamical critical exponent is given by $z = 2 - \eta_\psi + k\partial_k \ln Z_\omega$.

Let us briefly sketch the general strategy regarding the evaluation of the loop corrections, beginning with the (evidently more challenging) two-loop self-energy correction shown in Fig. 5.5(a). The diagram has the so-called *sunset* topology. For translationally invariant systems, the evaluation of such diagrams turns out to be particularly efficient when carried out in position space (Groote, Körner & Pivovarov 1999). This way, the evaluation of the diagram ultimately leads to a single position-space integral, which is a considerable technical simplification over the corresponding momentum-space version. In particular, the two-loop contribution to the self-energy simply becomes

$$\Sigma(\omega,\boldsymbol{p}) \propto \int \mathrm{d}\tau\,\mathrm{d}^2\boldsymbol{x}\,\mathrm{e}^{-\mathrm{i}(\omega\tau+\boldsymbol{p}\cdot\boldsymbol{x})}\left(\sigma^3\otimes\sigma^3\right)G_0(\tau,\boldsymbol{x})\left(\sigma^3\otimes\sigma^3\right) \\ \times G_0(-\tau,-\boldsymbol{x})\left(\sigma^3\otimes\sigma^3\right)G_0(\tau,\boldsymbol{x})\left(\sigma^3\otimes\sigma^3\right) \qquad (5.35)$$

where $G_0(\tau,\boldsymbol{x}) = [\partial_\tau + \mathcal{H}_0(-\mathrm{i}\boldsymbol{\partial})]^{-1}$ is the tree-level propagator and we have suppressed coupling constants, numerical prefactors, and contraction over spinor indices for brevity. Similarly, the contribution to the four-fermion vertex can be written in position space as

$$\delta\Gamma^{(4)} \propto \int \mathrm{d}\tau\,\mathrm{d}^2\boldsymbol{x}\,G_0(\tau,\boldsymbol{x})\left(\sigma^3\otimes\sigma^3\right)G_0(-\tau,-\boldsymbol{x})\left(\sigma^3\otimes\sigma^3\right), \qquad (5.36)$$

where we have also set external coordinates to zero.

All position-space integrals are now regularized simply using sharp cut-offs both in the short- and long-wavelength limits, viz. $\ell \propto 1/\Lambda \simeq a$ and $L \propto 1/k$. In the QBT regime, we put

$$\int_{\text{reg., QBT}} \mathrm{d}\tau\,\mathrm{d}^2\boldsymbol{x} = \int \mathrm{d}\tau\,\mathrm{d}^2\boldsymbol{x}\,\Theta(|\boldsymbol{x}| - \pi/(2k))\,\Theta(\pi/(2\Lambda) - |\boldsymbol{x}|), \qquad (5.37)$$

whilst in the Dirac regime, we choose

$$\int_{\text{reg., Dirac}} \mathrm{d}\tau\,\mathrm{d}^2\boldsymbol{x} = \int \mathrm{d}\tau\,\mathrm{d}^2\boldsymbol{x}\,\Theta\left(\sqrt{\tau^2+\boldsymbol{x}^2} - \pi/(2k)\right)\Theta\left(\pi/(2\Lambda) - \sqrt{\tau^2+\boldsymbol{x}^2}\right). \qquad (5.38)$$

This regularization prescription not only respects the different symmetries in the strict QBT and Dirac limits, but also allows us to perform the loop integrations analytically. Note also that (i) the presence of the IR cut-off allows the self-energy to be expanded in external momenta, and (ii) the derivative with respect to k collapses the 'radial' part of the loop integration, since the (weak) derivative of the Heaviside Θ-function is the Dirac δ-distribution. The *a priori* arbitrary constant $\pi/2$ in the definition of the position-space cutoffs has been chosen such that the resulting large-N critical coupling g_c in the Dirac limit $|f_1/f_2| \to \infty$ matches the mean-field result, Eq. (5.33). Evidently, a major part of the difficulty of evaluating the loop corrections now resides in computing the position space propagator $G_0(\tau,\boldsymbol{x})$, additional information pertaining to which is given in Appendix A.

The fact that the location and shape of the Fermi surface changes when a QBT point splits into four Dirac cones requires us to start with separate discussions of the two cases

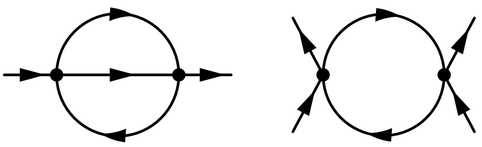

(a) (b)

Figure 5.5: Feynman diagrams representing the first non-vanishing loop corrections to self-energy and the four-fermion vertex.

$|f_1/f_2| \ll 1$ and $|f_1/f_2| \gg 1$. To obtain the full RG flow also for finite values of $|f_1/f_2| \sim 1$, we shall eventually interpolate between the respective limits by means of a suitable Padé approximation.

Let us start by discussing the QBT limit, to which an infinitesimal $|f_1/f_2| \ll 1$ has been added. Keeping the quadratic coefficient f_2 fixed, the β-function $\beta_g \equiv -k\partial_k g_k$ for the dimensionless short-range interaction g becomes

$$\beta_g = \frac{g^2(N-1)}{2\pi}\left[1 - \frac{7-4\ln 2}{240}\frac{\pi^2}{4}\left(\frac{f_1}{f_2}\right)^2 + \frac{1}{2}\left(\frac{f_1}{f_2}\right)\left(\frac{f_3}{f_2}\right) + \frac{32}{\pi^2}\left(\frac{f_3}{f_2}\right)^2\right], \tag{5.39}$$

where we have rescaled $f_1/(f_2 k) \mapsto f_1/f_2$, $f_3 k/f_2 \mapsto f_3/f_2$, and $g/f_2 \mapsto g$ as in the mean-field theory. Note that the above equation is valid only for $N > 1$. For $N = 1$, there is an additional Fierz identity which leads to a finite β-function for g in this case as well. The self-energy diagram in Fig. 5.5(a) leads to a nontrivial flow of the small parameters f_1 and f_3. To the leading order in f_1/f_2 and f_3/f_2, they are given by

$$\beta_{f_1/f_2} = \left(1 - \frac{g^2(2N-1)}{144\pi^2}\right)\left(\frac{f_1}{f_2}\right) + \frac{11g^2(2N-1)}{54\pi^4}\left(\frac{f_3}{f_2}\right) \tag{5.40}$$

and

$$\beta_{f_3/f_2} = -\left(1 + \frac{59g^2(2N-1)}{3456\pi^2}\right)\left(\frac{f_3}{f_2}\right) + \frac{g^2(2N-1)}{576}\left(\frac{f_1}{f_2}\right). \tag{5.41}$$

The anomalous field dimension η_ψ reads in this limit

$$\begin{aligned}\eta_\psi = \frac{g^2(2N-1)}{4\pi^2}\Bigg[&\frac{1}{18} - \frac{25-36\ln(4/3)}{2880}\frac{\pi^2}{4}\left(\frac{f_1}{f_2}\right)^2 \\ &- \left(\frac{3}{2}\ln\frac{4}{3} - \frac{179}{432}\right)\left(\frac{f_1}{f_2}\right)\left(\frac{f_3}{f_2}\right) + \frac{871}{243\pi^2}\left(\frac{f_3}{f_2}\right)^2\Bigg]\end{aligned} \tag{5.42}$$

and the dynamic critical exponent z becomes

$$z = 2 - \frac{g^2(2N-1)}{4\pi^2}\left[\frac{9\ln(4/3)-2}{72} + \frac{49-30\ln 2 - 9\ln 3}{5760}\frac{\pi^2}{4}\left(\frac{f_1}{f_2}\right)^2\right. \tag{5.43}$$

$$\left. - \frac{1593\ln(4/3)-422}{216}\left(\frac{f_1}{f_2}\right)\left(\frac{f_3}{f_2}\right) + \frac{1850-4860\ln(4/3)}{243\pi^2}\left(\frac{f_3}{f_2}\right)^2\right]. \tag{5.44}$$

Note that the contribution $\propto (f_1/f_2)^2$ to z is negative, tending to decrease the dynamic exponent from $z = 2$ towards the Dirac value of $z = 1$ for large enough $|f_1/f_2|$.

In the Dirac limit with a quadratic perturbation $\propto f_2$ added to the Hamiltonian, the effects of the strongly-irrelevant cubic coefficient f_3 can be safely neglected. We find, for $|f_1/f_2| \gg 1$, $f_3 = 0$, and $N_\mathrm{f} = 2N$ Dirac flavours, for the flow of the short-range interaction

$$\beta_g = -g + \frac{g^2(4N-1)}{\pi^2}\left[1 + \frac{4128}{35\pi^2}\left(\frac{f_2}{f_1}\right)^2\right], \tag{5.45}$$

where we now have rescaled $gk/f_1 \mapsto g$ and $f_2 k/f_1 \mapsto f_2/f_1$. The small parameter f_2/f_1 is irrelevant in the Dirac limit; its flow reads as

$$\beta_{f_2/f_1} = -\left[1 + \frac{29}{420}\frac{g^2(8N-1)}{\pi^4}\right]\left(\frac{f_2}{f_1}\right). \tag{5.46}$$

The anomalous dimension η_ψ and the dynamic critical exponent z become in this limit

$$\eta_\psi = \frac{g^2(8N-1)}{\pi^4}\left[\frac{1}{12} + \frac{1312}{105\pi^2}\left(\frac{f_2}{f_1}\right)^2\right], \tag{5.47}$$

$$z = 1 - \frac{8g^2(8N-1)}{\pi^6}\left(\frac{f_2}{f_1}\right)^2. \tag{5.48}$$

5.3.2 Basic flow properties

Before solving the full set of flow equations to construct phase diagrams, let us first extract some general characteristics by analytical means. We begin with the Dirac case, which in the limit $|f_1/f_2| \to \infty$ boils down to the $(2+1)$-dimensional relativistic Gross–Neveu theory. Apart from the fully attractive non-interacting Dirac fixed point

$$\mathrm{D}: \qquad (f_1/f_2, g)_* = (\pm\infty, 0)\,, \tag{5.49}$$

the only interacting fixed point for $|f_1/f_2| \gg 1$ is at

$$\mathrm{GN}_3: \qquad (f_1/f_2, g)_* = \left(\pm\infty, \frac{\pi^2}{4N-1}\right). \tag{5.50}$$

The fixed point GN_3 is characterized by a dynamic critical exponent $z = 1$ and an anomalous dimension

$$\eta_\psi = \frac{8N-1}{12(4N-1)^2}. \tag{5.51}$$

For $N = 2$, this yields $\eta_\psi = 0.026$. Within our approximation, the correlation-length exponent $\nu = 1$, but there will be N-dependent corrections once higher loop orders are taken into account. GN_3 has a unique RG relevant direction along the g axis, as f_2/f_1 is irrelevant in its vicinity. We also note that other short-range interactions, such as flavour-symmetry-breaking operators, are irrelevant at this fixed point (Gehring, Gies & Janssen 2015). GN_3 describes a transition from the semimetallic Dirac phase for $g < g_*$ to an ordered phase for $g > g_*$, in which the fermions acquire a dynamical mass gap as a consequence of spontaneous symmetry breaking. Hence, GN_3 is an incarnation of the celebrated relativistic Gross–Neveu critical point in 2 + 1 dimensions.[8] (This also explains the choice of notation.) In our interaction channel, the ordered state is characterized by $\langle\psi^\dagger(\sigma^3\otimes\sigma^3)\psi\rangle \neq 0$, which spontaneously breaks inversion symmetry between the layers (Vafek 2010). In the large-N limit, the Gross–Neveu fixed-point value is $g_* = \pi^2/(4N) + \mathcal{O}(1/N^2)$, in agreement with the result we found in the mean-field theory, Eq. (5.33). Note that values of couplings are in principle non-universal and depend on the regularization scheme. Here, the position-space regularization has been adapted to match the mean-field result for the critical coupling. However, it is worth emphasizing that this agreement may not carry over in the case of other nonuniversal quantities. For instance, this is the case for the separatrix that defines the phase boundary between the Dirac semimetal and the interaction-induced insulator for $|f_1/f_2| \gg 1$, which is obtained from the RG flow as

---

[8] For instance, see Hands, Kocić & Kogut (1993); Vasil'ev, Derkachev & Stepanenko (1993); Gracey (1994b); Vojta, Zhang & Sachdev (2000a,b); Braun, Gies & Scherer (2011); Gracey, Luthe & Schröder (2016); Mihaila *et al.* (2017); Zerf *et al.* (2017); Iliesiu *et al.* (2018); Ihrig *et al.* (2018).

$$g_{\mathrm{c}}(f_1/f_2) \simeq \frac{\pi^2}{4N-1}\left[1 - \frac{4128}{35\pi^2}\left(\frac{f_1}{f_2}\right)^{-2}\right]. \tag{5.52}$$

This is in qualitative, but not quantitative, agreement with the mean-field result, Eq. (5.33). Let us reiterate that this discrepancy is a consequence of the difference in regularization schemes and has no effect on universal observable quantities such as critical exponents, mass ratios, etc., which are scheme-independent.

Let us now proceed to the QBT limit for $0 \leqslant |f_1/f_2| \ll 1$. In this regime, there is only the Gaußian fixed point at

$$\mathrm{Q}: \qquad (f_1/f_2, g)_* = (0,0)\,, \tag{5.53}$$

describing a noninteracting Fermi system with a quadratic dispersion. The fixed point Q has a marginal direction along the g axis, while f_1 is power-counting relevant.

Let us first review the O(2)-invariant case for $f_1 = f_3 = 0$ and $g > 0$ in order to connect with previous work by Sun *et al.* (2009). In this case, β_g is positive and finite for all $g > 0$, implying an instability of the system towards the infrared. More precisely, integrating the RG flow equation for g, Eq. (5.39), we find for $f_1 = f_3 = 0$,

$$g(k) = \frac{1}{1/g_0 - \ln(\Lambda/k)(N-1)/(2\pi)}, \qquad \text{for } k \geqslant k_{\mathrm{SSB}}, \tag{5.54}$$

with initial value $g_0 \equiv g(k=\Lambda)$. Patently, the evolution of g exhibits a pole at a finite RG time $\ln(\Lambda/k_{\mathrm{SSB}}) = -2\pi/[g_0(N-1)]$. Informed by the mean-field analysis, we can trace back this runaway flow to an instability of the semimetallic state towards the interaction-induced insulator. The latter is characterized by inversion-symmetry breaking and a finite vacuum expectation value of the fermion bilinear $\langle\phi\rangle \propto \langle\psi_i^\dagger(\sigma^3\otimes\sigma^3)\psi^i\rangle \neq 0$. The effective amplitude of the condensate follows essentially from dimensional analysis,

$$\langle\phi\rangle \propto k_{\mathrm{SSB}}^2 \propto \mathrm{e}^{-4\pi/[g_0(N-1)]}, \tag{5.55}$$

where we have used the order parameter's scaling dimension $[\phi] = (z+2)/2 = 2$. It is conceptually satisfying to note that the exponential factor in the above estimate in the limit $N \to \infty$ agrees precisely with the mean-field result, Eq. (5.29). This furnishes a nontrivial consistency check.

The RG flow equations also allow one to compute the form of the phase boundary at finite $0 < |f_1/f_2| \ll 1$. To this end, consider trajectories in parameter space starting infinitesimally close to the non-interacting QBT fixed point Q. In this regime, f_1/f_2 flows according to its canonical scaling dimension, $(f_1/f_2)(k) = (f_1/f_2)_0\, k/\Lambda$, where

$(f_1/f_2)_0 \equiv (f_1/f_2)(k = \Lambda)$, whereas the RG evolution of g is given by Eq. (5.54) above. Eliminating k/Λ, one finds the RG trajectories near the fixed point Q as

$$g(f_1/f_2) = \frac{2\pi}{N-1}\frac{1}{\ln C - \ln|f_1/f_2|} \tag{5.56}$$

with a positive constant $C = \mathrm{e}^{2\pi/[g_0(N-1)]}|f_1/f_2|_0$ that is determined by the initial values $((f_1/f_2)_0, g_0)$ of the flow for $k = \Lambda$. Each member of the family of RG trajectories defined by Eq. (5.56) and parametrized by C can now be continued 'backwards' in RG time $\ln(\Lambda/k) \to -\infty$ and will eventually approach the noninteracting QBT fixed point Q. In the opposite RG time direction, $t \to \infty$, one member of the family must be the separatrix that precisely flows into the critical Gross–Neveu fixed point GN$_3$ in the Dirac limit for $|f_1/f_2| \gg 1$. In the mean-field theory, this happens for $C = \ln 4$, for which the large-N limit of Eq. (5.56) agrees with Eq. (5.31). Without the mean-field input, the perturbative RG analysis around Q for $|f_1/f_2| \ll 1$ alone has nothing to say on which of the trajectories is the separatrix; we shall discuss in the following subsection how to circumvent this problem by making use of the flow near the Gross–Neveu fixed point in the opposite limit $|f_1/f_2| \gg 1$. In this subsection, it shall suffice to note that a separatrix that connects Q with GN$_3$ exists for all N and has the form as given in Eq. (5.56).

Let us now discuss the situation for $f_3 \neq 0$, which induces non-trivial self-energy corrections that go beyond the mean-field result. To see this, consider the trajectories starting on the $f_1 = 0$ line. Inspecting the flow equations, one finds the slope of all trajectories with $g > 0$ as

$$\frac{\mathrm{d}(f_1/f_2)}{\mathrm{d}g} = \frac{\beta_{f_1/f_2}}{\beta_g} = \frac{11}{27\pi^3}\frac{2N-1}{N-1}\frac{f_3}{f_2}\frac{1}{1+\frac{32}{\pi^2}(f_3/f_2)^2} + \mathcal{O}(f_1/f_2). \tag{5.57}$$

Importantly, the slope is finite for all $g > 0$, implying that every RG trajectory (except the one that connects the free theories Q and D at fixed $g = 0$) crosses the line $f_1 = 0$ at a finite g when $f_3 \neq 0$. In particular, this is true for the separatrix that connects Q with GN$_3$. There must, therefore, be a critical coupling strength $g_\mathrm{c} > 0$, below which the system flows to a Dirac semimetal phase – in contrast to the situation at a symmetry-protected QBT (cf. Chap. 4). This hence provides a rigorous RG demonstration of the phenomenology found numerically by Pujari *et al.* (2017). It is also consistent with the result obtained within a random phase approximation by Honerkamp (2017).

We close by answering why the mean-field theory is unaware of this behaviour, the reason for which is more transparent when the above is expressed in terms of the 't Hooft coupling $g' \equiv gN$, which remains finite at the Gross–Neveu fixed point GN$_3$. In $(f_1/f_2, g')$ space, the same slope is

$$\frac{\mathrm{d}(f_1/f_2)}{\mathrm{d}g'} = \frac{22}{27\pi^3 N}\frac{f_3}{f_2} + \mathcal{O}\big(f_1/f_2, 1/N^2\big)\,, \tag{5.58}$$

and is therefore subleading when sending $N \to \infty$ while keeping $g' = \text{const}$. In other words, self-energy effects are suppressed in the large-N limit.

5.3.3 Phase diagrams

We proceed to construct the RG phase diagram in the full $(f_1/f_2, g)$ coupling space. As the configuration of the Fermi surface changes from the QBT limit for $|f_1/f_2| \ll 1$ to the Dirac limit for $|f_1/f_2| \gg 1$, the standard regularization scheme in momentum

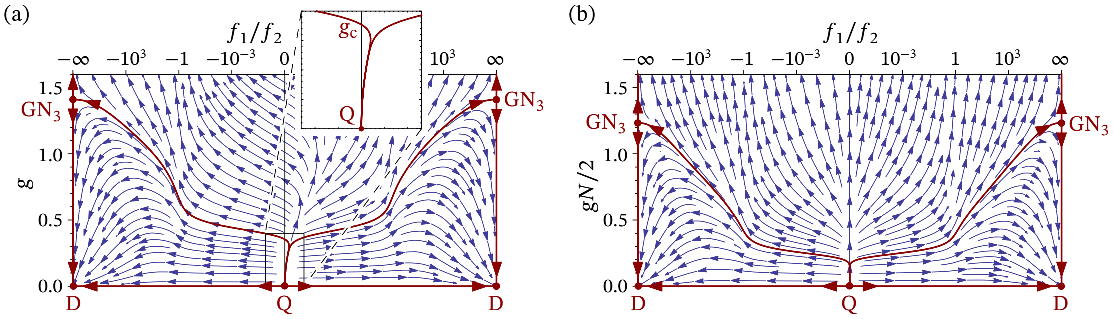

Figure 5.6: RG flow diagram in the plane spanned by (f_1/f_2) and g for constant $f_3 = (2\sqrt{3})^{-1}$ for (a) $N = 2$ and (b) in the limit $N \to \infty$. The Gaussian fixed points corresponding to the non-interacting Dirac and QBT systems are denoted D and Q respectively, while GN$_3$ is the $(2+1)$-dimensional Gross–Neveu fixed point. The separatrices connecting the different fixed points are shown in dark red.

space, as well as our position-space regularization scheme, required us to *a priori* treat these different regimes separately. This approach led us to the flow equations (5.39)–(5.41) in the former limit and (5.45)–(5.46) in the latter, and these equations should be understood as asymptotic expansions in the two different regimes of an unknown set of flow equations valid for all f_1/f_2. A useful approximation to these can be obtained by employing suitable Padé approximants which interpolate between the known limits. The $[m/n]$ Padé approximant is defined as a degree m/degree n rational function, where the coefficients in the polynomial numerator and denominator are chosen such that the approximant reproduces the correct expansions for $|f_1/f_2| \ll 1$ (QBT regime) and $|f_1/f_2| \gg 1$ (Dirac regime). For the flow equations of f_1/f_2 and f_3/f_2 we use $[3/2]$ and $[2/2]$ Padé approximants,

$$\beta_{f_1/f_2} = \frac{a_0 + a_1(f_1/f_2) + a_2(f_1/f_2)^2 + (f_1/f_2)^3}{1 + b_1(f_1/f_2) + b_2(f_1/f_2)^2}, \tag{5.59}$$

$$\beta_{f_1/f_2} = \frac{c_0 + c_1(f_1/f_2) + c_2(f_1/f_2)^2}{1 + (f_1/f_2)^2}, \tag{5.60}$$

which corresponds to the minimal degree necessary to match Eqs. (5.40), (5.41), and (5.46). Other choices are possible in principle as well, and the above approximants have been selected under the demand that they be of minimal degree needed to faithfully reproduce the asymptotic expansions for $f_1/f_2 \to 0$ and $f_2/f_1 \to 0$, respectively, and do not introduce any unphysical poles in the resulting Padé-approximated flow equations. For the flow equation of g, it proved advantageous to perform the interpolation separately for the even and odd parts in f_1/f_2, explicitly

$$\beta_g = \frac{d_0 + d_2(f_1/f_2)^2 + d_4(f_1/f_2)^4}{1 + e_2(f_1/f_2)^2 + (f_1/f_2)^4} + \frac{d_1(f_1/f_2)}{1 + (f_1/f_2)^4}. \tag{5.61}$$

Note that the coefficients a_i, b_i, c_i, d_i, and e_i are independent of f_1/f_2, but depend on g and f_3/f_2. Their explicit values are given in Appendix B.

The resulting RG flow diagram for $N = 2$, relevant for the honeycomb bilayer, is depicted in Fig. 5.6(a). The diagram shows a cut through parameter space at a fixed $f_3/f_2 = (2\sqrt{3})^{-1}$ in the QBT regime, chosen to match the microscopic tight-binding value in the honeycomb bilayer, Eq. (5.20). For simplicity, the UV cut-off Λ has been identified with the inverse of the lattice constant. Apart from the non-interacting fixed points Q at

$f_1/f_2 = 0$ and D at $|f_1/f_2| = \infty$, the critical Gross–Neveu fixed point GN$_3$ at $|f_1/f_2| = \infty$ is the only interacting fixed point. (Recall that the two vertical axes at $f_1/f_2 = +\infty$ and $f_1/f_2 = -\infty$ should be identified with each other, as they are related by inversion symmetry $\boldsymbol{p} \mapsto -\boldsymbol{p}$ emerging for $f_2 = f_3 = 0$.) All RG trajectories for $g > 0$ cross the QBT axis at $f_1/f_2 = 0$ with a finite slope. The separatrix connecting Q with GN$_3$ in the regime $f_1/f_2 \geqslant 0$ therefore crosses this line at a finite value of the coupling. The critical coupling g_c at which this happens for $N = 2$ and fixed $f_3/f_2 = (2\sqrt{3})^{-1}$ in the QBT regime is found to be $g_\mathrm{c} \approx 0.35$. We have checked numerically that the inclusion of the running of f_3/f_2 in the QBT regime does not change the qualitative characteristics of the flow diagram, and only moderately modifies its quantitative features. In particular, we find that the improved critical coupling that includes the running of f_3/f_2 is $g_\mathrm{c} \approx 0.40$ for the initial value $(f_3/f_2)(t = 0) = (2\sqrt{3})^{-1}$. This should be contrasted with the situation for $N \to \infty$, depicted in Fig. 5.6(b). In this limit, the flow diagram becomes symmetric with respect to $f_1/f_2 \mapsto -f_1/f_2$, and the separatrices no longer cross the QBT axis for strict $N = \infty$. Inclusion of a finite f_3/f_2 has qualitatively no influence. In the QBT limit, the critical coupling g_c, below which the semimetallic phase is stable, vanishes for large N, implying spontaneous symmetry breaking for all finite values of $g > 0$. As an aside, let us note the qualitative agreement between Figs. 5.6(b) and 5.4, which is reassuring.

The low-temperature physics conveyed by the RG flow can be summarized as follows:

1.) For initial couplings $f_1 = f_3 = 0$, which corresponds to the QBT with the full rotational O(2) symmetry, there is an instability already at infinitesimal coupling, in agreement with the previous works.[9] This is illustrated in Fig. 5.7(a).

2.) For the QBT systems with C_3 symmetry only and trigonal warping tuned to zero, $f_1 = 0$ and $f_3 \neq 0$, there is a stable Dirac semimetal phase for $g < g_\mathrm{c}$ with a finite critical coupling $g_\mathrm{c} > 0$, see Fig. 5.7(b). The instability occurs only for $g > g_\mathrm{c}$, in agreement with the numerics of Pujari *et al.* (2017). The critical coupling vanishes in the large-N limit, as well as when all O(2)-breaking microscopic perturbations, such as f_3, vanish.

3.) When the QBT point is split into the four symmetry-allowed Dirac points by a sufficiently small positive trigonal warping, a more complex scenario emerges. For initial (microscopic) parameters $0 < f_1/f_2 \ll 1$, lines of constant f_1/f_2 cross a separatrix connecting Q and GN$_3$ three times. This leads to a rich phase diagram as a function of the short-range coupling g, including three quantum phase transitions at $g_{\mathrm{c}i}$, $i = 1, 2, 3$, between semimetallic and symmetry-broken phases, see Fig. 5.7(c). In the limit $f_1/f_2 \searrow 0$, both $g_{\mathrm{c}1}$ and $g_{\mathrm{c}2}$ go to zero, and we recover the standard phase diagram comprising a single critical coupling $g_\mathrm{c} \equiv g_{\mathrm{c}3}$. This scenario is directly testable in current numerical setups (Lang *et al.* 2012; Pujari *et al.* 2017).

5.4 Discussion

Let us discuss the critical behaviour that one should expect for the continuous semimetal-insulator transitions established above for QBT systems with C_3 symmetry. To begin

---

[9] cf. Sun *et al.* (2009); Zhang *et al.* (2010); Vafek & Yang (2010); Vafek (2010); Uebelacker & Honerkamp (2011); Lang *et al.* (2012); Scherer, Uebelacker & Honerkamp (2012); Cvetkovic, Throckmorton & Vafek (2012); Song, Liang & Haas (2012)

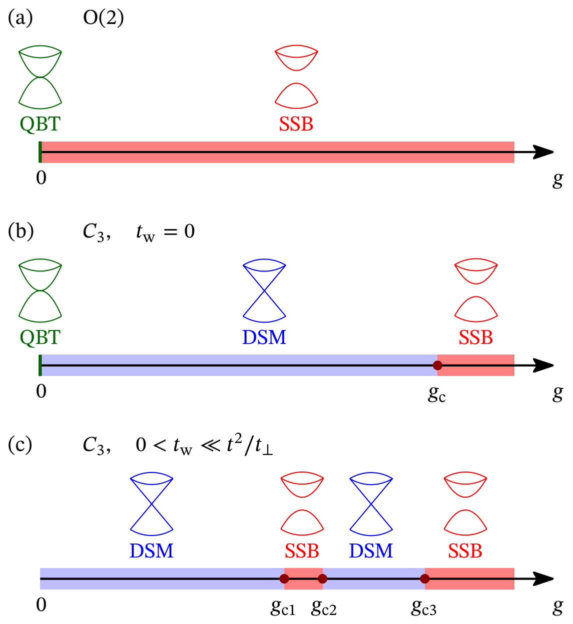

Figure 5.7: Schematic low-temperature phase diagram of QBT systems with (a) full rotational O(2) symmetry, (b) C_3 symmetry without trigonal warping $t_\mathrm{w} = 0$ and (c) sufficiently small trigonal warping $0 < t_\mathrm{w} \ll t^2/t_\perp$ on the microscopic level, as a function of the short-range interaction g. The insets indicate the low-energy fermion spectra in the quadratic band touching (QBT), Dirac semimetal (DSM), and spontaneous-symmetry-broken (SSB) phases.

with, note that all RG fixed points found by interpolating between the QBT and Dirac regimes are located in the strict limits $f_1/f_2 = 0$ and $|f_1/f_2| \to \infty$, respectively. That this must be so, at least on the level of perturbation theory, can be inferred from the following indirect argument: Assume that a fixed point at finite $0 < |f_1/f_2| < \infty$ exists. Such a fixed point would describe a scale-invariant Dirac system in which the coefficient f_2/f_1 of the quadratic term in the dispersion does not flow. This, however, is in contradiction with the fact that f_2/f_1 is power-counting irrelevant. Thence, the only possible path in parameter space for the separatrix emanating from the fixed point GN$_3$, when continued backwards in RG time, is through the QBT axis $f_1/f_2 = 0$ (crossing this axis, as we have seen above, at a finite angle), and eventually approaching the fixed point Q. This general argument is in agreement with our explicit findings, see Fig. 5.6.

The quantum critical transitions shown in Figs. 5.7(b) and (c) are therefore described by the fully relativistic Gross–Neveu universality class with dynamic exponent $z = 1$, comparatively large correlation-length exponent $\nu = 1 + \mathcal{O}(1/N)$, and large order-parameter anomalous dimension $\eta_\phi = 1 + \mathcal{O}(1/N)$. The $\mathcal{O}(1/N)$ corrections to these exponents depend on the symmetry of the order parameter and the number of fermion flavours, as we discuss in the following.

For the case of spinless fermions on the honeycomb bilayer, natural instabilities are towards an inversion-symmetry-broken state (Vafek 2010), a charge-density wave (Scherer, Uebelacker & Honerkamp 2012), or a quantum anomalous Hall phase (Sun *et al.* 2009; Zhu *et al.* 2016; Zeng, Zhu & Sheng 2018; Sur *et al.* 2018), all of which spontaneously break Ising $\mathbb{Z}_2$ symmetries. The critical exponents of the corresponding Gross–Neveu–Ising universality class are well-established.[10] Within the $1/N$ expansion, they read as (Vasil'ev, Derkachev & Stepanenko 1993; Gracey 1994b; Janssen & Herbut 2014)

---

[10] cf., e.g., Hands, Kocić & Kogut (1993); Vasil'ev, Derkachev & Stepanenko (1993); Gracey (1994b);

$$\begin{aligned}
1/\nu &= 1 - \frac{4}{3\pi^2 N} + \frac{632 + 27\pi^2}{27\pi^4 N^2} + \mathcal{O}(1/N^3) \\
&\approx 1.018(85) \qquad \text{for } N = 2, \qquad (5.62) \\
\eta_\phi &= 1 - \frac{8}{3\pi^2 N} + \frac{304 - 27\pi^2}{27\pi^4 N^2} + \mathcal{O}(1/N^3) \\
&\approx 0.868(4) \qquad \text{for } N = 2. \qquad (5.63)
\end{aligned}$$

Here, the size of the $\mathcal{O}(1/N^2)$ correction serves as a simple estimate for the numerical uncertainty at $N = 2$. Note that N in the present notation corresponds to the number of QBT points in the microscopic theory, each of which splits into four Dirac points with two-component (pseudo-)spinors (equivalent to two four-component Dirac flavours per QBT valley), in the case without a physical spin. The values of the other exponents α, β, γ, and δ can be obtained from ν and η_ϕ by means of the usual hyperscaling relations (Herbut 2007). For the fermion anomalous dimension, even the $\mathcal{O}(1/N^3)$ correction is known,

$$\begin{aligned}
\eta_\psi &= \frac{1}{3\pi^2 N} + \frac{28}{27\pi^4 N^2} - \frac{501 + 2268\zeta(3) - \pi^2(94 + 216\ln 2)}{1296\pi^6 N^3} + \mathcal{O}(1/N^4) \\
&\approx 0.0195(1) \qquad \text{for } N = 2. \qquad (5.64)
\end{aligned}$$

Although the precise determination of the exponents has not been the focus of our endeavours this chapter, it is satisfying to note broad agreement of the above results with our RG calculations, which led to the estimates $\nu \approx 1$ and $\eta_\psi \approx 0.026$ for $N = 2$, as noted earlier.

For the spin-1/2 case, the number of fermion flavours is doubled, i.e., $N = 4$ for the case of the honeycomb bilayer. An instability towards a charge density wave phase is possible in this case as well upon tuning the nearest-neighbor repulsion (Scherer, Uebelacker & Honerkamp 2012). Such a transition would be described by the Gross–Neveu–Ising universality class with the above equations evaluated for $N = 4$, leading to $1/\nu \approx 0.988(21)$, $\eta_\phi \approx 0.933(1)$, and $\eta_\psi = 0.00910(1)$. The most natural instability, however, which occurs upon tuning the on-site Hubbard repulsion, is towards the Néel antiferromagnet (Lang *et al.* 2012; Pujari *et al.* 2017), spontaneously breaking the Heisenberg SU(2) spin symmetry. The critical behaviour of the continuous transition is described by the corresponding Gross–Neveu–Heisenberg universality class.[11] In the $1/N$ expansion, the exponents are (Gracey 2018)

$$\begin{aligned}
1/\nu &= 1 - \frac{4}{\pi^2 N} + \frac{104 + 9\pi^2}{3\pi^4 N^2} + \mathcal{O}(1/N^3) \\
&\approx 0.940(41) \qquad \text{for } N = 4, \qquad (5.65) \\
\eta_\phi &= 1 + \frac{16 + 3\pi^2}{3\pi^4 N^2} + \mathcal{O}(1/N^3) \\
&\approx 1.010(10) \qquad \text{for } N = 4, \qquad (5.66)
\end{aligned}$$

Vojta, Zhang & Sachdev (2000a,b); Braun, Gies & Scherer (2011); Gracey, Luthe & Schröder (2016); Mihaila *et al.* (2017); Zerf *et al.* (2017); Iliesiu *et al.* (2018); Ihrig *et al.* (2018)

[11] cf. Janssen & Herbut (2014); Parisen Toldin *et al.* (2015); Otsuka, Yunoki & Sorella (2016); Zerf *et al.* (2017); Knorr (2018); Gracey (2018)

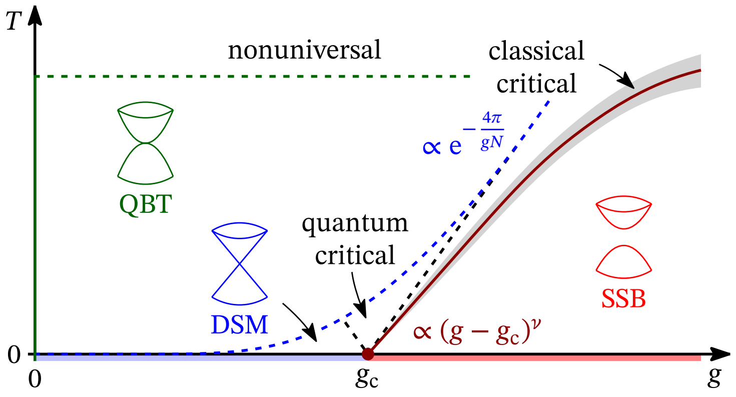

Figure 5.8: Schematic phase diagram of QBT systems with C_3 symmetry as a function of temperature T and short-range interaction g. Dashed curves denote crossovers, the solid curve denotes the finite-temperature phase transition for the case of discrete symmetry breaking. The dashed green horizontal line separates the universal regime at intermediate and low temperatures from the non-universal high-temperature regime. At intermediate temperatures, the fermion spectrum is effectively quadratic, characterized by dynamic exponent $z = 2$ (QBT). At temperatures below the blue dashed curve, the flow enters the Dirac regime with $z = 1$ (DSM). The black dashed lines emerging from the critical point at g_c denote the quantum critical regime, characterized by a continuum of excitations. The transition towards the ordered phase occurs at finite temperature in the case of discrete spontaneous symmetry breaking (SSB). The critical temperature $T_c \propto (g - g_c)^\nu$ is shown as solid red curve, together with its concomitant classical critical regime (grey shaded).

and

$$\begin{aligned}\eta_\psi &= \frac{1}{\pi^2 N} + \frac{4}{3\pi^4 N^2} - \frac{332 - 378\zeta(3) + 9\pi^2(5 + 4\ln 2)}{72\pi^6 N^3} + \mathcal{O}(1/N^4) \\ &\approx 0.0261(1) \qquad \text{for } N = 4, \end{aligned} \tag{5.67}$$

with $z = 1$. Let us note that the rough estimates $\nu = 1.0(2)$ and $z = 0.9(2)$ obtained by Pujari *et al.* (2017) in simulations of spin-1/2 fermions on the honeycomb bilayer are consistent with the above values for $N = 4$ (corresponding to eight flavours of four-component Dirac spinors).

Let us append a discussion on the expected finite-temperature phase diagram, assuming a QBT system without trigonal warping (i.e., $t_\mathrm{w} = 0$) on the microscopic level. The qualitative finite-temperature behaviour can be obtained from the RG by noting that temperature sets a scale at which the flow is effectively cut off. For weak interactions $g \ll g_c$, the RG scale at which the flow escapes the regime of fixed point Q is exponentially suppressed, leading to a large regime of temperature values at which the dynamic critical exponent is effectively $z = 2$, see Fig. 5.8. Signatures of the splitting into Dirac cones will only be observable at low enough temperatures $T \lesssim (T_*/N^2)\exp(-\frac{4\pi}{gN})$, where $T_* = \mathcal{O}(t^2/t_\perp)$ denotes the absolute energy scale in the honeycomb bilayer system and the factor $1/N^2$ accounts for the fact that self-energy effects are suppressed in the large-N limit, cf. Eq. (5.58). In the quantum critical regime at $g \simeq g_c$, there is a continuum of excitations and the specific heat C_V, for instance, will scale as

$$C_V \propto T^{d/z} \simeq \begin{cases} T & \text{for } T \gtrsim T_* N^{-2} \mathrm{e}^{-4\pi/(g_c N)}, \\ T^2 & \text{for } T \lesssim T_* N^{-2} \mathrm{e}^{-4\pi/(g_c N)}. \end{cases} \tag{5.68}$$

At stronger couplings $g > g_c$, there will be a finite-temperature phase transition towards an ordered state, assuming that the latter does not break a continuous symmetry. This is, for instance, the case for the inversion-symmetry-broken, charge density wave, or quantum anomalous Hall states discussed earlier. The critical temperature scales as $T_c \propto (g - g_c)^{\nu z}$ with $z = 1$ and ν as in Eq. (5.62) near the $(2+1)$D Gross–Neveu–Ising quantum critical point. The classical critical regime in the vicinity of the finite-temperature transition in this case is then described by the classical 2D Ising universality class, e.g., $\nu = 1$ and $\eta_\phi = 1/4$. It shrinks upon approaching $g \to g_c$ from above. Note that in the case of continuous symmetry breaking in the ordered ground state, such as in the spin-1/2 Hubbard model on the honeycomb bilayer for large on-site repulsion, there will be no genuine finite-temperature transition as a consequence of the Coleman–Mermin–Wagner theorem. Nevertheless, the finite-temperature crossovers depicted in Fig. 5.8 will persist.

5.5 Summary and outlook

We have performed a theoretical analysis of 2D Fermi systems with quadratic band touching on lattices with C_3 symmetry. A natural physical realization is given by the problem of interacting fermions on Bernal-stacked bilayer honeycomb lattices, such as in bilayer graphene. We have derived an effective low-energy continuum field theory that accounts for the explicit breaking of the continuous rotational symmetry characteristic for tricoordinate lattices and have shown, within a consistent perturbative RG calculation, that density-density interactions at two loops drive a splitting of each QBT point into four Dirac cones. In contrast to the QBT systems with full rotational symmetry, in the systems with C_3 symmetry only, the semimetallic state is stable within a finite range of interactions $0 < g < g_c$. At the critical coupling g_c, the system undergoes a continuous quantum phase transition that has no classical analogue due to the presence of gapless fermion degrees of freedom at criticality. This result is in agreement with previous quantum Monte Carlo (Pujari *et al.* 2017) and random phase approximation studies (Honerkamp 2017).

The RG flow demonstrates that the quantum critical behaviour near g_c is described by the celebrated Gross–Neveu–Ising (Gross–Neveu–Heisenberg) universality class for the case of Ising (Heisenberg) symmetry breaking, and we have given estimates for the universal critical exponents by employing known large-N calculations (Vasil'ev, Derkachev & Stepanenko 1993; Gracey 1994b; Janssen & Herbut 2014; Gracey 2018). Our RG results have also uncovered the complex phenomenology at finite temperature, revealing crossovers between QBT, Dirac, and quantum critical regimes. Furthermore, at small positive trigonal warping, $0 < t_w \ll t^2/t_\perp$, we have predicted an interesting sequence of three Gross–Neveu quantum phase transitions as a function of the short-range interaction. All these predictions are directly testable using current numerical setups (Lang *et al.* 2012; Pujari *et al.* 2017).

Concerning the real-world system of Bernal-stacked bilayer graphene, we can use the RG analysis presented in this chapter thus far to obtain a simple estimate for the interaction strength as follows: Bernal-stacked bilayer graphene exhibits an ordered ground state below $T_c \approx 5\,\mathrm{K}$ with a zero-temperature gap $\Delta(0) \sim 3\,\mathrm{meV}$ (Bao *et al.* 2012). The general scaling argument suggests $T_c \sim T_* \mathrm{e}^{-4\pi/(gN)}$, with the effective energy scale T_*, which may be estimated from the coefficient of the quadratic term in the dispersion [Eq. (5.9)] as $k_B T_* \sim t^2/t_\perp \sim 20\,\mathrm{eV}$ (Zhang *et al.* 2010). From this, we arrive at the estimate $g \sim 0.6$, which appears to be only slightly larger than our result for the critical coupling $g_c \approx 0.4$ (see Sec. 5.3.3). This suggest that Bernal-stacked bilayer graphene may be not too far from the Gross–Neveu quantum critical point and may show vestiges of the quantum critical scaling, e.g., in a regime above but close to the transition temperature, $T \gtrsim T_c$.[12)]

Let us also mention in this context that one may also be able to reveal this quantum critical regime directly in set-ups which allow one to tune the interaction strength experimentally – for instance, using cold atoms in an optical lattice (Sun *et al.* 2012).

A worthwhile theoretical issue that we have neglected here, but may be relevant for bilayer graphene, is the effect of the long-range tail of the Coulomb repulsion. In the QBT limit, with vanishing trigonal warping, the density of states is finite and a long-range interaction is expected to be screened at low energy. When the QBT points split into Dirac cones due to the self-energy corrections, by contrast, screening is effectively suppressed. This might lead to a nontrivial interplay between the long-range and short-range components of the Coulomb interaction, potentially with similarities to the intriguing higher-dimensional case.[13)] It may also be useful to study the self-energy effects in the context of the competing-order problem occurring in realistic models for Bernal-stacked bilayer graphene (Cvetkovic, Throckmorton & Vafek 2012). To this end, one would need to extend the present single-channel analysis by employing a suitable Fierz-complete basis of four-fermion interactions (Herbut, Juričić & Roy 2009; Gies & Janssen 2010; Vafek 2010) and studying the resulting interplay between these channels. This could lead to even richer physics at low and intermediate temperatures.

Throughout this work, we have assumed particle-hole symmetry. In real bilayer graphene, this will be broken due to the presence of longer-ranged hopping terms. In that case, the Dirac cones generated dynamically from self-energy effects would tend to form electron and hole pockets at tree-level. This, however, may be counteracted by the mechanism of emergent particle-hole symmetry, which we computed explicitly for the Luttinger semimetallic state in Chap. 4. Whether this mechanism also goes through for the Dirac semimetal may be an interesting topic for future research. (There may also be non-trivial interplay between the formation of pockets and the emergence of particle-hole symmetry.) If the emergence of particle-hole symmetry turns out to be subordinate to the formation of pockets, there may be further instabilites at the lowest temperatures, and potentially new universality classes beyond the relativistic Gross–Neveu–Yukawa family.

[12)] It is worth noting the contrast to graphene, where estimates for the interaction strength place it far from quantum criticality (cf., e.g., Castro Neto *et al.* 2009); the significantly reduced g_c, which allows Bernal-stacked bilayer graphene to avoid this fate, is an imprint of the (approximately) QBT dispersion at the microscopic level, even though the ultra-deep IR physics near quantum criticality is of the Gross–Neveu kind just like in monolayer graphene.

[13)] cf., e.g., Moon *et al.* (2013); Herbut & Janssen (2014); Savary, Moon & Balents (2014); Janssen & Herbut (2015, 2016b, 2017); Boettcher & Herbut (2017).

Chapter 6

Dirac from Luttinger II: Spontaneous Symmetry Breaking

In the previous chapter, we saw that based on some rough estimates, one may consider Bernal-stacked bilayer graphene (BBLG) to be situated close to a quantum critical point of the Gross–Neveu family. Beyond the general paucity of experimentally accessible signatures of Gross–Neveu quantum criticality, this is notable for two reasons: First, there is the emergence of relativistic Dirac fermions in BBLG, which is unusual given that the microscopic band structure hosts quadratic band touchings (QBTs), and thus the (bare) low-energy excitations are Luttinger fermions. The reason behind this is the fact that the lattice explicitly breaks the rotational symmetry down to C_3, which generates a linear term in the dispersion via a two-loop self-energy correction. Secondly, the proximity to quantum criticality is also somewhat unusual, given that its monolayer counterpart (i.e., monolayer graphene) is far from criticality. This, as we saw from the explicit computation, is because the critical coupling is significantly lowered compared to a pure Dirac semimetal. This in turn was – roughly speaking – because the RG flow is initiated with a quadratic dispersion, which has a comparatively high density of states.

The goal of this chapter is to study the complementary 'Dirac from Luttinger' scenario, namely where one Luttinger fermion splits into two Dirac fermions (or in terms of the band structure, a QBT into two Dirac cones). On honeycomb bilayers, such a process becomes symmetry-allowed, if the rotational symmetry is spontaneously broken down to C_2 – i.e., in the presence of nematic order.$^{1)}$ Signatures of a quantum critical point from the Gross–Neveu family will arise, if these emergent Dirac fermions subsequently undergo spontaneous symmetry breaking of their own. The final state will then feature two independent order parameters with non-vanishing vacuum expectation value: a coexistence phase.

That the ground state of BBLG may be in (or proximate to) such a phase is a plausible proposition. This is due to the fact that electrons on the honeycomb bilayer have many possible ground states to select from, which are very close to each other in energy (Jung, Zhang & MacDonald 2011). Indeed, for this reason, the ground state of BBLG has attracted considerable attention ever since its experimental realization by Novoselov *et al.* (2004); an unambiguous identification of the actual nature of the

---

1) In the present chapter, we shall only consider phases that arise from the 'Luttinger semimetal' by spontaneous symmetry breaking. At ultra-low temperatures – or equivalently, at the very longest length scales, this physics will be cut off in any case by the generation of Dirac cones by the mechanism discussed in Chap. 5.

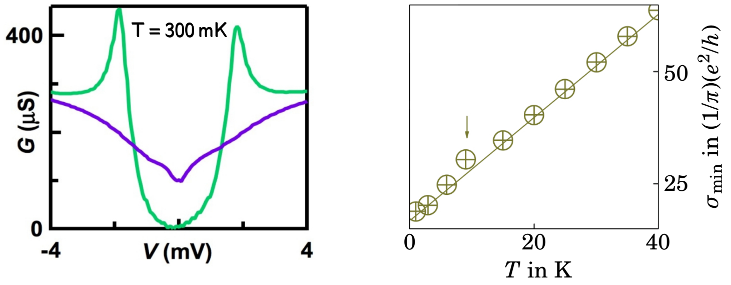

Figure 6.1: Ground state of two different BBLG samples. Left (adapted from Velasco Jr. *et al.* 2012): At low temperature, the differential conductance G as a function of gate voltage V vanishes in a finite range around the charge neutrality point $V = 0$, suggesting an insulating state with a gap of roughly 1.9 meV. Right (adapted from Mayorov *et al.* 2011): The conductivity minimum σ_{min} as a function of temperature T saturates at low temperatures to about $(20/\pi)(e^2/h)$, where $h = 2\pi\hbar$ is Planck's constant. This excludes a gapped state, but also the QBT state in BBLG, for which the zero-temperature conductivity minimum would be significantly lower, viz., $(8/\pi)(e^2/h)$ (see Snyman & Beenakker 2007). That this is indeed due to nematicity rather than trigonal warping (see Chap. 5 for details on the latter) can be demonstrated by measuring the degeneracy of the lowest Landau level, which comes out at 8 rather than 16, see again Mayorov *et al.* (2011).

material's zero-temperature ground state is, however, outstanding to date. Transport and spectroscopic experiments have indeed observed an interaction-driven reconstruction of the fermionic spectrum at temperatures below around 10 K – an ordered ground state is hence beyond doubt. However, while some of the experiments indicate an insulating ground state with a full bulk band gap (Velasco Jr. *et al.* 2012; Freitag *et al.* 2012; Bao *et al.* 2012; Veligura *et al.* 2012), others suggest only a partial gap opening in which four isolated Dirac cones remain gapless in the bulk spectrum (Mayorov *et al.* 2011), see Fig. 6.1. The latter would imply a low-temperature ground state that breaks part of the lattice rotational symmetry spontaneously. In fact, such an electronic nematic order had indeed previously been predicted on the basis of perturbative renormalization group (RG) analyses (Vafek & Yang 2010; Lemonik *et al.* 2010). Later theoretical studies[2] have shown, however, that an antiferromagnetic state, characterized by finite and opposite net magnetizations within the two layers (Lang *et al.* 2012; Kharitonov 2012), is at least comparable in energy and in fact prevails over a large section of parameter space. This layer antiferromagnet features a full gap in the electronic spectrum, and among the different candidate ground states it appears to be the one that is most consistent with the measurements on the samples that become insulating at low temperatures (Velasco Jr. *et al.* 2012).

Our strategy in this chapter will be as follows: First, we shall revisit the problem of the low-temperature ground state in bilayer graphene by investigating the phase diagram of a model of short-range-interacting electrons on the honeycomb bilayer. We shall focus on the competition between the nematic and antiferromagnetic orders, which appear to be the two most promising candidate ground states consistent with the experiments (Mayorov *et al.* 2011; Velasco Jr. *et al.* 2012). In particular, we study the possibility of coexisting orders, which was only insufficiently addressed in previous work (Cvetkovic, Throckmorton & Vafek 2012). At small to moderate coupling, we shall in this way show that the nematic and antiferromagnetic phases are generically separated by an intermediate coexistence phase, which features both layer antiferromagnetism and nematicity, see Fig. 6.2. (In the coexistence phase, the fermionic spectrum thus exhibits a full, but rotationally anisotropic band gap.) The main focus of this chapter will then be the transition between the coexistence phase and the nematic phase. At this transition, the electronic band gap closes at four isolated Fermi points in the Brillouin zone, with linear band dispersions in their vicinities. This is a necessary condition for Gross–Neveu quantum criticality, but it is not sufficient. Due to the non-vanishing nematic order parameter, not only Lorentz symmetry, but in fact even spatial rotational symmetry is broken [in other words, the spacetime symmetry is only $\mathbb{Z}_2 \times C_2$ instead of SO(3)]. We shall hence need to establish that Lorentz symmetry is indeed emergent. This we shall do so by computing the scaling dimension of symmetry-breaking perturbations to first order in perturbation theory, using two complementary approaches: (i) a $2+\varepsilon$ and (ii) a $4-\epsilon$ expansion around the lower and upper critical dimensions respectively (i.e., the spacetime dimensions where the 4-Fermi and the Yukawa theory are perturbatively renormalizable, respectively).

---

[2] cf., e.g., Vafek (2010); Cvetkovic, Throckmorton & Vafek (2012); Lemonik *et al.* (2012); Scherer, Uebelacker & Honerkamp (2012); Lang *et al.* (2012); Pujari *et al.* (2017); Honerkamp (2017); Leaw *et al.* (2019)

6.1 Model

Since a fully satisfactory microscopic model of the electronic interactions in bilayer graphene is currently not agreed upon,[3] we shall employ here a minimal theoretical description that allows us to study the competition between nematic and antiferromagnetic orders and the possibility of a coexistence phase on the honeycomb bilayer. The present approach may be viewed as a simple phenomenological modelling that captures the physics of the two most prominent candidate ordered states discussed in experimental works (Mayorov *et al.* 2011; Velasco Jr. *et al.* 2012). It restricts the multidimensional parameter space discussed in previous more comprehensive works[4] to a simple two-dimensional subspace. Explicitly, let us consider the Euclidean action $S = \int \mathrm{d}\tau \mathrm{d}^2\boldsymbol{x}\mathcal{L}_{\mathrm{QBT}}$ in imaginary time τ and two-dimensional space $\boldsymbol{x} = (x,y)^\top$ with

$$\mathcal{L}_{\mathrm{QBT}} = \Psi^\dagger[\partial_\tau + d_a(-\mathrm{i}\boldsymbol{\partial})(\Gamma_a \otimes \mathbb{1}_2)]\Psi - \frac{g}{2}\big[\Psi^\dagger(\Gamma_z \otimes \sigma_\alpha)\,\Psi\big]^2 - \frac{g'}{2}\big[\Psi^\dagger(\Gamma_a \otimes \mathbb{1}_2)\Psi\big]^2\,, \tag{6.1}$$

where $a = 1,2$ and $\alpha = x,y,z$. In the above and the following equations, the summation convention over repeated indices is implicitly assumed. The d_a functions are $\ell = 2$ real spherical harmonics in $d = 2$, given by

$$d_1(-\mathrm{i}\boldsymbol{\partial}) = -\partial_x^2 + \partial_y^2, \qquad d_2(-\mathrm{i}\boldsymbol{\partial}) = -2\partial_x\partial_y, \tag{6.2}$$

and transform under spatial rotations as components of a second-rank tensor (Janssen & Herbut 2015). The spinors Ψ and $\Psi^\dagger$ have eight components, corresponding to the layer, valley, and physical spin-1/2 degrees of freedom (Vafek & Yang 2010). The 2×2 Pauli matrices σ_α, $\alpha = x,y,z$, act on the physical spin index and transform as a vector under SU(2) spin rotations. The 4×4 matrices Γ_x, Γ_y, and Γ_z realize a four-dimensional representation of the Clifford algebra, and can be represented explicitly by tensoring Pauli matrices as

$$\Gamma_x = \mathbb{1}_2 \otimes \mu_x, \quad \Gamma_y = \tau_z \otimes \mu_y, \quad \Gamma_z = \mathbb{1}_2 \otimes \mu_z, \tag{6.3}$$

---

[3] See, nevertheless, Wehling *et al.* (2011) for ab-initio results for monolayer graphene and bulk graphite, as well as Zhang *et al.* (2008) for an overview of band structure model parameters for bilayer graphene.

[4] cf., e.g, Cvetkovic, Throckmorton & Vafek (2012); Lemonik *et al.* (2012); Szabo & Roy (2021)

where in the above tensor products the first (second) factors act on the layer (valley) indices. Here, the 2×2 Pauli matrices that serve as building blocks for the Γ matrices have been denoted by τ_α and μ_α to distinguish them from those acting on the physical spin index. While Γ_x and Γ_y transform as components of a second-rank tensor, Γ_z is a scalar under spatial rotations (cf. Chap. 5). In this representation, the time-reversal operator is given as $\mathcal{T} = (\tau_x \otimes \mathbb{1}_2) \otimes \sigma_y \mathcal{K}$, where $\mathcal{K}$ denotes complex conjugation. The first factor of the unitary part essentially represents interchanging the two valleys, while the second factor represents spin flip. Eq. (6.1) assumes particle-hole symmetry and a continuous spatial rotational symmetry. In particular, this model neglects the effects of trigonal warping that are expected to play a dominant role only in the weakly-interacting regime.[5] The units have been chosen such that the isotropic effective band mass is $m^* = 1/2$. The spectrum of the noninteracting Hamiltonian $\mathcal{H}_0(\boldsymbol{p}) = d_a(\boldsymbol{p})(\Gamma_a \otimes \mathbb{1}_2)$ then is simply $\varepsilon_0^\pm(\boldsymbol{p}) = \pm \boldsymbol{p}^2$, where $\boldsymbol{p}$ denotes the deviation from the corners $\boldsymbol{K}$ and $\boldsymbol{K}'$ of the hexagonal Brillouin zone. It describes the nonrelativistic two-dimensional 'Luttinger' semimetal (cf. Chap. 4) in which the valence and conduction bands touch quadratically at the two Fermi points at $\boldsymbol{K}$ and $\boldsymbol{K}'$.

The four-fermion interactions parametrized by the couplings g and g' in Eq. (6.1) are chosen such that they stabilize antiferromagnetic and nematic long-range order, respectively. This can be seen as follows: The three-component fermion bilinear $\boldsymbol{\phi} \sim \Psi^\dagger(\Gamma_z \otimes \boldsymbol{\sigma})\Psi$, associated at the mean-field level with the four-fermion coupling g, is even under time reversal, a scalar under spatial rotations and a vector under SU(2) spin rotations. Assigning a finite vacuum expectation value to $\boldsymbol{\phi}$ hence breaks spin-rotational symmetry while leaving spatial rotational symmetry and time reversal intact. It describes the layer antiferromagnet, in which the two honeycomb layers feature finite and opposite magnetizations (Cvetkovic, Throckmorton & Vafek 2012; Kharitonov 2012). Importantly, the corresponding operator $\Gamma_z \otimes \boldsymbol{\sigma}$ anticommutes with the single-particle Hamiltonian $\mathcal{H}_0$, and hence a vacuum expectation value of $\boldsymbol{\phi}$ opens a uniform gap in the fermionic spectrum, of size $\propto |\langle \boldsymbol{\phi} \rangle|$. Microscopically, the 4-Fermi term parametrized by g can be understood to arise from an interlayer interaction that couples spin densities on the two honeycomb layers (Vafek 2010; Cvetkovic, Throckmorton & Vafek 2012). On the other hand, the bilinear corresponding to the coupling g', $n_a \sim \Psi^\dagger(\Gamma_a \otimes \mathbb{1}_2)\Psi$, transforms as the components of a second-rank tensor under spatial rotations, while being even under spin rotations and time reversal. When n_a obtains a finite expectation value, the spatial rotational symmetry on the honeycomb bilayer is spontaneously broken while all other symmetries are left intact. The bilinear n_a corresponds to the nematic order parameter (Vafek & Yang 2010; Cvetkovic, Throckmorton & Vafek 2012). Its components commute with one of the matrices appearing in the single-particle Hamiltonian, while anticommuting with the other. A gap in the electronic spectrum is therefore not opened up in the state with nematic order alone; instead, each quadratic band touching point splits into two mini-Dirac cones located in close vicinity of the corners $\boldsymbol{K}$ and $\boldsymbol{K}'$ of the hexagonal Brillouin zone, along the axis chosen by $\langle n_a \rangle$. On a microscopic level, the coupling g' can be thought of as parametrizing inter-valley scattering processes between the $\boldsymbol{K}$ and $\boldsymbol{K}'$ points (Vafek & Yang 2010; Vafek 2010; Cvetkovic, Throckmorton & Vafek 2012).

The symmetry of the noninteracting Hamiltonian allows a number of further short-range interactions (Vafek 2010), which are neglected here for simplicity. These may change

---

[5] cf. Cvetkovic, Throckmorton & Vafek (2012); Pujari *et al.* (2017); Honerkamp (2017); Hesselmann *et al.* (2020); see also Chap. 5 of this thesis

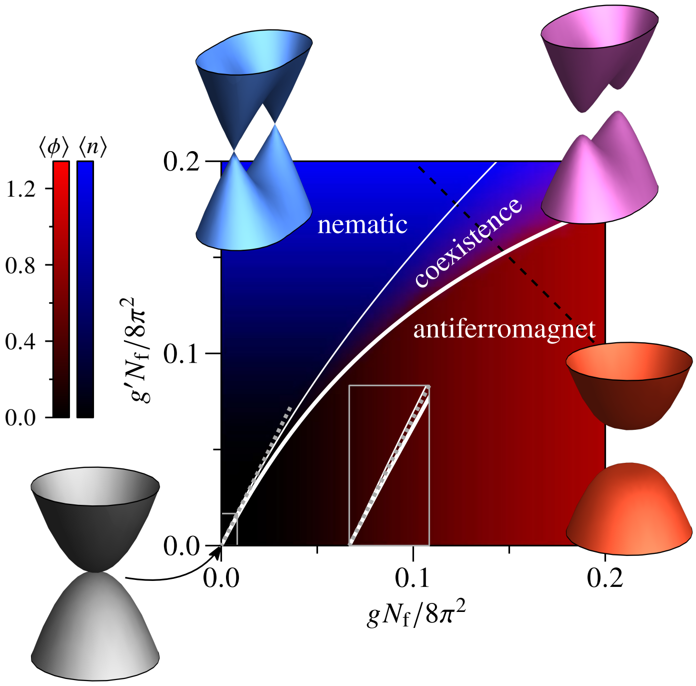

Figure 6.2: Mean-field phase diagram of interacting electrons on the Bernal-stacked honeycomb bilayer as a function of short-range couplings g and g' defined in Sec. 6.1. Blue and red colour codings indicate the magnitudes of the nematic and antiferromagnetic orders, respectively. The electronic spectra near the corners of the hexagonal Brillouin zone are depicted for the different states in the insets. The grey rectangle shows a zoom into the weakly-interacting regime, with the dotted grey line indicating the phase boundary between nematic and antiferromagnetic orders in the fermionic RG calculation (Sec. 6.2). The dashed black line indicates the cut used in Fig. 6.3. The antiferromagnetic-to-coexistence transition (thick white curve) becomes weakly first-order due to higher-order symmetry-breaking terms. The nematic-to-coexistence transition (thin white curve) is continuous and falls into the Gross–Neveu–Heisenberg universality class (Sec. 6.3).

some of our results on a quantitative level, such as the size of the phases and the location of the phase boundaries in parameter space. However, our main conclusions, including the existence of a coexistence phase and the nature of the transitions into and out of this phase are expected to be robust upon the inclusion of these further interactions, as long as they do not become too large. The same holds for the long-range tail of the Coulomb interaction, which may be included as well, but is expected to be screened at low energies (Lemonik *et al.* 2012).

6.2 Phase diagram and transitions

The object of this section is to explore the phases contained in the model (6.1) as a function of the coupling parameters g and g' at the level of mean-field theory, and establish some basic facts about possible transitions between them. The considerations are restricted to positive interactions $g, g' > 0$, which allows one to obtain an equivalent order-parameter field theory by means of a Hubbard–Stratonovich transform,

$$\begin{aligned}\mathcal{L}_{\mathrm{HST}} = {}& \frac{\phi^2}{2g} + \frac{n^2}{2g'} + \Psi^\dagger \left[\partial_\tau + d_a(-\mathrm{i}\boldsymbol{\partial})(\Gamma_a \otimes \mathbb{1}_2)\right] \Psi \\ & - \phi_\alpha \Psi^\dagger(\Gamma_z \otimes \sigma_\alpha)\Psi - n_a \Psi^\dagger(\Gamma_a \otimes \mathbb{1}_2)\Psi,\end{aligned} \tag{6.4}$$

where $\phi^2 \equiv \phi_\alpha\phi_\alpha$, $\alpha = x, y, z$ and $n^2 \equiv n_a n_a$, $a = 1, 2$. The collective fields ϕ_α and n_a are related to fermion bilinears via the equations of motion $\phi_\alpha = g\Psi^\dagger(\Gamma_z \otimes \sigma_\alpha)\Psi$ and $n_a = \Psi^\dagger(\Gamma_a \otimes \mathbb{1}_2)\Psi$. Let us now integrate out the fermions by performing the path integral of Ψ and $\Psi^\dagger$ in $\mathcal{L}_{\mathrm{HST}}$, allowing us to write down an effective description in terms of the two order parameters alone,

$$\mathcal{L}_{\mathrm{OP}} = \frac{\phi^2}{2g} + \frac{n^2}{2g'} - \frac{N_{\mathrm{f}}}{4} \operatorname{Tr} \ln \left[\partial_\tau + d_a(-\mathrm{i}\boldsymbol{\partial})(\Gamma_a \otimes \mathbb{1}_2) - \phi_\alpha(\Gamma_z \otimes \sigma_\alpha) - n_a(\Gamma_a \otimes \mathbb{1}_2)\right]. \tag{6.5}$$

In the above, an additional parameter N_{f} has been inserted; it counts the number of valley and spin degrees of freedom, with $N_{\mathrm{f}} = 4$ corresponding to the present case of spin-1/2 fermions on the honeycomb bilayer. In the limit $N_{\mathrm{f}} \to \infty$, bosonic fluctuations freeze out and mean-field theory becomes exact. One can then replace ϕ_α, n_a with corresponding classical fields and perform the trace in momentum space. Evaluating the frequency integral, one thus finds the familiar sum over energy of filled states for the mean-field effective potential

$$V_{\mathrm{MF}}(\phi, n_a) = \frac{\phi^2}{2g} + \frac{n^2}{2g'} + N_{\mathrm{f}} \int_{|\boldsymbol{p}| \leqslant \Lambda} \frac{\mathrm{d}^2\boldsymbol{p}}{(2\pi)^2}\, \varepsilon^-_{\phi,n}(\boldsymbol{p}), \tag{6.6}$$

where

$$\varepsilon^\pm_{\phi,n}(\boldsymbol{p}) = \pm\sqrt{p^4 + \phi^2 + n^2 - 2n_a d_a(\boldsymbol{p})} \tag{6.7}$$

denotes the fermion spectrum in the presence of a constant bosonic background, and Λ is a UV momentum cut-off. In the following, we shall assume $n_a = (n, 0)$ without loss of generality. The momentum integration and subsequent energy minimization is performed numerically. The resulting phase diagram assuming $\phi, n \ll \Lambda^2$ is shown in Fig. 6.2. If the interaction is predominantly g (g'), the antiferromagnetic (nematic) state is preferred. While the electronic spectrum in the antiferromagnetic phase is fully gapped, in the nematic phase each quadratic band touching point splits into two gapless mini-Dirac cones. In between, however, a state in which both $\langle\phi\rangle$ and $\langle n\rangle$ are nonvanishing is stabilized—a coexistence phase. This phase is characterized by an anisotropic, but fully gapped electronic spectrum, see inset in Fig. 6.2.

In the limit $g, g' \to 0$, the coexistence phase shrinks and is located around the line described by $g' = 2g$ (dotted grey line in Fig. 6.2). The latter can be understood from an RG perspective: The pertinent β-functions at one-loop order essentially[6] follow from the $N_{\mathrm{f}} \to \infty$ limit of Eqs. (7) and (8) of Vafek & Yang (2010). They are given by

$$\beta_g = 2g^2, \qquad \beta_{g'} = (g')^2, \tag{6.8}$$

---

[6] Note that in the strict mean-field limit $N_{\mathrm{f}} = \infty$, all that matters are the (anti-)commutation properties of the matrices appearing in the four-fermion interaction with the free fermion propagator. Hence, the fact that we are actually studying here the spin counterpart of the rotationally invariant gapped state considered by Vafek & Yang (2010) does not change the β-functions in this limit.

where the couplings have been rescaled à la 't Hooft as $(g, g')N_\mathrm{f}/(4\pi) \mapsto (g, g')$; any terms that vanish for $N_\mathrm{f} \to \infty$ have been dropped. The g axis, the g' axis, and the line $g' = 2g$ are invariant subspaces of the RG flow. We use conventions in which a positive β-function corresponds to an infrared relevant direction. Hence, for positive initial couplings, the flow always diverges as $(g, g') \to (\infty, \infty)$ in the infrared. In fact, this occurs within finite RG time and signifies spontaneous symmetry breaking. In the RG approach, the usual strategy to determine the nature of the symmetry-breaking ground state is then based on comparing susceptibilities of the corresponding order parameters.[7] It should be emphasized here, however, that such an analysis does not allow one to identify possible coexistence phases in a controlled way (Cvetkovic, Throckmorton & Vafek 2012). For the present large-N_f flow equations (6.8), the susceptibility analysis becomes particularly simple, as the ratio g'/g approaches either zero or infinity in the infrared, depending on the initial values of the couplings: For $g'/g > 2$, $g'/g \to \infty$ and the nematic susceptibility has the strongest divergence. For $g'/g < 2$, on the other hand, $g'/g \to 0$ and the antiferromagnetic susceptibility dominates. The RG invariant line $g'/g = 2$ hence represents the transition line between nematic and antiferromagnetic orders in the weakly-interacting limit, in agreement with the present mean-field analysis above, see Fig. 6.2. For finite short-range couplings, however, the mean-field calculation shows that the transition line is 'smeared out' into an extended coexistence phase. Upon increasing g and g', the higher-order corrections incorporated in this calculation shift the location of the coexistence phase towards smaller ratio g'/g.

Figure 6.3 shows the evolution of the nematic and antiferromagnetic order parameters along the cut indicated by the dashed black line in Fig. 6.2. In the present simplified model with continuous spatial rotational symmetry, both transitions into and out of the coexistence phase are continuous, see Fig. 6.3(a). In the vicinity of the nematic-to-coexistence transition, the antiferromagnetic order parameter develops an expectation value as $\langle \phi \rangle \propto g - g_\mathrm{c1}$ for $g \geqslant g_\mathrm{c1}$, where g_c1 denotes the critical coupling. The linear behaviour is consistent with Gross–Neveu-type quantum criticality in the large-N_f limit (Hands, Kocić & Kogut 1993). Near the antiferromagnetic-to-coexistence transition at $g_\mathrm{c2} > g_\mathrm{c1}$, the fermionic spectrum retains a finite gap; the corresponding nematic order parameter has a square-root behaviour, $\langle n \rangle \propto \sqrt{g_\mathrm{c2} - g}$ for $g \leqslant g_\mathrm{c2}$. This is consistent with the mean-field expectation for a purely bosonic transition, but it turns out to be an artifact of our simple modelling, which assumes a continuous rotational symmetry. However, the transition becomes discontinuous upon inclusion of higher-derivative terms such as

$$\mathcal{L}_\mathrm{QBT} \to \mathcal{L}_\mathrm{QBT} + f_3 \Psi^\dagger \partial^2 \mathrm{i} \bar{\partial}_a (\bar{\Gamma}_a \otimes \mathbb{1}_2) \Psi, \tag{6.9}$$

where $(\bar{\partial}_a) = (\partial_x, -\partial_y)$, $a = 1, 2$, and $\bar{\Gamma}_a = (\tau_z \otimes \mathbb{1}_2)\Gamma_a$. This term follows naturally from the next-to-leading order expansion of the tight-binding dispersion near the $\boldsymbol{K}$ points in the Brillouin zone (Pujari *et al.* 2017), and merely reflects the fact that the actual point group on the honeycomb bilayer includes only discrete C_3 rotations by 120° around a lattice site. Identifying for simplicity the ultraviolet momentum cutoff Λ with the inverse of the lattice constant a_0 as $\Lambda \sim \pi/a_0$, we obtain $f_3 \simeq \pi/(2\sqrt{3}\Lambda)$ in our units (see Chap. 5). As shown in Fig. 6.3(b), this indeed renders the transition first-order, and one can in fact show that the mean-field jump discontinuity at the phase boundary works out to (see App. C)

---

[7] cf., e.g., Vafek & Yang (2010); Vafek (2010); Cvetkovic, Throckmorton & Vafek (2012); Lemonik *et al.* (2012); Janssen & Herbut (2017); Boettcher & Herbut (2017).

$$\delta\langle n\rangle = \frac{1}{12} f_3^2 \langle\phi\rangle^2 \left(\ln\frac{1}{4\langle\phi\rangle^2} - \frac{8}{3}\right) + \mathcal{O}(\langle\phi\rangle^4 \ln\langle\phi\rangle^2). \tag{6.10}$$

In the purely antiferromagnetic phase $\langle n\rangle = 0$, the AF order parameter behaves as $\langle\phi\rangle \sim \mathrm{e}^{-C/gN_\mathrm{f}}$ with model-dependent constant C (cf. Chap. 4). Hence, the jump is small, and the transition – though strictly discontinuous – only weakly first-order for small to intermediate g.

Before moving on to our main object of interest, viz. the (putative) Gross–Neveu transition at the nematic-to-coexistence boundary, let us close the present section by discussing ways to improve on our mean-field analysis. Formally, mean-field theory represents the leading order of a systematic expansion in $1/N_\mathrm{f}$. To incorporate effects of order-parameter fluctuations on the effective potential at finite N_f, one would need to evaluate higher-loop vacuum diagrams, the simplest topology of which is shown in Fig. 6.4. We in fact encountered such a computation at the leading-logarithm level using the Callan–Symanzik equation in Chap. 4, but for a single-order-parameter effective potential. The present situation has the added subtlety that $\langle\phi\rangle$ and $\langle n\rangle$ allow for two independent large logarithms, and would require a so-called multiscale scheme to resum properly (Ford 1994; Ford & Wiesendanger 1997; Steele, Wang & McKeon 2014). Alternatively, order-parameter fluctuations could be incorporated along the lines of the works on competing orders in the monolayer case (Classen *et al.* 2015, 2016). Fluctuation effects may shift the location of phase boundaries in parameter space, but are expected to not alter our main conclusions concerning the existence of the coexistence phase and the order of the transitions into and out of this phase. They do, however, play an important role for the universal behaviour at the nematic-to-coexistence quantum critical point. Instead of a comprehensive analysis of the full phase diagram, here we shall therefore restrict our study of the effects of order-parameter fluctuations to the vicinity of the nematic-to-coexistence transition. This is the primary topic which will occupy our attention for the remainder of this chapter. We also note that we have assumed $\phi, n \ll \Lambda^2$ in the above calculation, so that the integral in Eq. (6.6) is dominated by universal logarithms such as $\ln(\Lambda^4/\phi^2)$ and $\ln(\Lambda^4/n^2)$. For larger interactions, this assumption no longer holds and non-universal effects that are beyond the effective analysis may become important. This is left for future work.

6.3 Emergent Lorentz symmetry

In the nematic phase, the low-energy excitations are massless fermions with linear dispersion; these then undergo further spontaneous symmetry breaking to acquire a full gap in the coexistence phase. At the transition, the antiferromagnetic order parameter $\boldsymbol{\phi}$ becomes critical. The nematic-to-coexistence transition is hence a promising candidate for realizing the Gross–Neveu–Heisenberg (= chiral Heisenberg) universality class.[8] The purpose of this section is to demonstrate that this is indeed the case. The Gross–Neveu–Heisenberg universality class is characterized by a dynamical critical exponent $z = 1$ and a relativistic Lorentz symmetry in (2+1)-dimensional spacetime. In the non-interacting limit, our model has $z = 2$, reflecting the non-relativistic dispersion in the Luttinger semimetal state (see Chap. 4). The finite background nematic order present across

---

[8] cf., e.g., Rosenstein, Yu & Kovner (1993); Herbut, Juričić & Vafek (2009); Janssen & Herbut (2017); Zerf *et al.* (2017); Knorr (2018); Gracey (2018)

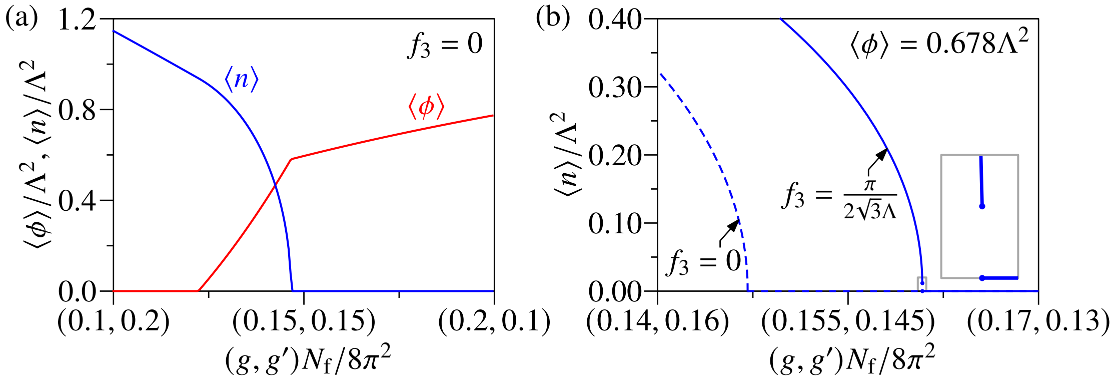

Figure 6.3: (a) Nematic order parameter $\langle n\rangle$ (blue) and antiferromagnetic order parameter $\langle\phi\rangle$ (red) along the cut through parameter space indicated by the dashed black line in Fig. 6.2, in the mean-field approximation. In the model with continuous spatial rotational symmetry, both transitions into and out of the coexistence phase are continuous. (b) Nematic order parameter in the vicinity of the antiferromagnet-to-coexistence transition, showing the effects of the f_3 term defined in Eq. (6.9), which breaks the continuous spatial rotational symmetry down to 120° rotations on the honeycomb bilayer. Here, the antiferromagnetic order parameter $\langle\phi\rangle = 0.678\Lambda^2$ has been held constant for simplicity. The inset shows a zoom into the region very close to the transition (grey rectangle), illustrating the fact that finite $f_3 \neq 0$ renders the transition weakly first order.

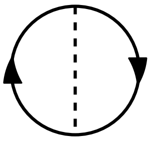

Figure 6.4: Simplest order-parameter fluctuation correction to the effective potential. The dashed (solid) lines refer to boson (fermion) propagators.

the nematic-to-coexistence transition cures the problem of the non-linear dispersion by splitting each quadratic band crossing into two linear crossings, but in doing so, it breaks the spatial rotation symmetry down to C_2. Nevertheless, in this section, we shall see that not only a continuous rotational symmetry, but even a full relativistic symmetry in $2 + 1$ space-time dimensions becomes emergent at the quantum critical point at low energy. To this end, the fate of perturbations that break both rotational and space-time symmetries of the relativistic subspace of theory space under RG flow shall be studied. In particular, we shall convince ourselves that such symmetry-breaking-perturbations are always RG irrelevant near the Gross–Neveu–Heisenberg fixed point. The nematic-to-coexistence transition on the honeycomb bilayer therefore falls into the same family of phase transitions known from the monolayer system. There is, nevertheless, one important difference: As each quadratic band touching point on the bilayer splits into two mini-Dirac cones in the nematic phase, the number of fermion flavours is doubled in comparison to the semimetal-to-antiferromagnetic transition on the monolayer. In the physical situation for spin-1/2 fermions on the Bernal-stacked honeycomb bilayer, we thus have $N_f = 4$ flavours of two-component Luttinger fermions in the non-interacting limit. In the nematic phase, this then leads to $N_f = 4$ flavours of *four*-component Dirac fermions (in other words, the total number of Dirac spinor components is $4N_f = 16$).

We wish to work to first order in perturbation theory, for which our strategy will be as follows: Near the lower critical space-time dimension $D_{\text{low}} = 2$, four-fermion interactions are perturbatively renormalizable; the pertinent description is in terms of a 4-Fermi theory, which we study in Sec. 6.3.1. The critical coupling is $O(D - D_{\text{low}})$, so that the physics in $D = 2 + \varepsilon$ dimensions is accessible in the 4-Fermi loop expansion. On the other hand, near the upper critical dimension of $D_{\text{up}} = 4$, the Yukawa and bosonic quartic self-couplings are perturbatively renormalizable, giving us access to $D = 4 - \epsilon$ dimensions from perturbation theory. This is the subject of Sec. 6.3.2. Indeed, the least-irrelevant symmetry-breaking perturbations are of significantly different natures in the two limits, and the two approaches complement each other thus. Agreement between the two (as we shall find out is indeed the case in the present setting) then serves as a strong indication that the extrapolation of the respective first-order perturbation theory results to the physical space-time dimension $D = 3$ (i.e., $\varepsilon, \epsilon \to 1$) is stable and well-defined.

6.3.1 Loop expansion near lower critical dimension

Unlike the better known Gross–Neveu–Ising case, in the Gross–Neveu–Heisenberg universality class, the renormalization of the pertinent 4-Fermi interaction is not closed. Already at the one-loop level, a spin current interaction is generated, which in turn generates further interactions. The upshot is that the renormalization of the chiral Heisenberg universality class in the vicinity of the lower critical space-time dimension $D_{\text{low}} = 2$ has so far not been systematically studied, even at one loop. Before investigating its stability with respect to perturbations, we hence need to first identify the Gross–Neveu–Heisenberg fixed point in the multi-dimensional space of 4-Fermi couplings.

6.3.1.1 Minimal 4-Fermi model

As a first step, we need to establish a basis in the space of 4-Fermi couplings. To this end, let us classify all possible 4-Fermi interactions in terms of symmetry. In order to retain the spinor structure relevant to the physical situation in bilayer graphene, we devise the minimal 4-Fermi model in fixed $D = 2 + 1$ space-time dimensions. The dimensional continuation to noninteger dimensions will be discussed in the context of the loop integration below. In accordance with previous works (cf. Herbut, Juričić & Roy 2009; Vafek 2010), we employ a four-dimensional reducible representation of the Clifford algebra $\{\gamma_\mu, \gamma_\nu\} = 2\delta_{\mu\nu}\mathbb{1}_4$ with $\mu, \nu = 0, 1, 2$. In addition, there exist two anticommuting matrices $\{\gamma_3, \gamma_\mu\} = \{\gamma_5, \gamma_\mu\} = \{\gamma_3, \gamma_5\} = 0$. Finally, a customary shorthand is $\gamma_{35} := \mathrm{i}\gamma_3\gamma_5$.

The Gross–Neveu–Heisenberg 4-Fermi interaction can then be written as

$$[\overline{\psi}_a(\mathbb{1}_4 \otimes \sigma_\alpha)\psi_a]^2,$$

where $\mathbb{1}_4$ acts on the layer and K-point degrees of freedom and the Pauli matrices σ_α, $\alpha = 1, 2, 3$, act on the spin degree of freedom of the eight-component spinor ψ_a. Furthermore, the flavor index $a = 1, 2$ corresponds to the two mini-Dirac cones that develop at both K points due to the background nematic order. We may restrict ourselves to interactions that have a singlet structure with respect to the flavour index a; non-singlet terms may be rewritten in terms of singlet ones using Fierz identities (cf., e.g., Gehring, Gies & Janssen 2015). There are then *a priori* 64 independent four-fermion interactions,

$$\sum_{M \in \mathcal{B}} G_M(\overline{\psi}_a M \psi_a)^2, \tag{6.11}$$

where M are complex 8×8 matrices and $\mathcal{B} = \mathcal{B}_{\text{s}} \cup \mathcal{B}_{\text{v}}$ is a basis of $\mathbb{C}^{8\times 8}$, with $\mathcal{B}_{\text{s}} = \{\mathbb{1}_4, \gamma_\mu, \gamma_3, \gamma_5, \gamma_\mu\gamma_3, \gamma_\mu\gamma_5, \gamma_{35}, \gamma_\mu\gamma_{35}\} \otimes \mathbb{1}_2$ corresponding to the scalar spin sector and

$\mathcal{B}_{\mathrm{v}} = \{\mathbb{1}_4, \gamma_\mu, \gamma_3, \gamma_5, \gamma_\mu\gamma_3, \gamma_\mu\gamma_5, \gamma_{35}, \gamma_\mu\gamma_{35}\} \otimes \sigma_\alpha$ to the vector spin sector, with $\mu = 0, 1, 2$ and $\alpha = x, y, z$.

The number of independent couplings may be narrowed down using Lorentz and SU(2) symmetry. To do so, we need to group the 4-Fermi interactions according to their behaviour under Lorentz and SU(2) spin transformations. To be precise, if the subset $\mathcal{A} \subset \mathcal{B}$ is invariant under combined Lorentz and SU(2) transformations, then $G_K = G_L$ for all $K, L \in \mathcal{A}$. The decomposition of $\mathcal{B}$ into disjoint subsets $\mathcal{A}$ is almost entirely taken care of automatically above by grouping them according to Lorentz and SU(2) indices. The grouping is almost exhaustive: For a final symmetry reduction, we need to take into account that (γ_3, γ_5) is a vector under the U(1) chiral symmetry generated by γ_{35}, which corresponds to translational invariance (Herbut, Juričić & Roy 2009). There are hence twelve symmetry-independent couplings. The 4-Fermi Lagrangian reads as

$$\begin{aligned}
\mathcal{L}_{\mathrm{GNH}} = {} & \overline{\psi}_a(\gamma_\mu \otimes \mathbb{1}_2)\partial_\mu\psi_a \\
& - \frac{G_1}{2N_{\mathrm{f}}}[\overline{\psi}_a(\mathbb{1}_4 \otimes \sigma_\alpha)\psi_a]^2 - \frac{G_2}{2N_{\mathrm{f}}}[\overline{\psi}_a(\gamma_\mu \otimes \sigma_\alpha)\psi_a]^2 - \frac{G_3}{2N_{\mathrm{f}}}[\overline{\psi}_a(\gamma_{35} \otimes \sigma_\alpha)\psi_a]^2 \\
& - \frac{G_4}{2N_{\mathrm{f}}}(\overline{\psi}_a\psi_a)^2 - \frac{G_5}{2N_{\mathrm{f}}}[\overline{\psi}_a(\gamma_\mu \otimes \mathbb{1}_2)\psi_a]^2 - \frac{G_6}{2N_{\mathrm{f}}}[\overline{\psi}_a(\gamma_{35} \otimes \mathbb{1}_2)\psi_a]^2 \\
& - \frac{G_7}{2N_{\mathrm{f}}}[\overline{\psi}_a(\gamma_\mu\gamma_{35} \otimes \sigma_\alpha)\psi_a]^2 - \frac{G_8}{2N_{\mathrm{f}}}\left\{[\overline{\psi}_a(\gamma_3 \otimes \sigma_\alpha)\psi_a]^2 + [\overline{\psi}_a(\gamma_5 \otimes \sigma_\alpha)\psi_a]^2\right\} \\
& - \frac{G_9}{2N_{\mathrm{f}}}\left\{[\overline{\psi}_a(\gamma_\mu\gamma_3 \otimes \sigma_\alpha)\psi_a]^2 + [\overline{\psi}_a(\gamma_\mu\gamma_5 \otimes \sigma_\alpha)\psi_a]^2\right\} \\
& - \frac{G_{10}}{2N_{\mathrm{f}}}[\overline{\psi}_a(\gamma_\mu\gamma_{35} \otimes \mathbb{1}_2)\psi_a]^2 - \frac{G_{11}}{2N_{\mathrm{f}}}\left\{[\overline{\psi}_a(\gamma_3 \otimes \mathbb{1}_2)\psi_a]^2 + [\overline{\psi}_a(\gamma_5 \otimes \mathbb{1}_2)\psi_a]^2\right\} \\
& - \frac{G_{12}}{2N_{\mathrm{f}}}\left\{[\overline{\psi}_a(\gamma_\mu\gamma_3 \otimes \mathbb{1}_2)\psi_a]^2 + [\overline{\psi}_a(\gamma_\mu\gamma_5 \otimes \mathbb{1}_2)\psi_a]^2\right\}
\end{aligned} \tag{6.12}$$

as a minimal (i.e., closed under RG at one-loop) 4-Fermi theory in which to embed the Gross–Neveu–Heisenberg fixed point. Note that the flavour number N_{f} has been reinstated, corresponding to the number of four-component Dirac spinors, with $a = 1, \dots, N_{\mathrm{f}}/2$ for N_{f} even. Let us remind ourselves here that the case pertaining to the nematic-to-coexistence transition of spin-1/2 fermions on the honeycomb bilayer corresponds to $N_{\mathrm{f}} = 4$.

6.3.1.2 Gross–Neveu–Heisenberg fixed point

To obtain the RG flow of the couplings $G_1, \dots, G_{12}$ in Eq. (6.12), one needs to perform the loop integration. Here, the angular integrals are evaluated in fixed $D = 2 + 1$ space-time dimensions, while the dimensions of the couplings are counted in general dimension (Vojta, Zhang & Sachdev 2000b; Janssen & Herbut 2017). This allows one to retain the spinor structure of the physical system in $d = 2$ spatial dimensions. The flow equations may be obtained at one-loop order by applying the general formula given by Gehring, Gies & Janssen (2015). In addition, it is expedient to perform a large-N_{f} expansion of the one-loop flow equations, for three reasons: (i) tractability, in that solutions of fixed-point equations can be found analytically in its entirety, with human-readable results; (ii) transparency, in that relations to mean-field theory ($N_{\mathrm{f}} \to \infty$) become more readily apparent; and (iii) simplicity, in that the fixed point pertaining to the SU(2)-symmetry-breaking transition is unambiguously identifiable. It is worth expanding on this last point a little: At general N_{f}, a fixed point generically has many nonzero 4-Fermi couplings. Determining unambiguously which one among the many fixed points pertains to the Gross–Neveu–Heisenberg universality class is typically a laborious exercise for arbitrary N_f, entailing the computation of scaling dimensions of every conceivable bilinear at every fixed point. In the large-N_f limit, however, this is unambiguous (and essentially known already from mean-field theory): the Gross–Neveu–Heisenberg universality class is governed by the fixed point satisfying $G_1 = \mathcal{O}(1)$ and $G_{i\neq 1} = \mathcal{O}(1/N_\mathrm{f})$. One may expect this large-N_f argument to be sufficient for the present case, since the spinor-space dimension $4N_\mathrm{f} = 16$, which effectively orders the $1/N_\mathrm{f}$ expansion, is comparatively large; the full investigation for arbitrary N_f is left to future work.

For the Gross–Neveu–Heisenberg fixed point in $D = 2 + \varepsilon$ dimensions, this leads to the following non-vanishing fixed-point couplings:

$$G_{1,*} = \left(\frac{2}{3} - \frac{2}{3N_\mathrm{f}}\right)\varepsilon + \mathcal{O}\left(\varepsilon^2, 1/N_\mathrm{f}^2\right), \tag{6.13}$$

$$G_{2,*} = -\frac{4}{9N_\mathrm{f}}\varepsilon + \mathcal{O}\left(\varepsilon^2, 1/N_\mathrm{f}^2\right) \tag{6.14}$$

Note that even if starting with a pure Heisenberg channel, a second channel is immediately generated at first subleading order, $\mathcal{O}(1/N_\mathrm{f})$. This is the four-fermion interaction $[\overline{\psi}_a(\gamma_\mu\otimes\sigma_\alpha)\psi_a]^2$, the SU(2)-vector counterpart of the conventional [SU(2)-scalar] Thirring interaction. From $\mathcal{O}(1/N_\mathrm{f}^3)$ onwards, all channels would get involved.

6.3.1.3 Fate of rotational symmetry breaking

We are now in the position to study the fate of rotational anisotropies under the RG flow. Since the background nematic order respects inversion and lattice translational symmetries, it is sufficient to restrict the discussion to perturbations that leave discrete symmetries intact and break explicitly only the continuous rotational symmetry of the Gross–Neveu–Heisenberg fixed point. Rotational-symmetry-breaking terms in the quadratic part of the fermionic Lagrangian, such as anisotropic Fermi velocities, are marginal within the one-loop expansion considered here. Their relevance (or lack thereof) will be studied within the Gross–Neveu–Yukawa-Heisenberg model discussed in Sec. 6.3.2. Here, let us focus on perturbations in the interacting quartic part of the Lagrangian. In general, every 4-Fermi interaction that has a spacetime index μ, schematically $\left(\overline{\psi}M_\mu\psi\right)^2$, allows for symmetry-breaking perturbations of the form $[(\overline{\psi}_a M_0\psi_a)^2 - (\overline{\psi}_a M_1\psi_a)^2]$ and $[(\overline{\psi}_a M_0\psi_a)^2 - (\overline{\psi}_a M_2\psi_a)^2]$. Within the present approximation, only the SU(2)-vector Thirring channel is present at the fixed point, so it is sufficient to consider an anisotropy of the form

$$\begin{aligned}\mathcal{L}'_\mathrm{GNH} = \mathcal{L}_\mathrm{GNH} & \\ & - \tfrac{1}{2}\delta_1\left\{[\overline{\psi}_a(\gamma_1\otimes\sigma_\alpha)\psi_a]^2 - [\overline{\psi}_a(\gamma_0\otimes\sigma_\alpha)\psi_a]^2\right\} \\ & - \tfrac{1}{2}\delta_2\left\{[\overline{\psi}_a(\gamma_2\otimes\sigma_\alpha)\psi_a]^2 - [\overline{\psi}_a(\gamma_0\otimes\sigma_\alpha)\psi_a]^2\right\},\end{aligned} \tag{6.15}$$

with couplings $\frac{1}{2}\delta_1$ and $\frac{1}{2}\delta_1$. Using again the general formula of Gehring, Gies & Janssen (2015) and working to first order in δ's, we find the eigenvalues of the stability matrix $(\partial\beta_{\delta_i}/\partial\delta_j)$ at the Gross–Neveu–Heisenberg fixed point to be

$$\theta_{1,2} = \left(-1 \pm \frac{1}{9N_\mathrm{f}}\right)\varepsilon + \mathcal{O}(\varepsilon, 1/N_\mathrm{f}^2) \tag{6.16}$$

For $N_\mathrm{f} = 4$, pertaining to the present case of the nematic-to-coexistence transition on the honeycomb bilayer, all eigenvalues are negative. Hence, at the transition, not just rotational symmetry, but also Lorentz symmetry is emergent in the infrared.

6.3.2 Loop expansion near upper critical dimension

The above one-loop four-fermion results are *a priori* valid only in the vicinity of the lower critical space-time dimension of $D_{\text{low}} = 2$. In $2 + 1$ space-time dimensions, corrections from higher loop orders may be sizeable. To check the robustness of the conclusions, let us now consider rotational-symmetry-breaking perturbations in the opposite limit near the upper critical space-time dimension $D_{\text{up}} = 4$.

6.3.2.1 Gross–Neveu–Yukawa–Heisenberg model

The perturbatively renormalizable field theory in this limit is the Gross–Neveu–Yukawa–Heisenberg model with Lagrangian

$$\begin{aligned}\mathcal{L}_{\text{GNYH}} &= \overline{\psi}_a[\mathbb{1}_4 \otimes (\gamma_0\partial_0 + v_x\gamma_1\partial_1 + v_y\gamma_2\partial_2)]\psi_a + \frac{1}{2}(\partial_\mu\phi_\alpha)^2 \\ &\quad - h\phi_\alpha\overline{\psi}_a\left(\mathbb{1}_4 \otimes \sigma_\alpha\right)\psi_a + \lambda(\phi_\alpha\phi_\alpha)^2, \end{aligned} \tag{6.17}$$

where $a = 1, \ldots, N_{\text{f}}/2$, in agreement with the representation used in Sec. 6.3.1. In Eq. (6.17), spatial rotational symmetry breaking is encoded in the direction-dependent Fermi velocities v_x and v_y. Their bosonic counterparts c_x and c_y can be subsumed into direction-dependent dynamical critical exponents, see below; c_x and c_y have hence been set to unity from the outset. The 4-Fermi interaction parametrized by G_1 in Sec. 6.3.1 has been replaced by a Yukawa interaction between the fermions and the SU(2) order-parameter field ϕ_α, parametrized by the coupling h; it becomes marginal at the upper critical space-time dimension $D_{\text{up}} = 4$. The quartic bosonic self-interaction with coupling λ is generated by the RG and has therefore been included as well. It also becomes marginal at the upper critical dimension.

In order to deal with the spatial anisotropy, it proves expedient to perform field-theoretic RG, with loop integrals carried out over all momenta. In the spirit of the ϵ expansion, the *time* axis is extended to a $(2-\epsilon)$-dimensional Euclidean space, keeping the spatial dimension $d = 2$ fixed and assuming that all integrands have been symmetrized in frequency q_0 before the dimensional continuation. The self-energy diagrams, which are the main subjects of study in this subsection, will turn out to be infrared divergent after expanding in powers of external momenta, which is then regularize with a cut-off; the renormalization scale μ is introduced thus. The measure of the loop integration can thus be written as

$$\int_{\text{reg.}} \frac{\mathrm{d}^D q}{(2\pi)^D} := \int \frac{\mathrm{d}^{2-\epsilon} q_0\, \mathrm{d}^2\boldsymbol{q}}{(2\pi)^{4-\epsilon}}\, \Theta(|q_0| - \mu). \tag{6.18}$$

The terms in the Lagrangian $\mathcal{L}_{\text{GNYH}}$ are accordingly promoted to bare quantities, with $v_i \to Z_{v_i} v_i$ ($i \in \{x, y\}$) and $\Phi \to \sqrt{Z_\Phi Z_{p,x} Z_{p,y}}\Phi$ ($\Phi \in \{\phi, \psi\}$). Note that the running of the bosonic velocities c_i are absorbed into 'inverse dynamical critical exponents' $\partial_i \to Z_{p,i}\partial_i$ (and the concomitant $\mathrm{d}x\mathrm{d}y \to Z_{p,x}^{-1} Z_{p,y}^{-1} \mathrm{d}x\mathrm{d}y$), where the $Z_{p,i}$ parametrize the relative scaling of momentum coordinates with respect to frequency. (In other words, the Fermi velocities v_x and v_y are measured in units of c_x and c_y, respectively.) Finally, since the regularization scheme above breaks Lorentz invariance, one requires non-multiplicative counterterms, such as

$$\mathcal{L}_{\text{rest.}} = D_\psi\, \overline{\psi}\partial_0\gamma_0\psi + \frac{1}{2}D_\phi\, \phi(-\partial_0^2)\phi. \tag{6.19}$$

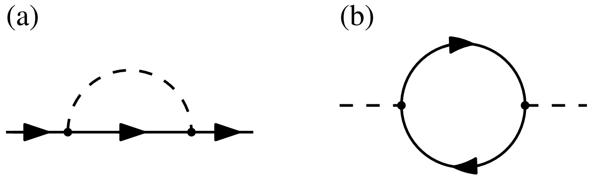

Figure 6.5: (a) Bosonic and (b) fermionic selfenergy Feynman diagrams.

These are required to ensure that in the Lorentz-invariant limit $v_x = v_y = 1$ there is no residual breaking of Lorentz symmetry (which would then solely be a regularization artefact). There are parallels to the treatment of supersymmetric gauge theories, where the often-used dimensional regularization breaks supersymmetry, and one has to resort to nonmultiplicative counterterms to restore it (Hollik & Stöckinger 2001). Just like usual multiplicative counterterms, these counterterms are often not unique, but can be judiciously constrained by demanding certain properties of the regularization procedure, see Appendix D. Eq. (6.19) represents the simplest choice that is sufficient for our purposes.

6.3.2.2 Gross–Neveu–Yukawa–Heisenberg fixed point

The theory defined by Eq. (6.17) features an interacting fixed point located within the relativistic subspace $v_{x,*} = v_{y,*} = 1$ at

$$h_*^2 = \frac{\pi}{N_\mathrm{f}+1}\epsilon + \mathcal{O}(\epsilon^2), \tag{6.20}$$

$$\lambda_* = \frac{\pi}{22}\left(-1 + \frac{2+\sqrt{1+N_\mathrm{f}(N_\mathrm{f}+9)}}{N_\mathrm{f}+1}\right)\epsilon + \mathcal{O}(\epsilon^2), \tag{6.21}$$

where $\epsilon = 4 - D$ and we have rescaled $\mu^{-\epsilon}S_{2-\epsilon}(2\pi)^{\epsilon-2}h^2 \mapsto h^2$ and $\mu^{-\epsilon}S_{2-\epsilon}(2\pi)^{\epsilon-2}\lambda \mapsto \lambda$, with $S_{2-\epsilon}$ being the surface area of the unit sphere in $2-\epsilon$ dimensions. We note that the above fixed-point values are regularization dependent and cannot be obtained by a simple rescaling of the corresponding values within, say, the Wilson scheme (Janssen, Herbut & Scherer 2018). As is well known,[9] in the vicinity of the Gross–Neveu–Heisenberg fixed point, the only relativistic-symmetry-allowed perturbation that is RG relevant towards the infrared is the quadratic term $\phi_\alpha\phi_\alpha$, which corresponds to the tuning parameter of the transition. Within the critical hyperplane, in which this term is tuned to vanish in the renormalized action by definition, the Gross–Neveu–Heisenberg fixed point is hence stable. In the following, we show that the stability holds also when small perturbations that break the rotational symmetry are taken into account, such that the fixed point hence features emergent Lorentz invariance in the low-energy limit.

6.3.2.3 Fate of rotational symmetry breaking

Within the Gross–Neveu–Yukawa–Heisenberg model, the fate of rotational symmetry breaking is determined by the flows of the Fermi velocities v_x and v_y in units of the boson velocities c_x and c_y. The corresponding selfenergy diagrams at one-loop order are shown in Fig. 6.5. The evaluation of these diagrams is somewhat involved; details thereof are deferred to Appendix D. Defining $\beta_{v_i} \equiv -\mu \mathrm{d}v_i/\mathrm{d}\mu$ in terms of the RG scale μ, we find

---

[9] cf., e.g., Herbut, Juričić & Vafek (2009); Janssen & Herbut (2017); Zerf *et al.* (2017); Janssen, Herbut & Scherer (2018)

$$\begin{aligned}\beta_{v_x} &= \frac{h^2}{2\pi}\Bigg\{\frac{1-v_x^2}{v_y}N_\mathrm{f} \\ &\quad + \left[4\pi I_{211}(v_x,v_y) - 4\pi I_{210}(v_x,v_y) + \tfrac{1}{4}\right] v_x N_\mathrm{b}\Bigg\}, \qquad (6.22)\\ \beta_{v_y} &= \frac{h^2}{2\pi}\Bigg\{\frac{1-v_y^2}{v_x}N_\mathrm{f} \\ &\quad + \left[4\pi I_{211}(v_y,v_x) - 4\pi I_{210}(v_y,v_x) + \tfrac{1}{4}\right] v_y N_\mathrm{b}\Bigg\}, \qquad (6.23)\end{aligned}$$

where $I_{211}(v_x, v_y)$ and $I_{210}(v_x, v_y)$ are functions of the velocities v_x and v_y alone. They are defined in Appendix D and and explicit forms are given in Appendix E. In Eqs. (6.22) and (6.23), the same rescaling of the Yukawa coupling has been employed as stated below Eq. (6.20). As before, N_f counts the number of four-component Dirac fermions, with $N_\mathrm{f} = 4$ for the case relevant for the nematic-to-coexistence transition on the honeycomb bilayer. For generality, a generic number N_b of boson species has also been introduced, which allows one to easily adapt the current analysis to Gross–Neveu–Yukawa models with a different number of order-parameter components. The antiferromagnetic order parameter discussed in the present setting corresponds to $N_\mathrm{b} = 3$. Note that Eq. (6.23) can be obtained from Eq. (6.23) by exchanging $v_x \leftrightarrow v_y$ and vice versa.

The constraint $v_x \equiv v_y =: v$ defines the rotationally-symmetric subspace, which is invariant under RG flow for symmetry reasons. The β-function for the rotationally-invariant Fermi velocity v within this subspace reads explicitly as

$$\beta_v = \frac{h^2}{2\pi}\left[\frac{1-v^2}{v}N_\mathrm{f} + \frac{v^4 + 4v^2 - 5 - 2\left(1+2v^2\right)\ln v^2}{4(1-v^2)^2} v N_\mathrm{b}\right]. \qquad (6.24)$$

In the vicinity of the relativistic fixed point at $v_* = 1$, the flow of the Fermi velocity can be expanded as

$$\beta_v = -\frac{N_\mathrm{f} h^2}{\pi}(v-1) + \mathcal{O}((v-1)^2). \qquad (6.25)$$

Within the rotationally-invariant subspace, the relativistic Gross–Neveu–Heisenberg fixed point is therefore stable, in agreement with previous results for similar models (Roy, Juričić & Herbut 2016; Janssen & He 2017).

To study whether the rotationally-invariant subspace is stable or not with respect to rotational-symmetry-breaking perturbations, it is expedient to set $v_x = v$ and $v_y = (1+\delta)v$, and expand $\beta_\delta = \beta_{v_y} - \beta_{v_x}$ to first order in the anisotropy parameter δ. For small $\delta \ll 1$, one thus obtains

$$\begin{aligned}\beta_\delta = -\frac{h^2}{2\pi}\left[\left(3v - \frac{1}{v}\right)N_\mathrm{f} - \left(\frac{\left(1+v^2+4v^4\right)\ln v^2}{2(1-v^2)^3} + \frac{v^4+10v^2+1}{4(1-v^2)^2}\right)N_\mathrm{b}\right]\delta \\ + \mathcal{O}(\delta^2). \qquad (6.26)\end{aligned}$$

Near the relativistic fixed point at $v_* = 1$, one thus finds

$$\beta_\delta = -\frac{h^2}{4\pi}(4N_\mathrm{f} + N_\mathrm{b})\delta + \mathcal{O}(\delta^2, v-1). \qquad (6.27)$$

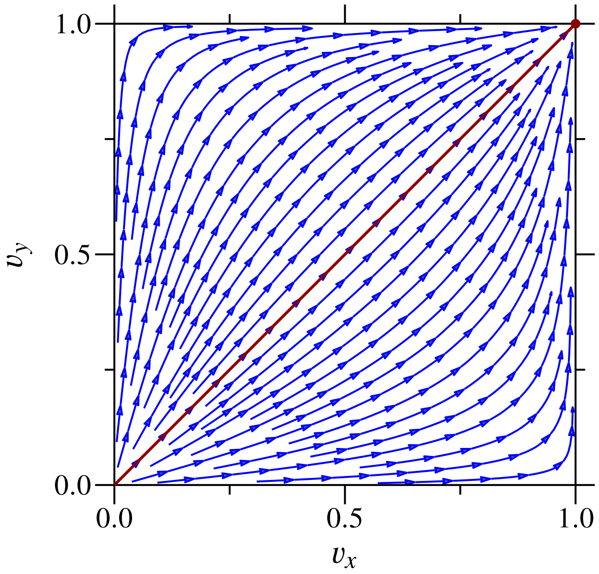

Figure 6.6: RG flow of Fermi velocities v_x and v_y in units of the boson velocities c_x and c_y for $N_\mathrm{f} = 4$ and $N_\mathrm{b} = 3$ at one-loop order. Dark red line represents the rotationally-invariant subspace $v := v_x = v_y$. All points flow ultimately to the relativistic fixed point $v_* = 1$ (dark red point), even though flow lines initially 'fan out' from the $v_x = v_y$ line for small enough initial values.

Importantly, a small rotational anisotropy is therefore irrelevant in the sense of the RG. In the vicinity of the Gross–Neveu–Heisenberg fixed point, the relativistic symmetry hence remains emergent even when a rotational anisotropy is symmetry-allowed on the microscopic level. This is illustrated in Fig. 6.6, which shows the RG flow of v_x and v_y using the full β-functions of Eqs. (6.22) and (6.23). All points flow ultimately to the relativistic fixed point $v_{x,*} = v_{y,*} = 1$, even though flow lines initially 'fan out' from the rotationally-invariant subspace line for small enough initial values. In agreement with the result from the $2 + \varepsilon$ expansion discussed in the previous subsection, we may thus conclude that the nematic-to-coexistence transition on the honeycomb bilayer features emergent Lorentz symmetry and is described by a relativistic fixed point of the Gross–Neveu–Heisenberg family of universality classes.

6.4 Critical exponents

We now proceed to providing estimates for the critical exponents characterizing the nematic-to-coexistence transition on the honeycomb bilayer, having established above that it falls into the Gross–Neveu–Heisenberg universality class with $N_\mathrm{f} = 4$ flavours of four-component Dirac fermions. As a consequence of the emergent Lorentz invariance, the transition is characterized by a unique dynamical critical exponent

$$z = 1. \tag{6.28}$$

Let us further discuss the correlation-length exponent ν, the order-parameter anomalous dimension η_ϕ, and the fermion anomalous dimension η_ψ. Higher-order corrections in perturbation theory are available in the literature for this universality class to fourth order in the $(4 - \epsilon)$ expansion (Zerf *et al.* 2017) and to second order in the large-N_f expansion, with the fermion anomalous dimension known up to third order (Gracey 2018, 2021).

Furthermore, a nonperturbative calculation using functional RG in the improved local potential approximation is also available Janssen & Herbut (2014). The main aim of this Section is to perform the necessary post-processing of these previous results to provide combined theoretical best-guess estimates for the nematic-to-coexistence transition on the honeycomb bilayer.

First, let us consider the series expansions. In fixed $D = 2 + 1$ space-time dimensions, the large-N_f expansions of the exponents are (Gracey 2018)

$$1/\nu = 1 - \frac{8}{\pi^2 N_\mathrm{f}} + \frac{36\pi^2 + 416}{3\pi^4 N_\mathrm{f}^2} + \mathcal{O}(1/N_\mathrm{f}^3), \tag{6.29}$$

$$\eta_\phi = 1 + \frac{4(3\pi^2 + 16)}{3\pi^4 N_\mathrm{f}^2} + \mathcal{O}(1/N_\mathrm{f}^3), \tag{6.30}$$

$$\eta_\psi = \frac{2}{\pi^2 N_\mathrm{f}} + \frac{16}{3\pi^4 N_\mathrm{f}^2} + \frac{378\zeta(3) - 36\pi^2\ln(2) - 45\pi^2 - 332}{9\pi^6 N_\mathrm{f}^3} + \mathcal{O}(1/N_\mathrm{f}^4) \tag{6.31}$$

where $\zeta(\cdot)$ denotes the Riemann zeta function and N_f corresponds to the number of four-component Dirac fermions. On the other hand, for the case of $N_\mathrm{f} = 4$ relevant here, the four-loop exponents in $D = 4 - \epsilon$ space-time dimensions read in numerical form (Zerf *et al.* 2017)

$$1/\nu = 2 - 1.4051\epsilon + 0.3018\epsilon^2 - 0.3032\epsilon^3 + 0.6725\epsilon^4 + \mathcal{O}(\epsilon^5) \tag{6.32}$$

$$\eta_\phi = 0.8889\epsilon + 0.1310\epsilon^2 + 0.0136\epsilon^3 + 0.0585\epsilon^4 + \mathcal{O}(\epsilon^5) \tag{6.33}$$

$$\eta_\psi = 0.1667\epsilon - 0.0661\epsilon^2 - 0.0697\epsilon^3 + 0.0156\epsilon^4 + \mathcal{O}(\epsilon^5) \tag{6.34}$$

It is worth emphasizing again at this point that the number of fermion flavours in the present setting is doubled in comparison with the previously much-studied scenario of spin-1/2 fermions on the honeycomb monolayer. Since the series expansions are at best only slowly convergent (if not outright divergent), it is necessary to study their Padé approximants, which are defined by

$$[m/n](x) := \frac{a_0 + a_1 x + \ldots + a_m x^m}{1 + b_1 x + \ldots + b_n x^n}, \tag{6.35}$$

where $x \in \{\epsilon, 1/N_\mathrm{f}\}$ for the $4 - \epsilon$ and large-N_f expansions, respectively, and m and n are non-negative integers chosen such that $m + n$ agrees with the order to which a particular exponent has been calculated. For a given choice of m and n, the coefficients $a_0, \ldots, a_m$ and $b_1, \ldots, b_n$ are then determined by imposing the boundary condition that the approximant $[m/n]$ produces the correct asymptotics for $x \ll 1$ in agreement with the series expansion. Evaluating $[m/n]$ at finite values of x yields resummed values of the corresponding observable.

The extrapolated values for the present case of $N_\mathrm{f} = 4$ flavours of four-component Dirac fermions in $D = 2 + 1$ space-time dimensions are displayed in Tab. 6.1. The spread of all admissible Padé approximants yields a measure of how close to convergence the given series happens to be. Some Padé approximants cannot mathematically fulfil all the boundary conditions imposed by the asymptotic expansions at the origin. On one hand, this concerns $[0/n]$-type approximants, which cannot describe exponents for which the zeroth-order terms vanish in the series expansion. This applies to η_ψ in both $4 - \epsilon$ and large-N_f expansions and η_ϕ in $4 - \epsilon$ expansion, as in all other Gross–Neveu–type universality classes (Janssen, Herbut & Scherer 2018). On the other hand, the $[1/1]$

Table 6.1: Critical exponents of the Gross–Neveu–Heisenberg universality class for $N_\mathrm{f} = 4$ four-component fermion flavours in $D = 2 + 1$ space-time dimensions, as pertaining to the nematic-to-coexistence transition on the honeycomb bilayer. Results from four-loop $4 - \epsilon$ expansion (Zerf *et al.* 2017), second-order $1/N_\mathrm{f}$ expansion (third-order for η_ψ) (Gracey 2018), and functional RG in the improved local potential approximation (Janssen & Herbut 2014) are used. In addition to the naïve extrapolations of the Taylor series, different Padé approximants $[m/n]$ of the series expansions are also displayed. Those for which it is mathematically impossible to match the original series expansion to all available orders are marked 'n.e.' A dash (—) in the entry for an approximant signifies either that sufficient terms are not available in the literature to compute it or that it does not exhaust all the terms available in the literature. $[m/n]_2$ denote two-sided Padé approximants, which take superuniversality relations (Gehring, Gies & Janssen 2015) into account. Here, approximants that exhibit a singularity in $D \in (2, 4)$ are marked with 'sing.' in lieu of any numerical value. The functional RG results employ two different regularization schemes, marked as 'linear' and 'sharp' in the table.

		$1/\nu$	η_ϕ	η_ψ
$1/N_\mathrm{f}$ expansion (Gracey 2018)	naïve	0.96232	1.03902	—
	[1/1]	0.88829	n.e.	—
	[0/2]	0.92700	1.04060	n.e.
	naïve	—	—	0.05306
	[1/2]	—	—	0.05292
	[2/1]	—	—	0.05329
	[0/3]	—	—	n.e.
$4 - \epsilon$ expansion (Zerf *et al.* 2017)	naïve	1.26604	1.09193	0.04654
	[3/1]	0.80250	1.01575	0.04368
	[2/2]	0.79277	1.04180	0.06413
	[1/3]	0.88152	1.11866	0.07337
	[0/4]	0.88841	n.e.	n.e.
Two-sided Padé	$[5/0]_2$	—	1.04988	—
	$[4/1]_2$	—	sing.	—
	$[3/2]_2$	—	sing.	—
	$[2/3]_2$	—	sing.	—
	$[1/4]_2$	—	1.06238	—
	$[0/5]_2$	—	n.e.	—
	$[6/0]_2$	0.89489	—	0.05906
	$[5/1]_2$	0.83956	—	sing.
	$[4/2]_2$	sing.	—	0.05949
	$[3/3]_2$	sing.	—	0.06418
	$[2/4]_2$	0.84007	—	n.e.
	$[1/5]_2$	0.86441	—	n.e.
	$[0/6]_2$	n.e.	—	n.e.
Functional RG (Janssen & Herbut 2014)	linear	0.87834	1.00929	0.03824
	sharp	0.87187	1.01089	0.03567

approximant cannot satisfy all the boundary conditions for η_ϕ in large-N_f expansion, because its $\mathcal{O}(1/N_\mathrm{f})$ correction happens to vanish – a peculiarity of the Gross–Neveu–Heisenberg universality class. All such non-existent approximants are marked 'n.e.' in Tab. 6.1.

For the $4-\epsilon$ expansion, one can refine the extrapolation by exploiting super-universality relations near the lower critical space-time dimension $D_\mathrm{low} = 2$ (Gehring, Gies & Janssen 2015). For Gross–Neveu–type universality classes in $2 < D < 4$ space-time dimensions, one thus has

$$1/\nu = (D-2) + \mathcal{O}((D-2)^2), \tag{6.36}$$

$$\eta_\phi = 2 + \mathcal{O}(D-2), \tag{6.37}$$

$$\eta_\psi = \mathcal{O}((D-2)^2), \tag{6.38}$$

independent of the particular member of the Gross–Neveu family and the number of fermion flavours N_f. These relations can be used to impose additional boundary conditions at $\epsilon = 2$ on Padé approximants to the $4-\epsilon$ expansion (Janssen & Herbut 2014; Janssen & He 2017; Ihrig *et al.* 2018). Note that for η_ϕ, only the zeroth-order coefficient in $D-2$ is superuniversal, in contrast to $1/\nu$ and η_ψ. The resulting Padé approximants are also shown in Tab. 6.1. Here, some Padé approximants develop singularities as a function of the expansion parameter, and are hence unreliable as extrapolators; these are marked as 'sing.' in lieu of any actual numerical value. For η_ϕ, various two-sided Padé approximants turn out to be singular, which may be due to the fact that only the zeroth-order term in $D-2$ is available to be included here. The refinement using two-sided Padé approximants is especially important for η_ψ, which is a highly non-monotonic function of ϵ, vanishing at both $\epsilon = 0$ and $\epsilon = 2$ separately. Such behaviour is particularly difficult to capture with a one-sided Padé approximation. It is satisfying to note that the estimates from the different two-sided Padé approximations appear overall more stable compared to the one-sided approximations.

A non-perturbative, and hence complementary, approach to estimating the exponents for $N_\mathrm{f} = 4$ and $D = 2+1$ employs the functional RG (Dupuis *et al.* 2021). This requires one to numerically solve the corresponding fixed-point equations in the improved local potential approximation (Janssen & Herbut 2014) for the present case of $N_\mathrm{f} = 4$. Two different cut-off schemes are employed in juxtapostion to assess the stability of the numerical results, viz., a linear cut-off (Litim 2001), which satisfies an optimization criterion, as well as a sharp cutoff (Janssen & Gies 2012) for comparison. The corresponding estimates for $1/\nu$, η_ϕ, and η_ψ are displayed in the last two rows of Tab. 6.1. In order to arrive at these estimates, a simple Taylor expansion of the bosonic effective potential up to 16th order in ϕ for the linear cut-off and 20th order for the sharp cutoff has been used. These orders are chosen such that the numbers displayed in the table are converged within the improved local potential approximation up to the fourth digit after the decimal point.

To arrive at final best-guess estimates combining the results of the three complementary approaches, the two-step averaging procedure outlined in Chap. 3 is employed. To recapitulate, the first step is to average over all well-behaved approximations within a given approach. The term well-behaved in this context applies to the existent and non-singular Padé approximants in the case of the series expansions, and to both regulators employed in the case of the functional RG calculations. As the results of the $4-\epsilon$ expansion are included implicitly in the two-sided Padé approximants, one should not incorporate the single-sided Padé approximants when evaluating the average in the case of the $4-\epsilon$ expansion. As for the large-N_f expansion, the naïve extrapolation in the average is included if it is sandwiched by two well-behaved proper approximants $[m/n]$ with $n \geqslant 1$. Note in this context that the two-sided approximants $[5/0]_2$ and $[6/0]_2$ are distinct from the untouched series of hypothetical $4 - \epsilon$ expansions of five-loop and six-loop order, respectively, and hence do not count as naïve extrapolations in the above sense. Having done the 'internal' average within each method, the second step is to take the mean of the three different averages. This finally leads to

$$1/\nu = 0.88(6), \qquad \eta_\phi = 1.035(23), \qquad \eta_\psi = 0.050(12). \tag{6.39}$$

In the above, the number in parenthesis is the larger of (i) the spread of the estimates of the three individual approaches and (ii) the sum of 'internal' uncertainties within the methods. The number can hence be understood as a measure of the degree of consistency between the different estimates. In the case of $1/\nu$ and η_ϕ, a particularly good agreement is found, in the sense that the uncertainty due to lack of consistency among the three methods is much smaller than the sum of the internal uncertainties. In other words, the three methods 'agree within error bars.' It is worth noting here that for the large-N_f expansion for η_ϕ, the uncertainty in the Padé extrapolation is technically ill-defined, since there exists only one well-defined nontrivial Padé approximant in this case (and hence there is no way of building a non-trivial average or sandwiching the naïvely extrapolated result). The internal uncertainty of the large-N_f estimate for η_ϕ is hence not included in the final error estimate in Eq. (6.39). However, given that the spinor-space dimension $4N_\mathrm{f} = 16$ is quite large and the naïvely-extrapolated result of the large-N_f expansion lies quite close to the Padé extrapolated value, the uncertainty due to lack of convergence of the large-N_f expansion is likely very small in any case. The estimate for η_ψ has a larger relative uncertainty, which is likely due to the aforementioned non-monotonous dependence on the space-time dimension for $D \in (2, 4)$, as well as the comparatively small absolute value of the estimate itself.

6.5 Discussion

In this chapter, we have studied the emergence of a Gross–Neveu–Heisenberg quantum phase transition as a result of competition between nematic and layer-antiferromagnetic orders on the Bernal-stacked honeycomb bilayer. The two ordered states appear to be the most promising candidate ground states consistent with experiments in Bernal-stacked bilayer graphene (BBLG).[10)] We saw that these orders generically allow a coexistence phase characterized by both nematicity and antiferromagnetism. The fact that both signs of nematic (Mayorov *et al.* 2011) as well as antiferromagnetic (Velasco Jr. *et al.* 2012) orders have been reported in low-temperature experiments on different samples lends credence to the proposition that the actual ground state of BBLG is potentially not too far from the coexistence phase, or may even be within that phase. We have mapped out the phase diagram of an effective model describing the competition between these two orders and discussed the occurring quantum phase transitions. The transition between the antiferromagnetic and coexistence orders is weakly first order as a consequence of a cubic term that is symmetry-allowed in the effective potential. By contrast – and most significantly for the purposes of this chapter, the transition between the nematic and coexistence orders turns out to be continuous; we have identified the corresponding universality class of this quantum critical point and have demonstrated in particular that

---

[10)] cf., e.g., Mayorov *et al.* (2011); Velasco Jr. *et al.* (2012); Freitag *et al.* (2012); Bao *et al.* (2012); Veligura *et al.* (2012)

in spite of rotational symmetry being spontaneously broken at an intermediate RG stage as a consequence of the background nematic order, Lorentz symmetry becomes emergent in the deep infrared at this transition. The transition therefore falls into the Gross–Neveu–Heisenberg quantum universality class. This universality class has previously been studied extensively in the context of the semimetal-to-antiferromagnetic transition on the honeycomb monolayer.[11)]

Consequently, the dynamical critical exponent, describing the relative scaling of time and space in the quantum critical regime, is $z = 1$ exactly. However, for spin-1/2 fermions on the honeycomb bilayer, the number of Dirac fermion flavours is doubled in comparison with the spin-1/2 realization on the monolayer. This can be understood as a consequence of the splitting of each of the two inequivalent quadratic band touching points in the noninteracting electron spectrum into two mini-Dirac cones in the nematic state. The universal exponents characterizing the nematic-to-coexistence quantum critical point on the honeycomb bilayer are therefore generically different from the monolayer situation. Exploiting previous results that were originally devised in the monolayer context, we have obtained estimates for the correlation-length exponent ν and the boson and fermion anomalous dimensions η_ϕ and η_ψ in the present case. In particular, we have used a four-loop ϵ expansion around the upper critical dimension (Zerf *et al.* 2017), a second-order large-N_f expansion (with the fermion anomalous dimension derived at third order) (Gracey 2018), and a functional RG approach in the improved local potential approximation (Janssen & Herbut 2014). We have obtained reasonable agreement among the results of these complementary approaches for all exponents calculated. These predictions may be tested in future numerical simulations of suitable models that realize a nematic-to-coexistence quantum critical point.

In BBLG, the nematic and layer-antiferromagnetic states are very close in energy,[12)] and the actual low-temperature ground state appears very sensitive to external perturbations. This suggests the possibility that BBLG could be tuned towards or maybe even through the nematic-to-coexistence quantum phase transition discussed in this chapter. The relativistic quantum critical point should then reveal itself in a broad quantum critical regime at finite temperatures, characterized by non-trivial scaling behaviour of various observables (Sachdev 2010a). For instance, the real-frequency dynamical spin structure factor should scale in this regime as $\mathcal{S}(\omega, \boldsymbol{k}) \propto (\omega^2 - c^2\boldsymbol{k}^2)^{-(2-\eta_\phi)/2}$ with $\eta_\phi \approx 1.04(2)$. The electronic specific heat should scale as $C_\mathrm{el}(T) \propto T^{d/z}$ with $d = 2$ and $z = 1$. Within the coexistence phase, the system develops a full, but anisotropic gap in the electronic spectrum. This should have characteristic consequences for transport experiments: Due to the nematic order in this phase, the electrical conductivity, for instance, should become anisotropic, with a two-fold oscillation as function of in-plane angle for fixed temperature, but at the same time also exhibit an activated behaviour as function of temperature, arising from the spectral gap.

In this work, we have employed a simple effective model that is expected to capture well the universal aspects of the competition between nematic and antiferromagnetic orders in BBLG. For the future, it would be desirable to identify a realistic microscopic model that allows one to study also non-universal aspects of the material. This includes the question whether signatures of the nematic-to-coexistence quantum critical point

---

[11)] For instance, see Herbut (2006); Herbut, Juričić & Vafek (2009); Janssen & Herbut (2014); Assaad & Herbut (2013); Parisen Toldin *et al.* (2015); Otsuka, Yunoki & Sorella (2016); Buividovich *et al.* (2018).

[12)] cf., e.g., Jung, Zhang & MacDonald (2011); Vafek & Yang (2010); Lemonik *et al.* (2010); Vafek (2010); Cvetkovic, Throckmorton & Vafek (2012); Lemonik *et al.* (2012)

should be expected to be readily observable in current experiments. Such an analysis might also reveal possible external parameters that could drive the system towards criticality.

A highly tunable and closely related system that has received significant interest in recent years is twisted bilayer graphene. For certain magic angles between the two honeycomb layers (Bistritzer & MacDonald 2011), it shows correlated insulating (Cao *et al.* 2018a) or unconventional superconducting (Cao *et al.* 2018b) instabilities, depending on the electronic filling. Furthermore, intertwined phases featuring nematic order, potentially also coexisting with superconductivity, have very recently been reported (Cao *et al.* 2021). These observations suggest that a scenario similar to the one proposed herein for BBLG may also be relevant for the twisted bilayer configuration. This represents an excellent direction for future investigation.

Chapter 7

Higgs Mass in Asymptotically Safe Gravity with a Dark Portal

Thus far, we have primarily concerned ourselves with systems where quantum scale symmetry emerges in the deep infrared. In this Chapter, we shall turn our attention to a scenario which is in some sense the opposite: Quantum scale symmetry that is (badly) broken in the infrared, but restored at high enough energies. In Sec. 1.1.1, we discussed how imposing quantum scale invariance in the high-energy limit enables the construction of a *fundamental* quantum field theory – i.e., one which does not break down at some 'new physics' energy scale – and how it is possible to in this way 'minimally' complete the Standard Model (SM) by including quantum gravity. 'Minimal' in this context means that there is no theoretical need for additional elementary particles beyond the graviton (as opposed to, e.g., supersymmetry), nor the abandonment of local quantum field theory as the underlying theoretical framework (as opposed to, e.g., string theory).

Theoretical self-consistency is a necessary condition for a 'Theory of Everything', but it is not sufficient. In particular, no amount of theoretical self-consistency can preclude the (experimental) discovery of, say, a new species of elementary particles. Particle accelerators, the most reliable source for new elementary particles in the past century (but also as late as 2012, in the form of the Higgs boson), have been ostensibly quiet in recent times. In their stead, astrophysical observations may provide indications towards the need for extensions of the SM. For instance, one may study the velocity profile of stars within a galaxy (Persic, Salucci & Stel 1996): Assuming a spherical mass distribution and Newtonian gravity, one can use the measured radial velocity to infer the enclosed mass. The rotational velocity has been observed to be approximately constant for radii larger than that of the optically observable disc (cf., e.g., Lisanti 2016). This implies that outside said region, despite there being practically no visible matter, the enclosed mass still appears to grow roughly in proportion to the radius. Another source of observational tension is gravitational lensing (Bartelmann 2010). A large mass (e.g., a galaxy or a galaxy cluster) bends the light emanating from a background source, such as a supernova (Umetsu *et al.* 2016; Caminha *et al.* 2017). The observed amount of light bending significantly exceeds that which could be caused by visible matter alone. A further phenomenon for which the visible matter budget of the universe is insufficient is the growth of cosmic structure, which can be estimated from the amplitude of cosmic microwave background fluctuations (Particle Data Group 2020). These – among many other – observations call for an additional matter component which does not react electromagnetically, but does interact gravitationally: so-called *dark matter*. At the time of writing, the precise constitution of dark matter is an open question. In this Chapter, we shall focus on particle dark matter, i.e., where dark matter is an additional elementary particle *beyond the Standard Model* (BSM). Scenarios of this kind have been explored in detail, see Chap. 26 of Particle Data Group (2020) or the lecture notes of Bauer & Plehn (2019) for a review. The space of all possible particle dark matter extensions to the SM is large: even for a fixed particle content, there are typically many additional free parameters from the perspective of effective field theory (EFT). To systematically explore such large spaces, a theoretical guiding principle is needed. Requiring quantum scale symmetry be restored in the deep UV – i.e., asymptotic safety – is precisely one such principle.

For concreteness, we shall consider in this Chapter on one of the most conservative dark-matter scenarios, namely where the dark sector is an additional Yukawa system (i.e., a dark scalar ϕ_d and a dark fermion ψ_d), coupled to the Standard Model via an operator of the form $\lambda_p H^\dagger H \phi_d^2$, a so-called *Higgs portal* (H is the Higgs field, λ_p is then called the portal coupling)$^{1)}$. For reasons of tractability, we shall furthermore replace the full Standard Model ('visible sector') by a Yukawa system representing the top quark and the radial mode of the Higgs boson. The general fixed-point structure of the RG flow of such a system (coupled to quantum gravity, which we shall tacitly assume henceforth) has been considered by Eichhorn & Pauly (2021a), cf. *ibid.* and Eichhorn & Pauly (2021b) for details on the computation of the pertinent β functions. Here, we shall take these flow equations as a given and focus on a concrete phenomenological question: What is the resulting Higgs mass?

The Higgs mass is an observable with far-reaching physical consequences. The discovery of the Higgs boson (ATLAS 2012; CMS 2012) with a mass of roughly $m_H \approx 125\,\mathrm{GeV}$ has striking implications: Were it only slightly heavier, a Landau pole well before the Planck scale would signal the onset of strong coupling or the presence of new degrees of freedom below the Planck scale M_{Pl}; were it only slightly lighter, the electroweak vacuum inhabited by our universe would be too unstable, thus providing a signal for the presence of new physics below the Planck scale. For the currently measured Higgs mass, the SM is self-consistent without need for new physics up to the Planck scale.

The electroweak potential might exhibit more than one local minimum. Depending on the depth of the additional minima, the SM vacuum at 246 GeV is either stable or metastable, but its stability is highly sensitive to the mass of the top quark. For a top quark mass of 172.8 GeV, the electroweak vacuum is metastable, with a life-time exceeding the age of the universe in the absence of higher-order terms in the microscopic Higgs potential. However, the top quark mass has not yet been precisely determined; the precise relation between the experimentally measured and the theoretically relevant parameter remains uncertain. Consequently, the fate of the SM vacuum remains an open question.

The asymptotic-safety perspective is in some sense the inverse of the above. Within a general RG setup, the question of vacuum stability may be formulated in terms of the sign of the running quartic coupling $\lambda(k)$, by assuming (roughly) that for large enough values of the Higgs field $|H|$, the effective potential behaves as $V_{\mathrm{eff}}(|H|) \sim \lambda(k = |H|)\,|H|^4$. In the canonical picture, λ being dimensionless renders it a free parameter, to be fixed by measuring the Higgs mass.$^{2)}$ Flowing to the UV, one can then ask whether λ turns negative

---

$^{1)}$ Strictly speaking, a dark sector comprising only a scalar would be even more conservative. We shall see later that it is insufficient from an asymptotic-safety perspective, because the portal coupling vanishes in such a scenario.

$^{2)}$ To get a general idea, one may think of the relation $m_H^2 \simeq \lambda(k_{\mathrm{IR}}) v_H^2$, where k_{IR} is an IR scale (such

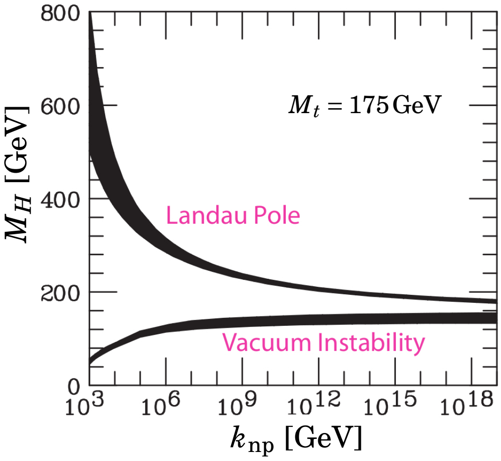

Figure 7.1: (Adapted from Particle Data Group 2002) Higgs mass window between Landau pole and vacuum instability: If the Higgs is too light, the Higgs potential is not bounded from below, whilst the Higgs being too heavy leads to a Landau pole (divergence of running couplings) at a finite scale. The scale k_{np} represents the 'new physics' scale, at which new degrees of freedom would have to be introduced to cure the relevant issue if the Higgs mass were to lie outside the window. Note that the Higgs masses are computed with a top mass of $M_t = 175\,\mathrm{GeV}$. This is historically accurate, but not in line with current consensus which places the top mass roughly between 172 and 173 GeV – cf., e.g., Particle Data Group (2020).

before the Planck scale or not (the flow above the Planck scale requires quantum gravity in any case). Inverting the question, one may then ask what Higgs mass $\lambda(k = M_{\mathrm{Pl}}) = 0$ (stability boundary) translates to. Using three loop SM β functions, a top mass of 173 GeV (and assuming the absence of higher-order interaction), this works out to a stability boundary of $m_H \approx 129\,\mathrm{GeV}$. By contrast, the measured value $m_H \approx 125\,\mathrm{GeV}$ leads to a small but negative value of the Planck-scale quartic coupling.[3] In asymptotic safety (AS), canonical power counting is no longer valid because of quantum corrections to scaling dimensions at an interacting fixed point. At the fixed point pertinent to quantum gravity (plus SM matter), it turns out that marginal operators become (weakly) irrelevant, and are thus predicted at all scales; it has been used to derive AS predictions for the Higgs mass (Shaposhnikov & Wetterich 2010) and other SM couplings (Harst & Reuter 2011; Eichhorn & Held 2018a,b; Eichhorn & Versteegen 2018; Alkofer *et al.* 2020). Vacuum stability is no longer a problem in AS, because at the Planck scale and higher, the Higgs quartic coupling is set to its fixed-point value, which is positive (and grows logarithmically below the Planck scale, as we shall discuss in more detail later). The problem is shifted instead to a tension between the predicted and measured Higgs mass, with the former coming out slighty above the stability boundary, and thus a few GeV above the observed value. The appropriate question for our setup is hence, whether the inclusion of dark matter will allow one to combine the highly predictive phenomenology of asymptotic safety with a Higgs mass closer to the measured one.

---

as the top scale) and v_H is the Higgs vev, the latter being fixed by measuring the W and Z boson masses (cf., e.g., Schwartz 2014).

[3] The difference of about 4 GeV between the measured Higgs mass and the calculated vacuum stability boundary is significant, in that it is much larger than the difference between the two-loop and three-loop calculations of the stability boundary. The small distance of the measured Higgs mass to the stability boundary essentially means that the time needed for our universe to tunnel into the true vacuum is much larger than the age of the universe itself.

The remainder of this Chapter is organized as follows: In Sec. 7.1, we shall review the asymptotic safety scenario for quantum gravity in the presence of matter degrees of freedom in some more detail. In Sec. 7.2, we shall review the relation between UV data for couplings and the Higgs mass measured in the IR, before presenting concrete calculations for our specific toy model in Sec. 7.3. We shall close the Chapter with a brief summary of our results in Sec. 7.4.

7.1 Review: The asymptotic safety scenario for quantum gravity and matter

If the asymptotic safety scenario for quantum gravity is realized, the quantum field theory (QFT) for the metric and the SM can be extended to arbitrarily high energies due to the presence of an interacting fixed point, see Eichhorn (2018, 2019) and Pawlowski & Reichert (2020) for recent reviews, and Percacci (2017), Reuter & Saueressig (2019), Eichhorn (2020), or Reichert (2020) for pedagogical introductions, and Donoghue (2020) as well as Bonanno *et al.* (2020) for critical discussions of the current status of the field. Based on the methodology pioneered by Reuter (1998), evidence for the existence of such a fixed point has been accumulated in pure gravity using functional RG techniques[4)]. In addition, lattice techniques (Ambjørn *et al.* 2012; Loll 2020; Laiho *et al.* 2017; Bassler *et al.* 2021) and analytical tensor-model techniques (Eichhorn, Koslowski & Pereira 2019) are used to search for asymptotic safety. A large body of literature indicates the existence of a fixed point with a finite (and small – typically two to three) number of relevant directions.

The fixed point persists under the inclusion of certain sets of matter fields. In particular, there are indications that it supports SM-like matter[5)]. The resulting combined fixed point has interesting properties, both, in the gravity and the matter sector. In the gravity sector it is shifted with respect to the one without matter: it appears at different fixed-point values for the gravitational couplings.

The relevant directions in the gravity sector include the Newton coupling and the cosmological constant, making the UV fixed point compatible with the measured IR values. Higher order curvature terms inevitably appear at the fixed point. Their couplings are canonically irrelevant starting from terms cubic in the curvature, while the terms quadratic in the curvature are canonically marginal. Various results studying extended truncations in the gravity sector[6)] and symmetry identities at the fixed point (Eichhorn *et al.* 2018, 2019; Eichhorn, Lippoldt & Schiffer 2019) as well as the existence of a weak-gravity bound in gravity-matter systems[7)] suggest that the gravitational fixed point could be near-perturbative in nature, in the sense that canonically irrelevant couplings typically remain irrelevant at the interacting gravity-matter fixed point because the

---

[4)] cf., e.g., Falls *et al.* (2013, 2016, 2018); Falls, Litim & Schröder (2019); Kluth & Litim (2020); Bendetti, Machado & Saueressig (2009); Gies *et al.* (2016); Falls, Ohta & Percacci (2020); Knorr (2021); Donkin & Pawlowski (2012); Eichhorn *et al.* (2018); Christiansen *et al.* (2018b); Denz, Pawlowski & Reichert (2018); Christiansen *et al.* (2015, 2014, 2016); Christiansen (2016); Knorr & Lippoldt (2017)

[5)] cf., e.g., Donà, Eichhorn & Percacci (2014); Meibohm, Pawlowski & Reichert (2016); Christiansen *et al.* (2018a); Alkofer & Saueressig (2018); Wetterich & Yamada (2019)

[6)] cf., e.g., Falls *et al.* (2013, 2016, 2018); Falls, Litim & Schröder (2019); Kluth & Litim (2020); Falls, Ohta & Percacci (2020); Knorr (2021)

[7)] cf., e.g., Eichhorn, Held & Pawlowski (2016); Christiansen & Eichhorn (2017); Eichhorn & Held (2017); Eichhorn & Schiffer (2019); de Brito, Eichhorn & dos Santos (2021) scaling spectrum is close to canonical scaling. This implies a finite number of relevant directions and hence predictivity.

In the matter sector, it is impossible to set all interactions to zero, because the interacting nature of the gravitational fixed point necessarily percolates into the matter sector. Nevertheless, there may be a choice of distinct universality classes, depending on the gravitational fixed-point values:
At the maximally symmetric fixed point (Eichhorn & Held 2017), higher-order interactions are necessarily present (Eichhorn & Gies 2011; Eichhorn 2012), but all canonically marginal and relevant couplings of the SM may be set to zero. At this fixed point, the Higgs quartic coupling is irrelevant, resulting in a prediction of the Higgs mass (Shaposhnikov & Wetterich 2010). All gauge couplings may become asymptotically free at this fixed point[8] and Yukawa couplings may be relevant for an appropriate range of the gravitational couplings (Oda & Yamada 2016; Eichhorn, Held & Pawlowski 2016; Eichhorn & Held 2017).
At a second fixed point, where shift symmetry in the scalar sector is explicitly broken, higher-order as well as marginally relevant interactions are non-vanishing. At this fixed point, some Yukawa couplings may be finite and irrelevant[9], the Abelian gauge coupling may be irrelevant (Harst & Reuter 2011; Eichhorn & Versteegen 2018) and the quartic Higgs and non-minimal Higgs-curvature couplings may also be irrelevant (Wetterich 2021; Eichhorn & Pauly 2021b), resulting in very high predictive power of this universality class.

Similarly, a number of BSM settings with gravity have been studied, with some indications for enhanced predictive power from asymptotic safety[10].

7.2 Review: Higgs mass, and RG flow in the SM and beyond

To set the stage for the main analysis, let us first review the Higgs mass in the SM, an extension of the SM by a portal to a dark scalar as well as the (conjectured) asymptotically safe versions of both – promising indications for which have been found in the literature, see the preceding section.

7.2.1 Higgs mass in the SM

In the SM, the Higgs mass is

$$M_H = \sqrt{2\lambda_H(k_{\mathrm{IR}})v_H^2}, \tag{7.1}$$

where λ_H is the Higgs quartic coupling evaluated at an IR scale k_{IR} (typically chosen as the top mass scale) and $v_H \approx 246\,\mathrm{GeV}$ is the vacuum expectation value (vev) of the Higgs field at the electroweak minimum. The Higgs vev is known from the measured masses of the weak gauge bosons; the Higgs mass measurement then fixes the quartic coupling at the electroweak scale. This measurement can be used to draw inferences on the microphysics at larger energies, e.g., the Planck scale M_{Pl}. This map between Planck scale and electroweak scale *starts* with couplings specified at the Planck scale, and follows the RG flow in its proper direction to the IR. Applied to different microscopic models, it allows one to identify those that yield the observed Higgs mass. Within the SM, the measured Higgs mass is achieved by starting from a near-vanishing value of the quartic coupling at the Planck scale. In fact, under the assumption of vanishing higher-order couplings, the measured Higgs mass requires a slightly negative Higgs quartic coupling at the Planck scale (Bezrukov *et al.* 2012).

---

[8] cf., e.g., Daum, Harst & Reuter (2010, 2011); Folkerts, Litim & Pawlowski (2012); Christiansen *et al.* (2018a)

[9] cf., e.g., Eichhorn & Held (2018a,b); Alkofer *et al.* (2020)

[10] cf., e.g., de Brito *et al.* (2019); Reichert & Smirnov (2020); Eichhorn & Pauly (2021a); Kowalska, Sessolo & Yamamoto (2021); Kowalska & Sessolo (2021); Hamada, Tsumura & Yamada (2020); Kwapisz (2019)

This finding depends on the mass of the top quark: because the top Yukawa contribution nearly cancels the gauge coupling contribution to the flow of the Higgs quartic coupling, the Higgs quartic coupling changes very little over a large range of scales. This balance is highly sensitive to the top Yukawa coupling and thus small changes in the top mass strongly alter the flow of the quartic coupling (Bezrukov & Shaposhnikov 2015). The top mass measurement is non-trivial, as is its translation into the parameter that enters the running (Hoang 2020); thus a significant uncertainty on the top Yukawa coupling remains. Novel direct measurements of the top pole mass (CMS 2017, 2020; ATLAS 2019) point to a slightly lower value than the central value recorded by Particle Data Group (2020). This difference of just 1–2 GeV in the top quark mass is sufficient to shift the Higgs quartic coupling at the Planck scale from a negative value to zero while keeping its IR value fixed to the measured one.

Using the running quartic coupling to RG improve the electroweak potential results in a potential on the boundary of stability and metastability. A metastable electroweak vacuum, tied to the larger top mass, has a lifetime longer than the age of the universe (Bezrukov *et al.* 2012; Degrassi *et al.* 2012; Butazzo *et al.* 2013; Bezrukov & Shaposhnikov 2015; Elias-Miro *et al.* 2012).

Going beyond the SM, one defines a model at some microscopic scale Λ, e.g., the Planck scale. Any physically viable model must feature a potential that is bounded from below at this scale Λ. Following the RG flow towards lower scales deforms that potential at field values $\phi \lesssim \Lambda$ and can therefore not result in an unstable electroweak potential. The minimum quartic coupling that is achievable in such a setting translates into a lower bound on the Higgs mass. The lower bound on the Higgs mass is then a prediction of the particular model. For instance, within the SM defined at $\Lambda = M_{\mathrm{Pl}}$, we have checked that a minimum quartic coupling $\lambda_H(M_{\mathrm{Pl}}) = 0$ results in a Higgs mass of 133 GeV (at one loop, 128 GeV at two loop)[11].

An asymptotically safe UV completion with gravity extends the theoretical validity of the quantum field theoretic description to infinite energies, $\Lambda \to \infty$.In this scenario a UV fixed point (i) provides a UV completion, (ii) could fix some of the marginal couplings in the gauge-Yukawa sector and (iii) is expected to predict the Planck-scale value of the Higgs quartic coupling. This determines the Higgs mass in an asymptotically safe model as a function of the relevant couplings of that model.

In the following, we shall first recapitulate the Higgs mass in a portal model to dark scalars in Sec. 7.2.2, and the Higgs mass in the (conjectured) asymptotically safe SM in Sec. 7.2.3. We shall then go on to combine the two and review the status of asymptotically safe portal models in Sec. 7.2.4. This provides the basis for new results on Higgs mass bounds in asymptotically safe portal models in Sec. 7.3.

---

[11] These values were obtained with a top mass $M_t = 172.8$GeV, taken from Particle Data Group (2020).

7.2.2 Higgs mass bounds in bosonic portal models

A gauge singlet ϕ_d may constitute dark matter[12) and reduce the lower bound on the Higgs mass[13). The dark scalar ϕ_d obeys a discrete $\phi_d \to -\phi_d$ symmetry to ensure its stability and is coupled to the Higgs scalar H via a portal operator

$$\mathcal{L}_{\mathrm{HP}} = \frac{\lambda_{\mathrm{P}}}{4} H^\dagger H \phi_d^2. \tag{7.2}$$

The portal coupling enables thermal production, see Roszkowski, Sessolo & Trojanowski (2018); Arcadi *et al.* (2018) for reviews on thermally produced dark matter and Arcadi, Djouadi & Raidal (2020) for a review of portal dark matter. Through the portal, dark bosonic fluctuations change the flow of the Higgs quartic coupling, counteracting the effect of top quark fluctuations and lowering the Higgs mass. Direct and indirect observational bounds on the value of the portal coupling and the value of the dark scalar mass were reported by GAMBIT (2017, 2019).

The portal coupling has two distinct effects on the Higgs mass:
First, starting from a fixed value of the Higgs quartic coupling in the UV, the additional bosonic fluctuations lower the quartic coupling in the IR. This is because the fluctuations of ϕ_d contribute a term $c_{\mathrm{P}}\lambda_{\mathrm{P}}^2$ with $c_{\mathrm{P}} > 0$ to β_λ. The sign of λ_{P} is immaterial for this effect, as has been discussed by, e.g., Gonderinger *et al.* (2010), Cline *et al.* (2013), and Khoze, McCabe & Ro (2014), as well as with the FRG[14) by Eichhorn & Scherer (2014). Second, if the dark scalar also acquires a vacuum expectation value, the resulting mixing between dark and visible scalar will affect the measured Higgs mass at tree level through off-diagonal terms in the scalar mass matrix. The physical masses are the eigenvalues of the mass matrix. Due to the mixing between H and ϕ_d, the corresponding eigenvalues repel each other, as one can demonstrate for a potential with real dark scalar coupled to the radial mode ϕ_v of the Higgs H of the form

$$V(\phi_v, \phi_d) = \frac{\bar{m}_v^2}{2}\phi_v^2 + \frac{\lambda_v}{8}\phi_v^4 + \frac{\lambda_{\mathrm{HP}}}{4}\phi_v^2\phi_d^2 + \frac{\bar{m}_d^2}{2}\phi_d^2 + \frac{\lambda_d}{8}\phi_d^4, \tag{7.3}$$

that we shall investigate in Sec. 7.3. In the symmetry-broken regime, it is sometimes expedient to rewrite the potential in terms of the vacuum expectation values $\langle\phi_{v(d)}\rangle =: v_{v(d)}$, to wit:

$$v_{v(d)}^2 = 2\frac{\bar{m}_{v(d)}^2\lambda_{d(v)} - \bar{m}_{d(v)}^2\lambda_{\mathrm{HP}}}{\lambda_{\mathrm{HP}}^2 - \lambda_v\lambda_d}. \tag{7.4}$$

The potential can then be written as

$$V(\phi_v, \phi_d) = \frac{\lambda_v}{8}\left(\phi_v^2 - v_v^2\right)^2 + \frac{\lambda_d}{8}\left(\phi_d^2 - v_d^2\right)^2 + \frac{\lambda_{\mathrm{HP}}}{4}\left(\phi_v^2 - v_v^2\right)\left(\phi_d^2 - v_d^2\right), \tag{7.5}$$

wherein a constant shift in the potential, being immaterial in the absence of gravity, has been neglected. In this potential, fluctuations around the minimum are massive with squared masses

$$M_{v/d}^2 = \frac{1}{2}\left(\lambda_v v_v^2 + \lambda_d v_d^2 \pm \sqrt{(\lambda_v v_v^2 - \lambda_d v_d^2)^2 + 4\lambda_{\mathrm{HP}} v_v^2 v_d^2}\right). \tag{7.6}$$

[12) This idea goes as far back as Silveira & Zee (1985) and McDonald (1994). See the lecture notes of Bauer & Plehn (2019) for a somewhat more recent review.

[13) cf., e.g., Eichhorn & Scherer (2014), and *ibid.* for a more extensive review of – primarily EFT-based – results on this topic

[14) For an FRG study of vacuum stability in the Higgs portal to fermionic dark matter, see Held & Sondenheimer (2019).

The repulsion between the two eigenvalues lowers the smaller of the two masses and increases the larger one. When the dark scalar is heavier than the Higgs this leads to a decrease of the Higgs mass (Lebedev 2012; Elias-Miro *et al.* 2012; Falkowski, Gross & Lebedev 2015). This effect does not vanish even for very large vacuum expectation values of the dark scalar. To describe the effect of the dark scalar in this limit, one solves the equation of motion for ϕ_d in the limit of slowly varying field in the potential (7.5). By reinserting the result into (7.5) one obtains a corrected quartic coupling $\tilde{\lambda}_v$,

$$\tilde{\lambda}_v = \lambda_v - \frac{\lambda_{\mathrm{HP}}^2}{\lambda_d}. \tag{7.7}$$

The correction $\lambda_{\mathrm{HP}}^2 \lambda_d^{-1}$ reduces the Higgs quartic coupling and lowers the Higgs mass. It remains finite for large v_d. Though we have performed the above analysis with λ_v the quartic self-coupling of a $\mathbb{Z}_2$ scalar ($\simeq$ radial mode of the Higgs), a similar result holds for the full Higgs self-coupling λ_H.

At a first glance, the correction appears to violate decoupling theorems in EFT. However, a massive degree of freedom only decouples in the limit of infinite mass, if its coupling to the remaining degrees of freedom is held constant. In the present case, both the dark scalar's mass and its coupling to the Higgs increase with v_d^2, such that a contribution from ϕ_d to the effective action remains in the limit $v_d \to \infty$.

The dark scalar ϕ_d might play the role of a dark matter candidate. This is only viable if the discrete $\mathbb{Z}_2$ symmetry for ϕ_d is unbroken; otherwise the dark matter decays. Observationally, this option is only viable for a narrow window of masses close to $M_{\mathrm{Higgs}}/2$, as well as for dark scalar masses $M_d \gtrsim 10^3\,\mathrm{GeV}$ (GAMBIT 2017; Athron *et al.* 2018), where the latter region is associated with fairly large portal couplings $\lambda_{\mathrm{HP}} \sim 1$. For unbroken $\mathbb{Z}_2$ symmetry, only the first of the two discussed effects contributes to the Higgs mass. This contribution to the flow of λ_H can lower the Higgs mass enough to match observations while maintaining a stable electroweak vacuum, see Athron *et al.* (2018).

7.2.3 Higgs mass in asymptotic safety

Asymptotically safe gravity-matter models might predict the ratio of the Higgs mass to the electroweak scale (Shaposhnikov & Wetterich 2010). This prediction relies on the irrelevance of the Higgs quartic coupling at an asymptotically safe matter-gravity fixed point.[15] At one loop and with the added gravitational contribution, the beta function for the Higgs quartic coupling λ_H reads as

$$\begin{aligned}\beta_{\lambda_H} := k\partial_k \lambda_H = -f_s \lambda_H + \frac{1}{16\pi^2}\left\{-6y_t^4 + \frac{3}{8}\left[2g_2^4 + \left(g_2^2 + \frac{5}{3}g_Y^2\right)^2\right]\right\} \\ + \frac{1}{16\pi^2}\left(12y_t^2 - 9g_2^2 - 5g_Y^2\right)\lambda_H + \frac{3}{2\pi^2}\lambda_H^2.\end{aligned} \tag{7.8}$$

Here f_s is a function of the gravitational couplings that is independent of the internal indices of the scalar field. It has been computed previously in various approximations[16]

---

[15] Here, we solely focus on the case where the Higgs mass parameter remains relevant. The mass parameter may become irrelevant – cf., e.g., Wetterich & Yamada (2017) – for sufficiently strong gravity fluctuations. Such strong gravity fluctuations are most likely not compatible with the weak-gravity bound discovered in several asymptotically safe matter-gravity systems (Eichhorn, Held & Pawlowski 2016; Christiansen & Eichhorn 2017; Eichhorn & Held 2017; Eichhorn & Schiffer 2019).

[16] cf., e.g., Narain & Percacci (2010); Percacci & Vacca (2015); Eichhorn *et al.* (2018); Pawlowski *et al.* (2019); de Brito, Eichhorn & Pereira (2019); Wetterich & Yamada (2019); Wetterich (2021); Eichhorn & Pauly (2021b)

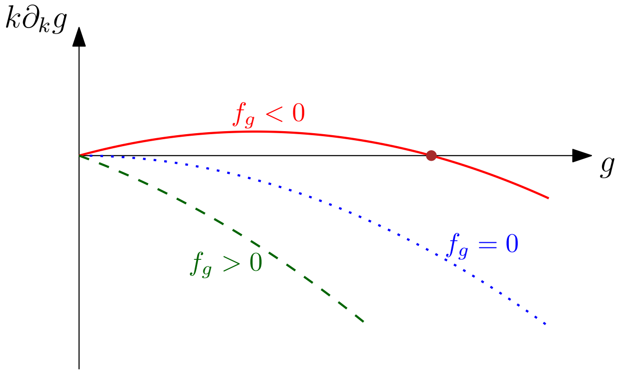

Figure 7.2: Effect of quantum gravity contribution $-f_g g$ to the flow of a generic marginally irrelevant coupling g. For $f_g > 0$ (blue, dashed), $g_* = 0$ becomes UV attractive – i.e., the fixed point is asymptotically free with respect to the coupling g, which may be the case for the abelian gauge coupling g_Y (cf., e.g., Eichhorn & Versteegen 2018). For $f_g < 0$ (red, solid), there is an IR attractive fixed point with non-vanishing g_* – i.e., asymptotic safety. This is the case for the Higgs self-coupling λ_H in the present setting, see discussion in main text ($\lambda_{H\,*} = 0$ is, however, only a fixed point if all gauge and Yukawa couplings are assumed to be asymptotically free). The case with no quantum gravity correction $f_g = 0$ is shown as a dotted blue curve for comparison.

and encodes the gravitational contributions to the beta function. The dependence of f_s on the fixed-point values of the dimensionless Newton coupling G_* and the dimensionless cosmological constant Λ_* in the approximation of Eichhorn & Pauly (2021a) is shown in Fig. 7.3(a). Further contributions to the beta function come from the gauge and the Yukawa sector, respectively, where we neglect all but the top quark Yukawa in the latter (g_Y and g_2 are the U(1) and SU(2) gauge couplings respectively, whilst y_t is the top Yukawa coupling). The Yukawa contributions come with the opposite sign to the gauge contribution due to the fermionic nature of the corresponding fluctuations. In this chapter, we shall use the convention $\beta_g = k\partial_k g$ for generic coupling g, as is conventional in high-energy physics. Note, however, that critical exponents in this convention are defined as *minus* the eigenvalues of the fixed-point Jacobian of the system of β functions, i.e., $\theta < 0$ (> 0) still corresponds to (ir-)relevant directions.

For $f_s < 0$, as has been found in several studies[17], there is an IR attractive fixed point in λ_H, as shown schematically in Fig. 7.2. It lies at either a vanishing or a non-vanishing value of λ_H, depending on the fixed-point structure in the gauge-Yukawa sector. The non-Abelian gauge couplings remain asymptotically free under the impact of quantum gravity (Daum, Harst & Reuter 2010; Folkerts, Litim & Pawlowski 2012; Christiansen *et al.* 2018a), the Abelian gauge coupling may be either asymptotically free or safe (Harst & Reuter 2011; Eichhorn & Versteegen 2018; Christiansen & Eichhorn 2017), with indications for an upper bound on its Planck-scale value Eichhorn & Versteegen (2018). Similarly, the top Yukawa coupling may be asymptotically free or safe, if conditions on the gravitational fixed-point values are met (Oda & Yamada 2016; Eichhorn, Held & Pawlowski 2016; Eichhorn & Held 2017).

Let us first assume that Yukawa and gauge couplings become asymptotically free under the impact of gravity, such that they may be set to zero to analyse the fixed point for the quartic coupling. The only fixed point at non-negative values for λ_H is

---

[17] cf., e.g., Narain & Percacci (2010); Percacci & Vacca (2015); Eichhorn *et al.* (2018); Pawlowski *et al.* (2019); de Brito, Eichhorn & Pereira (2019); Wetterich & Yamada (2019); Wetterich (2021); Eichhorn & Pauly (2021b)

$$\lambda_{H\,*} = 0, \quad \theta_{\lambda_H} = f_s < 0, \tag{7.9}$$

The quartic coupling λ_H vanishes and is irrelevant. Gravitational fluctuations hence dampen any deviation from the vanishing fixed-point value. Thereby the quartic coupling (nearly) vanishes at the Planck scale$^{18)}$. It is regenerated below the Planck scale by the other SM couplings which grow towards the IR from their asymptotically free fixed-point values. The resulting IR value for the quartic coupling corresponds to a Higgs mass in the vicinity of the measured value. In fact, this scenario predicts a Higgs quartic coupling at the stability bound of the SM (Shaposhnikov & Wetterich 2010).

Let us next consider non-vanishing fixed-point values for Yukawa and Abelian gauge coupling, i.e., a second potential gravity-matter universality class. This results in a positive fixed-point value for λ_H, given by

$$\lambda_{H\,*} = \frac{5}{48} g_Y^2 - \frac{1}{4} y_t^2 + \frac{\pi^2}{3} f_s + \frac{1}{48}\sqrt{\left(12 y_t^2 - 5 g_Y^2 - 16\pi^2 f_s\right)^2 + 576 y_t^4 - 100 g_Y^4}. \tag{7.10}$$

The larger fixed-point value translates into a larger IR value, and hence a larger Higgs mass. Thus, this universality class appears to be in tension with observations, unless additional degrees of freedom are added, as we shall do subsequently.

The resulting shift in the Higgs mass depends on the strength of gravitational corrections. Fig. 7.3 shows the shift computed in a one-loop approximation under the assumption that the predictions of Abelian gauge coupling and top quark mass from asymptotic safety match the observed values. To compute the flow, the Planck-scale values of the SM couplings are required as input. We obtain these by reversing the direction of the flow and mapping the IR values $g_Y(k_{\mathrm{IR}}) = 0.3587$, $g_2(k_{\mathrm{IR}}) = 0.6484$, $g_3(k_{\mathrm{IR}}) = 1.1647$, $y_t(k_{\mathrm{IR}}) = 0.9080$ at $k_{\mathrm{IR}} = 172.8\,\mathrm{GeV}$ $^{19)\,,\,20)}$ to their corresponding Planck-scale values. We use the one-loop beta functions for the top Yukawa coupling and the Abelian hypercharge g_Y. Based on this input, we determine $\lambda_{H\,*}$ from Eq. (7.10) for various values of f_s. We assume that $\lambda_{H\,*}$ is the Planck-scale value for the quartic coupling and flow to the IR using the SM one-loop beta function and compute the resulting Higgs mass. For $|f_s| \gg 1$ one approaches the limiting case $\lambda_H \approx 0$. For smaller values of $|f_s|$, the quartic coupling is larger at the Planck scale, translating to higher Higgs masses in the IR.

Assuming the current central value for the top mass, in both scenarios – i.e., at the Gaußian matter fixed point and at the interacting matter fixed point with dominant Yukawa contributions – the resulting IR Higgs mass is (slightly) too large. We take this as a motivation to explore which extensions of the SM could lower the IR Higgs mass

---

18) Due to the growth of the other SM couplings to non-zero Planck-scale values from their asymptotically free fixed-point values, the critical value of the Higgs quartic coupling that is reached from its vanishing fixed-point value is actually nonzero, but very small.

19) These values correspond to a top mass of $M_{\mathrm{top}} = 172.8\,\mathrm{GeV}$ and are obtained by three-loop QCD matching and two-loop matching for y_t and λ_H (Bezrukov *et al.* 2012; Chetyrkin & Zoller 2012).

20) In other words, we are using a 'quenched' approximation for the asymptotically safe flow, whereby above the Planck scale, the dimensionless versions of couplings do not flow (which for marginal couplings such as the quartic self-coupling correspond precisely to the full dimensionful couplings themselves). At the Planck scale, the metric fluctuations decouple from the matter sector dynamically, and the standard RG flow (i.e., without quantum gravity corrections) takes over. This decoupling is encoded in non-trivial threshold functions, and occurs continuously for smooth enough regulators. However, this takes place over a very small window of scales around the Planck scale, and a step function is a sufficiently good approximation (Eichhorn & Held 2018a).

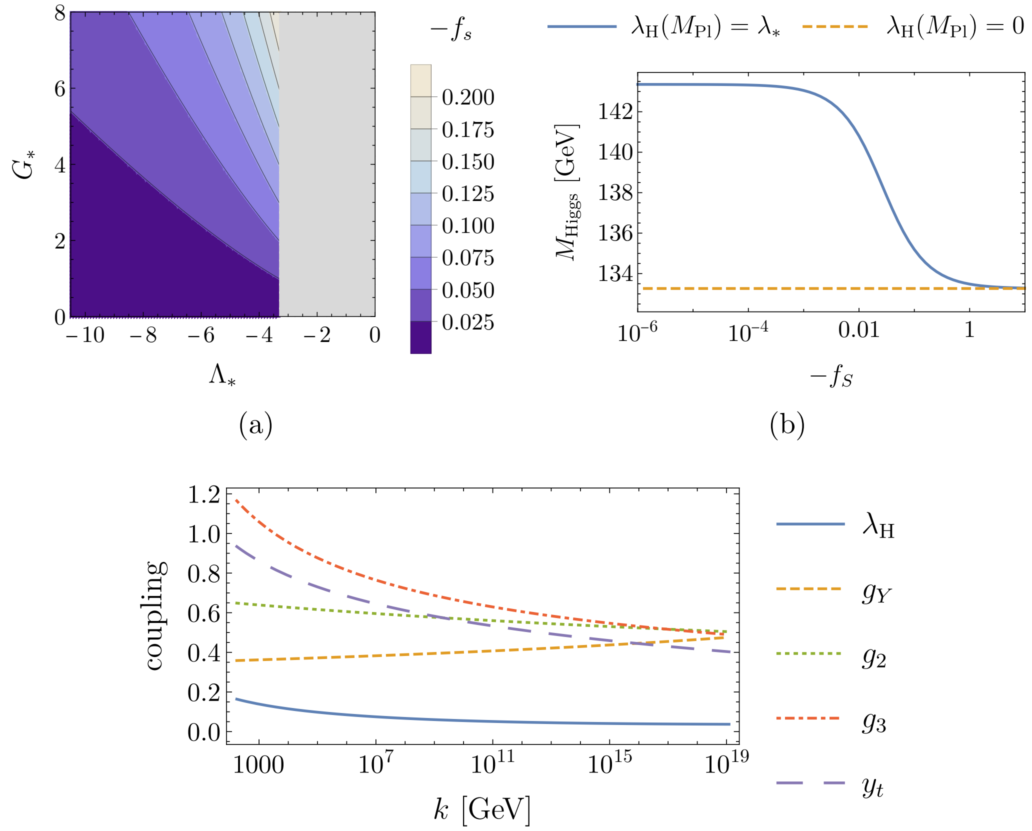

(a) (b)

(c)

Figure 7.3: Here, the RG flow has been reversed to evolve the IR values for the SM couplings to the scale M_{Pl} using the SM one-loop beta functions, whereupon the fixed-point condition (7.10) for λ_H is implemented. The Planck-scale Higgs quartic coupling extracted thus is finally RG-evolved to IR scales. (a) Contours of the quantity f_s which encodes the gravitational contributions to β_{λ_H} as a function of gravitational couplings (G_*, Λ_*). The grey region is excluded because it could result in a vanishing top mass, as found within an approximation by Eichhorn & Held (2018a). (b) Higgs mass as a function of f_s. For $|f_s| \gtrsim 1$, one approaches the Higgs mass corresponding to the vacuum stability bound with $\lambda_H(M_{\mathrm{Pl}}) = 0$ at one loop. (c) Illustration of the flow of SM couplings from the Planck scale $k = M_{\mathrm{Pl}} \approx 1.221 \times 10^{19}\,\mathrm{GeV}$ down to the scale of the top mass $k = M_t \approx 172.8\,\mathrm{GeV}$, with the Higgs self-coupling initialized to solve $\beta_{\lambda_H} = 0$ for $f_s = -0.01$ [cf. Eq. (7.8)] at the Planck scale.

and at the same time are compatible with asymptotically safe quantum gravity. The question of Higgs vacuum stability in asymptotic safety has previously been investigated in the context of a model with neutrino masses (Domènech, Goodsell & Wetterich 2021).

7.2.4 Higgs Portal and Asymptotic Safety

In the previous subsections we have reviewed results on the Higgs mass in the SM and its asymptotically safe extension with gravity. In the SM, requiring vacuum stability at a top mass of 173 GeV leads to a Higgs mass a few GeV above the measured values. In the asymptotically safe SM, two universality classes could be available for a UV completion. Both predict the Higgs quartic coupling and as a result the Higgs mass. The predictions lie at least a few GeV above the measured value. In the non-gravitational setting, a dark scalar coupled to a Higgs portal allows one to reach lower values of the Higgs mass. This motivates us to investigate whether the same mechanism may be available in an asymptotically safe extension of the model with gravity.

In the following, we shall review the implications of quantum scale symmetry on the portal coupling (Eichhorn *et al.* 2018). Quantum gravity fluctuations only produce a fixed point which is free in the portal coupling in Eq. (7.2), $\lambda_{\mathrm{P}\,*} = 0$. At this fixed point, quantum gravity fluctuations render the portal coupling irrelevant, $\theta_{\lambda_\mathrm{P}} < 0$ (we neglect operator mixing, since it is numerically very small). The dark scalar mass also features a vanishing fixed-point value, but remains relevant unless quantum-gravity fluctuations are very strong. These results hold even if the Higgs quartic coupling takes on a finite fixed-point value, as reviewed in Sec. 7.2.3. For this fixed-point structure, the portal coupling must vanish at the Planck scale. As no Yukawa or gauge degrees of freedom regenerate the coupling below the Planck scale, the portal coupling vanishes in the IR[21). Thus the scalar ϕ_d decouples at all scales, and the Higgs mass stays unchanged at low energies as a result.

To circumvent this decoupling result, an additional degree of freedom needs to couple to ϕ_d such that its fluctuations generate a non-vanishing portal coupling above or below the Planck scale. The scalar ϕ_d may be chosen to be charged under an additional gauge symmetry, as has been done, for instance, by Reichert & Smirnov (2020) and Hamada, Tsumura & Yamada (2020). The corresponding interactions regenerate the portal coupling below the Planck scale, similar to what happens for the SM Higgs at the fixed point with vanishing but relevant Yukawa and gauge coupling, see above.

As an alternative, the approach of Eichhorn & Pauly (2021a) is to introduce an additional dark fermion ψ_d with a Yukawa coupling to the dark scalar that generates an interacting fixed point for the portal. Here, we shall follow Eichhorn & Pauly (2021a) (see also Eichhorn & Pauly 2021b), and hence consider the scale-dependent effective action

$$\Gamma_k = \Gamma_k^{\text{visible}} + \Gamma_k^{\text{dark}} + \int \mathrm{d}^4x\sqrt{g}\left(\frac{1}{16\pi\bar{G}_N}(2\bar{\Lambda} - R) + \frac{\lambda_{\mathrm{HP}}}{4}\phi_v^2\phi_d^2\right), \tag{7.11}$$

with

$$\Gamma_k^{\text{visible}} = \int \mathrm{d}^4x\sqrt{g}\left(\frac{Z_\phi}{2}g^{\mu\nu}\partial_\mu\phi_v\partial_\nu\phi_v - \xi_v\phi_v^2R + \frac{\bar{m}_v}{2}\phi_v^2\right.$$

---

21) There is the possibility for a tiny portal coupling that is generated due to the curvature of the critical hypersurface: If both scalar masses, which are relevant couplings, are chosen to deviate from their fixed-point values already above the Planck scale, gravitational fluctuations enforce a tiny non-vanishing value for the portal coupling. Its value is too small to substantially impact the Higgs sector.

$$+\frac{\lambda_v}{8}\phi_v^4+\mathrm{i}Z_\psi\overline{\psi}_v\nabla\!\!\!/\,\psi_v+iy_v\phi_v\overline{\psi}_v\psi_v\Bigg), \tag{7.12}$$

and Γ_k^{dark} follows by the replacement $v\to d$ in Eq. (7.12). Here R is the Ricci scalar, $\bar{\Lambda}$ is the cosmological constant and $\bar{G}_N$ is the Newton coupling, and $G=\bar{G}_N k^2$ and $\Lambda=\bar{\Lambda}k^{-2}$ are their dimensionless counterpartsThe coupling λ_v is the representative of the quartic Higgs coupling λ_H in the SM. The $\Gamma_k^{\mathrm{visible}}$ part of the action ('visible sector') represents the SM, with ϕ_v the radial Higgs mode and ψ_v representing the top quark; Γ_k^{dark} is the dark sector.

This opens up a new universality class at which the dark and visible Yukawa couplings, scalar masses and non-minimal couplings are non-vanishing and in turn generate a non-vanishing portal coupling. At the same time, all couplings except for the Newton coupling, cosmological constant and the two mass parameters are irrelevant, endowing this fixed point with high predictive power. Here, we will investigate the impact of this extended dark sector on lower bounds on the Higgs mass. Our aim is to discover whether the single free parameter in the dark sector, namely the dark scalar mass, enables a lowering of the Higgs mass in an asymptotically safe setting.

7.3 Higgs mass in an asymptotically safe dark portal model

We are now in a position to investigate whether the presence of a dark scalar can lower the predicted value of the Higgs mass in asymptotic safety, bringing it into agreement with observations. In order to generate a non-vanishing Higgs portal coupling, we shall consider an extended dark sector with a dark scalar and a dark fermion. We shall work in a toy model for the SM, with a real scalar for the Higgs and a Dirac fermion for the top quark. The flowing action we consider is given by Eqs. (7.11) and (7.12). The beta functions have been computed by Gies & Scherer (2010) for the simple Yukawa model and Eichhorn & Pauly (2021b) for the full gravity-matter system specified in Eqs. (7.11) and (7.12).

We shall always use the beta functions of Eichhorn & Pauly (2021b) and treat the fixed-point values of G_* and Λ_* as free parameters, in order to understand the phenomenological constraints on the gravitational parameter space[22]. We shall furthermore limit ourselves to the regime $\Lambda_*<-3.3$, that might be reached in the presence of SM matter (Donà, Eichhorn & Percacci 2014). In this region, $f_y>0$ holds in the beta function for the Yukawa couplings $y_{v(d)}$ (Eichhorn, Held & Pawlowski 2016; Eichhorn & Held 2017, 2018a)

$$\beta_{y_{v(d)}}=\frac{5}{16\pi^2}y_{v(d)}^3-f_y y_{v(d)}, \tag{7.13}$$

where f_y encodes the effect of gravitational fluctuations and depends on the gravitational fixed point couplings Λ_* and G_*.[23]

The beta functions for both Yukawa couplings feature four fixed points: one at which both Yukawa couplings vanish, two at which one of the two Yukawa couplings has a non-vanishing value while the other one vanishes, and finally one at which both Yukawa couplings are non-vanishing. At this fully interacting fixed point, the Yukawa interactions break shift symmetry in both scalars. As a consequence, all scalar interactions are induced. This in particular includes the portal coupling. We will focus on this fixed point in the following.

---

[22] Many other references (cf., e.g., Eichhorn & Pauly 2021a,b; Eichhorn, Lippoldt & Schiffer 2019; Eichhorn, Held & Pawlowski 2016) follow the same procedure, i.e. solve the matter beta functions and vary the gravitational fixed point values as free parameters, but choose to omit the asterisk and just label the fixed point values with G or G_N and Λ.

[23] There is also a dependence on the non-minimal coupling $\xi_{v(d)}$ and the mass that we neglect in our discussion but consider in our numerical results, see Eichhorn & Pauly (2021b) for details.

The fixed point in question is highly predictive (Eichhorn & Pauly 2021a,b): The three quartics λ_v, λ_d and λ_{HP}, the Yukawa couplings y_v, y_d and the non-minimal couplings ξ_v, ξ_d are irrelevant at this fixed point. In the matter sector, the two mass parameters m_v^2 and m_d^2 remain as the only relevant couplings.

Our modus operandi for deriving IR predictions will be as follows: The RG flow to the IR is started at the fixed point. Deviations from quantum scale symmetry can occur along each of the two relevant directions, $m_{v,d}^2$. To mimic the SM Higgs sector, the UV deviation in m_v^2 from its fixed-point value is tuned such that ϕ_v undergoes spontaneous symmetry breaking along the RG flow and acquires a vacuum expectation value of $v_v \approx 246\,\mathrm{GeV}$ in the IR. For m_d^2, we may adjust the initial conditions such that ϕ_d either stays in the symmetric phase or undergoes spontaneous symmetry breaking. If ϕ_d remained in the symmetric phase, then the massive scalar ϕ_d could decay into the massless fermion ψ_d. This might lead to an over-abundance of relativistic degrees of freedom and thus contradict observational bounds from Big Bang Nucleosynthesis (BBN). We hence focus on the case where ϕ_d undergoes spontaneous symmetry breaking such that the dark fermion acquires a mass. We shall work in terms of the reparameterized potential displayed in Eq. (7.5). In this potential, fluctuations around the minimum $\langle \phi_{v(d)} \rangle = v_{v(d)}$ have masses $M_{v/d}$ given by Eq. (7.6). The value of M_d^2 in the IR is adjusted in terms of the relevant perturbation in m_d^2 in the UV. The visible mass M_v can be computed, once $v_v \approx 246\,\mathrm{GeV}$ is used to fix the second relevant parameter, m_v^2. The remaining couplings are all canonically marginal and irrelevant at the fixed point. They are thus fixed at all scales as a function of M_d.

If the symmetry $\phi_d \to -\phi_d$ is spontaneously broken, then ϕ_d particles decay (if they are heavy enough) into visible scalars and cannot play the role of a dark matter candidate. At the same time, ψ_d particles become massive. They are a dark matter candidate in this scenario. The observational bounds on this scenario have been discussed by Esch, Klasen & Yaguna (2013) and Bagherian *et al.* (2014) (and differ from those for a purely scalar portal discussed in Sec. 7.2.2). They constrain a dark scalar and a dark fermion as an extension of the SM. Instead of the SM, here we only consider a toy model of the visible sector. The toy model can indicate the magnitude of different effects but does not allow for precise quantitative statements. Hence, comparing between the relevant observational bounds and a more realistic model is left for future work.

The reference point for the visible mass in our toy model is different from the Higgs mass in the SM due to the absence of gauge field fluctuations. In the SM, gauge field fluctuations lead to an increase of the top Yukawa coupling towards the IR. In our toy model, the Yukawa coupling instead decreases towards the IR. The smaller Yukawa coupling causes a less strong increase of the Higgs quartic coupling towards the IR, leading to a lower Higgs mass. For fixed point values $\Lambda_* = -6.52$ and G_* adjusted such that $y_* = 0.37$ and without a dark sector, we obtain $M_v \approx 73\,\mathrm{GeV}$. Similarly, the quantitative amount of shifts in the visible mass that can be achieved due to the dark sector may differ. We expect that the qualitative (and semi-quantitative) effects of the dark sector remain the same, and will be our main focus in the following.

The dark sector impacts the visible mass M_v through the non-vanishing portal

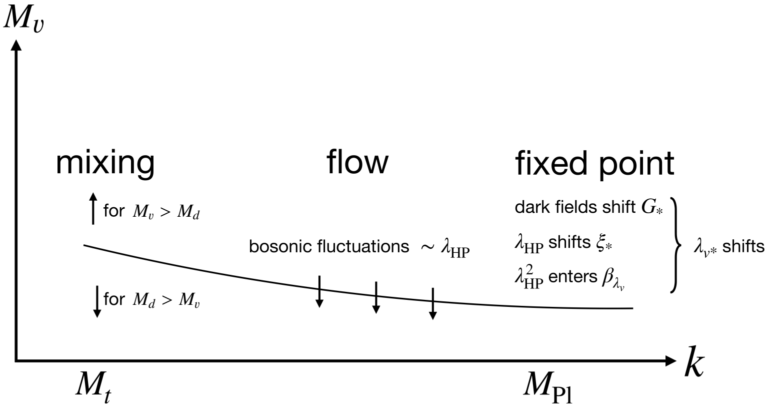
M_v
mixing
flow
fixed point
for $M_v > M_d$
for $M_d > M_v$
bosonic fluctuations $\sim \lambda_{\mathrm{HP}}$
dark fields shift G_*
λ_{HP} shifts ξ_*
λ_{HP}^2 enters β_{λ_v}
λ_{v*} shifts
k
M_t
M_{Pl}

Figure 7.4: Schematic depiction of all effects on the visible mass in asymptotic safety.

coupling in five ways. Three of these (UV1, UV2 and UV3) are shifts in the UV initial conditions for λ_v. The fourth (F) is a change in the flow of λ_v to the IR. The fifth (IR) is a mixing effect in the IR, see Fig. 7.4 for a schematic depiction of the effects.

(UV1) The gravitational fixed-point values are shifted due to quantum fluctuations of all dark sector fields. In turn, this leads to shifts in the fixed-point values in the matter sector. Thus, the UV initial conditions for the Higgs quartic coupling with and without dark sector would shift, even if the dark sector would be completely decoupled from the visible sector.

(UV2) The portal coupling contributes directly to β_{λ_v} with a term $\sim \lambda_{\mathrm{HP}}^2$. This shifts $\lambda_{v\,*}$ to smaller values than in the absence of a portal.

(UV3) The portal coupling contributes indirectly to β_{λ_v}: The non-minimal coupling, which enters β_{λ_v} linearly, depends on λ_{HP} linearly. Thus $\lambda_{v\,*}$ can be shifted to larger or smaller values, depending on the sign of $\lambda_{\mathrm{HP}\,*}$.

The shift of $\lambda_{v,*}$ depends on the balance of all three UV effects and does not have a unique sign across the gravitational parameter space.

(F) The λ_{HP}^2-term in β_{λ_v} changes the flow of λ_v to the IR. The integrated effect is negative, i.e., it decreases the quartic coupling in the IR. This decreases the Higgs mass in the absence of mixing.

(IR) The portal coupling causes mixing between ϕ_v and ϕ_d. Mixing increases (decreases) the resulting mass M_v for the visible scalar for $M_v > M_d$ ($M_v < M_d$).

In the following, we shall study each of these effects individually and investigate how they compare quantitatively. This is achieved by performing two types of parameter scans:

- In a *gravitational scan*, the gravitational fixed-point values are varied freely to explore the resulting fixed-point values in the matter sector.
- In a *fixed-Yukawa scan*, Λ_* is varied in the region $\Lambda_* < -3.3$ and g_* adjusted such that $y_* = 0.37$ remains constant. These scans follow the contour marked in red in Fig. 7.5.

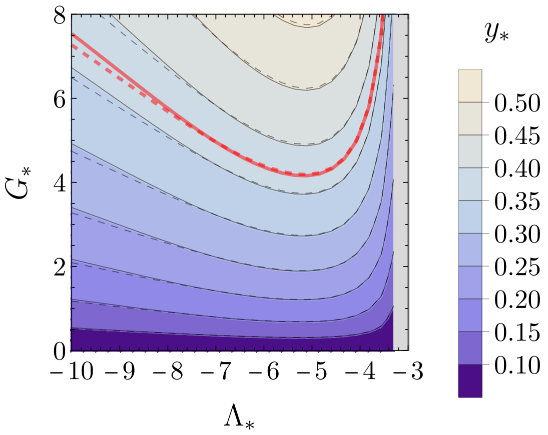

Figure 7.5: Contours of constant fixed-point value for the Yukawa coupling in the (G_*, Λ_*)-plane. Contours without a dark sector are shown in dashed, contours with the dark sector in continuous lines. The contours at $y_* = 0.37$, which determine $G_*(\Lambda_*)$ for our *fixed-Yukawa scan* are shown in red lines.

In addition, we shall distinguish between the cases *with* and *without* a dark sector.

The study of (UV1) – (UV3) is specific to our setup. The effect on the flow (F) and the IR mixing (IR) has been discussed before in an EFT context[24]. For a study employing the FRG in this context, see Eichhorn *et al.* (2015). The reader is cautioned that any quantitative comparison should only be viewed as a statement about the relative size of the different effects in our toy model. Any comparison to the measured Higgs mass will need to take into account a more elaborate visible sector than the one in the present toy model.

7.3.1 The UV regime

In the present asymptotically safe toy model, the quartic couplings are predicted at the Planck scale. The predicted values in turn depend on the fixed-point values of the gravitational and other matter couplings. We discuss these dependencies separately. The gravitational fixed-point values depend on the number of matter fields of different spin (Donà, Eichhorn & Percacci 2014). We shall compute them in the presence of SM matter with the beta functions reported by Eichhorn & Held (2018a), neglecting the back-reaction of non-vanishing masses and non-minimal couplings on the gravitational fixed point values. Due to the smallness of the fixed-point values in the matter sector, this is a viable approximation. In Fig. 7.6, the fixed-point values (G_*, Λ_*) with and without a dark sector are indicated by a square and a dot, respectively. The shift in (G_*, Λ_*) is nearly orthogonal to the contours of constant $\lambda_{v\,*}$. The fixed-point value of λ_v nearly doubles because of this shift in (G_*, Λ_*). The fixed-point values of the gravitional couplings have systematic uncertainties because the dynamics is truncated. Therefore, the square and dot in Fig. 7.6 should be understood as coming with significant uncertainties. These are difficult to estimate, but might even be as large as the difference in values between square and dot – see, e.g., Eichhorn & Held (2018a) for an estimate. Therefore, G_* and Λ_* will be treated as free parameters in much of the investigation below.

---

[24] cf., e.g., Lebedev (2012); Elias-Miro *et al.* (2012); Gonderinger *et al.* (2010); Cline *et al.* (2013); Khoze, McCabe & Ro (2014); see also Sec. 7.2.2.

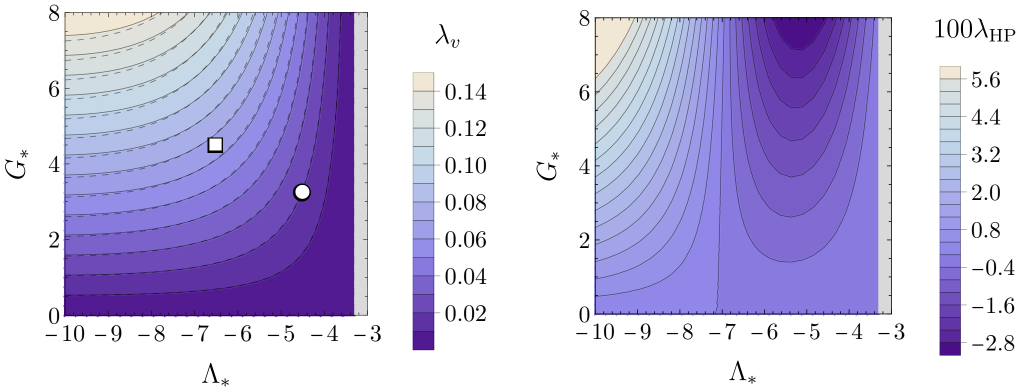

Figure 7.6: Contours for the fixed-point value $\lambda_{v\,*}$ ($\lambda_{\mathrm{HP}\,*}$) of the visible quartic coupling on the left (right) as a function of the gravitational fixed-point values G_* and Λ_* in a gravitational scan. The coupling λ_v is the representative of the quartic Higgs coupling in our toy model. The dot (square) marks the position of the gravitational fixed point without (with) a dark sector in an approximation detailed in the main text. In the left plot solid (dashed) contours mark the value with (without) the contributions from a dark sector.

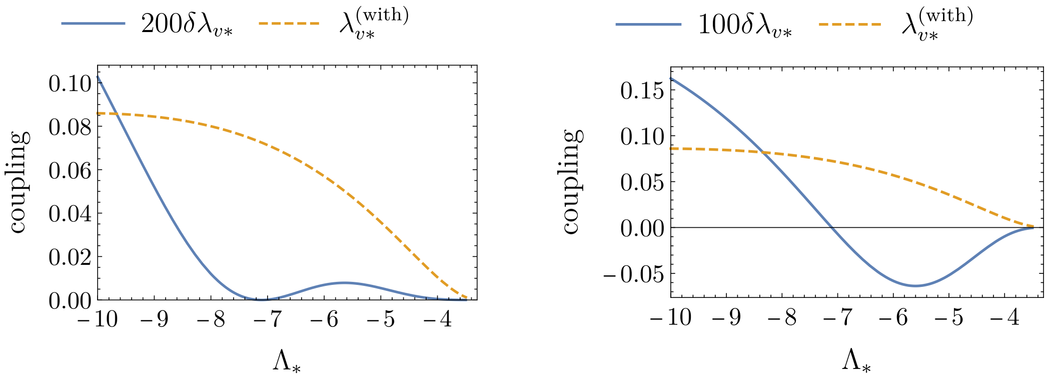

(a)

(b)

Figure 7.7: Difference $\delta\lambda_{v*} = \lambda_{v*}^{(\mathrm{without})} - \lambda_{v*}^{(\mathrm{with})}$ of the quartic coupling λ_v without and with a dark sector for varying fixed-point values of the cosmological constant Λ_* at fixed Newton coupling $G_* = 4.55$, i.e., in a gravitational scan. (a) $\lambda_{v*}^{(\mathrm{without})}$ is computed by setting $\lambda_{\mathrm{HP}} = 0$ in β_{λ_v}, while all other couplings are set to their λ_{HP}-dependent fixed-point values. The direct contribution $\sim \lambda_{\mathrm{HP}}^2$ lowers λ_{v*}, causing $\delta\lambda_{v*} > 0$. (b) $\lambda_{v*}^{(\mathrm{without})}$ is computed by solving the full matter beta functions self-consistently. Negative $\lambda_{\mathrm{HP}} < 0$ implies negative $\delta\lambda_{v*} < 0$.

The fixed-point value of λ_v depends on $\lambda_{\mathrm{HP}\,*}$ and therefore changes when the dark sector is included, even when G_* and Λ_* are (artificially) held constant. This effect is quantitatively small, cf. Fig. 7.7, because for most of the parameter space we shall explore, $\lambda_{v*} > \lambda_{\mathrm{HP}*}$. This difference is generated by fermionic fluctuations, because only β_{λ_v} contains a term $\sim y_v^4$, while $\beta_{\lambda_{\mathrm{HP}}}$ contains no such term. Fermionic fluctuations induce a quartic self-coupling but not the portal coupling[25]. Other contributions to β_{λ_v} and $\beta_{\lambda_{\mathrm{HP}}}$

---

[25] This statement is expected to hold at all loop orders/all orders of an FRG approximation, because the portal coupling breaks shift symmetry in the dark and the visible sector, whereas the Yukawa coupling only breaks shift symmetry in the visible sector. Thus the portal coupling is symmetry protected even

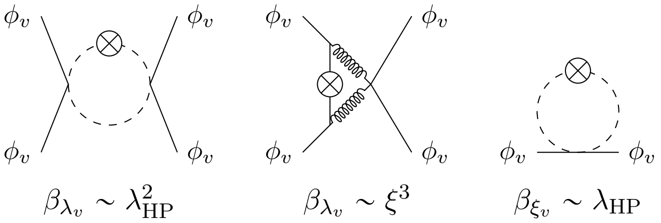
ϕ_v
ϕ_v
ϕ_v
ϕ_v
$\beta_{\lambda_v} \sim \lambda_{\mathrm{HP}}^2$
ϕ_v
ϕ_v
ϕ_v
ϕ_v
$\beta_{\lambda_v} \sim \xi^3$
ϕ_v
ϕ_v
$\beta_{\xi_v} \sim \lambda_{\mathrm{HP}}$

Figure 7.8: Diagrams representing different contributions of the portal coupling λ_{HP} to the beta function of the visible quartic self-coupling λ_v. A solid line represents the visible scalar, a dashed line the dark scalar, and a wavy line the graviton propagator respectively. The cross vertex corresponds to a regulator insertion. For each of the diagrams, there are corresponding diagrams of the same structure with regulator insertions on one of the other internal lines. (a) Direct contribution $\sim \lambda_{\mathrm{HP}}^2$ from dark scalar loop. (b) Indirect contribution from graviton triangle which is odd in the non-minimal coupling ξ, whose beta function in turn has a contribution (c) odd in λ_{HP} (the same remark applies, *mutatis mutandis*, to the flow of squared scalar masses, but typically $m_{v,d*}^2 \ll \xi_{v,d*}$ by roughly an order of magnitude).

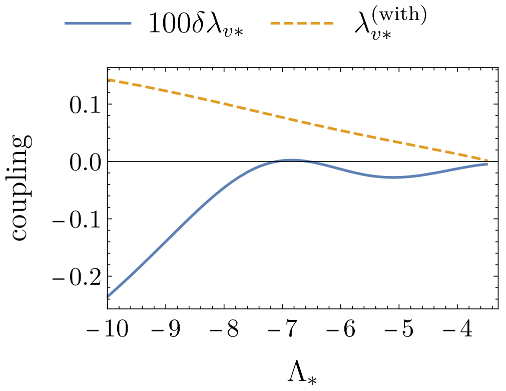

Figure 7.9: Difference $\delta\lambda_{v*} = \lambda_{v*}^{(\mathrm{without})} - \lambda_{v*}^{(\mathrm{with})}$ of the quartic coupling without and with a dark sector for constant fixed-point value of Yukawa coupling, i.e., in a fixed-Yukawa scan. Here $\lambda_{v*}^{(\mathrm{without})}$ is computed by solving the full matter beta functions self-consistently. For almost all values of Λ_*, the inclusion of the dark sector leads to larger values of λ_{v*}.

are subleading compared to this fermionic contribution. In turn, because of the small value of $\lambda_{\mathrm{HP}\,*}$, the addition of the dark sector results in a small change in $\lambda_{v\,*}$. This is exemplified by the contours of constant λ_{v*} with and without portal coupling in the (G_*, Λ_*) plane in Fig. 7.6. The difference is typically not larger than a few percent.

To further explore the difference, let us first perform a gravitational scan: The shift $\delta\lambda_* = \lambda_{v\,*}^{(\mathrm{without})} - \lambda_{v\,*}^{(\mathrm{with})}$ (at fixed gravitational coupling) arises due to both a direct contribution $\sim \lambda_{\mathrm{HP}}^2$ in β_{λ_v} as well as indirect contributions. The direct contribution is even in λ_{HP} and thus lowers λ_v. To isolate the effect of this direct contribution [given diagrammatically by Fig. 7.8(a)], let us now evaluate $\lambda_v^{(\mathrm{without})}$ by switching off the portal contribution in β_{λ_v}. All other couplings are to be determined self-consistently at finite λ_{HP} by solving the corresponding fixed-point conditions. The result is displayed in Fig. 7.7(a). As expected, the direct contribution λ_{HP}^2 comes with a positive sign and lowers the visible quartic self-coupling λ_{v*}. The indirect contribution is odd in λ_{HP} and thus lowers or increases $\lambda_{v\,*}$, depending on the sign of λ_{HP}. This indirect contribution

---

at finite Yukawa coupling.

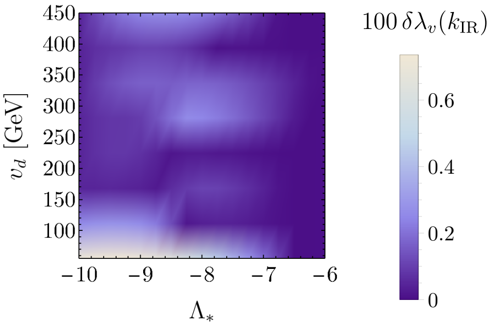

Figure 7.10: Difference $\delta\lambda_v(k_{\mathrm{IR}}) = \lambda_v^{(\mathrm{without})}(k_{\mathrm{IR}}) - \lambda_v^{(\mathrm{with})}(k_{\mathrm{IR}})$ in the IR visible self-coupling between a setup that considers portal terms in the flow of λ_v and a setup that ignores such terms. The UV initial conditions for both cases are the same, and obtained in a fixed-Yukawa scan.

[given diagrammatically in Fig. 7.8(b)] turns $\delta\lambda_v$ negative, when λ_{HP} is negative, see Fig. 7.7(b).

To keep the IR fermion mass approximately constant, let us also perform a fixed-Yukawa scan. Fig. 7.9 compares the resulting fixed point values in the case with and without dark sector; Λ_* is kept constant and G_* varied to obtain a constant Yukawa coupling. For constant fixed-point values of the Yukawa coupling, the dark sector shifts λ_{v*} towards larger values almost everywhere. For $\Lambda_* > -6.5$, the effect described above applies: the diagrams given in Fig. 7.8 lead to a larger λ_{v*}. For $\Lambda_* \ll -6.5$, the shift in G_* in the presence of the dark sector (cf. Fig. 7.5) also leads to larger values of $\lambda_{v\,*}$. Due to the smallness of $\lambda_{\mathrm{HP}\,*}$ compared to $\lambda_{v\,*}$ (as discussed above), the combined effect of direct and indirect contributions is typically of the order of 1‰. This is very much subleading compared to the change in $\lambda_{v\,*}$ that occurs due to the shift in the gravitational fixed-point values in the present truncation.

7.3.2 Flow towards the IR

Starting from the fixed point at the Planck scale, we shall now flow towards the IR. The flow of the quartic coupling receives an integrated negative contribution from the portal coupling. This lowers the quartic coupling in the IR. The effect occurs because bosonic fluctuations enter with a positive sign through a term $\sim \lambda_{\mathrm{HP}}^2$ into the beta function for the quartic coupling. This effect is small in the present setup, cf. Fig. 7.10, because $\lambda_{\mathrm{HP}} \ll 1$.

7.3.3 Infrared masses

In the IR, one of two distinct scenarios is realized: either the dark scalar ϕ_d undergoes spontaneous symmetry breaking (SSB) and develops a vacuum expectation value (vev), or it maintains its $\mathbb{Z}_2$ symmetry. In the case of unbroken symmetry, the dark sector only slightly affects the visible mass. In the case of SSB, the dark sector can strongly affect the visible mass because the mass matrix becomes non-diagonal. Both its eigenvalues depend on λ_{HP} and are therefore shifted compared to the case of unbroken symmetry. This shift in the eigenvalues of the mass matrix is illustrated in Fig. 7.11. The masses repel each other due to the non-vanishing portal coupling. This decreases the mass of the lighter scalar and increases the one of the heavier scalar.

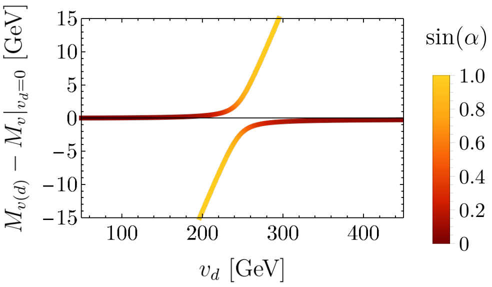

Figure 7.11: Eigenvalues of the mass matrix as a function of the dark scalar vacuum expectation value for a fiducial set of IR quartic couplings $\lambda_v = \lambda_d = 8.79 \times 10^{-2}$, $\lambda_{\text{HP}} = -6.22 \times 10^{-3}$. We choose these values as examples to illustrate the mixing between the two scalars. The overlap of the mass eigenstate with the dark scalar is colour coded. (The sine of the mixing angle by convention corresponds to the overlap of the heavier mass eigenstate with the dark scalar.)

When the visible scalar is the lighter one, $M_v < M_d$, its mass is lowered further when the dark vev is lowered. For a shift in the visible mass of the order of 1 GeV, the corresponding mixing angle is of the order of $\sin(\alpha) \sim 0.3$.

In consequence, the dark vev, which is a free parameter in asymptotic safety, can be used to dial in the desired value of the visible mass. Consequently, all properties of the dark sector are fixed.

7.3.4 From the UV to the IR – Contrasting effective field theory and asymptotic safety

The visible mass in asymptotic safety is predicted as a function of the two vevs. The predicted value is determined by the five effects (three fixed-point shifts in the UV, change in the flow to the IR, mass mixing in the IR). We shall now discuss the combination of the five effects. For each of the three regimes (UV, flow to IR, IR), we shall contrast effective and asymptotically safe theories. In doing so, we shall illustrate how asymptotic safety could strongly enhance the predictivity of a given theory.

In an effective perturbative field theory, the quartic couplings in the UV are only constrained by the two inequalities

$$\lambda_{v,d} > 0, \qquad \lambda_{\text{HP}}^2 - \lambda_v \lambda_d > 0, \tag{7.14}$$

ensuring a stable vacuum and by the requirement $\lambda_i/(16\pi^2) < 1$ (or stricter perturbativity requirements). Therefore, there are UV intervals of finite extent for all three couplings in an EFT. Each set of values $(\lambda_v, \lambda_d, \lambda_{\text{HP}})$ is translated to IR masses via the RG flow. One can adjust a combination of the portal coupling and the Higgs quartic coupling in the UV to obtain the correct IR Higgs mass even when the UV scale is chosen to be the Planck scale(26).

The same freedom is absent in asymptotic safety where the quartic couplings are fixed uniquely because they are irrelevant couplings at an interacting fixed point. This provides unique initial conditions for the RG flow at the Planck scale. These in turn yield a highly constrained IR phenomenology. Let us now compare the IR phenomenology to that of the EFT setting.

---

(26) cf., e.g., Lebedev (2012); Elias-Miro *et al.* (2012); Gonderinger *et al.* (2010); Cline *et al.* (2013); Khoze, McCabe & Ro (2014)

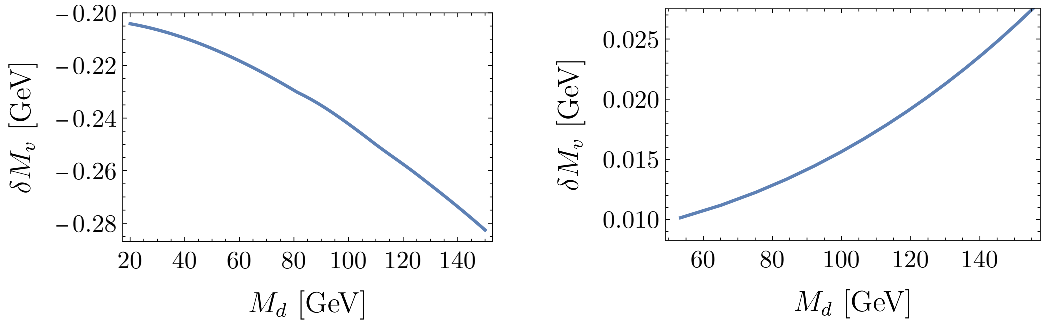

Figure 7.12: Change of the mass $\delta M_v = M_v^{(\text{without})} - M_v^{(\text{with})}$ with and without a dark sector respectively in the case where the dark scalar does not undergo spontaneous symmetry breaking. The cosmological constant is $\Lambda_* = -10$ ($\Lambda_* = -6.52$) in the left (right) panel, while the Newton coupling G_* is varied such that the Yukawa coupling is fixed at $y_{v*} = y_{d*} \equiv y_* = 0.37$.

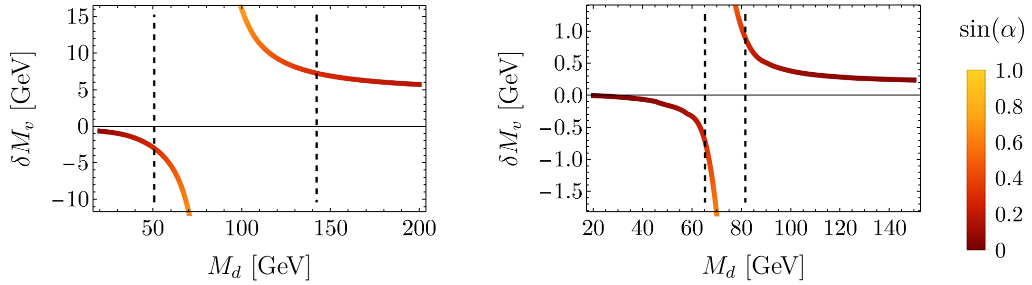

Figure 7.13: Change of the mass $\delta M_v = M_v^{(\text{without})} - M_v^{(\text{with})}$ with and without a dark sector in the case where the dark scalar does undergo spontaneous symmetry breaking. The cosmological constant is set to $\Lambda_* = -10$ (left) and $\Lambda_* = -6.52$ (right), while the Newton constant is adjusted so that the visible Yukawa coupling remains fixed at $y_* = 0.37$ (i.e., the graph is plotted for a fixed-Yukawa scan). The mixing angle is colour-coded; the dashed line demarcates the region satisfying $\sin(\alpha) < 0.3$, which is approximately the experimental constraint on the mixing of the SM Higgs.

Let us begin by considering the case in which the dark scalar does not undergo spontaneous symmetry breaking. As apparent from Fig. 7.12, the modifications are tiny. The dark sector does not change the Higgs mass substantially. This is a direct consequence of the magnitude of the portal coupling, $\lambda_{\text{HP}} \sim 10^{-3}$. The small value follows from the requirement of an asymptotically safe UV completion of our toy model. Assuming that these results carry over to the full SM setting, this would exclude large modifications to the Higgs mass due to the dark scalar without spontaneous symmetry breaking. This is different to the EFT case, where a sizeable portal coupling can be chosen [without violating the inequality (7.14), that is].

Second, let us consider the case where ϕ_d undergoes spontaneous symmetry breaking and acquires a vacuum expectation value. As apparent from Fig. 7.13 the modifications of the visible mass can be sizeable. Out of the various effects altering the mass, the IR mixing effect is dominant. For $v_d > v_v$, this allows one to lower the visible mass M_v. A lowering of about $\sim 7\,\text{GeV}$ ($\sim 1\,\text{GeV}$) implies a mixing angle $\sin(\alpha) \sim 0.3$ for $\Lambda_* = -10$ ($\Lambda_* = -6.5$). Note that these numbers are obtained in the present toy model; we may expect, however, that similar-sized effects can be achieved if an extension of our toy model to the full SM is asymptotically safe.

Assuming that an extension to the full SM exists, we make the following observations: The Higgs mass might be lower in the presence of a portal coupling to a dark scalar. This could reconcile the Higgs mass predicted from asymptotic safety with observations[27]. The results derived here indicate that to achieve a sufficiently large impact on the Higgs mass, the dark scalar needs to undergo spontaneous symmetry breaking and should be heavier than the Higgs particle.

A sizeable portal coupling requires the presence of additional dark degrees of freedom beyond the dark scalar. We have focused on a dark fermion, because a dark gauge field may not yield a symmetric phase for the dark scalar in the UV, cf. Eichhorn, Held & Wetterich (2020) and Wetterich (2021). The dark fermion ψ_d becomes massive once the dark scalar undergoes SSB. In the IR, no relativistic degree of freedom beyond those of the SM remain. Interestingly, this is compatible with bounds on additional relativistic degrees of freedom that arise from Big Bang Nucleosynthesis (Cyburt *et al.* 2016; Pitrou *et al.* 2018).

Similar models have been studied in an effective field theory context as dark matter candidates (Esch, Klasen & Yaguna 2013; Bagherian *et al.* 2014; Krnjaic 2016). Asymptotic safety constrains the parameter space of these models and is therefore not guaranteed to result in a viable dark-matter phenomenology. According to the preliminary study by Eichhorn & Pauly (2021a), the dark fermion might be available as a viable dark matter candidate. Taken together with the results in the present chapter, this strongly motivates a study of the SM together with a dark sector as considered here.

7.4 Discussion

There are promising indications that asymptotically safe quantum gravity could enhance the predictive power within the SM and some of its extensions. This could allow to compute the Higgs mass in (extensions of) the SM from first principles. Our focus here was on a toy model that features a real scalar and a fermion as the SM Higgs and top respectively. We postulated a dark sector containing a dark scalar and a dark fermion coupled through a Yukawa coupling to each other and a portal coupling to the SM. In addition to lowering the Higgs mass compared to the pure SM case, the dark sector might simultaneously provide a dark-matter candidate.

The dark sector, which contains several canonically marginal or relevant couplings m_d^2, $\xi_d, \lambda_d, \lambda_{\mathrm{HP}}, y_d$ (i.e., five free parameters according to canonical power counting) contains a single relevant coupling m_d^2 at an asymptotically safe fixed point found within the approximation of Eichhorn & Pauly (2021a). This free parameter can be used to vary the Higgs mass. We found that unless the dark scalar undergoes spontaneous symmetry breaking, the resulting modifications of the Higgs mass are small. If the dark scalar undergoes spontaneous symmetry breaking, then the resulting modifications can become sizeable. The most relevant effect is the tree-level mixing between the dark and the visible scalar. The various UV effects related to the dark sector are relatively small.

Once the single free parameter is used to obtain the measured Higgs mass, there is no free parameter left in the dark sector. Accordingly, the dark relic density and the cross-sections relevant for direct dark-matter searches could be predicted from first principles. If the indications from the present toy model and approximation go through in more extensive truncations and models with more complete particle content, asymptotic safety is quite distinct from other approaches to physics beyond the Standard Model which in general have less predictive power and thus more freedom to match observational data. For instance, observational data from cosmology constrain the dark sector. First, the dark fermion may not be massless in order to not violate constraints on the number of relativistic degrees of freedom at Big Bang Nucleosynthesis (BBN). Second, no field in the dark sector may be overproduced, so as to not overclose the universe. There are tentative indications that both constraints might be met: The dark fermion becomes massive, once the dark scalar acquires a vev, such that BBN constraints hold. The dark scalar is not stable, and therefore its relic density vanishes. The dark fermion is stable and has a finite relic density, which, according to estimates of Eichhorn & Pauly (2021a) is close to critical density.

---

[27] We are assuming a top mass of 173 GeV here. If the top quark is lighter, the scenario from Shaposhnikov & Wetterich (2010) could be viable without a dark sector. If the top quark weighs about 173 GeV, the present mechanism is applicable for the universality class at which some of the SM couplings are nonzero at the fixed point, but not in the scenario of Shaposhnikov & Wetterich (2010), where all SM couplings are zero at the fixed point, resulting in a vanishing portal coupling at all scales.

Overall, the present results serve to showcase the predictive power of asymptotic safety and how it could constrain the vast parameter space of models beyond the Standard Model. Combining these theoretical constraints with phenomenological constraints from particle physics and cosmology turns out to be non-trivial, as we have seen here. One may therefore hope that the asymptotic-safety paradigm results in a small set of viable models which make definite predictions for future experiments and observations.

Chapter 8

Conclusions

In this thesis, we have studied five instances of how low-energy physics can be impacted by quantum scale symmetry. In four of these instances, quantum scale symmetry emerges, when the system finds itself close to a quantum phase transition, over long length scales (i.e., in the IR) of the order of the correlation length. In the fifth scenario, quantum scale symmetry is restored only at very high energies (i.e., in the UV), but constrains the phenomenology at low energies, where quantum scale symmetry is no longer intact.

In Chapter 3, we have studied the Gross–Neveu SO(3) universality class in $D = 3$ spacetime dimensions. Generally, such transitions are interesting because they show similarities in terms of fixed-point structure with asymptotically safe completions of the Standard Model with quantum gravity, whilst having a simpler field content. Specific to the SO(3) context, however, is the fact that the model describes the transition from a spin-orbital liquid to a antiferromagnet. The constituent chiral fermions of the semimetallic ground state are spinons, which arise due to the fractionalization of local spin-orbital moments and are hence not directly probable by conventional experimental techniques. On the other hand, as gapless modes, they leave their imprint on the critical exponents of a quantum phase transition to a conventional state, such as the antiferromagnet considered here. The critical exponents themselves are amenable to field-theory techniques developed originally for calculations in elementary particle physics. Thus, the study furnishes not only an opportunity to 'learn about elementary particles by boiling water', as put by Polyakov, but also to understand spin-orbital liquids by colliding electrons. To this end, we employed a three-loop $4-\epsilon$ expansion, a second-order $1/N$ expansion, and a functional renormalization group (FRG) calculation in the improved local potential approximation (LPA$'$). The results from the different approaches turned out to be in fair agreement with each other. However, at the present order of approximation, a quantification of the error incurred by the respective methods using internal indicators (spread of Padé approximants in the case of series expansions, regulator-dependence in the case of FRG) proved difficult. However, having the three complementary methods at our disposal allows for a rough estimate of the overall error in terms of the deviation among the three methods, and the unweighted ('maximum ignorance') average of the three methods yielded the best-guess estimates. We thus arrived at $1/\nu = 1.03(15)$, $\eta_\phi = 0.42(7)$ and $\eta_\psi = 0.180(10)$ (with the understanding that ν and η_ϕ are predictions for measurements, whilst η_ψ is not directly measurable due to the fermion correlator not being gauge invariant). Going to higher orders in the series expansions is one way to improve accuracy; it would in particular also yield more well-behaved Padé approximants, whose spread would represent a more reliable error estimate. For the loop expansion, a complementary expansion within the 4-Fermi theory in $D = 2 + \varepsilon$ dimensions may be instructive. For the FRG, going to higher orders of derivative expansion (i.e., beyond LPA$'$) would allow for an error estimate beyond regulator dependence, namely by extrapolating the finite-order results to infinite order. Given the difficulty of directly observing fractionalized excitations, sufficiently accurate theoretical predictions for critical exponents may serve as a 'diagnostic toolkit' for spin-orbital liquids. Sharpening the estimates along the lines described above – possibly also for other flavour groups and/or different emergent gauge structures – may hence be a worthwhile subject of future investigation. As a byproduct of our analysis, we have found indications that a non-perturbative fixed-point collision may disconnect the Yukawa-type fixed point, which becomes perturbatively renormalizable in $D = 4$, from its Hubbard–Stratonovich transformed incarnation, the Gross–Neveu fixed point which has a perturbatively renormalizable description in terms of a 4-Fermi theory in $D = 2$. It would be interesting – albeit from a more academeic perspective – whether this kind of fixed-point structure may be reproduced within a perturbatively controllable setting, e.g., for a somewhat artificial combination of flavour numbers and/or flavour group.

In Chapter 4, we then turned our attention to *Luttinger* fermions in $D = 3$ spacetime dimensions (or equivalently, in $d = 2$ spatial dimensions, which is an often-used counting given the lack of Lorentz invariance; recall that in our convention, D always refers to the topological dimension of spacetime, rather than any 'effective' dimension). Luttinger fermions are the $z = 2$ analogue of chiral Dirac fermions, in that they have a quadratic dispersion but no energy gap. As such, they arise in semimetals when two bands touch quadratically, such as in Bernal-stacked bilayer graphene (within certain approximations), and in 3D semimetals such as grey tin and mercury telluride. In 2D, Luttinger semimetals have an instability at zero 4-Fermi interaction; the corresponding field theory is, in high-energy language, asymptotically free rather than safe. Nevertheless, the Gaußian fixed point governing the transition is marginal rather than critical, resulting in several pathologies. We saw how these pathologies may be understood as a collision between the IR-attractive Gaußian fixed point and an IR-repulsive (i.e., critical) fixed point distinct from the Gaußian one in $d = 2+\epsilon$. Observables like the order-parameter expectation value and correlation length develop essential rather than power-law singularities; the exponent, as we showed by explicit computation for the minimal model of two-component 'spinors', is distinct from the mean-field one. Whilst finite critical exponents often default to canonical power-counting values, the susceptibility exponent turns out to be *one-loop exact*, and in the minimal model we computed explicitly, takes the value $\gamma = 2\gamma_{\text{mean-field}} = 2$. Such an exact yet non-mean-field prediction can serve as a useful benchmark for numerical methods.

In the next two chapters, we considered the scenario where a quadratic band touching point splits into several Dirac cones. A major obstruction towards the realization of quantum criticality in (conventional) Dirac semimetals – e.g., graphene – is the fact that the fixed-point value of the 4-Fermi coupling translates to a large microscopic value of density-density interactions; in general, the concrete experimentally accessible system is difficult to tune past the quantum phase transition. If, however, the Dirac semimetal emerges from a Luttinger semimetal, the microscopic density of states is rather high, such that a smaller critical interaction strength is sufficient to trigger spontaneous symmetry breaking. Such a 'Dirac from Luttinger' scenario is possible if the rotational symmetry of the Luttinger semimetal is low enough. This may occur in Bernal-stacked bilayer graphene (BBLG) both due to explicit and spontaneous breaking of rotational invariance.

In Chapter 5, we considered the explicit breaking of continuous rotational symmetry due to the honeycomb structure of the lattice. We demonstrated by an explicit two-loop calculation, that self-energy effects induce a splitting of each QBT into three Dirac cones. As a corollary, we found the critical coupling strength when assuming a QBT dispersion in the UV is significantly lower than if one assumes a linear low-energy dispersion at the lattice scale. Based on the ordering temperature, we then estimated that the (effective) coupling strength in BBLG may be close to the critical value.

In Chapter 6, we investigated the consequences of the splitting of a QBT into two Dirac cones as a consequence of the spontaneous breakdown of rotational symmetry – i.e., in the presence of nematic order. In particular, we considered the quantum criticality arising due to the interaction-induced onset of antiferromagnetic order on top of such a nematic state. Such a *co-existence* scenario is an appealing one for the ground state of BBLG, since experiments are still not unequivocal as to whether a fully gapped state (such as a layer-polarized antiferromagnet) or a gapless one (such as nematic ones) is the true ground state. Within our mean-field calculation, we found an extended region in our (simplified phenomenological) theory space featuring coexisting antiferromagnetic and nematic order, with (pure) nematic order on one side and antiferromagnetic on the other. It is thus conceivable that, e.g., technical specificities of sample preparation may drive BBLG into one or the other phase. It also raises the possibility that BBLG may be tunable through a transition from the nematic phase, featuring gapless linearly dispersion fermionic excitations, into the coexistence phase where said excitations are gapped out. We have then demonstrated that this transition falls into the $D = 3$ chiral Heisenberg universality class, by showing that not only rotational, but in fact Lorentz invariance is emergent close to the transition, using a one-loop expansion in the anisotropic versions of 4-Fermi theory in $D = 2 + \varepsilon$ and Yukawa theory in $D = 4 - \epsilon$. As a by-product, we have constructed the full Fierz-complete basis for Gross–Neveu theory with SU(2) isospin in $D = 3$. We have also combined previously published results on four-loop $4 - \epsilon$ expansion, second-order $1/N$ expansion and FRG in LPA$'$ for the chiral Heisenberg universality class to derive best-guess estimates for the critical exponents of the nematic-to-coexistence transition in BBLG. Unlike its monolayer graphene counterpart, the increased number of fermion components leads to an overall lower uncertainty in the exponents.

In Chapter 7, we turned our attention to the problem of the Higgs mass in asymptotically safe (AS) quantum gravity (QG) with Standard Model (SM) matter in the presence of a Higgs portal to dark matter. The UV completion of the SM using ASQG has many attractive properties: By imposing quantum scale symmetry in the deep UV, one obtains a drastic reduction in the number of free parameters (even though the low-energy phenomenology is no longer scale-invariant, as evinced by the plethora of massive elementary particles). Furthermore, the Higgs self-coupling at the Planck scale and above is fixed by UV quantum scale symmetry such that the electroweak vacuum is stable, rather than merely meta-stable as in the vanilla SM. This, however, comes at the cost of the Higgs mass being a prediction rather than a free parameter – once the Higgs vacuum expectation value (vev) is fixed by measuring the weak gauge boson masses – and the ASQG prediction comes out a few GeV above the measured value. We therefore investigated whether this tension may be alleviated by taking into account the presence of dark matter (for which there is an abundance of independent experimental indications, such as gravitational lensing by supernovae), coupled to the SM via a so-called Higgs portal. For simplicity, we considered a toy SM modelled by a Yukawa system (representing the top quark and the radial mode of the Higgs boson) and Yukawa dark matter consisting of a dark scalar and a dark fermion. We found that within this setting and reasonable approximations (cf. Eichhorn & Pauly 2021a,b), the Higgs mass may be lowered by the necessary amount, provided the dark scalar undergoes spontaneous symmetry breaking and is heavier than the Higgs, as a function of the dark scalar vev. Once the dark scalar vev is fixed by the Higgs mass, there are no further free parameters, allowing for the first-principles prediction of observables such as the dark relic density and cross-sections relevant for direct dark-matter searches. Doing so whilst accounting for a more realistic SM matter content, though likely more challenging, is hence an excellent direction for future investigations.

Overall, our studies are witness to the fact that quantum scale symmetry, despite emerging (or being restored) only in certain limits, is a recurrent theme across many widely varying settings. From spin liquids to quantum gravity, it may hence serve as a vehicle that facilitates the systematic transfer of insight from one setting to another, beyond traditional boundaries of subdisciplines in physics, and generate new insight by their synthesis and cross-fertilization.

Appendices

A Position-space propagator for C_3-symmetric QBT

Let us consider here the position-space propagator $G_0(x)$ in the presence of (small) explicit rotational symmetry breaking $\mathrm{O}(2) \to C_3$. It is defined by $[\partial_\tau + \mathcal{H}_0(-\mathrm{i}\nabla)]\, G_0(\tau, \boldsymbol{x}) = \delta(\tau, \boldsymbol{x})$ with $\mathcal{H}_0$ given by Eq. (5.18). Translational invariance behooves us to solve this in Fourier space, to wit:

$$G_0(\tau, \boldsymbol{x}) = \int \frac{\mathrm{d}\omega\, \mathrm{d}^2\boldsymbol{p}}{(2\pi)^3}\, \mathrm{e}^{\mathrm{i}(\omega\tau + \boldsymbol{p}\cdot\boldsymbol{x})} \tilde{G}_0(\omega, \boldsymbol{p}), \tag{A.1}$$

with $\tilde{G}_0(\omega, \boldsymbol{p}) = [\mathrm{i}\omega + \mathcal{H}_0(\boldsymbol{p})]^{-1}$. Like in Sec. 4.6.3, the basic strategy now is to perform the Fourier integral in cylindrical coordinates

$$\boldsymbol{p} = (\rho\cos\varphi, \rho\sin\varphi); \quad \boldsymbol{x} = (r\cos\vartheta, r\sin\vartheta); \quad \boldsymbol{p}\cdot\boldsymbol{x} = r\rho\cos(\varphi - \vartheta).$$

For reasons of analytical tractability, we expanded the expression as a multilinear form in powers of rotational symmetry breaking (f_1, f_3 for the QBT theory and f_2 for the Dirac theory), keeping up to second order corrections, since that is the order to which β functions were computed subsequently. Let us first consider the QBT limit $|f_1/f_2| \ll 1$, and parameterize the expanded propagator as

$$\tilde{G}_0(\omega, \boldsymbol{p}) = \sum_{\mu n m} \sigma^\mu \otimes \left(\sigma^3\right)^n \left[\tilde{P}^{\mathrm{c}}_{\mu n m}(\omega, \rho)\cos(m\varphi) + \tilde{P}^{\mathrm{s}}_{\mu n m}(\omega, \rho)\sin(m\varphi)\right] \frac{\left(f_1 + \rho^2 f_3\right)^n}{\left(\omega^2 + \rho^4\right)^{1+n}} \tag{A.2}$$

where $\mu \in \{0, 1, 2\}$, $k, m, n \in \mathbb{N}_{\geqslant 0}$, and $(\sigma^\mu) = (\mathbb{1}_2, \sigma_x, \sigma_y)$. We have also set $f_2 = 1$ in the present QBT limit for convenience. We wish to expand to second order of rotational symmetry breaking, i.e., $n + m \leqslant 2$. The nonvanishing terms in $\tilde{G}_0(\omega, \boldsymbol{p})$ are then found to be:

$$\begin{aligned}
\tilde{P}^{\mathrm{c}}_{000}(\omega, \rho) &= -\mathrm{i}\omega, \\
\tilde{P}^{\mathrm{c}}_{102}(\omega, \rho) &= \rho^2 = \tilde{P}^{\mathrm{s}}_{102}(\omega, \rho), \\
\tilde{P}^{\mathrm{c}}_{013}(\omega, \rho) &= 2\mathrm{i}\omega\rho^3, \\
\tilde{P}^{\mathrm{c}}_{111}(\omega, \rho) &= \omega^2\rho = -\tilde{P}^{\mathrm{s}}_{111}(\omega, \rho), \\
\tilde{P}^{\mathrm{c}}_{115}(\omega, \rho) &= -\rho^5 = \tilde{P}^{\mathrm{s}}_{115}(\omega, \rho), \\
\tilde{P}^{\mathrm{c}}_{020}(\omega, \rho) &= \mathrm{i}\left(\omega^3\rho^2 - \omega\rho^6\right), \\
\tilde{P}^{\mathrm{c}}_{026}(\omega, \rho) &= -2\mathrm{i}\omega\rho^6, \\
\tilde{P}^{\mathrm{c}}_{122}(\omega, \rho) &= -2\omega^2\rho^4 = \tilde{P}^{\mathrm{s}}_{122}(\omega, \rho),
\end{aligned}$$

$$\begin{aligned}
\tilde{P}^{\mathrm{c}}_{124}(\omega,\rho) &= -\omega^2\rho^4 = -\tilde{P}^{\mathrm{c}}_{124}(\omega,\rho), \\
\tilde{P}^{\mathrm{c}}_{128}(\omega,\rho) &= \rho^8 = \tilde{P}^{\mathrm{s}}_{128}(\omega,\rho).
\end{aligned} \tag{A.3}$$

In the opposite Dirac limit, a similar expansion can be found in powers of f_2 (now setting $f_1 = 1$). The momentum space propagator is then parametrized as

$$\tilde{G}_0(\omega,\boldsymbol{p}) = \sum_{\mu n m} \sigma^\mu \otimes \left(\sigma^3\right)^{1+n} \left[\tilde{Q}^{\mathrm{c}}_{\mu n m}(\omega,\rho)\cos(m\varphi) + \tilde{Q}^{\mathrm{s}}_{\mu n m}(\omega,\rho)\sin(m\varphi)\right] \frac{f_2^n}{\left(\omega^2+\rho^2\right)^{1+n}} \tag{A.4}$$

where the $\tilde{Q}^{\mathrm{c,s}}_{\mu n m}(\omega,\rho)$ again are bivariate polynomials, the nonvanishing ones among which are given by

$$\begin{aligned}
\tilde{Q}^{\mathrm{c}}_{000}(\omega,\rho) &= -\mathrm{i}\omega, \\
\tilde{Q}^{\mathrm{c}}_{101}(\omega,\rho) &= \rho = -\tilde{Q}^{\mathrm{s}}_{201}(\omega,\rho), \\
\tilde{Q}^{\mathrm{c}}_{013}(\omega,\rho) &= \omega\rho^3, \\
\tilde{Q}^{\mathrm{c}}_{112}(\omega,\rho) &= \omega^2\rho^2 = \tilde{Q}^{\mathrm{s}}_{212}(\omega,\rho), \\
\tilde{Q}^{\mathrm{c}}_{114}(\omega,\rho) &= -\rho^4 = -\tilde{Q}^{\mathrm{s}}_{212}(\omega,\rho), \\
\tilde{Q}^{\mathrm{c}}_{020}(\omega,\rho) &= \mathrm{i}\left(\omega^3\rho^4 - \omega\rho^6\right), \\
\tilde{Q}^{\mathrm{c}}_{026}(\omega,\rho) &= -2\mathrm{i}\omega\rho^6, \\
\tilde{Q}^{\mathrm{c}}_{121}(\omega,\rho) &= -2\omega^2\rho^5 = -\tilde{Q}^{\mathrm{s}}_{221}(\omega,\rho), \\
\tilde{Q}^{\mathrm{c}}_{125}(\omega,\rho) &= -\omega^2\rho^5 = \tilde{Q}^{\mathrm{s}}_{225}(\omega,\rho), \\
\tilde{Q}^{\mathrm{c}}_{127}(\omega,\rho) &= \rho^7 = -\tilde{Q}^{\mathrm{s}}_{227}(\omega,\rho).
\end{aligned} \tag{A.5}$$

In both cases, the Fourier integral with respect to ω is elementary. Now that the angular dependence resides only in the numerator, the orthogonality relations of cos and sin in $L^2([0,2\pi])$, once $\mathrm{e}\mathrm{i}k\rho\cos(\varphi-\vartheta)$ is expanded using the Jacobi–Anger expansion [see Eq. (4.105)]. The remaining integral over ρ turns out to be in fact expressible in terms of elementary functions, whence one obtains explicit expressions for the tree-level propagator in position space. We abstain from quoting them here in their full splendour due to their extraordinary length, and because they are not particularly enlightening.

B Two-sided Padé approximants for C_3-symmetric QBTs

Let us write the coefficient of m-th order in (f_1/f_2) in the β function of a quantity X with $X \in \{g, (f_1/f_2), (f_3/f_2)\}$ as $\beta_X^{(\pm,m)}$ defined by

$$\beta(X) \simeq \begin{cases} \sum_{m\geqslant 0} \beta_X^{(+,m)} (f_1/f_2)^m & \text{for } f_1/f_2 \to 0, \\ \sum_{m\geqslant 0} \beta_X^{(-,m)} (f_1/f_2)^{-m} & \text{for } f_1/f_2 \to \infty. \end{cases} \tag{B.1}$$

Eqs. (5.39)–(5.41) allow to read off $\beta_X^{(+,m)}$, while the dual coefficients $\beta_X^{(-,m)}$ can be read off from Eqs. (5.45)–(5.46).

The Padé coefficients defined in Eqs. (5.59)–(5.61) are then given by

$$a_0 = \beta^{(+,0)}_{f_1/f_2}, \tag{B.2}$$

$$a_1 = \beta^{(+,1)}_{f_1/f_2} + \frac{\left(\beta^{(+,0)}_{f_1/f_2}\right)^2}{\left(\beta^{(-,1)}_{f_1/f_2}\right)^2 - \beta^{(+,1)}_{f_1/f_2}\beta^{(-,1)}_{f_1/f_2}}, \tag{B.3}$$

$$a_2 = \frac{\beta^{(+,0)}_{f_1/f_2}}{\beta^{(-,1)}_{f_1/f_2} - \beta^{(+,1)}_{f_1/f_2}}, \tag{B.4}$$

$$b_1 = \frac{\beta^{(+,0)}_{f_1/f_2}}{\left(\beta^{(-,1)}_{f_1/f_2}\right)^2 - \beta^{(+,1)}_{f_1/f_2}\beta^{(-,1)}_{f_1/f_2}}, \tag{B.5}$$

$$b_2 = \frac{1}{\beta^{(-,1)}_{f_1/f_2}}, \tag{B.6}$$

$$c_0 = \beta^{(+,0)}_{f_3/f_2}, \tag{B.7}$$

$$c_1 = \beta^{(+,1)}_{f_3/f_2}, \tag{B.8}$$

$$c_2 = \beta^{(-,0)}_{f_3/f_2}, \tag{B.9}$$

$$d_0 = \beta^{(+,0)}_{g}, \tag{B.10}$$

$$d_1 = \beta^{(-,1)}_{g}, \tag{B.11}$$

$$d_2 = \beta^{(+,2)}_{g} + \beta^{(+,0)}_{g}\frac{\beta^{(-,2)}_{g} - \beta^{(+,2)}_{g}}{\beta^{(+,0)}_{g} - \beta^{(-,0)}_{g}}, \tag{B.12}$$

$$d_4 = \beta^{(-,0)}_{g}, \tag{B.13}$$

$$e_2 = \frac{\beta^{(-,2)}_{g} - \beta^{(+,2)}_{g}}{\beta^{(+,0)}_{g} - \beta^{(-,0)}_{g}}. \tag{B.14}$$

C Corrections to the mean-field nematic order-parameter effective potential due to explicit symmetry breaking

Here, we shall work out the mean-field nematic order-parameter effective potential, in the presence of a background antiferromagnetic order, in a quadratic band touching semimetal, and thence the evolution of the nematic order parameter across the antiferromagnet-to-coexistence transition. Strictly speaking, this transition falls squarely within the Landau paradigm, since the antiferromagnetic order parameter gaps out the fermion spectrum (notation as in Chap. 6):

$$\varepsilon^{\pm}_{\phi,0}(\boldsymbol{p}) = \pm\sqrt{p^4 + \phi^2}. \tag{C.1}$$

The spontaneous breaking of spatial rotational symmetry is described by fluctuations of the two-component nematic order parameter n_a, $a = 1, 2$, which transforms as a second-rank tensor under spatial rotations, and acquires a vacuum expectation value across the transition. However, when modelling the honeycomb bilayer, it is important to note that the actual point group on the honeycomb bilayer includes only discrete C_3 rotations by 120° around a lattice site. Accounting for the explicit breaking of rotational symmetry $\mathrm{O}(2) \to C_3$ in an exact manner is difficult analytically; however, it is possible to perform a Taylor expansion in the symmetry-breaking parameter, which affords scope for some neat effective field theory (EFT)-type power counting arguments which may be entertaining, if not instructive.

To this end, let us amend the fermionic Lagrangian (6.1) by the irrelevant (in the usual power-counting sense) term

$$\mathcal{L}_{\mathrm{QBT}} \to \mathcal{L}_{\mathrm{QBT}} + f_3 \Psi^\dagger \boldsymbol{\partial}^2 \mathrm{i} \bar{\partial}_a (\bar{\Gamma}_a \otimes \mathbb{1}_2) \Psi, \tag{C.2}$$

where $(\bar{\partial}_a) = (\partial_x, -\partial_y)$, $a = 1, 2$, and $\bar{\Gamma}_a = (\tau_z \otimes \mathbb{1}_2)\Gamma_a$. This term follows naturally from the next-to-leading order expansion of the tight-binding dispersion near the $\boldsymbol{K}$ points in the Brillouin zone (Pujari *et al.* 2017). Identifying for simplicity the ultraviolet momentum cutoff Λ with the inverse of the lattice constant a_0 as $\Lambda \sim \pi/a_0$, we obtain $f_3 \sim \pi/(2\sqrt{3}\Lambda)$ in our units (cf. also Sec. 5.1). The term parametrized by f_3 is C_3 invariant, but not symmetric under the continuous rotation group in two spatial dimensions. Let us now consider the mean-field effective potential for small $n_a \ll \phi$ in a finite antiferromagnetic background $\phi \neq 0$ and for finite $f_3 \neq 0$. Since the fermions are already gapped out, we run into no infrared divergences when Taylor expanding in n_a. Using polar coordinates $(n_a) = (n \cos 2\vartheta, n \sin 2\vartheta)$, we can write the effective potential for n_a at the mean-field level in the form

$$V_{\mathrm{MF}}^{(\phi)}(n, \vartheta) = \frac{n^2}{2g'} + \frac{N_{\mathrm{f}}}{16\pi} \sum_{k,l=0}^{\infty} \big[C_{kl,+}(\phi; f_3) \cos(2k\vartheta) + C_{kl,-}(\phi; f_3) \sin(2k\vartheta) \big] n^{l+2}, \tag{C.3}$$

with coefficients $C_{kl,\pm}$ that only depend on ϕ and f_3. In Eq. (C.3), we have subtracted all n-independent offsets compared to Eq. (6.6), which are immaterial to the present analysis. Following standard practice in Landau theory, we shall now keep all terms up to and including $\mathcal{O}(n^4)$ (i.e., the lowest nontrivial order) in the effective potential. The coefficients $C_{kl,\pm}(\phi; f_3)$ can be expanded in f_3, which allows us to evaluate all momentum integrals analytically to leading nontrivial order in f_3. This way, we finally arrive at the explicit result

$$\begin{aligned} V_{\mathrm{MF}}^{(\phi)}(n, \vartheta) \simeq \frac{N_{\mathrm{f}}}{16\pi} \bigg\{ & \left[\frac{8\pi}{N_{\mathrm{f}} g'} + \frac{1}{4} \left(\ln \frac{1}{4}\phi^2 - 2 \right) + \frac{1}{8} f_3^2 \right] n^2 \\ & + f_3^2 \left(\frac{1}{24} + \frac{1}{64} \ln \frac{1}{4}\phi^2 \right) n^3 \cos(6\vartheta) \\ & + \left(\frac{3}{32\phi^2} + \frac{1}{64} + \frac{9}{128} f_3^2 \right) n^4 \bigg\}, \end{aligned} \tag{C.4}$$

where we have rescaled $V_{\mathrm{MF}}^{(\phi)}/\Lambda^4 \mapsto V_{\mathrm{MF}}^{(\phi)}$, $\phi^2/\Lambda^4 \mapsto \phi^2$, $n^2/\Lambda^4 \mapsto n^2$, $f_3\Lambda \mapsto f_3$, and have kept only the leading- and subleading-order terms assuming the hierarchy $n \ll \phi \ll 1$. The latter assumption is consistent with small to intermediate g, since $\langle \phi \rangle \simeq \mathrm{e}^{-2\pi/(gN_{\mathrm{f}})}$ in mean-field theory (Sun *et al.* 2009). We note that higher orders in f_3^2 also come with higher powers of ϕ for dimensional reasons; this defines *a posteriori* the regime in which the expansion in f_3 is justified purely on grounds of its canonical dimension and independently of its value at the ultraviolet scale. To be more precise, insertions of the f_3 term into the one-loop fermion bubble renders the integral increasingly ultraviolet divergent and infrared convergent; since finite ϕ is precisely what cures infrared divergences in this theory, the faster a given loop integrand vanishes in the limit of vanishing loop momenta, the faster its integral vanishes for $\phi \to 0$.

The middle term in Eq. (C.4) manifests the explicit symmetry breaking at the level of the effective potential for n_a: $\cos(6\vartheta)$ is only invariant under $\vartheta \mapsto \vartheta + \pi k/3$, $k \in \mathbb{Z}$.

Minimizing the potential with respect to ϑ, we find that the orientation of the vector n_a locks on to $\vartheta = 0$ at the minimum for sufficiently small ϕ, while $\vartheta = \pi/6$ for larger values of ϕ. Importantly, the presence of the cubic term renders the antiferromagnetic-to-coexistence transition first order, with the jump discontinuity at the phase boundary working out to

$$\delta\langle n\rangle = \frac{1}{12} f_3^2 \langle\phi\rangle^2 \left(\ln\frac{1}{4\langle\phi\rangle^2} - \frac{8}{3}\right) + O(\langle\phi\rangle^4 \ln\langle\phi\rangle^2). \tag{C.5}$$

Note that the above implies the emergence of a hierarchy among the order parameters, $\delta\langle n\rangle \sim \langle\phi\rangle^2 \ln\langle\phi\rangle^{-2} \ll \langle\phi\rangle$ in the limit of small interaction strengths. Technically, the smallness of $\delta\langle n\rangle$ justifies expanding its effective potential in powers of n, as well as treating ϕ as a background field with no backreaction from n, even though the transition itself is not continuous. Physically, $\delta\langle n\rangle$ measures how badly the transition fails to be continuous. Since $\delta n \to 0$ for $g \to 0$, the transition is only weakly first order for small to intermediate four-fermion coupling.

D Self-energy in anisotropic Yukawa theory

The aim of this appendix is to present details of the derivation of the β functions of the Fermi velocities v_x and v_y in the Gross-Neveu-Yukawa-Heisenberg model [Eqs. (6.22) and (6.23)]. As will be manifest shortly, at one loop, the question whether anisotropy perturbations are relevant or not is independent of the fixed-point values $(h_\star^2, \lambda_\star)$, so the computation of the Yukawa vertex and quartic self-coupling corrections are immaterial. At this order, it is therefore sufficient to consider the selfenergy contributions represented by the diagram in Fig. 6.5. The corresponding loop integrals are

$$\text{Fig. 6.5(a)} = -h^2 \int_q (\mathbb{1}_{2N_\mathrm{f}} \otimes \sigma_\alpha)\langle\psi\bar{\psi}\rangle((1-w)p+q)(\mathbb{1}_{2N_\mathrm{f}} \otimes \sigma_\beta)\langle\phi_\alpha\phi_\beta\rangle(wp-q) \equiv \Sigma(p), \tag{D.1}$$

$$\text{Fig. 6.5(b)} = h^2 \int_q \mathrm{tr}\left[(\mathbb{1}_{2N_\mathrm{f}} \otimes \sigma_\alpha)\langle\psi\bar{\psi}\rangle(q)(\mathbb{1}_{2N_\mathrm{f}} \otimes \sigma_\beta)\langle\psi\bar{\psi}\rangle(q+p)\right] \equiv \Pi(p)\delta_{\alpha\beta}, \tag{D.2}$$

where $\Sigma(p)$ and $\Pi(p)$ denote the fermion and boson selfenergies, respectively, with $p = (p_0, p_1, p_2) \equiv (\omega, \boldsymbol{p})$ as the in-flowing 3-momentum in $D = 2+1$ space-time dimensions. In the above a momentum-routing parameter $w \in [0,1]$ has been introduced for the vacuum polarization, because the limit of standard routing ($w \to 0$ or 1) turns out to be singular in this case. This is another artefact of the regularization scheme that can be resolved by a judicious choice of symmetry-restoring counterterms, as shown below. Let us note in passing that the vacuum polarization $\Pi(p)$ in Eq. (D.2) is well-defined due to the Pauli matrix relation $\mathrm{tr}(\sigma_\alpha\sigma_\beta) = 2\delta_{\alpha\beta}$.

As mentioned in the main text, to carry out the loop integrals, the Euclidean time direction is first extended to a $(D-2)$-dimensional plane, where $D = 4 - \epsilon$ is the space-time dimension. The spatial dimension $d = 2$ is held fixed, which allows one to deal with the spatial anisotropy in a controlled way. Before performing the $(D-2)$-dimensional frequency integration, let us rescale the momenta as $(v_x q_x, v_y q_y) \mapsto |q_0|\tilde{\boldsymbol{q}}$, where $|q_0|$ denotes the radial component of the $(D-2)$-dimensional frequency vector q_0. For the frequency part of the vacuum polarization, this yields

$$\frac{\partial}{\partial p_0^2}\Pi(p)\bigg|_{p=0} = \frac{4N_\mathrm{f}h^2}{v_x v_y}\int_q \left[\frac{2\left(2w^2-2w+1\right)\left(v_x^2 q_x^2 + v_y^2 q_y^2\right)}{\left(q_0^2 + v_x^2 q_x^2 + v_y^2 q_y^2\right)^3} - \frac{3w^2-3w+1}{\left(q_0^2 + v_x^2 q_x^2 + v_y^2 q_y^2\right)^2}\right]$$

$$\begin{aligned}
&= \frac{\mu^{-\epsilon}}{\epsilon}\frac{4N_\mathrm{f}h^2 S_{2-\epsilon}}{v_x v_y (2\pi)^{2-\epsilon}} \int \frac{\mathrm{d}^2\tilde{\boldsymbol{q}}}{(2\pi)^2}\left[\frac{\left(2w^2-2w+1\right)\tilde{\boldsymbol{q}}^2}{(1+\tilde{\boldsymbol{q}}^2)^3} - \frac{3w^2-3w+1}{(1+\tilde{\boldsymbol{q}}^2)^2}\right] \\
&= \frac{\mu^{-\epsilon}}{\epsilon}\frac{4N_\mathrm{f}h^2 S_{2-\epsilon}}{(2\pi)^{2-\epsilon}}\frac{(1-w)w}{4\pi v_x v_y}.
\end{aligned} \tag{D.3}$$

Analogously, for the momentum part, one finds

$$\frac{\partial}{\partial p_1^2}\Pi(p)\bigg|_{p=0} = \frac{\mu^{-\epsilon}}{\epsilon}\frac{4N_\mathrm{f}h^2 S_{2-\epsilon}}{(2\pi)^{2-\epsilon}}\frac{1}{4\pi}\frac{v_x}{v_y}, \qquad \frac{\partial}{\partial p_2^2}\Pi(p)\bigg|_{p=0} = \frac{\mu^{-\epsilon}}{\epsilon}\frac{4N_\mathrm{f}h^2 S_{2-\epsilon}}{(2\pi)^{2-\epsilon}}\frac{1}{4\pi}\frac{v_y}{v_x}. \tag{D.4}$$

To evaluate the fermion selfenergy, it is useful to introduce the 'master integral'

$$I_{nml}(r,s) := \int_{\mathbb{R}^2} \frac{\mathrm{d}x\mathrm{d}y}{(2\pi)^2}\frac{(x^2)^l}{(1+x^2+y^2)^n\,(1+r^2x^2+s^2y^2)^m} \tag{D.5}$$

with $n, m, l \in \mathbb{N}$. In terms of the I-functions, one finds

$$\begin{aligned}
\frac{1}{4N_\mathrm{f}}\operatorname{tr}\left(\gamma_0\frac{\partial}{\partial \mathrm{i}p_0}\Sigma(p)\right)\bigg|_{p=0} &= N_\mathrm{b}h^2\int_q \frac{2q_0^2}{\left(q_0^2+q_x^2+q_y^2\right)^2\left(q_0^2+q_x^2v_x^2+q_y^2v_y^2\right)} \\
&= \frac{\mu^{-\epsilon}}{\epsilon}\frac{N_\mathrm{b}h^2 S_{2-\epsilon}}{(2\pi)^{2-\epsilon}}\int\frac{\mathrm{d}q_x\mathrm{d}q_y}{(2\pi)^2}\frac{2}{\left(1+q_x^2+q_y^2\right)^2\left(1+q_x^2v_x^2+q_y^2v_y^2\right)} \\
&= \frac{\mu^{-\epsilon}}{\epsilon}\frac{2N_\mathrm{b}h^2 S_{2-\epsilon}}{(2\pi)^{2-\epsilon}}I_{210}(v_x,v_y),
\end{aligned} \tag{D.6}$$

$$\begin{aligned}
\frac{1}{4N_\mathrm{f}}\operatorname{tr}\left(\gamma_1\frac{\partial}{\partial \mathrm{i}p_1}\Sigma(p)\right)\bigg|_{p=0} &= N_\mathrm{b}h^2\int_q \frac{2v_xq_x^2}{\left(q_0^2+q_x^2+q_y^2\right)^2\left(q_0^2+v_x^2q_x^2+v_y^2q_y^2\right)} \\
&= \frac{N_\mathrm{b}h^2 S_{2-\epsilon}}{(2\pi)^{2-\epsilon}}\frac{\mu^{-\epsilon}}{\epsilon}(2v_x)\int\frac{\mathrm{d}q_x\mathrm{d}q_y}{(2\pi)^2}\frac{q_x^2}{\left(1+q_x^2+q_y^2\right)^2\left(1+v_x^2q_x^2+v_y^2q_y^2\right)} \\
&= \frac{\mu^{-\epsilon}}{\epsilon}\frac{2N_\mathrm{b}h^2 S_{2-\epsilon}}{(2\pi)^{2-\epsilon}}v_xI_{211}(v_x,v_y),
\end{aligned} \tag{D.7}$$

$$\begin{aligned}
\frac{1}{4N_\mathrm{f}}\operatorname{tr}\left(\gamma_2\frac{\partial}{\partial \mathrm{i}p_2}\Sigma(p)\right)\bigg|_{p=0} &= N_\mathrm{b}h^2\int_q \frac{2v_yq_y^2}{\left(q_0^2+q_x^2+q_y^2\right)^2\left(q_0^2+v_x^2q_x^2+v_y^2q_y^2\right)} \\
&= \frac{\mu^{-\epsilon}}{\epsilon}\frac{2N_\mathrm{b}h^2 S_{2-\epsilon}}{(2\pi)^{2-\epsilon}}v_yI_{211}(v_y,v_x),
\end{aligned} \tag{D.8}$$

where $w = 1$ has been set for simplicity, since standard momentum routing is nonsingular in this case. We have also inserted N_b as the number of bosonic degrees of freedom, with $N_\mathrm{b} = 3$ corresponding to the present Heisenberg case. The above equations are valid for general N_b as long as the generators of the symmetry under which ϕ_α transform as a vector commute with the Clifford algebra. Besides the chiral Heisenberg example, this includes the chiral Ising case with $N_\mathrm{b} = 1$, the chiral XY case with $N_\mathrm{b} = 2$, as well as further members of the Gross–Neveu family with $N_\mathrm{b} > 3$ (Janssen, Herbut & Scherer 2018).

Before extracting renormalization constants from the above results, one needs to fix the symmetry-restoring counterterms in Eq. (6.19). A minimal prescription would be

$$D_\psi = \lim_{v_x=v_y\to 1}\left[\frac{1}{4N_\mathrm{f}}\operatorname{tr}\left(\gamma_0\frac{\partial}{\partial \mathrm{i}p_0}\Sigma(p)\right)\bigg|_{p=0} - \frac{1}{4N_\mathrm{f}}\operatorname{tr}\left(\gamma_0\frac{\partial}{\partial \mathrm{i}p_0}\Sigma(p)\right)\bigg|_{p=0}\right], \tag{D.9}$$

$$D_\phi = \lim_{v_x = v_y \to 1} \left[\frac{\partial}{\partial p_1^2} \Pi(p) \bigg|_{p=0} - \frac{\partial}{\partial p_0^2} \Pi(p) \bigg|_{p=0} \right], \tag{D.10}$$

which is precisely what we shall choose for D_ψ. For the bosonic counterterm, we shall use a slightly modified prescription

$$D_\phi = \frac{D_\phi[\text{Eq. (D.10)}]}{v_x v_y}, \tag{D.11}$$

which has the advantage of furthermore cancelling all momentum-routing dependence at once (rather than, e.g., at the fixed-point level). We can then read off the remaining renormalization constants in usual manner. Using $-\mu \mathrm{d}(\mu^{-\epsilon}/\epsilon)/\mathrm{d}\mu = \mu^{-\epsilon}$, one then arrives at the β functions quoted in Eqs. (6.22) and (6.23).

E Master integrals for anisotropic Yukawa theory

The derivation of the β functions of the Fermi velocities v_x and v_y in the anisotropic Gross–Neveu–Yukawa–Heisenberg model involves the master integrals $I_{nml}(v_x, v_y)$ defined in Eq. (D.5), more specifically the two functions $I_{210}(v_x, v_y)$ and $I_{211}(v_x, v_y)$. These can be evaluated explicitly, and the results are recorded here for completeness. For general $v_x, v_y > 0$, they work out to

$$\begin{aligned} I_{210}(v_x, v_y) = {} & \frac{1}{4\pi \left(1 - v_x^2\right) \left(v_y^2 - 1\right)^2 \sqrt{\frac{1 - v_x^2}{v_y^2 - 1}}} \\ & \times \left[\left(v_y^2 - 1\right) \left(v_x v_y - 1\right) \sqrt{\frac{1 - v_x^2}{v_y^2 - 1}} + \left(v_x^2 + v_y^2 - 2 v_x^2 v_y^2\right) \arcsin\left(\sqrt{\frac{v_y^2 - 1}{v_y^2 - v_x^2}} \right) \right. \\ & \left. - \left(v_x^2 + v_y^2 - 2 v_x^2 v_y^2\right) \arcsin\left(v_x \sqrt{\frac{v_y^2 - 1}{v_y^2 - v_x^2}} \right) \right], \end{aligned} \tag{E.1}$$

$$\begin{aligned} I_{211}(v_x, v_y) = {} & \frac{1}{8\pi \left(v_x^2 - 1\right) \left(v_y^2 - 1\right) \left(v_x + v_y\right) \sqrt{\frac{1 - v_x^2}{v_y^2 - 1}}} \\ & \times \left[2 v_x \left(v_y^2 - 1\right) \sqrt{\frac{1 - v_x^2}{v_y^2 - 1}} - 3 v_y^2 \left(v_x + v_y\right) \arcsin\left(\sqrt{\frac{v_y^2 - 1}{v_y^2 - v_x^2}} \right) \right. \\ & + 2 \left(v_x + v_y\right) \arcsin\left(v_x \sqrt{\frac{v_y^2 - 1}{v_y^2 - v_x^2}} \right) \\ & \left. + \left(3 v_y^2 - 2\right) \left(v_x + v_y\right) \arcsin\left(\sqrt{\frac{v_y^2 - 1}{v_y^2 - v_x^2}} \right) \right]. \end{aligned} \tag{E.2}$$

Whenever the argument of a square root obtains a negative value, it is continued analytically as $\sqrt{-a^2} = a\mathrm{i}$ for $a \in \mathbb{R}_{\geqslant 0}$. The trigonometric functions are then understood to be replaced by hyperbolic functions in the usual manner. The limits $v_x \to 1$ or $v_y \to 1$ are removable singularities,

$$\lim_{v_x \to 1} I_{210}(v_x, v_y) = \frac{1 + 2 v_y}{6\pi (1 + v_y)^2}, \qquad \lim_{v_x \to 1} I_{211}(v_x, v_y) = \frac{1 + 2 v_y}{12\pi (1 + v_y)^2}, \tag{E.3}$$

$$\lim_{v_y \to 1} I_{210}(v_x, v_y) = \frac{1+2v_x}{6\pi(1+v_x)^2}, \qquad \lim_{v_y \to 1} I_{211}(v_x, v_y) = \frac{1}{4\pi(1+v_x)^2}. \tag{E.4}$$

In the rotationally-invariant case $v \equiv v_x = v_y$, one obtains the limits

$$I_{210}(v, v) = \frac{1 - v^2 + 2v^2 \ln v}{4\pi\left(1-v^2\right)^2}, \qquad I_{211}(v, v) = \frac{v^2 - 2\ln v - 1}{8\pi\left(1-v^2\right)^2}. \tag{E.5}$$

For $v \to 1$, the singularities are again removable, with the pertinent limits given by

$$\lim_{v \to 1} I_{210}(v, v) = \frac{1}{8\pi}, \qquad \lim_{v \to 1} I_{211}(v, v) = \frac{1}{16\pi}, \tag{E.6}$$

in agreement with the limits $v_y \to 1$ and $v_x \to 1$, respectively, of Eqs. (E.3) and (E.4).

Bibliography

Abrikosov, A. A. (1974): Calculation of critical indices for zero-gap semiconductors. *Sov. Phys. JETP* **39** 709.

Abrikosov, A. A.; Beneslavskii, S. D. (1971): Some properties of gapless semiconductors of the second kind. *J. Low Temp. Phys.* **5** 141.

Alexandru, A.; Başar, G.; and Bedaque, P. F. (2016): Monte Carlo algorithm for simulating fermions on Lefschetz thimbles. *Phys. Rev. D* **93** 014504.

Alexandru, A.; Başar, G.; Bedaque, P. F.; Ridgway, G. W.; and Warrington, N. C. (2016): Sign problem and Monte Carlo calculations beyond Lefschetz thimbles. *J. High Energy Phys.* **5** 053.

Alkofer, R.; Eichhorn, A.; Held, A.; Nieto, C. M.; Percacci R.; and Schröfl, M. (2020): Quark masses and mixings in minimally parameterized UV completions of the Standard Model. *Ann. Phys.* **421** 168282.

Alkofer, N.; and Saueressig, F. (2018): Asymptotically safe $f(R)$-gravity coupled to matter I: the polynomial case. *Ann. Phys.* **396** 173.

Altland, A.; and Simons, B. (2010): *Condensed Matter Field Theory* (2nd edn.). Cambridge, Cambridge University Press.

Ambjørn, J.; Goerlich, A.; Jurkiewicz, J.; Loll, R. (2012): Nonperturbative Quantum Gravity. *Phys. Rept.* **519** 127.

Andrianov, A. A.; Espriu, D.; Kurkov, M. A.; and Lizzi F. (2013): *Phys. Rev. Lett.* **111** 011601.

Appelquist, T.; Nash, D.; and Wijewardhana, L. C. R. (1988): Critical behavior in $(2+1)$-dimensional QED. *Phys. Rev. Lett.* **60** 2575.

Arcadi, G.; Djouadi, A.; and Raidal, M. (2020): Dark Matter through the Higgs portal. *Phys. Rept.* **842** 1.

Arcadi, G.; Dutra, Maíra; Ghosh, P.; Lindner, M.; Mambrini, Y.; Pierre, M.; Profumo, S.; and Queiroz, F. S. (2018): The waning of the WIMP? A review of models, searches, and constraints. *Eur. Phys. J. C* **78** 203.

Ashrafi, B.; and Schweber, S. (2003): Interview with Alexander Polyakov. Published online at: `https://authors.library.caltech.edu/5456/1/hrst.mit.edu/hrs/renormalization/Polyakov/index.html`

Assaad, F. F.; and Herbut, I. F. (2013): Pinning the Order: The Nature of Quantum Criticality in the Hubbard Model on Honeycomb Lattice. *Phys. Rev. X* **3** 031010.

Athron, P.; Cornell, J. M.; Kahlhoefer, F.; Mckay, J.; Scott, P.; and Wild, S. (2018): Impact of vacuum stability, perturbativity and XENON1T on global fits of $\mathbb{Z}_2$ and $\mathbb{Z}_3$ scalar singlet dark matter. *Eur. Phys. J. C* **78** 830.

ATLAS Collaboration (Aad, G. *et al.*) (2012): Observation of a new particle in the search for the Standard Model Higgs boson with the ATLAS detector at the LHC. *Phys. Lett. B* **716** 1.

ATLAS Collaboration (Aad, G. *et al.*) (2019): Measurement of the top-quark mass in $t\bar{t}$ + 1-jet events collected with the ATLAS detector in pp collisions at $\sqrt{s} = 8$ TeV. *J. High Energy Phys.* **11** 150.

Avramidi, I. (2002): Heat Kernel Approach in Quantum Field Theory. *Nucl. Phys. Proc. Suppl.* **104** 3.

Bagherian, Z.; Ettefaghi, M. M.; Haghgouyan, Z.; and Moazzemi, R. (2014): A new parameter space study of the fermionic cold dark matter model. *J. Cosmol. Astropart. Phys.* **10** 033.

Baldazzi, A.; Zinati, R. B. A.; and Falls, K. (2021): Essential renormalisation group. *arXiv:2105.11482.*

Banks, T.; and Zaks, A. (1982): On the phase structure of vector-like gauge theories with massless fermions. *Nucl. Phys. B* **196** 189.

Bao, W.; Velasco Jr, J.; Zhang, F.; Jing, L.; Standley, B.; Smirnov, D.; Bockrath, M.; MacDonald, A. H.; and Lau, C. N. (2012): Minimum conductivity and evidence for phase transitions in ultra-clean bilayer graphene. *Proc. Natl. Acad. Sci. USA* **109** 10802.

Bartelmann, M. (2010): Gravitational Lensing. *Class. Quant. Grav.* **27** 233001.

Bassler, S.; Laiho, J; Schiffer, M; and Unmuth-Yockey, J. (2021): The de Sitter Instanton from Euclidean Dynamical Triangulations. *Phys. Rev. D* **103** 114504.

Bauer, M.; and Plehn, T. (2019): *Yet Another Introduction to Dark Matter: The Particle Physics Approach* (Lecture Notes in Physics, Vol. 959). Springer Nature.

Benedetti, D.; Machado, P. F.; Saueressig, F. (2009): Asymptotic safety in higher-derivative gravity. *Mod. Phys. Lett. A* **24** 2233.

Berges, J.; Tetradis, N.; and Wetterich, C. (2002): Non-perturbative renormalization flow in quantum field theory and statistical physics. *Phys. Rep.* **363** 223.

Bezrukov, Fedor; Kalmykov, M. Y.; Kniehl, B. A.; and Shaposhnikov, M. (2012): Higgs Boson Mass and New Physics. *J. High Energy Phys.* **10** 140.

Bezrukov, F.; and Shaposhnikov, M. (2015): Why should we care about the top quark Yukawa coupling? *J. Exp. Theor. Phys.* **120** 335.

Bistritzer, R.; and MacDonald, A. H. (2011): Moiré bands in twisted double-layer graphene. *Proc. Natl. Acad. Sci. U.S.A.* **108** 12233.

Boettcher, I.; and Herbut, I. F. (2017): Anisotropy induces non-Fermi-liquid behavior and nematic magnetic order in three-dimensional Luttinger semimetals. *Phys. Rev. B* **95** 075149.

Bollini, C.; and Giambiagi, J. J. (1972): Dimensional Renormalization: The Number of Dimensions as a Regularizing Parameter. *Il Nuovo Cimento B* **12** 20.

Bonanno, A.; Eichhorn, A.; Gies, H.; Pawlowski, J. M.; Percacci, R.; Reuter, M.; Saueressig, F.; and Vacca, G. P. (2020): Critical reflections on asymptotically safe gravity. *Front. Phys.* **8** 269.

Borchardt, J.; and Eichhorn, A. (2016): Universal behavior of coupled order parameters below three dimensions. *Phys. Rev. E* **94** 042105.

Borchardt, J.; Gies, H.; and Sondenheimer, René (2016): Global flow of the Higgs potential in a Yukawa model. *Eur. Phys. J. C* **76** 472.

Borchardt, J.; and Knorr, B. (2015): Global solutions of functional fixed point equations via pseudospectral methods. *Phys. Rev. D* **91** 105011.

Borchardt, J.; and Knorr, B. (2016): Solving functional flow equations with pseudospectral methods. *Phys. Rev. D* **94** 025027.

Boyack, R.; Rayyan, A.; and Maciejko, J. (2019): Deconfined criticality in the QED$_3$ Gross-Neveu-Yukawa model: The $1/N$ expansion revisited. *Phys. Rev. B* **99** 195135.

Boyd, J. P. (2001): *Chebyshev and Fourier spectral methods.* Courier Corporation.

Braun, J.; Gies, H.; Janssen, L.; and Roscher, D. (2014): Phase structure of many-flavor QED_3 *Phys. Rev. D* **90** 036002.

Braun, J.; Gies, H.; and Scherer, D. D. (2011): Asymptotic safety: a simple example. *Phys. Rev. D* **83** 085012.

Bravyi, S.; DiVincenzo, D. P.; and Loss, D. (2011): Schrieffer–Wolff transformation for quantum many-body systems. *Ann. Phys.* **326** 2793.

Breitenlohner, P.; and Maison, D. (1977): Dimensional renormalization and the action principle. *Commun. Math. Phys.* **52** 11.

de Brito, G. P.; Eichhorn, A.; and Pereira, A. D. (2019): A link that matters: Towards phenomenological tests of unimodular asymptotic safety. *J. High Energy Phys.* **09** 100.

de Brito, G. P.; Eichhorn, A.; and dos Santos, R. R. L. (2021): The weak-gravity bound and the need for spin in asymptotically safe matter-gravity models. *J. High Energy Phys.* **2021** 110.

de Brito, G. P.; Hamada, Y.; Pereira, A. D.; and Yamada, M. (2019): On the impact of Majorana masses in gravity-matter systems. *J. High Energy Phys.* **08** 142.

Buividovich, P.; Smith, D.; Ulybyshev, M.; and von Smekal, L. (2018): Hybrid Monte Carlo study of competing order in the extended fermionic Hubbard model on the hexagonal lattice. *Phys. Rev. B* **98** 235129.

Butazzo, D.; Degrassi, G.; Giardino, P. P.; Giudice, G. F.; Sala, F.; Salvio, A.; and Strumia, A. (2013): Investigating the near-criticality of the Higgs boson. *J. High Energy Phys.* **12** 089.

Caminha, G. B.; Grillo, C.; Rosati, P.; Balestra, I.; Mercurio, A.; Vanzella, E.; Biviano, A.; Caputi, K. I.; Delgado-Correal, C.; Karman, W.; Lombardi, M.; Meneghetti, M.; Sartoris, B.; and Tozzi, P. (2017): A refined mass distribution of the cluster MACS J0416.1-2403 from a new large set of spectroscopic multiply lensed sources. *Astron. Astrophys.* **600** A90.

Cao, Y.; Fatemi, V.; Demir, A.; Fang, S.; Tomarken, S. L.; Luo, J. Y.; Sanchez-Yamagishi, J. D.; Watanabe, K.; Taniguchi, T.; Kaxiras, E.; Ashoori, R. C.; Jarillo-Herrero, P. (2018): Correlated insulator behaviour at half-filling in magic-angle graphene superlattices. *Nature* **556** 80.

Cao, Y.; Fatemi, V.; Fang, S.; Watanabe, K.; Taniguchi, T.; Kaxiras, E.; Jarillo-Herrero, P. (2018): Unconventional superconductivity in magic-angle graphene superlattices. *Nature* **556** 43.

Cao, Y.; Rodan-Legrain, D.; Park, J. M.; Yuan, N. F. Q.; Watanabe, K.; Taniguchi, T.; Fernandes, R. M.; Fu, L.; and Jarillo-Herrero, P. (2021): Nematicity and competing orders in superconducting magic-angle graphene. *Science* **372** 264.

de Carvalho, V. S.; Freire, H.; Miranda, E.; and Pereira, R. G. (2018): Edge magnetization and spin transport in an SU(2)-symmetric Kitaev spin liquid. *Phys. Rev. B* **98** 155105.

Castro Neto, A. H.; Guinea, F.; Peres, N. M. R.; Novoselov, K. S.; and Geim, A. K. (2009): The electronic properties of graphene. *Rev. Mod. Phys.* **81** 109.

Caswell, W. E. (1974): Asymptotic behavior of non-abelian gauge theories to two-loop order. *Phys. Rev. Lett.* **33** 244.

Chester, S. M.; and Pufu, S. S. (2016): Anomalous dimensions of scalar operators in QED_3. *J. High Energy Phys.* **2016** 69.

Chetyrkin, K. G.; and Zoller, M. F. (2012): Three-loop β-functions for top-Yukawa and the Higgs self-interaction in the Standard Model. *J. High Energy Phys.* **06** 033.

Chulliparambil, S.; Seifert, U. F. P.; Vojta, M.; Janssen, L.; and Tu, H.-H. (2020): Microscopic models for Kitaev's sixteenfold way of anyon theories. *Phys. Rev. B* **102** 201111.

Christiansen, Nicolai (2016): Four-Derivative Quantum Gravity Beyond Perturbation Theory. *arXiv:1612.06223.*

Christiansen, N.; and Eichhorn, A. (2017): An asymptotically safe solution to the U(1) triviality problem. *Phys. Lett. B* **770** 154.

Christiansen, N.; Falls, K.; Pawlowski, J. M.; and Reichert, M. (2018): Curvature dependence of quantum gravity. *Phys. Rev. D* **97** 046007.

Christiansen, N.; Knorr, B.; Meibohm, J.; Pawlowski, J. M.; and Reichert, M. (2015): Local Quantum Gravity. *Phys. Rev. D* **92** 121501.

Christiansen, N.; Knorr, B.; Pawlowski, J. M.; and Rodigast, A. (2016): Global Flows in Quantum Gravity. *Phys. Rev. D* **93** 044036.

Christiansen, N.; Litim, D. F.; Pawlowski, J. M.; and Reichert, M. (2018): Asymptotic safety of gravity with matter. *Phys. Rev. D* **97** 106012.

Christiansen, N.; Litim, D. F.; Pawlowski, J. M.; and Rodigast, A. (2014): Fixed points and infrared completion of quantum gravity. *Phys. Lett. B* **728** 114.

Classen, L.; Herbut, I. F.; Janssen, L.; and Scherer, M. M. (2015): Mott multicriticality of dirac electrons in graphene. *Phys. Rev. B* **92** 035429.

Classen, L.; Herbut, I. F.; Janssen, L.; and Scherer, M. M. (2016): Competition of density waves and quantum multicritical behavior in Dirac materials from functional renormalization. *Phys. Rev. B* **93** 125119.

Classen, L.; Herbut, I. F.; and Scherer, M. M. (2017): Fluctuation-induced continuous transition and quantum criticality in Dirac semimetals. *Phys. Rev. B* **96** 115132.

Cline, J. M.; Kainulainen, K.; Scott, P.; and Weniger, C. (2013): Update on scalar singlet dark matter. *Phys. Rev. D* **88** 055025.
[Erratum: *Phys. Rev. D* **92** 039906 (2015)]

CMS Experiment (Chatrchyan, S. *et al.*) (2012): Observation of a New Boson at a Mass of 125 GeV with the CMS Experiment at the LHC *Phys. Lett. B* **716** 30.

CMS Experiment (Sirunyan, A. M. *et al.*) (2017): Measurement of double-differential cross sections for top quark pair production in pp collisions at $\sqrt{s} = 8$ TeV and impact on parton distribution functions. *Eur. Phys. J. C* **77** 459.

CMS Experiment (Sirunyan, A. M. *et al.*) (2020): Measurement of $\mathrm{t\bar{t}}$ normalised multi-differential cross sections in pp collisions at $\sqrt{s} = 13$ TeV, and simultaneous determination of the strong coupling strength, top quark pole mass, and parton distribution functions. *Eur. Phys. J. C* **80** 658.

Codello, A.; Demmel, M.; and Zanusso, O. (2014): Scheme dependence and universality in the functional renormalization group. *Phys. Rev. D* **90** 027701.

Coleman, S. (1985): *Aspects of Symmetry.* Cambridge, Cambridge University Press.

Coleman, S.; and Weinberg, E. (1973): Radiative corrections as the origin of spontaneous symmetry breaking. *Phys. Rev. D* **7** 1888.

Cristoforetti, M.; di Renzo, F.; Scorzato, L. (2012): New approach to the sign problem in quantum field theories: High density QCD on a Lefschetz thimble. *Phys. Rev. D* **86** 074506.

Cvetkovic, V.; Throckmorton, R. E.; and Vafek, O. (2012): Electronic multicriticality in bilayer graphene. *Phys. Rev. B* **86** 075467.

Cyburt, R. H.; Fields, B. D.; Olive, K. A.; and Yeh, T.-H. (2016): Big Bang

Nucleosynthesis: 2015. *Rev. Mod. Phys.* **88** 015004.

Czakon, M. (2005): The Four-loop QCD beta-function and anomalous dimensions. *Nucl. Phys. B* **710** 485.

Daum, J.-E.; Harst, U.; and Reuter, M. (2010): Running Gauge Coupling in Asymptotically Safe Quantum Gravity. *J. High Energy Phys.* **01** 084.

Daum, J.-E.; Harst, U.; and Reuter, M. (2011): Non-perturbative QEG Corrections to the Yang-Mills Beta Function. *Gen. Rel. Grav.* **43** 2393.

Degrassi, G.; di Vita, S.; Elias-Miro, J.; Espinosa, J. R.; Giudice, G. F.; Isidori, G.; Strumia, A. (2012): Higgs mass and vacuum stability in the Standard Model at NNLO. *J. High Energy Phys.* **08** 098.

Denz, T.; Pawlowski, J. M.; and Reichert, M. (2018): Towards apparent convergence in asymptotically safe quantum gravity. *Eur. Phys. J. C* **78** 336.

Derkachov, S. E.; Kivel, N. A.; Stepanenko, A. S.; and Vasil'ev, A. N. (1993): On calculation of $1/n$ expansions of critical exponents in the Gross-Neveu model with the conformal technique. *arXiv:hep-th/9302034*.

Domènech, G.; Goodsell, M.; and Wetterich, C. (2021): Neutrino masses, vacuum stability and quantum gravity prediction for the mass of the top quark. *J. High Energy Phys.* **01** 180.

Donà, P.; Eichhorn, A.; and Percacci, R. (2014): Matter matters in asymptotically safe quantum gravity. *Phys. Rev. D* **89** 084035.

Donkin, I.; and Pawlowski, J. M. (2012): The phase diagram of quantum gravity from diffeomorphism-invariant RG-flows. *arXiv:1203.4207*.

Donoghue, J. F. (2020): A Critique of the Asymptotic Safety Program. *Front. Phys.* **8** 56.

Dupuis, N.; Canet, L.; Eichhorn, A.; Metzner, W.; Pawlowski, J. M.; Tissier, M.; and Wschebor, N. (2021): The nonperturbative functional renormalization group and its applications. *Phys. Rep.* **910** 1.

Eichhorn, A. (2012): Quantum-gravity-induced matter self-interactions in the asymptotic-safety scenario. *Phys. Rev. D* **86** 105021.

Eichhorn, A. (2018): Status of the asymptotic safety paradigm for quantum gravity and matter. *Found. Phys.* **48** 1407.

Eichhorn, A. (2019): An asymptotically safe guide to quantum gravity and matter. *Front. Astron. Space Sci.* **5** 47.

Eichhorn, A. (2020): Asymptotically safe gravity. In: *57th International School of Subnuclear Physics: In Search for the Unexpected* (arXiv:2003.00044).

Eichhorn, A.; and Gies, H. (2011): Light fermions in quantum gravity. *New J. Phys.* **13** 125012.

Eichhorn, A.; Gies, H.; Jaeckel, J.; Plehn, T.; Scherer, M. M.; and Sondenheimer, R. (2015): The Higgs Mass and the Scale of New Physics. *J. High Energy Phys.* **04** 022.

Eichhorn, A.; Hamada, Y.; Lumma, J.; and Yamada, M. (2018): Quantum gravity fluctuations flatten the Planck-scale Higgs potential. *Phys. Rev. D* **97** 086004.

Eichhorn, A.; and Held, A. (2017): Viability of quantum-gravity induced ultraviolet completions for matter. *Phys. Rev. D* **96** 086025.

Eichhorn, A.; and Held, A. (2018): Top mass from asymptotic safety. *Phys. Lett. B* **777** 217.

Eichhorn, A.; and Held, A. (2018): Mass difference for charged quarks from asymptotically safe quantum gravity. *Phys. Rev. Lett.* **121** 151302.

Eichhorn, A.; Held, A.; and Pawlowski, J. M. (2016): Quantum-gravity effects on a Higgs-Yukawa model. *Phys. Rev. D* **94** 104027.

Eichhorn, A.; Held, A.; and Wetterich, C. (2020): Predictive power of grand unification from quantum gravity. *J. High Energy Phys.* **08** 111.

Eichhorn, A.; and Koslowski, T. (2013): Continuum limit in matrix models for quantum gravity from the Functional Renormalization Group. *Phys. Rev. D* **88** 084016.

Eichhorn, A.; Koslowski, T.; Pereira, A. D. (2019): Status of background-independent coarse-graining in tensor models for quantum gravity. *Universe* **5** 53.

Eichhorn, A.; Labus, P.; Pawlowski, J. M.; and Reichert, M. (2018): Effective universality in quantum gravity. *SciPost Phys.* **5** 031.

Eichhorn, A.; Lippoldt, S:; Pawlowski, J. M.; Reichert, M.; and Schiffer, M. (2019): How perturbative is quantum gravity? *Phys. Lett. B* **792** 310.

Eichhorn, A.; Lippoldt, S.; and Schiffer, M. (2019): Zooming in on fermions and quantum gravity. *Phys. Rev. D* **99** 086002.

Eichhorn, A.; and Pauly, M. (2021): Safety in darkness: Higgs portal to simple Yukawa systems. *Phys. Lett. B* **819** 136455.

Eichhorn, A.; and Pauly, M. (2021): Constraining power of asymptotic safety for scalar fields *Phys. Rev. D* **103** 026006.

Eichhorn, A.; and Scherer, M. M. (2014): Planck scale, Higgs mass, and scalar dark matter. *Phys. Rev. D* **90** 025023.

Eichhorn, A.; and Schiffer, M. (2019): $d = 4$ as the critical dimensionality of asymptotically safe interactions. *Phys. Lett. B* **793** 383.

Eichhorn, A.; and Versteegen, F. (2018): Upper bound on the Abelian gauge coupling from asymptotic safety. *J. High Energy Phys.* **2018** 030.

Elias-Miro, J.; Espinosa, J. R.; Giudice, G. F.; Isidori, G.; Riotto, A.; and Strumia, A. (2012): Higgs mass implications on the stability of the electroweak vacuum. *Phys. Lett. B* **709** 222.

Elias-Miro, J.; Espinosa, J. R.; Giudice, G. F.; Lee, H. M.; and Strumia, A. (2012): Stabilization of the Electroweak Vacuum by a Scalar Threshold Effect. *J. High Energy Phys.* **06** 031.

Ellwanger, U. (1994): Flow equations for N point functions and bound states. *Z. Phys. C* **62** 503.

d'Eramo, M.; Peliti, L.; and Parisi, G. (1972): Theoretical predictions for critical exponents at the λ-point of Bose liquids. *Lett. Nuovo Cimento* **2** 878.

Esch, S.; Klasen, M.; and Yaguna, C. E. (2013): Detection prospects of singlet fermionic dark matter. *Phys. Rev. D* **88** 075017.

A. F. Faedo, C. Hoyos, D. Mateos, and J. G. Subils (2020): Holographic Complex Conformal Field Theories. *Phys. Rev. Lett.* **124** 161601.

Falls, K.; King, C. R.; Litim, D. F.; Nikolakopoulos, K.; and Rahmede, C. (2018): Asymptotic safety of quantum gravity beyond Ricci scalars. *Phys. Rev. D* **97** 086006.

Falls, K.; Litim, D. F.; Nikolakopoulos, K.; and Rahmede, C. (2013): A bootstrap towards asymptotic safety. *arXiv:1301.4191.*

Falkowski, A.; Gross, C.; and Lebedev, O. (2015): A second Higgs from the Higgs portal. *J. High Energy Phys.* **05** 057.

Falls, K.; Litim, D. F.; Nikolakopoulos, K.; and Rahmede, C. (2016): Further evidence for asymptotic safety of quantum gravity. *Phys. Rev. D* **93** 104022.

Falls, K. G.; Litim, D. F.; and Schröder, J. (2019): Aspects of asymptotic safety for quantum gravity. *Phys. Rev. D* **99** 126015.

Falls, K. G.; Ohta, N.; and Percacci, R. (2020): Towards the determination of the dimension of the critical surface in asymptotically safe gravity. *Phys. Lett. B* **810** 135773.

Feldman, B. E.; Martin, J.; and Yacoby, A. (2009): Broken-symmetry states and divergent resistance in suspended bilayer graphene. *Nat. Phys.* **5** 889.

Fischer, C. S.; and Gies, H. (2004): Renormalization flow of Yang-Mills propagators. *J. High Energy Phys.* **10** 048.

Floerchinger, S.; and Wetterich, C. (2002): Exact flow equation for composite operators. *Phys. Lett. B* **680** 371.

Folkerts, S.; Litim, D. F.; and Pawlowski, J. M. (2012): Asymptotic freedom of Yang-Mills theory with gravity. *Phys. Lett. B* **709** 234.

Ford, C. (1994): Multiscale renormalization group improvement of the effective potential. *Phys. Rev. D* **50** 7531.

Ford, C.; and Wiesendanger, C. (1997): Multiscale subtraction scheme and partial renormalization group equations in the O(N)-symmetric ϕ^4 theory. *Phys. Rev. D* **55** 2202.

Franz, M.; Tešanović, Z.; and Vafek, O. (2002): QED$_3$ theory of pairing pseudogap in cuprates: From d-wave superconductor to antiferromagnet via an algebraic Fermi liquid. *Phys. Rev. B* **66** 054535.

Freitag, F.; Trbovic, J.; Weiss, M.; and Schönenberger, C. (2012): Spontaneously gapped ground state in suspended bilayer graphene. *Phys. Rev. Lett.* **108** 076602.

GAMBIT Collaboration (Athron, P. *et al.*) (2017): Status of the scalar singlet dark matter model. *Eur. Phys. J. C* **77** 568.

GAMBIT Collaboration (Athron, P. *et al.*) (2019): Global analyses of Higgs portal singlet dark matter models using GAMBIT. *Eur. Phys. J. C* **79** 38.

Gehring, F.; Gies, H.; and Janssen, L. (2015): Fixed-point structure of low-dimensional relativistic fermion field theories: Universality classes and emergent symmetry. *Phys. Rev. D* **92** 085046.

Gies, H.; Janssen, L.; Rechenberger, S.; and Scherer, M. M. (2010): Phase transition and critical behavior of $d = 3$ chiral fermion models with left-right asymmetry. *Phys. Rev. D* **81** 025009.

Gies, H.; and Jaeckel, J. (2006): Chiral phase structure of QCD with many flavors *Eur. Phys. J. C* **46** 433.

Gies, H.; and Janssen, L. (2010): UV fixed-point structure of the three-dimensional Thirring model. *Phys. Rev. D* **82** 085018.

Gies, H.; Knorr, B.; Lippoldt, S.; and Saueressig, F. (2016): Gravitational Two-Loop Counterterm Is Asymptotically Safe. *Phys. Rev. Lett.* **116** 211302.

Gies, Holger and Scherer, Michael M. (2010): Asymptotic safety of simple Yukawa systems. *Eur. Phys. J. C* **66** 387.

Gies, H.; and Wetterich, C. (2002): Renormalization flow of bound states. *Phys. Rev. D* **65** 065001.

Gonderinger, M.; Li, Y.; Patel, H.; and Ramsey-Musolf, M. J. (2010): Vacuum Stability, Perturbativity, and Scalar Singlet Dark Matter. *J. High Energy Phys.* **01** 053.

Gorbenko, V.; Rychkov, S.; and Zan, B. (2018): Walking, weak first-order transitions, and complex CFTs. *J. High Energy Phys.* **2018** 108.

Gorbenko, V.; Rychkov, S.; and Zan, B. (2018): Walking, Weak first-order transitions, and Complex CFTs II. Two-dimensional Potts model at $Q > 4$ *SciPost Phys.* **5** 050.

Gorishnii, S. G.; Larin, S. A.; Surguladze, L. R.; and Tkachov, F. V. (1989): Mincer: Program for Multiloop Calculations in Quantum Field Theory for the Schoonschip System. *Comput. Phys. Commun.* **55** 381.

Gracey, J. A. (1991): Calculation of exponent η to $O(1/N^2)$ in the $O(N)$ Gross Neveu model. *Int. J. Mod. Phys. A* **06** 395.

Gracey, J. A. (1994a): Computation of $\beta'(g_c)$ at $O(1/N^2)$ in the $O(N)$ Gross Neveu model in arbitrary dimensions. *Int. J. Mod. Phys. A* **09** 727.

Gracey, J. A. (1994b): Computation of critical exponent η at $O(1/N^3)$ in the four-Fermi model in arbitrary dimensions. *Int. J. Mod. Phys. A* **9** 727.

Gracey, J. A. (2018): Large N critical exponents for the chiral Heisenberg Gross-Neveu universality class. *Phys. Rev. D* **97** 105009.

Gracey, J. A. (2021): Generalized Gross-Neveu universality class with non-abelian symmetry. *SIGMA* **17** 064.

Gracey, J. A.; Herbut, I. F.; and Roscher, D. (2018): Tensor O(N) model near six dimensions: Fixed points and conformal windows from four loops. *Phys. Rev. D* **98** 096014.

Gracey, J. A.; Luthe, T.; and Schröder, Y. (2016): Four loop renormalization of the Gross-Neveu model. *Phys. Rev. D* **94** 125028.

Groote, S.; Körner, J. G.; and Pivovarov, A. A. (1999): On the evaluation of sunset-type Feynman diagrams. *Nucl. Phys. B* **542** 515.

Grosse, H.; and Wulkenhaar, R. (2005): Renormalisation of ϕ^4-theory on noncommutative $\mathbb{R}^4$ in the matrix base. *Comm. Math. Phys.* **256** 305.

Gross, D. J.; and Neveu, A. (1974): Dynamical symmetry breaking in asymptotically free field theories. *Phys. Rev. D.* **10** 3235.

Guida, R.; and Zinn-Justin, J. (1998): Critical exponents of the N-vector model. *J. Phys. A: Math. Gen.* **31** 8103.

Harlander, R.; Seidensticker, T.; and Steinhauser, M. (1998): Corrections of $\mathcal{O}(\alpha\alpha_s)$ to the Decay of the Z Boson into Bottom Quarks. *Phys. Lett. B* **426** 125.

Halperin, B. I.; Lubensky, T. C.; and Ma, S.-K. (1974): First-Order Phase Transitions in Superconductors and Smectic-A Liquid Crystals. *Phys. Rev. Lett.* **32** 292.

Hamada, Y.; Tsumura, K.; and Yamada, M. (2020): Scalegenesis and fermionic dark matters in the flatland scenario. *Eur. Phys. J. C* **80** 368.

Hands, S.; Kocic, A.; and Kogut, J. B. (1993): Four-Fermi theories in fewer than four dimensions. *Ann. Phys. (N. Y.)* **224** 29.

Hands, S. J.; Kogut, J. B.; Scorzato, L.; and Strouthos, C. G. (2004): Non-compact three-dimensional quantum electrodynamics with $N_f = 1$ and $N_f = 4$. *Phys. Rev. B* **70** 104501.

Harst, U.; and Reuter, M. (2011): QED coupled to QEG. *J. High Energy Phys.* **05** 119.

Hasenbusch, M. (2019): Monte Carlo study of an improved clock model in three dimensions. *Phys. Rev. B* **100** 224517.

Hasenfratz, A.; and Hasenfratz, P. (1992): The Equivalence of the $SU(N)$ Yang-Mills theory with a purely fermionic model. *Phys. Lett. B* **297** 166.

He, Y. C.; Bhattacharjee, S.; Pollmann, F.; and Moessner, R. (2015): Kagome chiral spin liquid as a gauged U(1) symmetry protected topological phase. *Phys. Rev. Lett.* **115** 267209.

Held, A. (2020): Effective asymptotic safety and its predictive power: Gauge-Yukawa theories. *arXiv:2003.13642.*

Held, A.; and Sondenheimer, R. (2019): Higgs stability-bound and fermionic dark matter. *J. High Energy Phys.* **02** 166.

Hermele, M.; Fisher, M. P.; and Balents, L. (2004): Pyrochlore photons: The U(1) spin liquid in a $S = 1/2$ three-dimensional frustrated magnet. *Phys. Rev. B* **69** 064404.

Hermele, M.; Senthil, T.; and Fisher, M. P. (2005): Algebraic spin liquid as the mother of many competing orders. *Phys. Rev. B* **72** 104404.

Herbut, I. F. (2002): QED_3 theory of underdoped high-temperature superconductors. *Phys. Rev. B* **66** 094504.

Herbut, I. F. (2006): Interactions and phase transitions on graphene's honeycomb lattice. *Phys. Rev. Lett.* **97** 146401.

Herbut, I. F. (2007): *A modern approach to critical phenomena.* Cambridge, Cambridge University Press.

Herbut, I. F. (2016): Chiral symmetry breaking in three-dimensional quantum electrodynamics as fixed point annihilation. *Phys. Rev. D* **94** 025036.

Herbut, I. F. and Janssen, L. (2014): Topological Mott insulator in three-dimensional systems with quadratic band touching. *Phys. Rev. Lett.* **113** 106401.

Herbut, I. F.; Juricič, V.; and Roy, B. (2009): Theory of interacting electrons on the honeycomb lattice. *Phys. Rev. B* **79** 085116.

Herbut, I. F.; Juričić, V.; and Vafek, O. (2009): Relativistic Mott criticality in graphene. *Phys. Rev. B* **80** 075432.

Hesselmann, S.; Honerkamp, C.; Wessel, S.; and Lang, T. C. (2020): Quantifying the fragility of unprotected quadratic band crossing points. *Phys. Rev. B* **101** 075128.

Hoang, André H. (2020): What is the Top Quark Mass? *Ann. Rev. Nucl. Part. Sci.* **70** 225.

Höfling, F. and Nowak, C. and Wetterich, C. (2002): Phase transition and critical behavior of the $d = 3$ Gross-Neveu model. *Phys. Rev. B* **66** 205111.

Hollik, W.; and Stöckinger, D. (2001): Regularization and supersymmetry-restoring counterterms in supersymmetric QCD. *Eur. Phys. J C* **20** 105.

Hollowood, T. (2013): *Renormalization Group and Fixed Points in Quantum Field Theory.* Heidelberg, Springer.

Honerkamp, C. (2017): Influence of hopping self-energy effects and quasiparticle degradation on the antiferromagnetic ordering in the bilayer honeycomb Hubbard model. *Phys. Rev. B* **96** 245134.

Ihrig, B. (2021): *Deconfined Quantum Critical Behavior of Dirac Materials* (PhD thesis, Universität zu Köln).

Ihrig, B.; Mihaila, L. N.; and Scherer, M. M. (2018): Critical behavior of Dirac fermions from perturbative renormalization. *Phys. Rev. B* **98** 125109.

Ihrig, B.; Zerf, N.; Marquard, P.; Herbut, I. F.; and Scherer, M. M. (2019): Abelian Higgs model at four loops, fixed-point collision, and deconfined criticality. *Phys. Rev. B* **100** 134507.

Iliesiu, L.; Kos, F.; Poland, D.; Pufu, S. S.; and Simmons-Duffin, D. (2018): Bootstrapping 3D fermions with global symmetries. *J. High Energy Phys.* **2018** 36.

Janssen, L. (2016): Spontaneous breaking of Lorentz symmetry in $(2 + \varepsilon)$-dimensional QED. *Phys. Rev. D* **94** 094013.

Janssen, L.; and Gies, H. (2012): Critical behavior of the $(2 + 1)$-dimensional Thirring model. *Phys. Rev. D* **86** 105007.

Janssen, L.; and He, Y.-C. (2017): Critical behavior of the QED_3-Gross-Neveu model: Duality and deconfined criticality. *Phys. Rev. B* **96** 205113.

Janssen, L.; and Herbut, I. F. (2014): Antiferromagnetic critical point on graphene's honeycomb lattice: A functional renormalization group approach. *Phys. Rev. B* **89** 205403.

Janssen, L.; Herbut, I. F. (2015): Nematic quantum criticality in three-dimensional Fermi system with quadratic band touching. *Phys. Rev. B* **92** 045117.

Janssen, L.; and Herbut, I. F. (2016): Critical O(2) and O(3) ϕ^4 theories near six dimensions. *Phys. Rev. D* **93** 085005.

Janssen, L.; and Herbut, I. F. (2016): Excitonic instability of three-dimensional gapless semiconductors: Large-N theory. *Phys. Rev. B* **93** 165109.

Janssen, L.; Herbut, I. F. (2017): Phase diagram of electronic systems with quadratic Fermi nodes in $2 < d < 4$: $2 + \epsilon$ expansion, $4 - \epsilon$ expansion, and functional renormalization group. *Phys. Rev. B* **95** 075101.

Janssen, L.; Herbut, I. F.; and Scherer, M. M. (2018): Compatible orders and fermion-induced emergent symmetry in Dirac systems. *Phys. Rev. B* **97** 041117(R).

Janssen, L.; Wang, W.; Scherer, M. M.; Meng, Z. Y.; and Xu, X. Y. (2020): Confinement transition in the QED$_3$-Gross-Neveu-XY universality class. *Phys. Rev. B* **101** 235118.

Jung, J.; Zhang, F.; and MacDonald, A. H. (2011): Lattice theory of pseudospin ferromagnetism in bilayer graphene: Competing interaction-induced quantum Hall states. *Phys. Rev. B* **83** 115408.

Kadanoff, L. P. (1966): Scaling laws for Ising models near T_c. *Phys. Phys. Fiz.* **2** 263.

Kaplan, D. B.; Lee, J. W.; Son, D. T.; and Stephanov, M. A. (2009): Conformality lost. *Phys. Rev. D* **80** 125005.

Karthik, N.; and Narayanan, R. (2016): Scale invariance of parity-invariant three-dimensional QED. *Phys. Rev. D* **94** 065026.

Katsnelson, M. (2006): Zitterbewegung, chirality, and minimal conductivity in graphene. *Eur. Phys. J B* **51** 157.

Kharitonov, M. (2012): Antiferromagnetic state in bilayer graphene. *Phys. Rev. B* **86** 195435.

Khoze, V. V.; McCabe, C.; and Ro, G. (2014): Higgs vacuum stability from the dark matter portal. *J. High Energy Phys.* **08** 026.

Kitaev, A. (2003): Anyons in an exactly solved model and beyond. *Ann. Phys.* **321** 2.

Kluth, Y.; and Litim, D. F. (2020): Fixed Points of Quantum Gravity and the Dimensionality of the UV Critical Surface. *arXiv:2008.09181.*

Knorr, B. (2016): Ising and Gross-Neveu model in next-to-leading order. *Phys. Rev. B* **94** 245102.

Knorr, B. (2018): Critical chiral Heisenberg model with the functional renormalization group. *Phys. Rev. B* **97** 075129.

Knorr, B. (2021): The derivative expansion in asymptotically safe quantum gravity: general setup and quartic order. *arXiv:2104.11336.*

Knorr, B.; and Lippoldt, S. (2017): Correlation functions on a curved background. *Phys. Rev. D* **96** 065020.

Kompaniets, M. V.; and Panzer, E. (2017): Minimally subtracted six loop renormalization of O(n)-symmetric ϕ^4 theory and critical exponents. *Phys. Rev. D* **96** 036016.

Kowalska, K.; and Sessolo, E. M. (2021): Minimal models for g-2 and dark matter confront asymptotic safety. *Phys. Rev. D* **103** 115032.

Kowalska, K.; Sessolo, E. M.; and Yamamoto, Y. (2021): Flavor anomalies from asymptotically safe gravity. *Eur. Phys. J. C* **81** 272.

Krnjaic, G. (2016): Probing Light Thermal Dark-Matter With a Higgs Portal Mediator.

Phys. Rev. D **94** 073009.

Kuipers, J. and Ueda, T. and Vermaseren, J. A. M. and Vollinga, J. (2013): FORM version 4.0. *Comput. Phys. Commun.* **184** 1453.

Kwapisz, J. H. (2019): Asymptotic safety, the Higgs boson mass, and beyond the standard model physics. *Phys. Rev. D* **100** 115001.

Laiho, J.; Bassler, S.; Coumbe, D.; Du, D.; Neelakanta, J. T. (2017): Lattice Quantum Gravity and Asymptotic Safety. *Phys. Rev. D* **96** 064015.

Lang, T. C.; Meng, Z. Y.; Scherer, M. M.; Uebelacker, S.; Assaad, F. F.; Muramatsu, A.; Honerkamp, C.; and Wessel, S. (2012): Antiferromagnetism in the Hubbard model on the Bernal-stacked honeycomb bilayer. *Phys. Rev. Lett.* **109** 126402.

Landau, L. D.; and Lifshitz, E. M. (2013): *Course of Theoretical Physics* (Vol. 5, 3rd rev. edn) (J. B. Sykes and M. J. Kearsley, Trans.). London, Pergamon Press.

Larin, S. A.; Tkachov, F. V.; and Vermaseren, J. A. M. (1991): The FORM version of MINCER. *NIKHEF-H–91-18.*

Lauscher, O.; and Reuter, M. (2005): Fractal spacetime structure in asymptotically safe gravity. *J. High Energy Phys.* **10** 050.

Leaw, J. N.; Tang, H.-K.; Sengupta, P.; Assaad, F. F.; Herbut I. F.; and Adam, S. (2019): Electronic ground state in bilayer graphene with realistic Coulomb interactions. *Phys. Rev. B* **100** 125116.

Lebedev, O. (2012): On Stability of the Electroweak Vacuum and the Higgs Portal. *Eur. Phys. J. C* **72** 2058.

Lemonik, Y.; Aleiner, I. L.; Toke, C.; and Fal'ko, V. I. (2010): Spontaneous symmetry breaking and Lifshitz transition in bilayer graphene. *Phys. Rev. B* **82** 201408(R).

Lemonik, Y.; Aleiner, I.; and Fal'ko, V. I. (2012): Competing nematic, antiferromagnetic, and spin-flux orders in the ground state of bilayer graphene *Phys. Rev. B* **85** 245451.

Léonard, F.; and Delamotte, B. (2015): Critical exponents can be different on the two sides of a transition: A generic mechanism. *Phys. Rev. Lett.* **115** 200601.

Lipa, J. A.; Nissen, J. A.; Stricker, D. A.; Swanson, D. R.; and Chui, T. C. P. (2003): Specific heat of liquid helium in zero gravity very near the lambda point. *Phys. Rev. B* **68** 174518.

Lisanti, M. (2016): Lectures on Dark Matter Physics. In Polchinski, J.; and Vieira, P. (eds.): *New Frontiers in Fields and Strings*, pp. 399. London, World Scientific.

Litim, D. F. (2001): Optimized renormalization group flows. *Phys. Rev. D* **64** 105007.

Litim, D. F.; and Vergara, L. (2004): Subleading critical exponents from the renormalisation group. *Phys. Lett. B* **581** 263.

Liu, Z. H.; Vojta, M.; Assaad, F. F.; and Janssen, L. (2021): Exotic quantum criticality in Dirac systems: Metallic and deconfined. *arXiv:2108.06346.*

Loll, R. (2020): Quantum Gravity from Causal Dynamical Triangulations: A Review. *Class. Quant. Grav.* **37** 013002.

Luperini, C.; and Rossi, P. (1991): Three-loop β function(s) and effective potential in the Gross-Neveu model. *Ann. Phys. (N. Y.)* **212** 371.

Luttinger, J. M. (1956): Quantum theory of cyclotron resonance in semiconductors: General theory. *Phys. Rev.* **102** 1030.

Mahan, G. D. (2000): *Many-Particle Physics* (3rd edn.). New York (USA), Kluwer Academic/Plenum Publishers.

Martin, J.; Feldman, B. E.; Weitz, R. T.; Allen, M. T.; and Yacoby, A.

(2010): Local Compressibility Measurements of Correlated States in Suspended Bilayer Graphene. *Phys. Rev. Lett.* **105** 256806.

Mayorov, A. S.; Elias, D. C.; Mucha-Kruczynski, M.; Gorbachev, R. V.; Tudorovskiy, T.; Zhukov, A.; Morozov, S. V.; Katsnelson, M. I.; Fal'ko, V. I.; Geim, A. K.; and Novoselov, K. S. (2011): Interaction-driven spectrum reconstruction in bilayer graphene. *Science* **333** 860.

McCann, E.; and Fal'ko, V. I. (2006): Landau-level degeneracy and quantum Hall effect in a graphite bilayer. *Phys. Rev. Lett.* **96** 086805.

McCann, E.; and Koshino, M. (2013): The electronic properties of bilayer graphene. *Rep. Prog. Phys.* **76** 056503.

McDonald, J. (1994): Gauge singlet scalars as cold dark matter. *Phys. Rev. D* **50** 3637.

Meibohm, J.; Pawlowski, J. M.; and Reichert, M. (2016): Asymptotic safety of gravity-matter systems. *Phys. Rev. D* **93** 084035.

Migdal, A. A. (1976): Recursion equations in gauge field theories. *Sov. Phys. JETP* **42** 743.

Mihaila, L. N.; Zerf, N.; Ihrig, B.; Herbut, I. F.; and Scherer, M. M. (2017): Gross-Neveu-Yukawa model at three loops and Ising critical behavior of Dirac systems. *Phys. Rev. B* **96** 165133.

Moon, E. G.; Xu, C.; Kim, Y. B.; and Balents, L. (2013): Non-Fermi-liquid and topological states with strong spin-orbit coupling. *Phys. Rev. Lett.* **111** 206401.

Morris, T. R. (1994): The exact renormalization group and approximate solutions. *Int. J. Mod. Phys. A* **09** 2411.

Morris, T. R.; and Percacci, R. (2019): Trace anomaly and infrared cutoffs. *Phys. Rev. D* **99** 105007.

Nahum, A.; Chalker, J. T.; Serna, P.; Ortuño, M.; and Somoza, A. M. (2015): Deconfined Quantum Criticality, Scaling Violations, and Classical Loop Models. *Phys. Rev. X* **5** 041048.

Nakai, R.; Ryu, S.; and Furusaki, A. (2012): Time-reversal symmetric Kitaev model and topological superconductor in two dimensions. *Phys. Rev. B* **85** 155119.

Narain, G.; and Percacci, R. (2010): Renormalization Group Flow in Scalar-Tensor Theories I. *Class. Quant. Grav.* **27** 075001.

Nogueira, P. (1993): Automatic Feynman graph generation. *J. Comput. Phys.* **105** 279.

Natori, W. M.; and Knolle, J. (2020): Dynamics of a two-dimensional quantum spin-orbital liquid: spectroscopic signatures of fermionic magnons. *Phys. Rev. Lett.* **125** 067201.

Nogueira, P. (2006): Abusing QGRAF. *Nucl. Instrum. Methods Phys. Res. A* **559** 220.

Novoselov, K. S.; Geim, A. K.; Morozov, S.; Jiang, D.; Zhang, Y.; Dubonos, S.; Grigorieva, I.; and Firsov, A. (1994): Electric field effect in atomically thin carbon films. *Science* **306** 666.

Oda, K.-Y.; and Yamada, M. (2016): Non-minimal coupling in Higgs–Yukawa model with asymptotically safe gravity. *Class. Quant. Grav.* **33** 125011.

Otsuka, Y.; Yunoki, S.; and Sorella, S. (2016): Universal quantum criticality in the metal-insulator transition of two-dimensional interacting Dirac electrons. *Phys. Rev. X* **6** 011029.

Toldin, F. P.; Hohenadler, M.; Assaad, F. F.; and Herbut, I. F. (2015): Fermionic quantum criticality in honeycomb and π-flux Hubbard models: Finite-size scaling of renormalization-group-invariant observables from quantum Monte Carlo. *Phys. Rev. B* **91** 165108.

Parisi, G. (1972): On self-consistency conditions in conformal covariant field theory. *Lett. Nuovo Cimento* **4** 777.

Pawlowski, J. M.; and Reichert, M. (2020): Quantum gravity: a fluctuating point of view. *arXiv:2007.10353.*

Pawlowski, J. M.; Reichert, M.; Wetterich, C.; and Yamada, M. (2019): Higgs scalar potential in asymptotically safe quantum gravity. *Phys. Rev. D* **99** 086010.

Particle Data Group (K. Hagiwara *et al.*) 2002 Review of Particle Physics. *Phys. Rev. D* **66** 010001.

Particle Data Group (Patrignani, C. *et al.*) (2016): Review of Particle Physics. *Chin. Phys. C* **40** 100001.

Particle Data Group (Zyla, P. A. *et al.*) (2020): Review of Particle Physics. *PTEP* **2020** 083C01.

Percacci, R. (2017): *An Introduction to Covariant Quantum Gravity and Asymptotic Safety* (100 Years of General Relativity, Vol. 3). London, World Scientific.

Percacci, R.; and Vacca, G. P. (2015): Search of scaling solutions in scalar-tensor gravity. *Eur. Phys. J. C* **75** 188.

Persic, M.; Salucci, P.; and Stel, F. (1996): The Universal rotation curve of spiral galaxies: 1. The Dark matter connection. *Mon. Not. Roy. Astron. Soc.* **281** 27.

di Pietro, L.; Komargodski, Z.; Shamir, I.; and Stamou, E. (2016): Quantum Electrodynamics in $d = 3$ from the ϵ expansion. *Phys. Rev. Lett.* **116** 131601.

Pitrou, C.; Coc, A.; Uzan, J.-P.; and Vangioni, E. (2018): Precision big bang nucleosynthesis with improved Helium-4 predictions. *Phys. Rept.* **754** 1.

Polchinski, J. (1984): Renormalization and Effective Lagrangians. *Nucl. Phys. B* **231** 269.

Polchinski, J. (1992): Effective Field Theory and the Fermi Surface. *arXiv:hep-th/9210046.*

Polyakov, A. M. (1970): Conformal symmetry of critical fluctuations. *JETP Lett.* **12** 381.

Polyakov, A. M. (2012): *Quarks, strings and beyond.* In Cappelli, A.; Castellani, E.; Colomo, F.; and di Vecchia, P. (eds.): *The Birth of String Theory*, Chap. 44, pp. 544. Cambridge, Cambridge University Press.

Pujari, S.; Lang, T. C.; Murthy, G.; and Kaul, R. K. (2016): Interaction-induced Dirac fermions from quadratic band touching in bilayer graphene. *Phys. Rev. Lett.* **117** 086404.

Ran, Y.; Hermele, M.; Lee, P. A.; and Wen, X. G. (2007): Projected-wave-function study of the spin-1/2 heisenberg model on the kagomé lattice. *Phys. Rev. Lett.* **98** 117205.

Raviv, O.; Shamir, Y.; and Svetitsky, B. (2014): Nonperturbative beta function in three-dimensional electrodynamics. *Phys. Rev. D* **90** 014512.

Reichert, M. (2020): Lecture notes: Functional Renormalisation Group and Asymptotically Safe Quantum Gravity. *PoS Proc. Sci.* **384** 005

Reichert, M.; and Smirnov, J. (2020): Dark Matter meets Quantum Gravity. *Phys. Rev. D* **101** 063015.

Reisser, R.; Kremer, R. K.; and Simon, A. (1995): Magnetic phase transition in the metal-rich rare-earth carbide halides $\mathrm{Gd}_2X\mathrm{C}$ ($X = \mathrm{Br, I}$) *Phys. Rev. B* **52** 3546.

Reuter, M. (1998): Nonperturbative evolution equation for quantum gravity. *Phys. Rev. D* **57** 971.

Reuter, M.; and Saueressig, F. (2002): Renormalization group flow of quantum gravity in the Einstein-Hilbert truncation *Phys. Rev. D* **65** 065016.

Reuter, M.; and Saueressig, F. (2019): *Quantum Gravity and the Functional Renormalization Group: The Road towards Asymptotic Safety.* Cambridge, Cambridge University Press.

Rosa, L.; Vitale, P; and Wetterich, C. (2001): Critical Exponents of the Gross-Neveu Model from the Effective Average Action. *Phys. Rev. Lett.* **86** 958.

Roscher, D.; and Herbut, I. F. (2018): Critical O(2) field theory near six dimensions beyond one loop. *Phys. Rev. D* **97** 116019.

Rosenstein, B.; Yu, H.-L.; and Kovner, A. (1993): Critical exponents of new universality classes. *Phys. Lett. B* **314** 381.

Roszkowski, L.; Sessolo, E. M.; and Trojanowski, S. (2018): WIMP dark matter candidates and searches—current status and future prospects. *Rept. Prog. Phys.* **81** 066201.

Roy, B.; Juričić, V.; and Herbut, I. F. (2016): Emergent Lorentz symmetry near fermionic quantum critical points in two and three dimensions. *J. High Energy Phys.* **2016** 04.

Ruijl, B.; Ueda, T.; and Vermaseren, J. A. M. (2017): FORM version 4.2. *arXiv:1707.06453.*

Rychkov, S. (2017): *EPFL Lectures on Conformal Field Theory in $D \geqslant 3$ Dimensions.* Springer Nature.

Sachdev, S. (2010): *Quantum Phase Transitions* (2nd edn). Cambridge, Cambridge University Press.

Sachdev, S. (2010): Where is the quantum critical point in the cuprate superconductors? *Phys. Status Solidi B* **247** 537.

Savary, L.; Moon, E. G.; and Balents, L. (2014): New type of quantum criticality in the pyrochlore iridates. *Phys. Rev. X* **4** 041027.

Scherer, D. D.; Braun, J.; and Gies, H. (2013): Many-flavor phase diagram of the $(2+1)d$ Gross-Neveu model at finite temperature. *J. Phys. A Math. Theor.* **46** 285002.

Scherer, M. M.; Uebelacker, S.; and Honerkamp, C. (2012): Instabilities of interacting electrons on the honeycomb bilayer. *Phys. Rev. B* **85** 235408.

Schwab, J.; Janssen, L.; Sun, K.; Meng, Z. Y.; Herbut, I. F.; Vojta, M.; and Assaad, F. F. (2021): Nematic quantum criticality in Dirac systems. *arXiv:2110.02668.*

Schwartz, M. D. (2014): *Quantum Field Theory and the Standard Model.* New York (USA), Cambridge University Press.

Schweber, S. S. (1994): *QED And The Men Who Made It: Dyson, Feynman, Schwinger And Tomonaga.* Princeton (New Jersey, USA), Princeton University Press.

Seidensticker, T. (1999): Automatic application of successive asymptotic expansions of Feynman diagrams. *arXiv:hep-ph/9905298.*

Seifert, U. F. P.; Dong, X. Y.; Chulliparambil, S.; Vojta, M.; Tu, H.-H.; and Janssen, L. (2020): Fractionalized fermionic quantum criticality in spin-orbital mott insulators. *Phys. Rev. Lett.* **125** 257202.

Shaposhnikov, M.; and Wetterich, C. (2010): Asymptotic safety of gravity and the Higgs boson mass. *Phys. Lett. B* **683** 196.

Shitade, A.; Katsura, H.; Kuneš, J.; Qi, X.-L.; Zhang, S.-C.; and Nagaosa, N. (2009): Quantum Spin Hall Effect in a Transition Metal Oxide Na_2IrO_3. *Phys. Rev. Lett.* **102** 256403.

Siegel, W. (2005): Fields. *arXiv:hep-th/9912205v3.*

Silveira, V.; and Zee, A. (1985): Scalar Phantoms. *Phys. Lett. B* **161** 136.

Sinner, A.; and Ziegler, K. (2010): Effect of the Coulomb interaction on the gap in monolayer and bilayer graphene. *Phys. Rev. B* **82** 165453.

Snyman, I.; and Beenakker, C. W. J. (2007): Ballistic transmission through a graphene bilayer. *Phys. Rev. B* **75** 045322.

Song, K. W.; Liang, Y. C.; and Haas, S. (2012): Excitonic instabilities and insulating states in bilayer graphene. *Phys. Rev. B* **86** 205418.

Stander, N.; Huard, B.; and Goldhaber-Gordon, D. (2009): Evidence for Klein tunneling in graphene pn junctions. *Phys. Rev. Lett.* **102** 26807.

Steele, T. G.; Wang, Z. W.; and McKeon, D. G. C. (2014): Multiscale renormalization group methods for effective potentials with multiple scalar fields. *Phys. Rev. D* **90** 105012.

Stöckinger, D. (2005): Regularization by dimensional reduction: consistency, quantum action principle, and supersymmetry. *J. High Energy Phys.* **2005** 03.

Stüsser, N.; Rekveldt, M. Th.; and Spruijt, T. (1985): Determination of the critical exponents β and γ in iron by neutron depolarization. *Phys. Rev. B* **31** 5905.

Sun, K.; Yao, H.; Fradkin, E.; and Kivelson, S. A. ((2009)): Topological insulators and nematic phases from spontaneous symmetry breaking in 2D Fermi systems with a quadratic band crossing. *Phys. Rev. Lett.* **104** 046811.

Sun, K.; Liu, W. V.; Hemmerich, A.; and Das Sarma, S. (2012): Topological semimetal in a fermionic optical lattice. *Nat. Phys.* **8** 67.

Sur, S.; Gong, S. S.; Yang, K.; and Vafek, O. (2018): Quantum anomalous Hall insulator stabilized by competing interactions. *Phys. Rev. B* **98** 125144.

Szabo, A.; and Roy, B. (2021): Extended Hubbard model in undoped and doped monolayer and bilayer graphene: Selection rules and organizing principle among competing orders. *Phys. Rev. B* **103** 205135.

't Hooft, G.; and Veltman, M. (1972): Regularization and renormalization of gauge fields. *Nucl. Phys. B* **44** 189.

Tiesinga, E.; Mohr, P. J.; Newell, D. B.; and Taylor, B. N. (2021): CODATA recommended values of the fundamental physical constants: 2018. *J. Phys. Chem. Ref. Data* **50** 033105.

Torres, E.; Classen, L.; Herbut, I. F.; and Scherer, M. M. (2018): Fermion-induced quantum criticality with two length scales in Dirac systems. *Phys. Rev. B* **97** 125137.

Torres, E.; Weber, L.; Janssen, L.; Wessel, S.; and Scherer, M. M. (2020): Emergent symmetries and coexisting orders in Dirac fermion systems. *Phys. Rev. Research* **2** 022005.

Uebelacker, S.; and Honerkamp, C. (2011): Instabilities of quadratic band crossing points. *Phys. Rev. B* **84** 205122.

Umetsu, K.; Zitrin, A.; Gruen, D.; Merten, J.; Donahue, M.; and Postman, M. (2016): CLASH: Joint Analysis of Strong-Lensing, Weak-Lensing Shear and Magnification Data for 20 Galaxy Clusters. *Astrophys. J.* **821** 116.

Vafek, O.; and Yang, K. (2010): Many-body instability of Coulomb interacting bilayer graphene: Renormalization group approach. *Phys. Rev. B* **81** 041401.

Vafek, O. (2010): Interacting fermions on the honeycomb bilayer: From weak to strong coupling. *Phys. Rev. B* **82** 205106.

Vasil'ev, A. N.; Pis'mak, Y. M.; and Honkonen, J. R. (1981a): Simple method of calculating the critical indices in the $1/n$ expansion. *Theor. Math. Phys.* **46** 104.

Vasil'ev, A. N. and Pis'mak, Yu. M. and Honkonen, J. R. (1981b): $1/n$ Expansion: Calculation of the exponents η and ν in the order $1/n^2$ for arbitrary number of dimensions. *Theor. Math. Phys.* **47** 465.

Vasil'ev, A. N. and Pis'mak, Yu. M. and Honkonen, J. R. (1982): $1/n$ Expansion:

Calculation of the exponent ν in the order $1/n^3$ by the Conformal Bootstrap Method. *Theor. Math. Phys.* **50** 127.

Vasil'ev, A. N.; Derkachev, S. E.; and Stepanenko, A. S. (1993): The $1/n$ expansion in the Gross-Neveu model: Conformal bootstrap calculation of the index η in order $1/n^3$ *Theor. Math. Phys.* **94** 127.

Vasil'ev, A. N.; and Stepanenko, A. S. (1993): The $1/n$ expansion in the Gross-Neveu model: Conformal bootstrap calculation of the exponent $1/\nu$ to the order $1/n^2$. *Theor. Math. Phys.* **97** 1349.

Velasco Jr., J.; Jing, L.; Bao, W.; Lee, Y.; Kratz, P.; Aji, V.; Bockrath, M.; Lau, C. N.; Varma, C.; Stillwell, R.; Smirnov, D.; Zhang, F.; Jung, J.; and MacDonald, A. H. (2012): Transport spectroscopy of symmetry-broken insulating states in bilayer graphene. *Nat. Nanotech.* **7** 156.

Veligura, A.; Van Elferen, H. J.; Tombros, N.; Maan, J. C.; Zeitler, U.; and Van Wees, B. J. (2012): Transport gap in suspended bilayer graphene at zero magnetic field. *Phys. Rev. B* **85** 155412.

Vermaseren, J.A.M. (2000): New features of FORM. *arXiv:math-ph/0010025.*

Vojta, M. (2003): Quantum phase transitions . *Rep. Prog. Phys.* **66** 2069.

Vojta, M. (2018): Frustration and quantum criticality. *Rep. Prog. Phys.* **81** 064501.

Vojta, M.; Zhang, Y.; and Sachdev, S. (2000): Competing orders and quantum criticality in doped antiferromagnets. *Phys. Rev. B* **62** 6721.

Vojta, M.; Zhang, Y.; and Sachdev, S. (2000): Quantum phase transitions in d-wave superconductors. *Phys. Rev. Lett.* **85** 4940.

Wang, C.; and Senthil, T. (2016): Time-reversal symmetric U(1) quantum spin liquids. *Phys. Rev. X* **6** 011034.

Wehling, T. O.; Şaşioğlu, E.; Friedrich, C.; Lichtenstein, A. I.; Katsnelson, M. I.; and Blügel, S. (2011): Strength of effective coulomb interactions in graphene and graphite. *Phys. Rev. Lett.* **106** 236805.

Weinberg, S. (1979): Ultraviolet divergences in quantum theories of gravitation. In Hawkin, S. W.; and Israel, W. (eds.): *General Relativity: An Einstein centenary survey* Chap. 16 pp. 790. Cambridge, Cambridge University Press.

Weitz, R. T.; Allen, M. T.; Feldman, B. E.; Martin, J.; and Yacoby, A. (2010): Broken-symmetry states in doubly gated suspended bilayer graphene. *Science* **330** 812.

Wetterich, C. (1991): Average action and the renormalization group equations. *Nucl. Phys. B* **352** 529.

Wetterich, C. (2021): Effective scalar potential in asymptotically safe quantum gravity. *Universe* **7** 45.

Wetterich, C.; and Yamada, M. (2017): Gauge hierarchy problem in asymptotically safe gravity–the resurgence mechanism. *Phys. Lett. B* **770** 268.

Wetterich, C.; and Yamada, M. (2019): Variable Planck mass from the gauge invariant flow equation. *Phys. Rev. D* **100** 066017.

Wilson, K. G. (1971): Renormalization Group and Critical Phenomena. I. Renormalization Group and the Kadanoff Scaling Picture. *Phys. Rev. B* **4** 3174.

Winter, S. M.; Tsirlin, A. A.; Daghofer, M.; van den Brink, J.; Singh, Y.; Gegenwart, P.; and Valentí, R. (2017): Models and materials for generalized Kitaev magnetism. *J. Phys.: Condens. Matter* **29** 493002.

Witczak-Krempa, W.; Chen, G.; Kim Y. B.; and Balents, L. (2014): Correlated Quantum Phenomena in the Strong Spin-Orbit Regime. *Annu. Rev. Condens. Matter Phys.* **5** 57.

WU, C.; AROVAS, D.; AND HUNG, H. H. (2009): Γ-matrix generalization of the Kitaev model. *Phys. Rev. B* **79** 134427.

YAO, H.; ZHANG, S. C.; AND KIVELSON, S. A. (2009): Algebraic spin liquid in an exactly solvable spin model. *Phys. Rev. Lett.* **102** 217202.

YOUNG, A.; AND KIM, P. (2009): Quantum interference and Klein tunnelling in graphene heterojunctions. *Nature Phys.* **5** 222.

ZENG, T. S.; ZHU, W.; AND SHENG, D. (2018): Tuning topological phase and quantum anomalous Hall effect by interaction in quadratic band touching systems. *npj Quantum Mater.* **3** 49.

ZERF, N.; MIHAILA, L. N.; MARQUARD, P.; HERBUT, I. F.; AND SCHERER, M. M. (2017): Four-loop critical exponents for the Gross-Neveu-Yukawa models. *Phys. Rev. D* **96** 096010.

ZHANG, L. M.; LI, Z. Q.; BASOV, D. N.; FOGLER, M. M.; HAO, Z.; AND MARTIN, M. C. (2008): Determination of the electronic structure of bilayer graphene from infrared spectroscopy. *Phys. Rev. B* **78** 235408.

ZHANG, F.; MIN, H.; POLINI, M.; AND MACDONALD, A. H. (2010): Spontaneous inversion symmetry breaking in graphene bilayers. *Phys. Rev. B* **81** 041402.

ZHU, W.; GONG, S. S.; ZENG, T. S.; FU, L.; AND SHENG, D. N. (2016): Interaction-driven spontaneous quantum Hall effect on a kagome lattice. *Phys. Rev. Lett.* **117** 096402.

ZIEBELL, J. (2021): Existence and construction of exact functional-renormalization-group flows of a UV-interacting scalar field theory. *Phys. Rev. D* **103** 025002.

ZIEBELL, J. (2021): A Rigorous Derivation of the Functional Renormalisation Group Equation. *arXiv:2106.09466.*

Acknowledgements

First and foremost, I am grateful for the opportunity to work with my supervisor Lukas Janssen during the course of my PhD studies. I would like to thank him for countless helpful discussions in and around theoretical physics, often going well beyond the confines of the particular project at hand, and sometimes beyond the confines of physics itself. It was all in all a very inspiring experience. I would also like to thank Matthias Vojta for co-supervising the first two projects (in a chronological sense) of this thesis, as well as for many enlightening discussions. My gratitude also extends to all current and former members of the condensed matter theory groups in Dresden for a very lively and stimulating atmosphere.

I thank Holger Gies for agreeing to referee this thesis.

This work has been supported by the Deutsche Forschungsgemeinschaft (DFG) through SFB 1143 (Project A07, Project id No. 247310070), the Würzburg-Dresden Cluster of Excellence ct.qmat (EXC2147, Project id No. 390858490), and the Emmy Noether programme (JA2306/4-1, Project id No. 411750675).

I am furthermore grateful to have had the opportunity to spend time on a research stay at the CP3 Origins in Odense; I wish to thank Astrid Eichhorn for her generous hospitality, and for a very enjoyable collaboration on the Higgs mass project. Likewise, I owe much thanks to the members of the quantum gravity group in Odense for immediately making me feel welcome amongst their midst and ensuring a very pleasant atmosphere throughout.

I wish to thank my scientific collaborators Bernhard Ihrig, Daniel Kruti, Michael Scherer, John Gracey and Martin Pauly.

I gratefully acknowledge instructive discussions with Dominik Stöckinger, Günter Plunien, Carsten Timm, Santanu Dey, Tobias Meng, Konstantinos Ladovrechis, Wilhelm Krüger and Clara Lapp.

Eidesstattliche Erklärung

Hiermit versichere ich, dass ich die vorliegende Arbeit ohne unzulässige Hilfe Dritter und ohne Benutzung anderer als der angegebenen Hilfsmittel angefertigt habe; die aus fremden Quellen direkt oder indirekt übernommen Gedanken sind als solche kenntlich gemacht. Die Arbeit wurde bisher weder im In- noch Ausland in gleicher oder ähnlicher Form einer anderen Prüfungsbehörde vorgelegt.

Diese Dissertation wurde am Institut für Theoretische Physik der Technischen Universität Dresden unter der wissenschaftlichen Betreuung von Dr. Lukas Janssen und Prof. Dr. Matthias Vojta angefertigt.

Ich erkenne die Promotionsordnung des Bereichs Mathematik und Naturwissenschaften der Technischen Universität Dresden vom 23.02.2011 an.

Dresden, den *Shouryya Ray*